Table of Contents

A Appendix – Task Force #2: Convective Weather

Note: *This appendix is a consolidated version of Appendix A from the report 2022 with additional results from 2023. The main author of this appendix is Christiane Schmidt.*

In this section of the appendix, we consider the effect of climate change on trends regarding convective storms (i.e., thunderstorms) and one of the phenomena associated with convective storms, hail, in detail. We start with a description of the development of these weather phenomena, we then discuss, both for hail and convective storms, the existing observation data, the proxies used, and we give an overview on the existing literature on future projections according to various greenhouse gas emission scenarios and highlight knowledge gaps and sources of uncertainty. Because dynamical downscaling could alleviate some of the problems with current projections for severe convective storms, we additionally detail the concept, existing research, and limitations. Finally, we give a preliminary review on results on the effect of climate change on lightning.

The main interest of aviation stakeholders in this topic are future projections for the middle of the 21st century. However, only a very limited number of studies for that time range has been performed: climate models give a clear picture for the end of the 21st century, but for the midcentury this is less clear, and researchers aim for statistically significant results. Thus, we do not only focus on projections for the midcentury in this appendix.

For the reader's convenience, we present some frequently-used acronyms in Table A.0.

Table A.0 Frequently-used acronyms in Appendix A

Acronym	Meaning	Definition
CAPE	Convective available potential energy	Describes the instability of the atmosphere
CIN	Convective inhibition	Amount of energy that will prevent an air parcel to rise from the surface level to the level of free convection
CMIP5/6	Coupled Model Intercomparison Project Phase 5/6	Global climate models from 20 research groups that are publically available
CONUS	Contiguous US	48 adjoining US states and the District of Columbia (US minus Alaska and Hawaii, and US territories)
dBz	Decibel relative to Z	Dimensionless logarithmic technical unit used in radar
ECMWF	European Centre for Medium-Range Weather Forecasts	
ERA5	ECMWF Reanalyis version 5	Fifth generation of the ECMWF atmospheric reanalysis of the global climate from January 940 to present
GCM	General ciruclation model (also global climate model)	Numerical climate model to simulate the response of the global climate system to increasing greenhouse gas

		concentrations; the horizontal resolution of their 3D grid is usually about 250-600km
HALO	Hail aloft	
HCW	Hazardous convective weather	
MLH	Melting level height	Altitude at which the temperature is 0°C and where ice crystals and snowflakes begin to melt as they descent through the atmosphere
MCS	Mesoscale convective systems	Complex of storms
NDSEV	Number of days in which severe thunderstorm environmental conditions appear	
NCEP/NCAR Reanalysis	Reanalysis data from a joint project between the National Centers for Environmental Prediction (NCEP) and the National Center for Atmospheric Research (NCAR)	Atmospheric reanalysis of the global climate from 1948 onwards
RCM	Regional climate model	Numerical climate model that simulates atmospheric and land-surface processes; covers only a limited spatial domain
RCP	Representative concentration pathway	Greenhouse-gas concentration trajectory, a method to capture assumptions about the economic, social and physical changes to our environment with a set of scenarios
S06	Deep tropsohperic wind shear	Magnitude of vector difference of wind at the 6km level to the wind above ground level
SCS	Severe convective storms	Minimum criteria defined in Section A.3
SigSCS	Significant severe convective storms	Minimum criteria defined in Section A.3

A.1 Development of Convective Activity and Associated Phenomena

In this subsection, we give a brief overview on the development of convective storms and their associated phenomena. For a more detailed introduction to these processes, we refer to, e.g., [1] [2] [3]. We refer to Figure A.1 and Figure A.2 for illustrations of (some of) the described processes.

Solar radiation heats up the Earth's surface unevenly because of different elevation levels, surface orientation to solar irradiation and different thermal properties of the surface (e.g., a large area of tarmac will heat up more than surrounding grassland). Instability occurs when less dense air with higher temperature than the surrounding parcels is lifted due to the net upward buoyancy force. Apart from local heating, this lifting of air parcels can be triggered by, for example, convergent winds, fronts and orographically driven circulations. The atmospheric conditions that allow the uplifting of air parcels are generally called an *unstable atmosphere*. In the process of rising, the air expands and cools adiabatically following the Dry Adiabatic Lapse Rate (DALR) of 9.8°C every kilometer. The air will continue to rise as long as the temperature of the air parcel exceeds the temperature of the surrounding air (and starts to sink once the temperature is below that of the surrounding air parcels), where the temperature of the atmosphere decreases with height. These rising masses of air are called thermals, thermal columns, or convective cells. If during the uplift the parcel becomes saturated (in the process of rising and cooling, the air parcel's temperature reaches its dew point and the relative humidity is 100%), the water vapor released from the air parcel condenses into cloud droplets. Hence, a cloud starts to form at that height that becomes the base of a cumulus cloud (lifting condensation level (LCL)). Starting at this point, the rising still cools the air parcel whilst the condensation process releases latent heat and warms the air parcel. Thus, the lapse rate is reduced (that is, the air still cools while rising, but in a lower rate) and the air parcel's buoyancy increases. With the rising air and the condensation of water vapor, the cloud grows upwards. Once the temperature of the air parcel drops below the temperature of the surrounding air, the cloud formation stops, and the air starts to sink—a downward flow of air that surrounds the thermal column (which will also happen if the dew point is not reached while rising). The warmer air column that created and sustains the cloud formation is called an updraft/updraught.

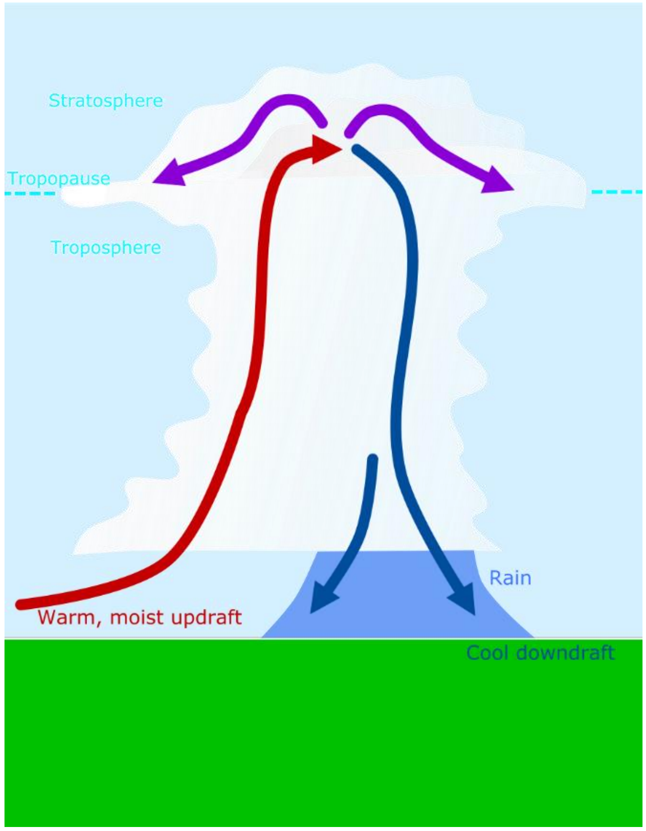

Figure A.1 Updraft, downdraft, and rain in a thunderstorm

If the convective cells grow tall enough (above the zero-degree isotherm), ice crystals will form at the top using ice nucleating particles (INPs), e.g., dust particles, as nuclei. The ice crystals coexist with supercooled cloud droplets, which are very small (with a size range of 10—50 microns to 1 millimeter, typically about 0.02 millimeters). As opposed to larger bodies of liquid water that freeze at 0°C, these microscopical pure water droplets can exist in the liquid state at temperatures down to -40°C—so-called supercooled water (because they do not have something to freeze onto). The melting level height (MLH) is the altitude at which the temperature is 0°C and ice crystals and snowflakes begin to melt as they descent through the atmosphere. A cumulonimbus cloud has three zones with ice at the top (cooler than -40°C), a mixture of ice and supercooled water below that, and, finally, at the bottom, below MLH, liquid water (warmer than 0°C). When ice crystals from the highest layer drift down (where we have a coexistence of water vapor, liquid water droplets and ice crystals), they grow at the expense of the liquid droplets (Bergeron process [4]). The crystals eventually grow heavy enough to fall to earth because of gravity. When they fall, these ice crystals will often pass the melting level, change phase to liquid, and fall as rain. Another process creates the precipitation in the warmer parts of the cloud: the small cloud droplets bump into each other and coalesce into larger droplets, when these become too large (max 5 millimeters), they break apart because of friction and air resistance into smaller, but still large, rain drops. The precipitation moving downwards drags the air molecules it finds in its path and creates a downward moving draft, the downdraft/downdraught, that comes out from the bottom of the cloud together with the precipitation. As soon as the rain drops leave the cloud, they enter an area with relative humidity below 100%, and evaporation takes place (removing latent heat), and the column of air and rain gets colder and denser. The drier the atmosphere below the base of the Cumulonimbus cloud is, the less precipitation is reaching the ground and the stronger the downdraft is.

(Note: Convective storms can be triggered by a different process in the tropics; this process is central for tropical cyclones [69].)

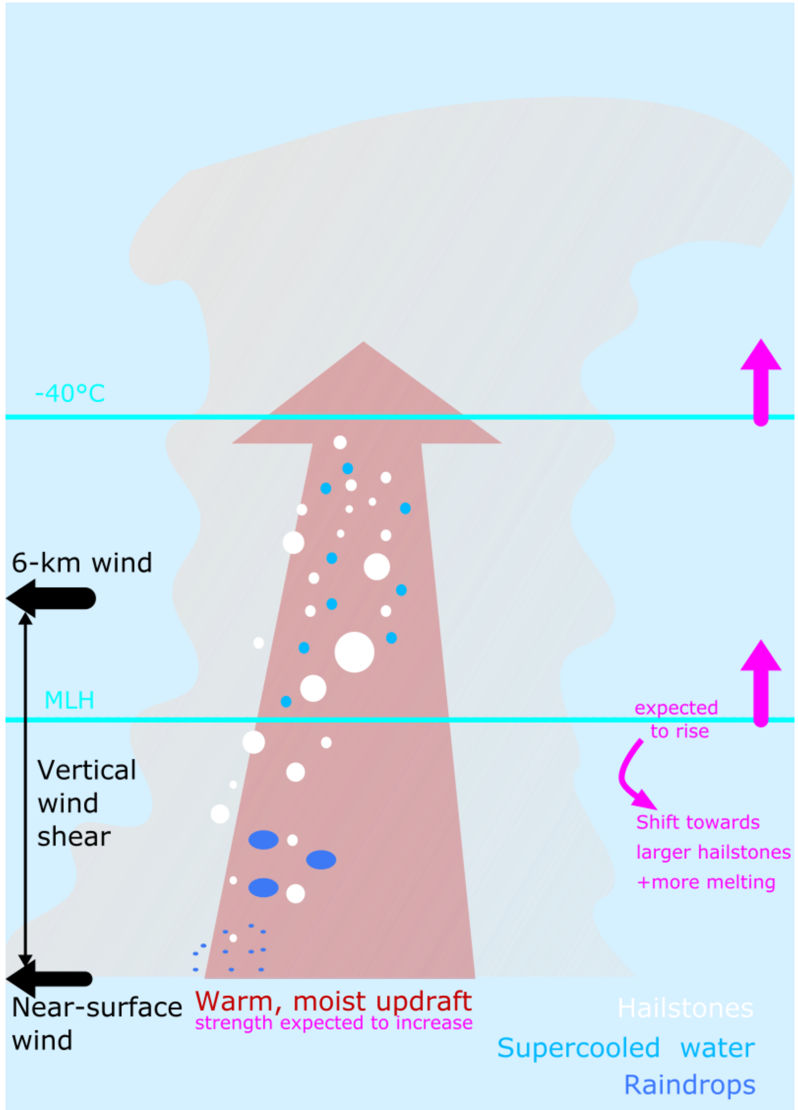

Figure A.2 Hail development and atmospheric phenomena relevant to hail. Expected future changes with climate change are indicated in pink.

A.1.1 Hazardous Winds in Convective Storms

The evaporation of rain at the cloud base produces cool air, which sinks and then spreads out reinforcing the downdraft; this is called a downburst, with the associated cold front referred to as a gust front. This downburst is spreading out from the cloud and encapsulates and eventually disrupts the warm, moist inflow, by which airmass thunderstorm cells cease to exist. However, the outflow may trigger other thunderstorms in the close vicinity of the storm.

The presence of wind shear in the atmospheric profile of the convective environment usually increases both the intensity and the lifespan of a storm—although it in some cases delays or hinders the initial development of the deep convection. Wind shear is the difference of the surface wind vector to a wind vector higher in the atmosphere (usually the 500hpa level), in magnitude or direction or both. The vertical wind shear yields changes of the storm's structure: the inflow and the outflow (from evaporative cooling) coexist but at two adjacent locations. This results in an organized storm structure and severe long-lived thunderstorms (associated with heavy rains, flooding, hail, lightning, tornadoes, gust-front winds).

A.1.2 Types of Convection

Depending on the strength of the vertical wind shear a spectrum of storm types can be distinguished [66,79]:

- In environments with weak wind shear, of less than 10 ms^{-1}, single cells of convection form. This is an isolated type of convection with a short live cycle of 30-60 minutes. Singlecellular convection is usually non-severe. The gust front is in this case unable to initiate new cells (at least in an organized way).
- In environments with a moderate vertical wind shear, 10-20 ms^{-1}, multicells are more likely to form. These storms often form as a complex of storms (a mesoscale convective system). The gust front repeatedly intitiates new cells. Multicells have a live cycle of multiple hours and can produce strong winds, flash floods and large hail.
- In an environment with strong vertical wind shear of around 20 ms^{-1} or higher, supercells can form. These usually last multiple hours and are characterized by a single persistent rotating updraft. Supercells are very rare, but responsible for many severe weather occurences as strong downbursts, large and very large hail, heavy precipitation and tornadoes.

A.1.3 Formation of Hail (see [5], [6])

The processes of initiation, growth and melting of hailstones are called microphysical processes. Hailstones grow from hail embryos (ice particles), when these collide with supercooled liquid: the supercooled water freezes onto the hail embryo's surfaces, during which latent heat is released. Thus, the hail embryos growing from collisions with supercooled liquid have a higher surface temperature than the surrounding air. The process of heating up is counterbalanced by cooling from heat transfer to the surrounding air by conduction (and possibly evaporation). There are two mechanisms for hailstone growth: the dry and the wet growth.

Dry growth: the main requirement of dry growth is that all accreted mass is either frozen or freezes completely after collection. No vapor diffusion and accretion of liquid (which subsequently freezes) result in latent heat release. For dry growth, the temperature of the ice particle must remain below the freezing point of water so that the surface remains dry (solid ice). The density of the added mass may be at a different density than that of the ice particle. For example, rime density can be as low as 170 kg/m3 or as high as 917 kg/m3 (solid ice).

Wet growth: during wet growth, large ice particles collect significant amounts of supercooled liquid water, some of which does not freeze because latent heat release warms the ice particle to the freezing point. Vapor diffusion and accretion of liquid (which subsequently freezes) result in latent heat release. For wet growth, the latent heat release that results from vapor diffusion and freezing of collected supercooled water is significant enough so that the ice particle's surface temperature rises to 273.15K (0°C), the freezing point of water. The unfrozen water can remain on the ice-particle surface, soak porous ice (re-densification), or be shed as droplets. The wet ice surface during wet growth results in efficient ice-ice sticking. This results in efficient mixed-phase growth. Wet growth is most likely for large ice particles in regions with larger liquid water contents (> 1 g/kg) and temperatures above -25°C.

While it is clear that large hailstones cause more harm—for a (spherical) hailstone of diameter *d* the kinetic energy is approximately proportional to d^4 [7]—the size of a hailstone depends on several factors. In the hail-growth region, there must be enough supercooled water that the hailstone can collect for it to be able to grow to a large hailstone. Moreover, if we have a high concentration of hail embryos, these compete for the supercooled water and cannot grow into larger hailstones. Additionally, the hailstone must have enough time to grow, and the time increases the stronger the updraught. In addition, the embryo's trajectory must spend as much time as possible in the region of the updraught with a lot of supercooled water [8]. For this, the hailstones fall speed must be at most the speed of the updraught suspending it (if it is above this limit, the hailstone is no longer supported by the storm), so, the updraught speed limits the hailstone size. However, if the updraught is too strong, the embryo might get ejected from the growth region, thus, large hailstones are associated with a broad, moderate-strength rotating updraught. Moreover, vertical wind shear influences both the hail embryo and the trajectory within the growth region with high impact of the size of the hailstone. Finally, for hail reaching the Earth's surface, the hailstone size is reduced by the melting below the MLH: small hailstones melt more easily completely until the surface than large hailstones, thus, hailstone sizes distributions (for hailstones reaching the Earth's surface) are shifted towards larger hailstones [9].

If we have many hail embryos that compete for supercooled liquid, but low-strength updraught and little growth time, it is possible to have many small hailstones.

A.2 Hail Trends

For hail, in contrast to many other weather phenomena, an overview article by Raupach et al. [5] entitled "The effects of climate change on hailstorms" (convective storms with hail) appeared in Nature Reviews Earth & Environment in 2021. We had meetings with four authors of this study [10] [11], and the paper plus these interviews/discussions build the major foundation for this section.

While several projections for hail in different parts of the world exist, and also some (more or less scarce) observational records (see Section 1.2.1), these usually concern surface hail, that is, the hail that reaches Earth's surface. Hail exceeding a diameter of 2cm when reaching the earth's surface is considered as severe hail. For a (spherical) hailstone of diameter d the kinetic energy is approximately proportional to d^4.

A.2.1 Past Trends

Hail is a local and rare event at any given point (in space and time)—it appears during at most 18 days during a year at any given location [10]. Consequently, any observational records are sparse.

Prein and Heymsfield [12], found that during 1979-2010, over land areas the MLH has increased by 32±14 m per decade. This yielded a pronounced melting area. This may explain the shift of the hailstone size distribution towards larger hailstones in China and France [13, 12] and the almost complete elimination of hail events with the concomitant increase in MLH in Colorado.

Past-trend studies are based on observations, hailpads, reports, proxies (e.g., regional climate models, reanalysis data), and indirect observations (e.g., radar, insurance data). Most of these measurements have weaknesses: reports are biased towards population centers; many automatic stations tend to not have any instruments (hailpads etc.) for hail measurements.

Table A.1 Past-trend studies

Geogra-phical area	Geographical restriction	Measurement	Trend
Africa	Northern Algeria, Northern Morocco	Proxies	Positive trend for severe hail in Northern Algeria negative trend for severe hail in Northern Morocco
	Northern Arfica	Proxies	Significant positive trends during spring and autumn Decrease in summer
Asia	China, South Korea, Mongolia, Tibetan Plateau, Northern Caucasus	Observations	Negative trend for China, , South Korea, Mongolia, Tibetan Plateau, Northern Caucasus Positive trend for Northern Caucasus
	Xinjiang, Turkey	Reports	Positive trend for Xinjiang, Turkey
Europe	Romania, Croatia, Serbia, Bulgaria	Observations	Increases in Romania and Croatia, a negative trend in Serbia and Romania, and no trend in Serbia and Bulgaria

	Italy, France, Pyrenees, Greece	Hailpads	No trend in Italy and France, a positive trend for the Pyrenees, and a negative trend for Greece
	UK, Finland, Spain, Europe in general	Reports	positive trend in the UK, Finland, and Europe in general; and no trend for Spain
	Europe in general, Germany, Italy, France, Spain, Eastern Europe	Proxies	Increase for Europe in general (also for severe hail), for Germany, Italy, France, Switzerland, and Spain Decrease for Eastern Europe No trend for Europe in general and for Germany
	Europe, Germany, Greece	Indirect observations	Positive trend for severe hail for Europe and Germany Negative trend for Greece
	Europe	Proxies	Strongest upward and significant trend for the Po Valley, in particular, in summer Smaller significant increases: France, Benelux, northern Germany, Switzerland, Austria, north-western Balkans into southern Poland, across northeast Turkey and Georgia Negative signficant trends across Aegean Sea and parts of western Russia
North America	Alberta, Ontario, Central Rockies, Eastern USA, High Plains, Canada, Northern Midwest	Observations	Positive trend for Alberta, Ontario, the Central Rockies, the Eastern USA and the High Plains No trend for Canada, the Eastern USA, and the Northern Midwest USA Negative trend for the complete USA
	Central and Eastern USA, Western North America	Proxies	Positive trend for the Central and Eastern USA No trend for the complete USA Negative trend for Western North America for severe hail
	Eastern Colorado	Reports	Positive trend for severe hail and no trend otherwise for the complete USA Positive trend for severe hail for Eastern Colorado
		Indirect observations	Negative trend for severe hail and a positive trend otherwise for the complete USA
	US	Proxies	Both hail larger than 2 and larger than 5cm more frequent than in Europe, also frequently in spring No large areas with positive significant trends
South America	Argentina, Southern Brazil, Cuyo, Patagonia	Observations	Positive trend for Northwestern and Northeastern Argentina Negative trend for central and eastern Argentina No trend for Southern Brazil, Argentina, Cuyo, and Patagoni
Oceania	Sydney	Reports	Negative trend for Sydney

For more details, we refer to [5]; with a list, Table A.1, and Figure A.3, we summarize the findings presented by Raupach et al. For several world regions the studies are not consistent and hardly comprehensive. The past-trend studies (usually on hail frequency) show:

- Africa: Proxies indicate a positive trend for the number of severe hail cases in Northern Algeria and a negative trend for severe hail in Northern Morocco
- Asia:

-
  - Observations indicate a negative trend for hail frequency for China (with a large network), South Korea, Mongolia, the Tibetan Plateau, and the Northern Caucasus; as well as a positive trend for the Northern Caucasus.
  - Reports indicate a positive trend for Xinjiang and Turkey.
- Europe:
  - Observations indicated increases in Romania and Croatia, a negative trend in Serbia and Romania, and no trend in Serbia and Bulgaria.
  - Hailpads indicate no trend in Italy and France, a positive trend for the Pyrenees, and a negative trend for Greece.
  - Reports indicate a positive trend in the UK, Finland, and Europe in general; and no trend for Spain.
  - Proxies indicate an increase for Europe in general (also for severe hail), for Germany, Italy, France, Switzerland, and Spain; a decrease for Eastern Europe; and no trend for Europe in general and for Germany.
  - Indirect observations indicate a positive trend for severe hail for Europe and Germany, and a negative trend for Greece.
- North America:
  - Observations indicate a positive trend for Alberta, Ontario, the Central Rockies, the Eastern USA, and the High Plains; no trend for Canada, the Eastern USA, and the Northern Midwest USA; and a negative trend for the complete USA.
  - Proxies indicate a positive trend for the Central and Eastern USA, no trend for the complete USA, and a negative trend for Western North America for severe hail.
  - Reports indicate a positive trend for severe hail and no trend otherwise for the complete USA, and a positive trend for severe hail for Eastern Colorado.
  - Indirect observations indicate a negative trend for severe hail and a positive trend otherwise for the complete USA.
- South America: Observations indicate a positive trend for Northwestern and Northeastern Argentina; a negative trend for central and eastern Argentina; and no trend for Southern Brazil, Argentina, Cuyo, and Patagonia.
- Oceania: Reports indicate a negative trend for Sydney.

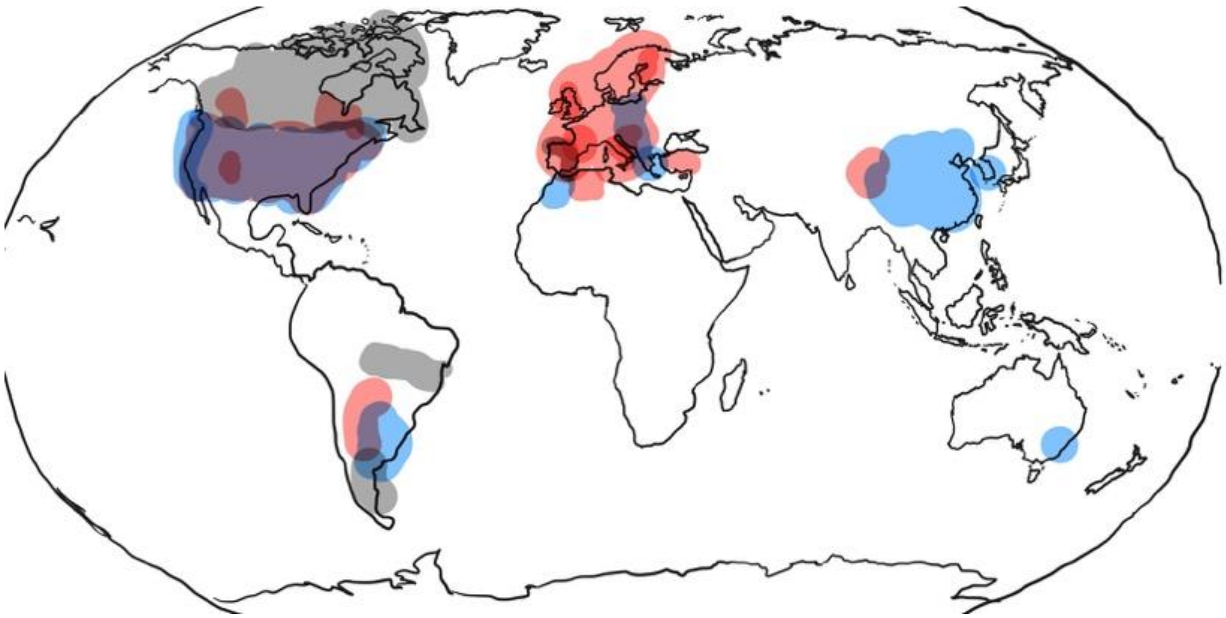

Figure A.3 Hail-frequency past trends, blue, red, and gray represent a negative trend, a positive trend, and no trend, respectively. Some trends are for very large hail.

In a very recent study from November 2023, Battaglioli et al. [76] presented trends for lightning and (very) large hail in both Europe and North America for the period 1950-2021. They extended a model developed by Rädler [66] (see details in Subsection A.3.2) and developed five-dimensional model for lightning and four-dimensional models for hail larger than 2 cm and larger than 5 cm (that is, the models use five and four predictors, respectively). They conclude for hail:

- For Europe:
  - Strongest upward and significant trend: Po Valley (both for ≥2cm and for ≥5cm), in particular, in summer
  - Smaller significant increases: France, Benelux, northern Germany, Switzerland, Austria, north-western Balkans into southern Poland, across northeast Turkey and Georgia
  - Negative significant trends: across Aegean Sea and parts of western Russia
- For Northern Africa:
  - Significant positive trends during spring and autumn
  - Decrease in summer
- For the US:
  - Both hail categories more frequent than in Europe, also frequently in spring
  - No large areas with positive significant trends
  - For hail≥2cm: modest positive statistically significant trends in summer across northern Colorado southern Florida, southern Canada; decrease across the Southeast, the upper Midwest, the Colorado Plateau, the Great Basin

In an interview, Battaglioli and Groenemeijer [77] summarized that it is clear that Europe, especially some areas of Europe, stand out with the increases in hail frequency.
In addition to these results, Battaglioli et al. investigated the evaluation of hail in two hail-prone regions, Northern Italy in Europe and Oklahoma in the US, they give a very descriptive time series of these in Figure 8 of their paper, see https://journals.ametsoc.org/view/journals/apme/62/11/JAMC-D-22-0195.1.xml.
Battaglioli and Groenemeijer [77] concluded that very large hail is now (2012-2021) three times more likely than it was in the 1960s.

A.2.2 Proxies for Projections

Most projections are based on proxies, where researchers use:

1. Low-level moisture, convective instability, e.g., convective available potential energy (CAPE). CAPE as a proxy may be misleading since it is the “potential” of instability and in most cases, it is not released into the atmosphere since no initiation occurs. A future increase in CAPE may not lead to subsequent change in the frequency and intensity of severe weather events.
2. Microphysics, mainly MLH.
3. Vertical wind shear (measured as the magnitude of vector difference between the horizontal wind at surface with a certain atmospheric level. The deep tropospheric wind shear (S06) is defined as the magnitude of the vector difference of the wind at 6km level and to the wind above ground level.)

The National Weather Service [14] defines CAPE as “CAPE or Convective Available Potential Energy is the amount of fuel available to a developing thunderstorm. More specifically, it describes the instability of the atmosphere and provides an approximation of updraft strength within a thunderstorm. “

A.2.3 Projections

The three components that impact hail formation (atmospheric phenomena relevant to hail), are expected to change with climate change [5, 10]:

1. An increase in temperature yields air that can hold more moisture, this increased low-level moisture yields increased convective instability and updraught strength. Per degree of global warming, approximately 7% more tropospheric water vapor is expected [15]. The increased low-level moisture and higher temperatures yield more potential energy, this can be released through condensation of water vapor in a rising air parcel. Hence, this results in increased convective instability [16] [17].
2. For the microphysics, the largest impact is expected to be on the MLH: an increased MLH results in warmer and moister clouds, and possibly more supercooled liquid water, which would yield

wet growth of larger hail. The increased MLH yields that more hail will melt into rain before reaching the Earth's surface, which will further shift the distribution of hailstone size towards larger hailstones. However, for hail aloft, the MLH does not play a role.

3. Overall deep-tropospheric vertical wind shear (S06) is expected to reduce with climate change [18]. However, these changes in vertical wind shear are overshadowed by instability changes, hence, the impact of these vertical-wind-shear changes are expected to be negligible. Here, the interest is not generally on vertical wind shear, but on the vertical wind shear at the time of thunderstorms. Raupach et al. [5] state "This outcome is because changes to wind shear either occur at times when hail is unlikely to form or are outweighed by the relatively greater effect of changes to instability or MLH. Thus, decreases in wind shear generally do not inhibit expected increases in the occurrence of thunderstorm environments driven by rising convective instability".

Apart from these proxies, there exist direct projections, an example is HAILCAST [19] (based on [20, 7, 21]): a one-dimensional model used in a fine grid, where in each grid cell the growth of a hailstone is projected on a vertical profile. Because these models are one dimensional, they cannot represent the hailstone trajectory in the storm, including the width of the updraft, which play an important role in the growth of hailstones as detailed in Subsection A.1. Brimelow et al. [7] evaluated the performance of HAILCAST and deemed it "a useful aid for objectively forecasting hail" and HAILCAST "being capable of distinguishing between nonsevere- and severe-hail events".

In contrast to HAILCAST, the large-scale proxies only predict favorable conditions, how hail is actually initiated (see a more detailed discussion in Subsection A.3.2) is not clear and the problem of good predictors is highlighted also by proxy-based projections for hail.

Modeling the process of hail formation is computationally expensive, hence, at least until now, these are not fully modelled in projections, and studies that investigate the climate-change impact on these microphysical processes are limited [5].

Many factors of uncertainty exist for the expected changes [10]:

- Trigger mechanisms/initiation not considered in many studies—and even if the atmosphere is prone to produce hail, this still seldom happens
- The microphysical processes of hail are still associated with high uncertainties
- Hail events have high annual variability [22]
- Proxy-based studies have a low spatial resolution, while for simulating the actual formation of hail a high spatial resolution is needed, which in turn is very computationally expensive

The existing future-trend studies are very limited, for an overview see Figure A.4 based on [5], Table A.2 (results), and Table A.3 (time frame and models used). We also summarize all results in a list; projections for the midcentury (in contrast to the more frequent end-of-century projections) are highlighted in italics.

In particular, the near-future projections show only minor increases or little statistical significance because of high annual variability and ensemble spread.

Table A.2 Future-trend studies for hail: Geographical area, seasonal projections and projections without seasonal distinction. Results for the end of the century are highlighted in gray, results for the middle of the century are highlighted in yellow.

Geogra-phical area	Geographical area restriction	Authors/ Reference	Spring	Summer/Warm Season	Without Seasonal Distinction
Europe		Rädler et al. [23]			Frequency of hail will increase
	Germany	Kapsch et al. [24]			7-15% more hail days
	Germany	Mohr et al. [25]		Increasing potential for hail events (in particular: northwest, south of Germany)	
	Italy	Piani et al. [26]			Frequency of hailstorms will increase
	UK	Sanderson et al. [27]			Fewer damaging hailstorms, fewer hailstones of diameter 21-50mm, places where hail appears remains the same
	Netherlands	Botzen et al. [28]			25-50% increase in damage to outdoor farming from hail
	Partly Germany& Alps and Western& Central Europe	Rädler [66]			For hail≥2cm: - Increase in number of mean annual hail cases for RCP2.6, 4.5, and 8.5, for both middle and end of century - Strongest increase of RCP8.5, 2071-2100, with over 100% in north-east of European region For hail≥5cm: Similar results, but maximum of 160%, i.e., much stronger
North America	Partly central US	Trapp et al. [38]	Increases in very large hail (≥50 mm diameter)	Increases in very large hail (≥50 mm diameter)	Higher frequency of large hail ((≥35 mm diameter)
	Limited for spring and summer	Brimelow et al. [30]	More hail damage potential over southern North America; Decrease hail frequency and damage potential for eastern +	More hail damage potential over Rocky Mountains; Decrease hail frequency and damage potential for eastern + southeastern North America	Fewer hail days, shift to larger hail sizes

			southeastern North America		
	Colorado	Childs et al. [31]			Increase in hail days
	Colorado	Mahoney et al. [32]		Near-elimination of surface hail	
	Eastern United States	Diffenbaugh et al. [16]			Increase of severe thunderstorm environments that might support formation of hail
	Largest increase for regions close to the Gulf of Mexico and the Atlantic	Trapp et al. [18]		Largest increase	Increase in number of days with severe thunderstorm conditions that support the growth of large hailstones
	Contiguous US (CONUS)	Goodin [59]		Decrease in frequency of severe-hail days in Central/Southern Plains and Southeast; decrease in large-hail days	Increase in frequency of severe-hail days in Midwest/Eastern CONUS; Increase in frequency of large-hail days in Eastern CONUS
Oceania	New South Wales	McMaster [33]			Hail losses (not statistically significant)
	Mount Gambier and Melbourne	Niall and Walsh [34]		August-October: increase hail incidence	
	Northern and eastern Australia	Allen et al. [35]			Increase of severe thunderstorm enbironments
	Sydney Basin	Leslie et al. [36]			Increase in frequency and intensity of hailstorms

Table A.3 Future-trend studies for hail: time frame, climate models and emission scenarios considered in the different studies. Results for the end of the century are highlighted in gray, results for the middle of the century are highlighted in yellow.

Geogra-phical area	Geographical restriction	Authors/ Reference	Time frame	Climate models	Scenario, other information
Europe		Rädler et al. [23]	1971-2000 vs. 2071-2100	14 regional climate models (RCMs)	RCP4.5 (emission pathway of stabilization without overshoot) and RCP8.5 (rising emissions pathway)
	Germany	Kapsch et al. [24]	1971-2000 vs. 2031-2045	Eight RCMs	Reananalysis with ERA-40
	Germany	Mohr et al. [25]	1971-2000 vs. 2021-2050	Seven RCMs	Different emission scenarios used: A1B and B1
	Italy	Piani et al. [26]	1961-2003 vs. 2004-2040 and 1961-2040	(Use forcings for hailstones from NCEP-NCAR Reanalysis to	Reanalysis and the CGCM2-A2 climate scenario from the Canadian Centre of Climate modeling and analysis

				evaluate expected changes)	
	UK	Sanderson et al. [27]	2010-2039, 2040-2069, 2070-2099	Single RCM	A1B emission scenario (future world of rapid economic growth, balance between all energy sources)
	Netherlands	Botzen et al. [28]	2050	-	Estimate relations between normalized insured hailstorm damage to agriculture and several temperature and precipitation indicators KNMI scenarios moderate (+1°C) and warm (+2°C)
	Partly Germany&Alps and Western&Central Europe	Rädler [66]	1979-2016 vs. 2021-2050 and 2071-2100	14 EURO-CORDEX simulations 4 RCMs	RCP2.6, RCP4.5, RCP8.5 ERA-Interim reanalysis AR-CHaMo
North America	Partly central US	Trapp et al. [38]	1971-2000 vs. 2071-2100	Global Climate Model (GCM)CM (GFDLCM3 (MIP5)), downscaling	Dynamical downscaling RCP8.5
	Limited for spring and summer	Brimelow et al. [30]	1971-2000 vs. 2041-2070	HAILCAST and one RCM	A2 scenario (describing a heterogenous world and business as usual)
	Colorado	Childs et al. [31]	199 7-2017 vs. 20 71-2100	GCM (GFDLCM3 (MIP5)), dynamical downscaling	RCP8.5 pathway
	Colorado	Mahoney et al. [32]	1971-2041-2070	GCM, RCM	Three-tiered downscaling, explicit simulation of intense thunderstorm events
	Eastern United States	Diffenbaugh et al. [16]	1970-1999 vs. 2070-2099	GCM (GFDLCM3 (MIP5))	RCP8.5 pathway
		Trapp et al. [18]	1962-1989 vs. 2072-2099	Model suite of GCMs and a high-resolution RCM	A2 emission scenario
	CONUS	Goodin [59]	1990-2005 vs. 2085-2100	GCM from CESM, RCM Weather Research and Forecasting (WRF) Model V4.1.2[1]	RCP 4.5 and RCP 8.5 Dynamical downscaling
Oceania	New South Wales	McMaster [33]	1969 vs. 1978	Three GCMs	Doubled-CO_2 scenario; no significant results
	Mount Gambier and Melbourne	Niall and Walsh [34]	1980-2001	August-October: increase hail incidence	Doubled-CO_2 scenario
	Northern and eastern Australia	Allen et al. [35]	1980-2000 vs. 2079-2099	Two GCMs	High-warming climate scenario
	Sydney Basin	Leslie et al. [36]	1990-2002 vs. 2001-2050	GCM (OU-CGCM)	SREAS A1B future climate scenario (future world of rapid economic growth, balance between all energy sources)

[1] For more details on that model, see Powers et al. [74]

- Europe:
  - Rädler et al. [23] showed that the frequency of hail will likely increase by the end of the century. They used an ensemble of 14 regional climate models (RCMs) and showed an increase in likelihood of 40- 80% for environmental conditions favorable for hail in large parts of Europe in a high-emissions scenario—where they perform a comparison of the years 1971-2000 and 2071-2100 and used two benchmark scenarios, so-called Representative Concentration Pathways (RCPs), RCP4.5 and RCP8.5, where RCP4.5 indicates an emission pathway of stabilization without overshoot and RCP8.5 a rising emissions pathway [37]—the number after RCP indicates the estimated increase in greenhouse-gas-induced mean global radiative forcing in watts/m^2 by the end of the century [58].
  - *Kapsch et al.* [24] *projected a slight increase (7-15%) in the number of hail days in Germany for the period 2031-2045 in comparison with 1971-2000. They used an ensemble of eight RCMs and reanalysis with ERA-40.*
  - *Mohr et al.* [25] *considered the hail frequency in Germany in the summer. They developed a statistical model and by applying it to an ensemble of seven RCMs, they found an increasing potential for hail events for the period of 2021-2050 in comparison to 1971-2000, which is statistically significant for the northwest and south of Germany. However, these projections feature a high variability between simulations.*
  - *Piani et al.* [26] *projected that hailstorm frequency over Italy will likely grow in the future (using reanalysis and the CGCM2-A2 climate scenario from the Canadian Centre of Climate modeling and analysis, CCCma): they compared a reanalysis for 1961-2003 with the CCCma results for 1961-2003, 2004-2040, and 1961-2040. The annual probability of hailstorms will likely increase in the interval 2004-2040, and Piani et al. projected an increase in hail frequency for spring, summer, and autumn.*
  - *Sanderson et al.* [27] *projected a downward trend for the total number of damaging hailstorms for the UK, with statistically significant downward trends for hailstone diameters of 21-50mm.* They projected a decrease for the number of damaging hailstorms by a factor of 2 during the century. *They considered a single RCM and a simple hail-stone formation model, they studied the time periods 2010-2039, 2040-2069, and 2070-2099. Moreover, they found that the spatial distribution did not change: the highest values continued to be in southeast England. This outlier decreasing trend is attributed in a decrease of the CAPE, the climate model's convective instability proxy.*
  - *Botzen et al.* [28] *projected that the annual hailstorm damage to outdoor farming could increase with 25-50% by 2050 in the Netherlands.*
  - *Rädler [66] projected an increase in the number of mean annual hail cases for hail≥2cm, for all RCP scenarios and both for the middle and the end of the century, the strongest increase is projected for RCP8.5, 2071-2100 with over 100% in the north-east of the*

considered European domain. Strong and robust increases in hail≥2cm are projected for most of central and eastern Europe. The results for hail≥5cm are similar (but maximum of 160%, i.e., much stronger as for hail ≥ 2cm).

- North America:
    - Trapp et al. [38] projected increases in the frequency of large hail (≥35 mm diameter) over broad geographical areas of the US during all seasons; and increases in very large hail (≥50 mm diameter) for the central US during boreal spring and summer. The authors used high-resolution dynamical downscaling (4 km resolution) to integrate the environmental conditions for and initiation of convective storms that support formation of hail, the storm volume and the depth of the lower atmosphere conductive to melting. They compared the periods 1971-2000 and 2071-2100.
    - *Brimelow et al.* [30] *projected fewer hail days over most areas of North America, but a shift toward larger hail sizes, comparing the periods 1971-2000 and 2041-2070. This includes an increase in hail damage potential over southern North America in the spring, and in higher altitudes and the Rocky Mountains in the summer. Moreover, they projected a strong decrease in both hail frequency and damage potential for eastern and southeastern North America in spring and summer (because of increased melting). Generally, drier and cooler regions in North America will experience the largest increased in hail threat, while warmer and more humid regions will experience a reduced threat. The authors used HAILCAST and North American Regional Climate Change Assessment Program (NARCCAP) simulations and the A2 scenario (describing a heterogenous world and business as usual* [39]*).*
    - Childs et al. [31] projected an increase in hail days in Colorado by the end of the century based on proxies.
    - *Mahoney et al.* [32] *project a near-elimination of surface hail in Colorado during warm season. They attribute this change to an increased MLH. They compare the periods 1971-2000 and 2041-2070. The authors employ a three-tiered downscaling approach: first downscaling GCM simulations to a 50-km grid of NARCCAP RCMs, driven by A2-scneario GCMs; extreme precipitation events occurring in NARCCAP are further downscaled using a high-resolution model with a 1.3-km grid, where intense thunderstorm events can be explicitly simulated.*
    - Diffenbaugh et al. [16] projected robust increases of severe thunderstorm environments over the eastern United States based on a GCM ensemble (CMIP5, RCP8.5 pathway). They projected these increases for spring and autumn already before a mean global warming of 2°C. Additionally, they projected an increase in the number of days with high CAPE and strong low-level wind shear—they find decreases in vertical wind shear are concentrated on low-CAPE days and, hence, have little effect. Moreover, they project a shift to high

CAPE mostly concentrated on days with low convective inhibition[2]. They mainly compare the periods 1970-1999 and 2070-2099. The authors' criteria for severe thunderstorm environments might support the formation of hail.

- Trapp et al. [18] projected an increase in the number of days in which severe thunderstorm environmental conditions (NDSEV) appear in the US, based on a model suite of GCMs and a high-resolution RCM. The largest NDSEV increases are projected during the summer, for regions close to the Gulf of Mexico and the Atlantic (e.g., >100% increase in Atlanta, GA, and New York, NY). They compare the periods 1962-1989 and 2072-2099. As proxies, they use CAPE and S06. Because large CAPE is associated with strong updrafts, these conditions support the growth of large hailstones; and NDSEV is used as a proxy for thunderstorms that can potentially produce hail.
- Goodin [59] studied the frequency and intensity of hail and compared the period 1990-2005 with the future period 2085-2100 under RCP4.5 and RCP8.5. . She projected significant increases in frequency of severe-hail days (hail ≥ 2.54cm) in broad areas of the Midwest and Eastern CONUS, especially for RCP8.5. The most robust increases are projected in boreal winter and spring; in summer, she projected a significant decrease in frequency of severe-hail days in the Central/Southern Plains and the Southeast. Moreover, she projected a significant increase in large-hail days (hail ≥ 4cm) for RCP8.5 in the Eastern CONUS; for many regions in the Southern Plains and Southeast the number of large-hail days are projected to nearly double. On the other hand, she projected a robust decrease in large-hail days during summer in the Southern Plains. Furthermore, in the projections, slight shifts in the maximum diameter hail values can be observed—both annually and seasonally; hail-size extremes are projected to increase in the Midwest, the Southeast and the Southern Plains. She used dynamical downscaling with 3.75km grid spacing and the RCM WRF V4.1.2, and a GCM from the Community Earth System Model (CESM), where she re-gridded and bias-corrected the data using ERA-Interim reanalysis data

- Oceania:
  - McMaster [33] used hail-loss models and three GCMs with doubled-CO_2 scenarios to project hail losses for New South Wales. Generally, he obtained declines in winter cereal crop hail losses, but these changes (comparing 1969 and 1978) were not statistically significant.
  - Niall and Walsh [34] considered August-October during the years 1980-2001 in Mount Gambier and Melbourne (both in southeastern Australia) and found a statistically significant relationship between hail incidence and CAPE values for reanalysis data and sounding data. They showed that for a doubled-CO_2 scenario that the mean CAPE decreases by 10%.

[2] Amount of energy that will prevent an air parcel to rise from the surface level to the level of free convection.

- Allen et al. [40] studied the occurrence of severe thunderstorm environments in Australia using two GCMs, they compared the periods 1980-2000 and 2079-2099 (with high-warming climate scenarios). They projected significant increases of severe thunderstorm environments for northern and eastern Australia—attributed to increasing CAPE, particularly close to warm sea surface temperatures. The authors projected a decrease in frequency of environments with high vertical wind shear, but they predicted that this will be outweighed by the CAPE increase. This result contrasts the changes obtained by McMaster and Niall and Walsh (based on coarse-resolution data).
- *Leslie et al.* [36] *compared the periods 1990-2002 and 2001-2050 for the Sydney Basin. They used a six-member ensemble of a high-resolution version of the Oklahoma Coupled General Circulation Model with a hierarchy of graded meshes and including cloud microphysics in the 1-km horizontal grid of the model. Under the SREAS A1B future climate scenario (future world of rapid economic growth, balance between all energy sources* [39]*), they obtained significant increase in frequency and intensity of hailstorms in compared both to 1990-2002 and no-change 2001-2050. During the next one or two decades (starting in 2008), the increases in frequency may be masked by natural inter-decadal variability.*

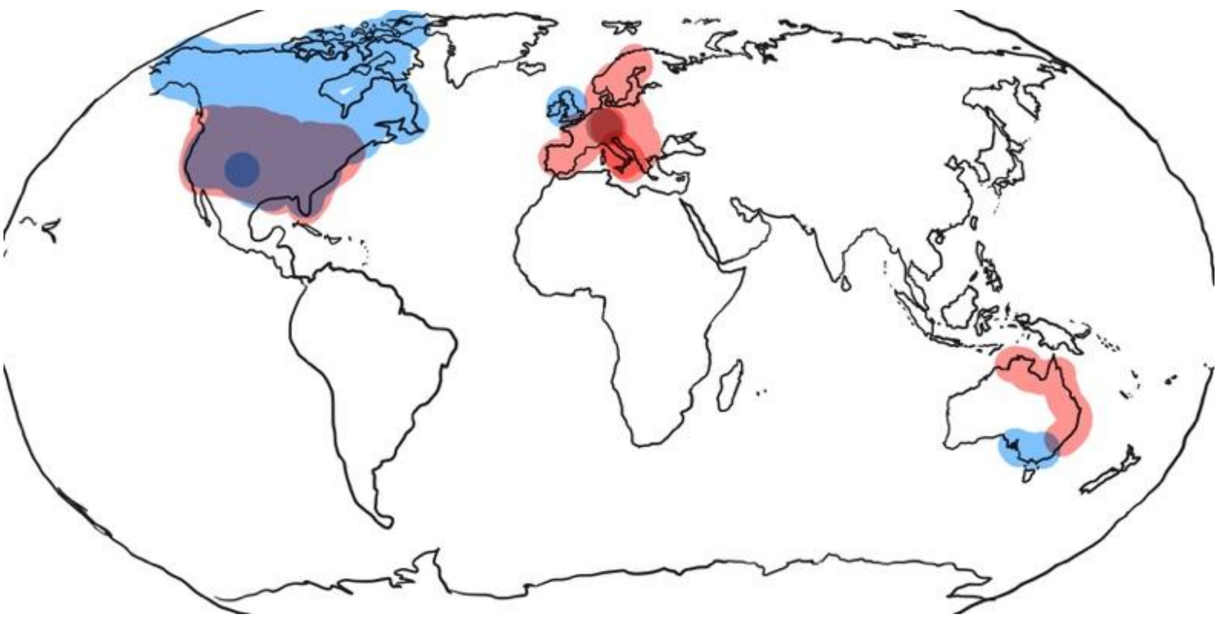

Figure A.4 Hail future trends studies: blue, red, and gray represent a negative trend, a positive trend, and no trend, respectively. Both trends for frequency, but also shifts to larger hail sizes are shown.

A.2.4 Summary of Hail Past and Future Trends

In summary, for Europe, observational trends show little agreement, but a slight increase for environments that are favorable for hail (with low significance and some contradictions, e.g., the UK) is projected—with a strong upward trend for the Po Valley. Changes are attributed to more convective instability because of low-level moisture and an increasing MLH. In North America, observations do not show clear trends or only modest trends. However, projections of hail intensity (hail sizes/damaging hail stones) and frequency are consistent between approaches based on different climate models, and an increase of days favoring severe convective storms/hailstorms within most regions and seasons is projected. The changes are attributed to an increase in convective stability, which will outweigh a simultaneous decrease in mean vertical wind shear [16, 18, 38, 41]. Moreover, thunderstorms have become and will become more likely to produce hail. The increase in hail-favorable environments is particularly projected for warm seasons and warm and humid regions, the increase in hail intensity/severity is projected for dry and cool regions, but with fewer events. Altogether a shift to larger hail is projected. For Oceania, projections are scarce, but the existing studies agree in trends: an increase in frequency, severity and favorable environments, but also large inter-decadal variability.

A.2.5 Knowledge Gaps and Uncertainties

Kunz [10] indicated a lack of data for 500 hPA (about 5000-6000 meters altitude). At 500 hPA—in contrast to 850 hPA, so far only minor temperature trends have been observed.

Figure A.4 clearly indicates large spatial gaps in future studies. However, the same proxies cannot be used for different world regions, e.g., for the UK a completely different method is used than for the rest of Europe. This indicates that the existing spatial gaps (as evident from Figure A.5) cannot be closed by simply using existing proxies.

Uncertainties stem from a variety of factors, as detailed in Subsection A.2.3 [10]:

- Trigger mechanisms/initiation not considered in many studies—and even if the atmosphere is prone to produce hail, this still hardly happens
- The microphysical processes of hail are still associated with high uncertainties
- Hail events have high annual variability
- Proxy-based studies have a low spatial resolution, while for the actual formation of hail a high spatial resolution is needed, which in turn are very computationally expensive

Studies on hail aloft (HALO) do not exist but would be very interesting for aviation. John T. Allen [11] specifically highlighted the need for EASA to raise this topic to trigger research on HALO. On the other hand, Pieter Groenemeijer [77] stated that if HALO has a size of several centimeters, then the hailstones usually fall so rapidly that they will not shrink significantly (that is, situations with hailstone sizes of 5cm aloft and hardly any hail on the ground will not appear). Hence, he considers studies on hail on the ground an acceptable first estimate for HALOs. Moreover, he stated that HALO will usually appear close to the storm's updraft. Possibly, microwave observation data from satellites could give more information on altitudes for HALO.

A.3 Convective Weather (Thunderstorms) Trends

In literature, usually two categories are studied:

- Severe convective storms (SCS)
- Significant severe convective storms (SigSCS)

These include some minimum criteria for associated phenomena, as detailed by Allen [42]:

	SCS	SigSCS
Hail stones diameter	≥ 2cm	≥ 5cm
Winds	≥ 90 km/h	≥ 120 km/h
Tornadoes	Existence	At least F2 intensity[3]
Precipitation (not used in all countries)	Excessive	excessive

For a classification as SCS/SigSCS at least one of these criteria must be met. The strong winds will always be present, while other phenomena may, but need not be present [43]. While the criteria listed here seem to allow for a very clear classification, Allen [42] highlights that "arbitrary criteria […] are used to define [SCS]", that almost severe and severe thunderstorms are hardly distinguished (there is little physical difference between a near-severe storm with 1.9cm diameter hail and a severe storm with 2cm diameter hail [35] [44]), and that definitions of what constitutes a SCS/SigSCS vary from country to country. For convective storms that do not meet the criteria of an SCS, observational records are not very good.

SCS come with a variety of aviation hazards: hail encounter, lightning strike, low-level wind shear, severe turbulence, runway flooding. In this appendix, we focus on SCS in general and hail, other phenomena are of interest for future reports.

The general expected impact of climate change on convective storms [42] is shown in Figure A.5, however, this includes various uncertain factors, hence, such a clear connection has not been shown in studies.

[3] F2 is a measure on the Fujita scale and describes tornadoes with 113-157mph and considerable damage

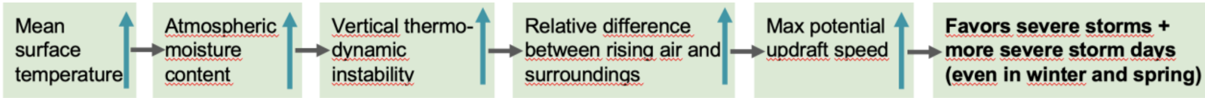

Figure A.5 Expected impact of climate change on severe convective storms

For a more detailed overview on climate change and severe thunderstorms, we refer to the paper of the same name by Allen [42]. This paper and our interview/discussions with the single author of this survey article [11] build the major foundation of this section.

A.3.1 Observations

There do not exist “reliable, long-term record[s] of severe thunderstorms” [16]. The same restrictions for observations exist as for hail (Subsection A.2.1): observations are skewed towards populations centers (where possible observers are more likely located), surface stations are too scarce. The largest set of records exists for the US, otherwise records are very limited [42]. These factors favor the usage of radar- or satellite-based data, which has fewer spatial limitations, however, it is available for only about the last 10 years due to changes in quality of both the radar network or satellite sensors.

In the 2023 study described in Subsection A.2.1, Battaglioli et al. [76] presented also trends for lightning in both Europe and North America for the period 1950-2021. They concluded for thunderstorms:

- The occurrence of thunderstorm environments has significantly increased across most of Europe during the past 72 years.
- The largest absolute increase occurred in the Alpine and Caucasus Mountains with up to 5h of lightning more per decade.
- The largest relative increase occurred in Scandinavia with 2 more hours lightning per decade—with an annual mean of 20-25h.
- Increases in lightning appear throughout the year, but particularly during summer.
- In a belt Finland-Turkey only insignificant lightning changes occurred.
- Across parts of Russia, a significant decrease in thunderstorms occurred.
- The strongest positive trends in the US occurred in the southern States, specifically Florida and the Texas-Louisiana coasts.
- Upward trends occurred also in the Midwest and southern Canada, mostly during summer.
- Significant negative trends occurred across the Colorado Plateau and the Great Basin.

A.3.2 Proxies for Projections

Severe convective storms and the associated hazards happen on a small scale (they are mesoscale processes). On the other hand, most climate models have a significantly coarser resolution. Thus, severe convective weather cannot be modeled explicitly in these models. Proxies have been created to "relate atmospheric conditions extracted from reanalyses to severe convective weather occurrence" [66]. These environmental proxies should reflect conditions that are favorable for SCS. However, favorable conditions for SCS do not mean that a SCS actually forms, the actual initiation of an SCS is a large problem for projections; Púčik et al. [45] state that "[t]he presence of latent instability does not guarantee that a thunderstorm will form, so that it is not clear whether increases in instability are associated with increases in thunderstorm activity". Already in 2006, a complete volume of Monthly Weather Review [46] was devoted to convection initiation.

Generally, environmental proxies for three main components are used:

1. Thermodynamic propensity for updraft development, proxies used in literature include:
    a. CAPE
    b. Convective inhibition (CIN)
    c. Lapse rate
    d. Lifted condensation level
    e. Occurrence of convective precipitation
2. Vertical wind shear (to predict the organization and longevity of severe convection of significantly severe convection), proxies used in literature include:
    a. S06
    b. Storm relative helicity (SRH)
    c. Vertical wind shear between surface and lower levels, e.g., S01
3. Convective initiation, proxies used in literature include:
    a. Occurrence of convective precipitation
    b. Boundary-layer convergence zones
    c. Magnitude and depth of lifting at boundaries
    d. Cold-pool strength
    e. Amount of moisture

Many researchers use the product of CAPE and S06. Allen [11] highlighted that many proxies are correlated hence, the use of a specific proxy does not have a large impact on the results. On the other hand, the models used by researchers play a large role for the results because of known biases.

The most frequent approach using proxies is to formulate thresholds for the proxies, which yields a binary approach. Another approach is to classify the environments probabilistically. An example of the latter approach is the additive regressive convective hazard model (AR-CHaMo) developed by Anja Rädler in her PhD thesis [66] and applied in its substudies (e.g., [45]).

In addition to these proxy-based approaches, dynamical downscaling nests high-resolution regional models, in which severe convective storms can be explicitly modelled, with a general low-resolution GCM.

Because dynamical downscaling can help with several problems of projections for convective storms and the associated hazards, we detail the concept, existing research and its limitations in Section A.4.

To exemplify the statistical-model approach based on proxies, we detail here the AR-CHaMo: Rädler [66] expressed the predicted probability of a hazard as the product of the probability that a storm occurs and the conditional probability of a hazard given the presence of a storm[4]. She investigated the relation between atmospheric parameters and the occurrence of convective storms based on lightning data and ERA-Interim reanalysis data. To determine the probabilities, she used data on cloud-to-ground lightning from the European Cooperative of Lightning Detection (EUCLID) as an indicator for deep, moist convection (two lightning strikes in the same grid cell and 6h time interval). She then employed hazard reports from the European Severe Weather Database (ESWD) to identify hazard cases (one hazard report with a lightning case in the same grid cell and 6h interval) for the hazards hail ≥2cm, hail ≥5cm, severe wind gusts, tornadoes, and heavy precipitation. To derive the probability that a storm occurs, she studied the dependence of lightning on different proxies, to derive the conditional probability, she studied the relation between the relative frequency of hazards under a lightning case and potential predictor proxies. She then uses a general additive model to obtain continuous probability functions. Battaglioli et al. [76] expanded on this work by using a larger set of proxies that they test as candidate predictors for the model and using ERA5. Battaglioli and Groenemeijer [77] stated that the trends they discovered based on ERA5 are a little higher than those discovered by Rädler [66], that is, they project slightly larger increases.

For wind shear, Pieter Groenemeijer [77] emphasized that low-level wind shear is a very important predictor for thunderstorms, in particular, for tornadoes and extreme wind gust, and that it needs to be studied in more detail. Moreover, for aviation, wind shear even closer to the surface than what is considered low-level is important. Moreover, this very strong low-level wind shear does not have to be thunderstorm-related.

A.3.3 Projections

For two of the three main components listed in Subsection A.3.2 (convective instability and vertical wind shear), the expected changes with climate change as detailed in Subsection A.2.3 hold (increased convective instability, reduced vertical wind shear that is outweighed by the increase in convective instability).

For severe thunderstorms, the same holds as for hail: future studies are very sparce. Diffenbaugh et al. [16] highlight “First, there is no reliable, independent, long-term record of severe thunderstorms—and particularly tornadoes—with which to systematically analyze variability and trends. Second, theoretical arguments and climate model experiments both predict conflicting influences of the large-scale—or

[4] P(hazard) = P(storm) x P(hazard|storm)

"environmental"—conditions that support severe thunderstorms. Third, a suite of processes important for the realization of individual storms in the real atmosphere has remained mostly inaccessible in climate model experiments because of deficiencies in model development and/or computational resources."
Allen [11] described RCMs to be preferable over GCMs because of the spatial resolution.
For an overview of the projections see Figure A.6 based on [5], in Table A.4 (results), and Table A.5 (time frame and models used). We also summarize all results in a list; again, projections for the midcentury (in contrast to the more frequent end-of-century projections) are highlighted in italics.

Table A.4 Future-trend studies for convective weather: Geographical area, seasonal projections and projections without seasonal distinction. Results for the end of the century are highlighted in gray, results for the middle of the century are highlighted in yellow.

Geographical area	Geographical restriction	Authors/ Reference	Spring	Summer/Warm Season	Fall	Winter	Without Seasonal Distinction
Europe	Central and south-central Europe	Púčik et al. [45]					Increase in frequency of unstable environments (robust for end of century, smaller and less robust for middle of century), for middle of century only changes of the Mediterranean coastlines and parts of southeastern Europe robust.
	See the different season results	Marsh et al. [47]	Decrease in mean CAPE, but increase on the Faroe Islands	Nearly complete CAPE decrease, with an exception of western Norway	CAPE increase for the Mediterranean Sea and mainland Europe, as well as a decrease for the Atlantic Ocean and the Faroe Islands	Mean CAPE increase in in the Mediterranean Sea, the Strait of Gibraltar, the Balearic Islands, southern Italy and the southern Black Sea	Small increase in favorable environments for severe thunderstorms for most locations in Europe
	Iberian Peninsula (often restricted to Mediterranean)	Viceto et al. [48]	Small changes in CAPE; increase in S06	Largest increase in conditions favorable for severe thunderstorms (mostly for the Mediterranean and its surroundings);	Large increase in conditions favorable for severe thunderstorms (mostly for the Mediterranean and its surroundings);	Small changes in CAPE; increase in S06	

Geogra-phical area	Geogra-phical restriction	Authors/ Reference	Spring	Summer/Warm Season	Fall	Winter	Without Seasonal Distinction
				Significant increase in CAPE for the Mediterranean; decrease in S06	Significant increase in CAPE for the Mediterranean; decrease in S06		
		Rädler et al. [23]					Frequency of convective weather events (lightning, hail, severe wind gusts) will likely increase over Europe. Slight decrease in thunderstorms for southwestern and southeastern Europe.
	Partly Germany &Alps and Western& Central Europe (hail results see that section)	Rädler [66]					Already for the period 1979-2016: - Positive trend for lightning and all hazards (hail≥2,5; wind; tornadoes; heavy precipitation) - Thunderstorms have become more likely to produce severe weather over the last decades. - Driven by an increase in instability instead of changes in deep-layer shear or mid-tropospheric humidity BUT: for past an attribution to climate change cannot be concluded (analysis not made). For all future simulations: increase in lightning cases for central and eastern Europe Decrease in southern Spain, northern Africa, Greece, Turkey, northwest Ireland Largest increases for RCP8.5 and end of the century

Geogra-phical area	Geogra-phical restriction	Authors/ Reference	Spring	Summer/Warm Season	Fall	Winter	Without Seasonal Distinction
							Robust increases only for north-eastern region **Increase in convective hazards until the end of the century: driving factor is therefore that thunderstorms are more likely to produce severe weather in future climates**
North America	Eastern US	Diffenbaugh et al. [16]	Increase of severe thunderstorm environments already before a global warming of 2°C		Increase of severe thunderstorm environments already before a global warming of 2°C		Increase of severe thunderstorm environments
	US Largest increases for regions close to the Gulf of Mexico and the Atlantic	Trapp et al. [18]		Largest increase in NDSEV			Increase in number of days with severe thunderstorm environmental conditions (NDSEV)
	US	Trapp et al. [29]	Decrease in cyclone frequency over the conterminous US			Decrease in cyclone frequency over the conterminous US	Increase in NDSEV
	Northeasten United States, the Great Lakes, and Southeastern Canada	Gensini et al. [41]					Increase in NDSEV
	US east of continental divide, increases primarily found in	Gensini and Mote [53]	Statistically significant increase in hazardous convective weather				Most of the increase in hazardous convective weather around local sunset; peak-season severe weather more

Geogra-phical area	Geogra-phical restriction	Authors/ Reference	Spring	Summer/Warm Season	Fall	Winter	Without Seasonal Distinction
	the Mississippi, Tennessee, and Ohio River valleys						variable, potentially more frequent
	CONUS	Rasmussen et al. [54]					Frequency decrease for weak to moderate convection; frequency increase for strong convection; CAPE and CIN increase downstream of Rockies
	CONUS	Haberlie et al. [61]	Overall increase in thunderstorm activity	Decrease in thundertorm activity	Overall increase in thunderstorm activity	Overall increase in thunderstorm activity	40dBZ[5] days: significant decrease in Southern Plains and coastal Carolinas; significant increase in Northeast 50/60dBZ days: Significant increase in many areas east of the High Plains in RCP8.5
	CONUS	Ashley et al. [63]	Highest supercell risk in early spring; Increased supercell frequency and footprint	Supercells decrease from midsummer	Supercells decrease until early fall	Highest supercell risk in late winter Increased supercell frequency and footprint	Supercells will be more frequent and intense in future climates, robust spatiotemporal shifts; Supercells more frequent in eastern CONUS, less frequent in parts of the Great Plains; Intense storm rotation more prevalent in future
		Prein et al. [68]					All regions (except Central US) increase in mesoscale convective systems (MCS) frequency In Central US: decrease by 30%, but extreme MCSs increase by 380% Similar high increases for extreme MCSs for other regions

[5] Decibel relative to Z; dimensionless technical unit used in radar, the units of reflectivity are given in mm^6/m^3, to obtain values that are easier to work with, a logarithmic scales is applied to compress these values, which results in dBZ, with a scale running from -35 to +85 dBZ; 20-40 dBZ are associated with light precipitation, 40-50 dBZ with moderate precipitation, 50-65dBZ with heavy precipitation or some hail, and values above 65dBZ are associated with extremely heave precipitation including water-coated hail [78].

Geogra-phical area	Geogra-phical restriction	Authors/ Reference	Spring	Summer/Warm Season	Fall	Winter	Without Seasonal Distinction
							Highest relative increase in MCS frequency: Canada and Northeast US Maximum hourly precipitation: • Increase by 25-40% northern regions • Increase by 15-20% otherwise Significant increase in CAPE allows MCSs to grow larger Rapid increase in MCSs with high hourly rainfall relative to their size yields higher flooding potential
		Hoogewind et al. [17]		Conditional probability of hazardous convective weather (HCW) given NDSEV declines over much of central US			Longer HCW season (perhaps by more than a month)
Oceania	Northern and eastern Australia	Allen et al. [35]					Increase of severe thunderstorm environments
Asia	Japan	Muramatsu et al. [49]	Frequency of strong tornadoes will double	Frequency of strong tornadoes will double on the Japan Sea side of the Japanese Islands			
World	See the different season results	Lepore et al. [65]	Largest increases in CIN, more substantial over northern hemisphere				Statistically significant increases of CAPE for relevant convectively active regions Relative to historical period, for CAPE:

Geogra-phical area	Geogra-phical restriction	Authors/ Reference	Spring	Summer/Warm Season	Fall	Winter	Without Seasonal Distinction
							- Increase of order 0.5 σ over tropical regions - Increase of order 1-1.5σ in extratropics Stronger increase over northern hemisphere (NH) than for southern hemisphere (SH) Changes to CIN comparatively small, but robust
			significant decreases of CAPE over the eastern Atlantic during boreal spring			significant decreases of CAPE over the southern hemisphere during winter	Increase in environments favorable to convective storms—a **frequency increase of 5-20 percent per °C of global warming** Driver: strong increase in CAPE, not offset by offset by factors resisting convection of modifying likelihood of storm organization Relative to historical period, for CAPE: - Increase of order 2-3σ for much of NH - Increase of order 1-2σ for the SH Widespread robust increases of CIN Regional increases in low-level wind shear will be offset by decreased deep-layer shear

Table A.5 Future-trend studies for convective weather: time frame, climate models and emission scenarios considered in the different studies. Results for the end of the century are highlighted in gray, results for the middle of the century are highlighted in yellow.

Geogra-phical area	Geographical restriction	Authors/ Reference	Time frame	Climate models	Scenario, other information
Europe	Central and south-central Europe	Púčik et al. [45]	1971-2000 vs. 2021-2050 and 2071-2100	14 RCMs	RCP4.5 and RCP8.5 emission scenarios

Geogra-phical area	Geographical restriction	Authors/ Reference	Time frame	Climate models	Scenario, other information
	See the different season results	Marsh et al. [47]	1870-1999 vs. 2000-2099	GCM	A2 emission scenario Compared against NCEP/NCAR Global Reanalysis data
	Iberian Peninsula (often restricted to Mediterranean)	Viceto et al. [48]	1986-2005 vs. 2081-2100	-	RCP8.5 emission scenario ERA-Interim reanalysis MPI Earth System Model
		Rädler et al. [23]	1979-2016	14 RCMs	Statistical model applied to ERA-Interim reanalysis data
	Partly Germany&Alps and Western&Central Europe	Rädler [66]	1979-2016 vs. 2021-2050 and 2071-2100	14 EURO-CORDEX simulations 4 RCMs	RCP2.6, RCP4.5, RCP8.5 ERA-Interim reanalysis AR-CHaMo
North America	Eastern US	Diffenbaugh et al. [16]	1970-1999 vs. 2070-2099	GCM ensemble (CMIP5)	RCP8.5 emission scenario (In reanalysis, CMIP5 did yield too many days with high CAPE.)
	US Largest increases for regions close to the Gulf of Mexico and the Atlantic	Trapp et al. [18]	1962-1989 vs. 2072-2099	Model suite of GCMs and a high-resolution RCM	A2 emission scenario
	US	Trapp et al. [29]	1950-2099	5 GCMs	A1B emission scenario (future world of rapid economic growth, balance between all energy sources)
	Northeastern United States, the Great Lakes, and Southeastern Canada	Gensini et al. [41]	1981-1995 vs. 2041-2065	Regional model forced with output from a GCM	A2 emission scenario
	US, east of continental divide	Gensini and Mote [53[	1980-1990 vs. 2080-2090	Weather Research and Forecasting (WRF-ARW) as RCM GCM: CCSM3	A2 emission scenario Dynamical downscaling
	CONUS	Rasmussen et al. [54[	2000-2013 vs. that period with climate perturbation for RCP8.5	RCM: WRF V3.4.1; GCM: ERA-Interim reanalysis; for the second period plus climate perturbation from a 19-model CMIP5 ensemble monthly mean	RCP8.5 Dynamical downscaling

Geogra-phical area	Geographical restriction	Authors/ Reference	Time frame	Climate models	Scenario, other information
	CONUS	Haberlie et al. [61]	1990-2005 vs. 2085-2100	RCM: WRF-ARW V4.2.1 GCM: CESM	RCP4.5 and RCP8.5 Dynamical downscaling
	CONUS	Ashley et al. [63]	1990-2005 vs. 2085-2100	RCM: WRF-ARW V4.2.1 GCM: CESM	RCP4.5 and RCP8.5 Dynamical downscaling
		Prein et al. [68]	2000-2013 vs. that period with climate perturbation for RCP8.5	RCM: WRF V3.4.1; GCM: ERA-Interim reanalysis; for the second period plus climate perturbation from a 19-model CMIP5 ensemble monthly mean	RCP8.5 Dynamical downscaling
	CONUS	Hoogewind et al. [17]	1971-2000 vs. 2071-2100	RCM: WRF-ARW v3.6 GCM: GFDL CM3	RCP8.5 Dynamical downscaling
Oceania	Northern and eastern Australia	Allen et al. [35]	1980-2000 vs. 2079-2099	2 GCMs	High-warming climate scenarios
Asia	Japan	Muramatsu et al. [49]	1979-2003 vs. 2075-2099	GCM	A1B emission scenario
World		Lepore et al. [65]	1980-2014 vs. 2015-2100 And 1980-2010 vs. 2030-2060 vs. 2070-2100	7 CPIM6 GCMs	RCP8.5

- Europe:
  - *Púčik et al.* [45] *used 14 RCM covering Europe and the Mediterranean, they considered two climate scenarios (RCP4.5 and RCP8.5* [37]*) and compared the period 1971-2000 to the future periods 2021-2050 and 2071-2100. They projected a robust increase in the frequency of unstable environments in central and south-central Europe for the RCP8.5 scenario and the end of the century. The changes for the mid of the century are smaller and less robust both for the RCP4.5 and the RCP8.5 scenario. The only robust changes for the middle of the century appear for the RCP8.5 scenario (less so for the RCP4.5 scenario) for the Mediterranean coastlines and parts of southeastern Europe. For the midcentury, the ensemble-mean change is ca. 50% of that for the end of the century. Moreover, the authors project small, non-robust changes in the frequency of strong deep-layer shear but identify a decrease in shear for the North of Europe. The authors state "By the end of the*

century, the simultaneous occurrence of latent instability, strong deep-layer shear, and model precipitation is simulated to increase by up to 100% across central and eastern Europe in the RCP8.5 and by 30%–50% in the RCP4.5 scenario. Until midcentury, increases in the 10%–25% range are forecast for most regions".

- Marsh et al. [47] compared the periods 1870-1999 and 2000-2099, using a GCM (Community Climate System Model v3 (CCSM3)) and the A2 emission scenario (and compared again NCEP/NCAR Global Reanalysis data). The reanalysis showed that the CCSM3 underestimates frequency of severe thunderstorm environments. The authors projected a CAPE increase in winter in the Mediterranean Sea, the Strait of Gibraltar, the Balearic Islands, southern Italy and the southern Black Sea; a spring decrease in mean CAPE—but an increase on the Faroe Islands; a nearly complete CAPE decrease in the summer, with an exception of western Norway; and an autumn CAPE increase for the Mediterranean Sea and mainland Europe, as well as a decrease for the Atlantic Ocean and the Faroe Islands. Altogether, a slight increase in mean CAPE in the cool season and a slight decrease in the warm season. Moreover, they projected little changes in mean wind shear. Thus, the authors projected a small increase in favorable environments for severe thunderstorms for most locations in Europe because of "an increase in the joint occurrence of high CAPE and high deep layer shear". The largest increase was projected for the Mediterranean Sea.
- Viceto et al. [48] studied conditions favorable to the development of atmospheric stability indices: CAPE, S06 and Severe Weather Threat (SWEAT) for the Iberian Peninsula, comparing the period 1986-2005 with 2081-2100 under the RCP8.5 emission scenario. They projected an increase in CAPE: a significant increase in summer for the Mediterranean and its surroundings; a similar pattern for autumn, but smaller differences; and non-significant differences for spring and winter. They projected an increase in S06 for spring and winter and a decrease for summer and autumn. For the conditions favorable for severe thunderstorms, the authors projected the largest changes in summer (and autumn), mostly for the Mediterranean and its surroundings.
- Rädler et al. [23] showed that the frequency of convective weather events (lightning, hail, severe wind gusts) will likely increase over Europe by the end of the century. They used 14 RCMs. The increase is attributed to increasing humidity near the earth's surface. They projected a slight decrease in thunderstorms for southwestern and southeastern Europe.
- In her PhD thesis, Rädler [66] developed a new approach computing the predicted probability of a hazard as the product of the probability that a storm occurs and the probability of a hazard given the presence of a storm, based on observational a reanalysis data of central Europe, see Subsection A.3.2. She used 14 ensemble members from EURO-CORDEX (with ca. 50km grid spacing) for 1971-2000 with 13 ensemble members for *2021-2050* and 2071-2100 for RCP2.6, 4.5 and 8.5. She modeled hazards separately: large hail,

severe wind gusts, tornadoes, and heavy precipitation. Already for the past, she analyzed that **thunderstorms have become more likely to produce severe weather over the last decades**. *For all future simulations, an increase in lightning cases is projected for central and eastern Europe, decreases are projected for southern Spain, northern Afrika, Greece, Turkey, northwest Ireland*. The largest increases are projected for RCP8.5 for the end of the century—with up to 60% more lightning cases. *Robust increases are projected only for the north-eastern part of the considered European domain and a small region in northern Italy and Austria. For hail≥2cm, she projects an increase in the number of mean annual hail cases for all RCP scenarios and both for the middle* and the end of the century, the strongest increase is projected for RCP8.5, 2071-2100 with over 100% in the north-east of the considered European domain. As detailed in Subsection A.2.3, strong and robust increases in hail≥2cm are projected for most of central and eastern Europe. The results for hail≥5cm are similar (but with a maximum of 160%, i.e., much stronger as for hail ≥ 2cm). The projected relative increases in mean annual number of wind cases are slightly smaller than for hail ≥2cm, with robust increases over central and eastern Europe, with values of 100% in the northeast of the considered European domain. Until the end of the 21st century, the smallest relative changes are projected for lightning, the strongest and most robust increases are projected for hail ≥5cm for RCP8.5. Her conclusion is: **"The increase in convective hazards until the end of the century can only for a small part and in some regions be attributed to the more frequent occurrence of thunderstorms. […] The driving factor is therefore that thunderstorms are more likely to produce severe weather in future climates."**

- North America:
    - Diffenbaugh et al. [16] projected robust increases of severe thunderstorm environments over the eastern United States based on a GCM ensemble (CMIP5, RCP8.5 pathway). They projected these increases for spring and autumn already before a mean global warming of 2°C. Additionally, they projected an increase in the number of days with high CAPE and strong low-level wind shear[6]—they find decrease in vertical wind shear are concentrated on low-CAPE days and, hence, have little effect. Moreover, they project a shift to high CAPE mostly concentrated on days with low convective inhibition. They mainly compare the periods 1970-1999 and 2070-2099. In reanalysis, CMIP5 did yield too many days with high CAPE.
    - Trapp et al. [18] projected an increase in the number of days in which severe thunderstorm environmental conditions (NDSEV) appear in the US, based on a model suite of GCMs and a high-resolution RCM. The largest NDSEV increases are projected

[6] Low-level wind shear is an aviation hazard in itself; however, it was not the focus of this first report, hence, we have not made an extensive literature review on it, and do not report on it separately.

during the summer, for regions close to the Gulf of Mexico and the Atlantic (e.g., >100% increase in Atlanta, GA, and New York, NY). They compare the periods 1962-1989 and 2072-2099. As proxies, they use CAPE and S06. They observe an increasing CAPE and a decreasing vertical wind shear, again dominated by the CAPE increase.

- Trapp et al. [29] projected an increase in frequency of severe-thunderstorm forcing (quantified as NDSEV) for the US and the A1B scenario for greenhouse-gas emissions (future world of rapid economic growth, balance between all energy sources [39]) for the period 1950-2099 based on a five-member ensemble of GCMs. Moreover, they project a decrease in cyclone frequency over the conterminous US in winter and early spring.
- *Gensini et al.* [41] *projected statistically significant increases in NDSEV in Northeastern United States, the Great Lakes, and Southeastern Canada comparing the periods 1981-1995 and 2041-2065.*
- Rasmussen et al. [54] considered convective environments for CONUS and compared the period 2000-2013 based on reanalysis data with the same period plus perturbation for the RCP8.5 scenario (pseudo global warming approach). They projected that weak to moderate convection will decrease in frequency and that strong convection will increase in frequency. Moreover, they projected that CAPE and CIN will increase downstream of the Rockies.
- Haberlie et al. [61] studied thunderstorm activity in three categories (40dBZ—thunderstorms, 50 dBZ—stronger thunderstorms, 60 dBZ—potential for hail) and CAPE and CIN in CONUS. They compared the period 1990-2005 with the future period 2085-2100 with both RCP4.5 and RCP8.5. They projected significant decreases in days with 40dBZ in the Southern Plains (RCP4.5 and 8.5) and Florida and coastal regions of the Carolinas (RCP8.5), while they projected significant increases in days with 40dBZ limited to parts of the Northeast under RCP4.5, but widespread in the Northern Plains and northern Mississippi River valley for RCP8.5. For days with 50 and 60 dBZ, they projected increases for many areas east of the High Plains. Generally, they projected a significant increase in annual thunderstorm activity despite decreases during summer (where fewer 40 and 50dBZ days, but more 60dBZ days are projected)—during fall, winter and spring more days in all three categories are projected.
- Ashley et al. [63] considered supercells (intense, long-lived thunderstorms, responsible for most damaging hail and deadly tornadoes) in CONUS. They compared the period 1990-2005 with the future period 2085-2100 with both RCP4.5 and RCP8.5. They projected that supercells will be more frequent in the eastern CONUS, but less frequent in parts of the Great Plains. The supercell risk will not be highest in the traditional severe-storm season, but will increase in late winter and early spring. Even the spatial extent of the supercells (the footprint) will increase in a future climate. Together, this yields a potential for more significant tornadoes, hail and extreme rainfall.

- Prein et al. [68] investigated mesoscale convective systems (MCSs) in North America, comparing the period 2000-2013 forced with ERA-Interim reanalysis data with a future simulation using the pseudo-global warming (PGW) approach, where the ERA-Interim boundary conditions are perturbed by a climate-change signal, which is the average monthly mean of 19 CMIP5 GCMs for the periods 1976-2005 and 2071-2100. They projected that all regions in North America, except for the Central US, experience an increase in MCS frequency in the future period. In the Central US MCS reduce by 30%, but extreme MCSs (with maximum hourly precipitation of more than 90mm/h) increase by 380%. Similar high increases in extreme MCSs are projected for other regions. The maximum hourly precipitation increases by 25-40 percent in northern regions of the considered area, and 15-20 percent elsewhere. The size of MCS (spatial extent) increases in all regions, with the largest increases in the South. CAPE increases significantly, this change yields more environments favorable for convection and allows MCSs to grow larger. Prein et al. detail that the projected increase in both maximum hourly precipitation and size of MCSs results in a significant increase in the hourly total rainfall in MCSs of 20-40 percent in mid- and high-latitude regions and 40-80 percent in lower latitudes. Moreover, the projection of a rapid increase in MCSs that have a high hourly total rainfall relative to their size will yield a higher flooding potential (a lot of precipitation in a small area). Additionally, a large flood risk stems from MCSs with a high hourly total rainfall and slow storm motion—these are projected to have the highest increase in all regions of North America.
- Hoogewind et al. [17] considered hazardous convective weather and compared the period 1971-2000 with the future period 2071-2100 under RCP8.5. As GCM they used GFDL CM3, and as RCM WRF-ARW v3.6 with 4km horizontal grid spacing. They project that the HCW season will be longer, possibly by as much as one month, and that the conditional probability of HCW given NDSEV will decline during summer over large parts of the central US.

* Oceania:
  - Allen et al. [40] studied the occurrence of severe thunderstorm environments in Australia using two GCMs, they compared the periods 1980-2000 and 2079-2099 (with high-warming climate scenarios). They project significant increases of severe thunderstorm environments for northern and eastern Australia—attributed to increasing CAPE, particularly close to warm sea surface temperatures. The authors project a decrease in frequency of environments with high vertical wind shear, but they predict that this will be outweighed by the CAPE increase.
* Asia:
  - Muramatsu et al. [49] compared the periods 1979-2003 and 2075-2099 under the A1B emission scenario for Japan. They studied strong tornadoes (F2 or greater on the Fujita

scale). They projected that the frequency of strong tornadoes will double in almost all of Japan in spring, and on the Japan Seaside of the Japanese Islands in summer. The increase is attributed to an increase in the water-vapor missing ratio and an increase in the temperature in the lower troposphere. (Strong vertical wind shear is again projected to not change or to undergo a slight decrease.)

- World:
  - Lepore et al. [65] studied the global response of convective proxies: CAPE, CIN, S06, storm relative helicity (SRH), and indexes that combine these. They compared the periods 1980-2014 and 2015-2100 with RCP8.5, using seven CPIM6 global climate models. They projected an increase in environments favorable to convective storms—a **frequency increase of 5-20 percent per °C of global warming**—based on proxies (CAPE, CIN, S06, SRH). *They also investigated changes comparing the periods 1980-2010, 2030-2060, and 2070-2100 and projected CAPE increases in the relevant convectively active regions. The midcentury changes are statistically significant for the vast majority.* They projected robust increases over all continents except of desert regions*, over high latitudes of the Arctic a robust increase in CAPE is already projected by mid-century*. Lepore et al. project significant decreases of CAPE over the eastern Atlantic during boreal spring and over the southern hemisphere during winter. *The projected changes to CIN for the middle of the century are small in comparison to CAPE, but the projected increases are robust*. The largest increases are projected for transition seasons, in particular, in spring, and more increases are projected over the northern hemisphere. However, over high latitudes in both hemispheres, no robust increases for CIN are projected. For the end of the century, widespread robust increases for CIN are projected. Lepore et al. project that regional increases to low-level wind shear will be offset by decreased deep-layer wind shear, that is, while the first trend would result in more frequent environments favorable for convective storms, this effect is counterbalanced by the second trend.

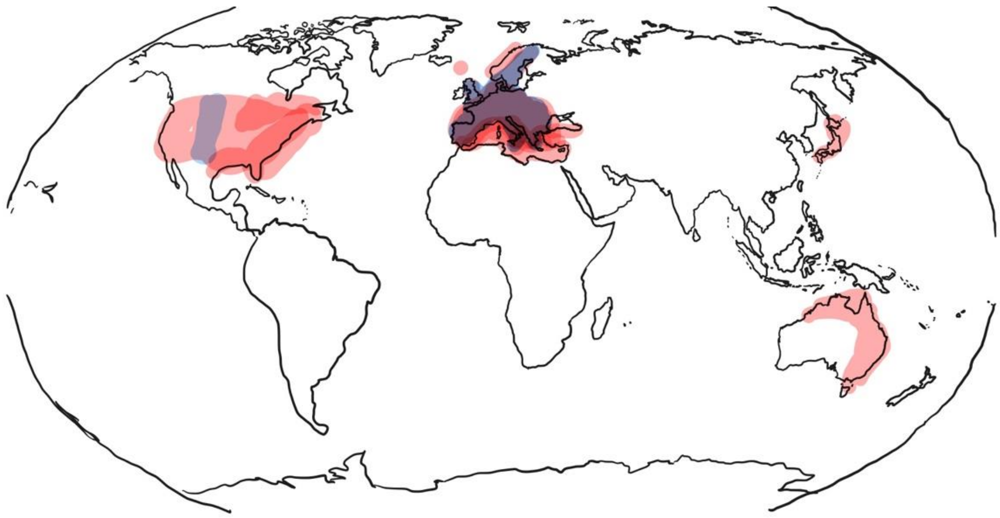

Figure A.6 Severe thunderstorms future studies: blue and red represent a negative and a positive trend, respectively. Most trends are on the frequency of severe thunderstorms.

Allen [11] highlighted that the cleanest upwards trend can be described for Europe, in particular, for Southern Germany, Italy and Southern France, while he described competing trends for the US. Generally, the trend is more instable, thus, initiated storms tend to be a bigger problem, but they occur less frequently. However, this is not well reflected in climate models.

A.3.4 Summary of Past and Future Trends for Convective Weather (Thunderstorms)

In summary, for Europe, the frequency of unstable environments is projected to increase for large parts of the continent, with some exceptions, e.g., for southwestern and southeastern Europe. For some regions slight decreases are projected (e.g., southern Spain). Additionally, thunderstorms are projected to be more likely to produce severe weather in future climates. Moreover, researchers project a slight increase in mean CAPE in the cool season and a slight decrease in the warm season—and little changes in mean wind shear. In North America, an increase in the number of days in which severe thunderstorm environmental conditions (NDSEV) is projected—with particularly large increases, e.g., in summer close to the Gulf of Mexico and the Atlantic Ocean, but also in spring for the Mississippi, Tennessee and Ohio River valleys. However, the results for the summer do not show agreement over all studies, decreases in thunderstorm activity from midsummer to early fall are also projected. Moreover, while the frequency for strong convections is projected to increase, the frequency for weak to moderate convection is projected to decrease. In addition, in particular, extreme mesoscale convective systems are projected to increase a lot in parts of the US. Finally, even the season for hazardous convective weather is projected to become longer. For Australia, significant increases of severe thunderstorm environments for northern and eastern Australia are projected. For the worlds, an increase in 5-20 percent in the frequency of environments favorable to convective storms is projected per °C of global warming.

Long-term reliable records do not exist, but the occurrence of thunderstorm environments has significantly increases across most of Europe over the last 72 years, with strong increases in some regions.

A.3.5 Knowledge Gaps and Uncertainties

Similar as for hail, spatial gaps for the future development of severe thunderstorms are evident. Allen [11] underlined that for outside of the USA and Europe no good proxies are known, e.g., the lapse rate in subtropical storms is rarely above 6, while in mid-latitude storms values of 7-9 are common. Even the observational records are temporally and spatially limited.

Moreover, very few authors focus on the middle of the 21st century—the main interest of EASA. The main reason is that statistically significant results can easier be obtained for the end of the century. Hence, to obtain results even for the midcentury, EASA must specifically communicate its interest.

Additionally, the global climate models and SCS have different scales: most convective systems have a scale of max 10km and last up to 2-3 hours (but these spatial and temporal limits still allow severe weather phenomena); GCMs have a resolution of hundred(s of) km and 6h. These do not match well, and many severe storms cannot be detected by the current generation of GCMs. Moreover, in GCMs convective processes are parameterized and storms are not directly simulated—these parameterizations are considered a major source for both model errors and uncertainty [51]. Recently, dynamical downscaling[7] has been used to bridge that gap for simulating future climates. The different resolutions in models may also yield projections that reflect model biases rather than future trends. Given the local properties, Allen [11] estimated downscaling to help with several of the current problems in SCS projections. However, he deems it currently as too computationally expensive to make it a feasible option. We present the concept of dynamical downscaling, existing research and limitations in Section A.4.

In addition, many of the phenomena feature large interannual variability. This is most pronounced for tornadoes. This yields the problem of discriminating climate change vs. natural variability.

A major problem when projecting SCS/SigSCS is that different phenomena (wind, hail, tornadoes) are aggregated. However, large hail, damaging winds, and tornadoes are not favoured by the same environmental conditions, which contradicts considering severe thunderstorms as a unified set of hazards.

Battaglioli and Greonemeijer [77] highlighted the need for coordination of different research groups for projections: for each of the models, the crucial parameters (e.g., the vertical wind shear) are either

[7] In global climate models, convective processes are parameterized instead of simulating storms directly. Thus, the resolution on SCS is significantly larger than that used in operational weather forecasting. To achieve that granularity even for projections, comparable to high-resolution regional climate models, dynamical downscaling is needed: in areas of interest high resolution is nested with the general low-resolution global climate model. That is, the scale is reduced, but dynamically only in those locations that are of interest for SCS.

computed or need to be available as data. If a large part of these would be stored as data, calculations could still be made afterwards.

Finally, environments that are favorable for SCS/SigSCS must not result in a storm, the likelihood for initiation is very local (which is not well reflected in GCMs). Allen [11] described proxies for initiation as nearly stochastic.

A.4 Using Dynamical Downscaling to Study Trends for Convective Weather

As dynamical downscaling could help with several of the current problems in SCS projections [11], we give a brief overview on the concept, the existing research and its limitations. In Subsection A.4.1, we detail what dynamical downscaling is, ibn Subsection A.4.2, we present results from future-trend studies using dynamical downscaling, and in Subsection A.4.3, we highlight obstacles for using dynamical downscaling today.

A.4.1 Dynamical Downscaling

Using GCMs, mesogamma-scale processes (phenomena larger than microscale, but below 20km scale), like thunderstorm convection, cannot be simulated directly. The main idea for dynamical downscaling is to use such a high resolution (horizontal grid with edge length of max 4km) that deep convection (or generally mesogamma-scale processes) must not be parameterized, but can be resolved explicitly [51,55,56]—convection-permitting models (CPMs), also called cloud-resolving, convection-resolving, cloud-permitting, or convection-permitting. Muller et al. [69] define such a model as “a computer model that solves the governing equations at kilometer-scale horizontal resolution and that is capable of explicitly simulating deep convective clouds”. That is, in these models, the convection is explicitly simulated instead of using parameters/proxies to simulate its occurrence. Horizontal grid spacings larger than 4km do not allow for an accurate representation of certain dynamics [51]. Generally, there are four approaches to obtain CPM simulations, but the most frequently used approach nests small-grid-spacing domains and GCM (or reanalysis) output is passed to these simulations as initial and boundary conditions [51,52,59]. Giorgi and Gutowski [58] described the idea in detail: a GCM is run first to integrate effects of large-scale forcings (e.g., those resulting from greenhouse gases) and processes on the general circulation of the atmosphere (e.g., the El Nino-Southern Oscillation); initial conditions and lateral boundary conditions (e.g., wind components, temperature) from the GCMs are then used as input in high-resolution RCMs, which—over a limited area of interest—can describe forcings and phenomena not resolved in GCMs. The lateral boundary conditions are applied only in a lateral buffer zone (between the area of interest and the ``rest’’), such that model equations can be freely integrated in the area’s interior [58]. The resulting models, extensions of RCMs, are also referred to as convection-permitting RCMs (CPRCMs) [55]. The term ``dynamic’’ in dynamical downscaling stems from the GCMs not only providing initial conditions, but driving them through the lateral boundary conditions, which make the RCM dynamically consistent to the large-scale flow [51]. Often, intermediate nesting steps are used until the goal resolution of ~4km is reached [51], but Gensini [57] stated that nesting is not necessary, as the intermediate resolution of 12-40 km does not yield much information but is computationally expensive. Studies by several groups of authors have shown that these simulations reasonably reproduce observations of rainfall and convective hazards [51,56,60,67,70, 71]—in particular, the models can overcome limitations of models with a grid spacing larger than 10km, like a too early onset and peak of convective precipitation over land during summer [51]. Cui et al. [73] confirmed that with HAILCAST and a lightning performance index diagnostic, a CPRCM “performed well in simulating precipitation, hail and lightning”. However, Kumar Srivastava et al. [70] showed that dynamical downscaling is also susceptible to regional-climate-model biases and suggest moderate bias correction.

The use of dynamical downscaling is only advisable when it comes with added value—however, Giorgi and Gutowski point out that assessing this is often difficult because it depends on various factors, for example, scale, region, and season. They discuss that scenarios that usually have the potential for a high added value are those where “local forcings substantially modulate the climate signal at fine scales, e.g., complex topography and coastlines, land surface heterogeneity, lakes, mesoscale convective systems, and complex aerosol emissions and distributions.” Hence, our interest in convective systems falls exactly in this category. Observational data sets that have a fine-grained spatial and temporal resolution, which are needed to verify the developed models, have recently become available [55]—for example, the Deutschwer Wetterdienst has reprocessed and analyzed gauge-adjusted radar-based precipitation estimates starting from 2001 [80] (not long enough for climiatologies, but for verification). We refer the reader to a recent survey paper by Lucas-Picher et al. [51] on methodology and research results.

A.4.2 Projections using Dynamical Downscaling

Several authors have successfully applied dynamical downscaling, for an overview of the projections see Figure A.7, and Table A.4.1 (results) and Table A.4.2 (models used and time frame). If these projections are made for hail or convective storms, the results also appear in the previous sections. One observation is that the large majority of studies with dynamical downscaling have been made for North America, specifically, for CONUS. We also summarize all results in a list, again, projections for the middle of the century are highlighted in italics:

- Europe
    - Kahraman et al. [72] studied lightning in Europe, comparing the period 1998-2007 with a future period of 10 years corresponding to ~2100 under RCP8.5. For the RCM they used a horizontal grid spacing of 2.2km and a graupel and ice-flux-based scheme applied to a pan-European simulation of the UK Met Office Unified Model (UM), initial and boundary

conditions stem from the HadGEM3 GCM (with ca. 25km grid spacing). They focus on cloud-to-ground lightning. They projected:

- A net increase in lightning counts over southern parts of the Nordic countries, the British Isles and parts of the Atlantic Ocean further west; in Scandinavia they are projected to increase by a factor of 2.6 (future August in Scandinavia has a higher lightning density than current June in central Europe).
- A decrease in lightning counts over most of the rest of Europe (except for higher terrain), which occurs mainly during summer and spring
- Increases over north and south land areas and decreases over the sea, which are less pronounced towards the north; they project local increases over both the North and Baltic Sea
- A summer increase in lightning in the north and a decrease in central Europe—an indication of a circulation regime shift
- Decreases in lightning across most of Europe (in particular, in summer) accompanied by a pronounced reduction in mean cloud ice, which yields fewer lightning strikes/thunderstorm; this decrease is projected while a sharp increase in the fraction of unstable cases is projected (changes in microphysics and increase in CIN). This appears because of uncertainty in convective initiation, that is, a projected increase in unstable cases does not mean an increase in thunderstorm frequency.
- In the autumn, an increase in MLH of up to 1.5km (which is considered to be a large increase). This increase strongly reduces cloud ice, in particular, over northern and central Europe. Thus, increases in precipitating unstable cases must not yield an increase in lightning.
- For the North Sea during winter, increases in lightning days and lightning density (number of flashes per km per year)
- In Southern European mountains in spring, increases in lightning days

Their projected lightning changes for Europe are strongly correlated with elevation: grid points over 3km show an increase of more than 25flashes/km^2, while only a quarter of sea grid points show an increase; in the Alps, they projected a large increase in lightning counts and thunderstorm activity in summer. They find no single key driver for lightning changes over Europe, moisture, convective instability, CIN play a role

- North America:
  - Trapp et al. [38] studied large and very large hail in the US and compared the periods 1971-2000 and 2071-2100. They employed WRF V3.6 as RCM with 4km grid spacing and the Geophysical Fluid Dynamics Laboratory Climate Model v3 (GFDL CM3) as GCM. They projected increases in the frequency of large hail (≥35 mm diameter) over broad geographical areas of the US during all seasons; and increases in very large hail (≥50 mm diameter) for the central US during boreal spring and summer. The authors used high-resolution dynamical

downscaling (4 km resolution) to integrate the environmental conditions for and initiation of convective storms that support formation of hail, the storm volume and the depth of the lower atmosphere conductive to melting.

- Gensini and Mote [53] considered hazardous convective weather (e.g., tornadoes, damaging wind gusts, large hail) for the US east of the continental divide and compared the peak season in the period 1980-1990 to the future period 2080-2090. They used dynamical downscaling with 4km grid spacing, the Weather Research and Forecasting (WRF-ARW) model as RCM, and as a GCM the Community Climate System Model version 3 (CCSM3). They projected a significant future increase in hazardous convective weather frequency and variability for the A2 emission scenario; in particular, for the afternoons in March and April; they project the largest increase for the Middle Mississippi, Lower Mississippi, Ohio, and Tennessee River valleys.
- Rasmussen et al. [54] considered convective environments for CONUS and compared the period 2000-2013 based on reanalysis data with the same period plus perturbation for the RCP8.5 scenario (pseudo global warming approach). As convection-permitting RCM they used WRF V3.4.1 with 4-km horizontal spacing and ERA-Interim reanalysis data plus a 19-model CMIP5 ensemble monthly mean climate change signal. They projected that weak to moderate convection will decrease in frequency and that strong convection will increase in frequency. Moreover, they projected that CAPE and CIN will increase downstream of the Rockies.
- Goodin [59] studied the frequency and intensity of hail and compared the period 1990-2005 with the future period 2085-2100 under RCP4.5 and RCP8.5. She used dynamical downscaling with 3.75km grid spacing and the RCM WRF V4.1.2, and a GCM from the Community Earth System Model (CESM), where she re-gridded and bias-corrected the data using ERA-Interim reanalysis data. She projected significant increases in frequency of severe-hail days (hail ≥ 2.54cm) in broad areas of the Midwest and Eastern CONUS, especially for RCP8.5. The most robust increases are projected in boreal winter and spring; in summer, she projected a significant decrease in frequency of severe-hail days in the Central/Southern Plains and the Southeast. Moreover, she projected a significant increase in large-hail days (hail ≥ 4cm) for RCP8.5 in the Eastern CONUS; for many regions in the Southern Plains and Southeast the number of large-hail days are projected to nearly double. On the other hand, she projected a robust decrease in large-hail days during summer in the Southern Plains. Furthermore, in the projections, slight shifts in the maximum diameter hail values can be observed—both annually and seasonally; hail-size extremes are projected to increase in the Midwest, the Southeast and the Southern Plains.
- Haberlie et al. [61] studied thunderstorm activity in three categories (40dBZ—thunderstorms, 50 dBZ—stronger thunderstorms, 60 dBZ—potential for hail) and CAPE and CIN in CONUS. They compared the period 1990-2005 with the future period 2085-2100 with both RCP4.5 and

RCP8.5. As GCM they used a bias-corrected and re-grided CESM, as RCM they employed WRF-ARW V.41.2 with a 3.75km horizontal grid spacing. They projected:

- A significant decrease in days with 40 dBZ in Southern Plains both for RCP4.5 and 8.5
- A significant decrease in days with 40 dBZ over Florida and coastal regions of the Carolinas for RCP8.5
- A significant increase in days with 40 dBZ limited to parts of Northeast in RCP4.5, but widespread in Northern Plains and northern Mississippi River Valley for RCP8.5
- The largest changes in days with 40 dBZ for RCP8.5
- A significant increase for days with the higher thresholds (50,60) in many areas east of the High Plains in RCP8.5
- A significant increase in 60-dBZ days, but a significant decrease in 40-dBZ days for parts of the southern and eastern Plains
- For Tennessee, Ohio, Upper Mississippi River Valley increases of 3-9 50-dBZ days; for Texas and Florida: decreases of 3-9 50-dBZ days, but no decrease for 60-dBZ days
- Significant increases in annual thunderstorm activity despite decreases (some significant) during summer, which currently is the peak season for annual thunderstorm activity; overall increase in winter, fall and spring thunderstorm activity. Summertime decreases in 40 and 50-dBZ days, but more 60-dBZ days; fall, winter and spring more days in all categories

- Ashley et al. [63] considered supercells (intense, long-lived thunderstorms, responsible for most damaging hail and deadly tornadoes) in CONUS. They compared the period 1990-2005 with the future period 2085-2100 with both RCP4.5 and RCP8.5. As GCM they used a bias-corrected and re-grided CESM, as RCM they employed WRF-ARW V.41.2 with a 3.75km horizontal grid spacing. They projected that:
  - Supercells will be more frequent and intense in future climates, with robust spatiotemporal shifts
  - Supercells will be more frequent in eastern CONUS, for RCP8.5 mostly in north Texas and in the Ark-La-Tex region and Ozark Plateau, for RCP4.5 maxima in midsouth and central Gulf Coast
  - Supercells less frequent in parts of the Great Plains (south Texas to South Dakota), with a notable reduction from the High Plains of Colorado through the middle of the Missouri valley; these changes are caused by reduced supercell counts during the summer
  - Supercell risk will be highest not in traditional severe-storm season, but project an increase in late winter and early spring (February, March, April) for both RCP4.5 and 8.5; supercells are expected to decrease from midsummer to early fall (June, July, September)
  - The largest track change of supercells occurs for RCP8.5

   - Particularly intense storm rotation is more prevalent in a future climate both for RCP4.5 and 8.5
   - Little change will occur in the diurnal cycle of supercell counts in eastern CONUS,
   - The Mid-South and northern Plains have shifts over the day, with a large change for the mid-South with large increases in supercell occurrences for midafternoon through overnight hours (for both RCP4.5 and 8.5)
   - Over the mid-South supercells will have a larger footprint (extent of the supercell) by 70% in both RCP4.5 and 8.5
   - Supercell frequency and footprint will increase over the mid-South clustered in winter and early spring, hence, this may result in a larger threat of nocturnal tornadoes
   - Supercells in the northern Plains will decrease, where most decline occurs during afternoon and evening
   - This yields the potential for more significant tornadoes, hail and extreme rainfall
- Prein et al. [68] investigated mesoscale convective systems (MCSs) in North America, comparing the period 2000-2013 forced with ERA-Interim reanalysis data with a future simulation using the pseudo-global warming (PGW) approach, where the ERA-Interim boundary conditions are perturbed by a climate-change signal, which is the average monthly mean of 19 CMIP5 GCMs for the periods 1976-2005 and 2071-2100. As RCM they used WRF v3.4.1 with 4km horizontal grid spacing. They projected that:
   - All regions in North America, except for the Central US, experience an increase in MCS frequency in the future period.
   - In the Central US MCSs reduce by 30%, but extreme MCSs (with maximum hourly precipitation of more than 90mm/h) increase by 380%. Similar high increases in extreme MCSs are projected for other regions.
   - The highest relative increases in MCS frequency occur for Canada and the Northeast US, where MCSs with maximum hourly precipitation of more than 80mm/h become frequent, while they currently are underrepresented.
   - The maximum hourly precipitation increases by 25-40 percent in northern regions of the considered area, and 15-20 percent elsewhere.
   - The size of MCS (spatial extent) increases in all regions, with the largest increases in the South.
   - CAPE will increase significantly, this change yields more environments favorable for convection and allows MCSs to grow larger.
   - MCSs slower than 20km/h slow down by up to 20 percent in the US Midwest, Mid-Atlantic region and Canada, but they become faster in Mexico and the US Northeast.

  Prein et al. detail that the projected increase in both maximum hourly precipitation and size of MSCs results in a significant increase in the hourly total rainfall in MSCs of 20-40 percent in mid- and high-latitude regions and 40-80 percent in lower latitudes. Moreover, the projection of a rapid increase in MCSs that have a high hourly total rainfall relative to their size will yield a higher flooding potential (a lot of precipitation in a small area). Additionally, a large flood risk stems from MCSs with a high hourly total rainfall and slow storm motion—these are projected to have the highest increase in all regions of North America.

- *Mahoney et al.* [32] *project a near-elimination of surface hail in Colorado during warm season. They attribute this change to an increased MLH. They compare the periods 1971-2000 and 2041-2070. The authors employed a three-tiered downscaling approach: first downscaling GCM simulations to a 50-km grid of NARCCAP RCMs, driven by A2-scneario GCMs; extreme precipitation events occurring in NARCCAP are further downscaled using a high-resolution model with a 1.3-km grid, where intense thunderstorm events can be explicitly simulated.*
- *Gensini et al.* [41]*, in 2014, used the WRF-G RCM with a resolution of 50km—clearly showing a development in the grid spacing—forced by the CCSM3 GCM. They projected statistically significant increases in NDSEV in Northeastern United States, the Great Lakes, and Southeastern Canada comparing the periods 1981-1995 and 2041-2065.*
- Trapp et al. [18], in 2007, projected an increase in NDSEV appear in the US, based on a model suite of the FV-GCM and the RegCM3 RCM with a horizontal grid spacing of 25km—again assumingly due to the publication date. The largest NDSEV increases are projected during the summer, for regions close to the Gulf of Mexico and the Atlantic (e.g., >100% increase in Atlanta, GA, and New York, NY). They compare the periods 1962-1989 and 2072-2099. As proxies, they use CAPE and S06. They observe an increasing CAPE and a decreasing vertical wind shear, again dominated by the CAPE increase.
- Hoogewind et al. [17] considered hazardous convective weather and compared the period 1971-2000 with the future period 2071-2100 under RCP8.5. As GCM they used GFDL CM3, and as RCM WRF-ARW v3.6 with 4km horizontal grid spacing. They project that the HCW season will be longer, possibly by as much as one month, and that the conditional probability of HCW given NDSEV will decline during summer over large parts of the central US.
- Trapp and Hoogewind [75] considered tornadoes, in particular, three extreme tornadic storm events in Kansas and Oklahoma in 2007, 2010 and 2013, to understand how current-day tornadic-supercellular storm events might be realized under a future climate. In the future climate, the combined effect of increased CIN and decreased parcel lifting led to a failure of convection initiation in many ensemble members. For those ensemble members with sufficient matching between CIN and lifting, they observed stronger convective updrafts and enhanced vertical rotation.

Table A.4. 1 Future-trend studies using dynamical downscaling: Geographical area, considered phenomena, seasonal projections and projections without seasonal distinction. Results for the end of the century are highlighted in gray, results for the middle of the century are highlighted in yellow. The considered phenomena is indicated by font color: lightning in green, hail in dark blue, precipitation in light blue, tornadoes in dark red, and convective storms in dark orange.

Geogra-phical area	Geogra-phical restriction	Authors/ Reference	Considered phenomena	Spring	Summer/Warm Season	Fall	Winter	Without Seasonal Distinction
Europe		Kahraman et al. [72]	Lightning	Decrease in lightning counts central Europe; Increase in Southern European mountains	Increase in lightning counts in the north; Decrease in central Europe In the Alps: large increase in lightning counts and thunderstorm activity	Increase in MLH of up to 1.5km→ strongly reduces cloud ice	Increases for the North Sea in lightning days and density	Increase in lightning counts over southern parts of the Nordic countries, the British Isles and parts of the Atlantic Ocean further west Changes strongly correlated with elevation No single key driver for lightning changes
North America	US	Trapp et al. [38]	hail	Increases in very large hail (≥50 mm diameter)	Increases in very large hail (≥50 mm diameter)			Higher frequency of large hail ((≥35 mm diameter)
	CONUS	Gensini et al. [52]	Precipitation and temperature					Statistically significant decreases of precipitation across southern Great Plains and Intermountain West; statistically significant increases in precipitation Tennessee and Ohio Valleys and across parts of the Pacific Northwest Robust and significant changes in mean temperatures (for many areas in central CONUS by 5-6°C, for boreal summer and fall 6-7°C)
	US east of continental divide, increases primarily found in the Mississippi,	Gensini and Mote [53]	Hazardous convective weather (e.g., tornadoes,	Statistically significant increase in hazardous convective weather				Most of the increase in hazardous convective weather around local sunset; peak-season severe weather more varialbe, potentially more frequent

Geogra-phical area	Geogra-phical restriction	Authors/ Reference	Considered phenomena	Spring	Summer/Warm Season	Fall	Winter	Without Seasonal Distinction
	Tennessee, and Ohio River valleys		damaging wind gusts, large hail)					
	CONUS	Rasmussen et al. [54]	Convective environments					Frequency decrease for weak to moderate convection; frequency increase for strong convection; CAPE and CIN increase downstream of Rockies
	CONUS	Goodin [59]	Hail	Most robust increases in frequency of severe-hail (≥2.54cm) days in broad areas of Midwest and Eastern CONUS	Significant decrease in frequency of severe-hail days in Central/Southern Plains and the Southeast; robust decrease in large-hail (≥4cm) days in Southern Plains		Most robust increases in frequency of severe-hail days in broad areas of Midwest and Eastern CONUS	Significant increase in large-hail days in Eastern CONUS, slight shifts in maximum diameter hail values both annually and seasonally, hail-size extremes increased in Midwest, Southeast and Southern Plains
	CONUS	Haberlie et al. [61]	Thunderstorms (40, 50, 60 dBZ[8])	Overall increase in thunderstorm activity; more days with 40/50/60dBZ thunderstorms	Decrease in thunderstorm activity; decrease in 40 and 50dBZ days, but increase in 60dBZ days	Overall increase in thunderstorm activity; more days with 40/50/60dBZ thunderstorms	Overall increase in thunderstorm activity; more days with 40/50/60dBZ thunderstorms	40dBZ days: significant decrease in Southern Plains and coastal Carolinas; significant increase in Northeast 50/60dBZ days: Significant increase in many areas east of the High Plains in RCP8.5
	CONUS	Ashley et al. [63]	Supercells[9]	Highest supercell risk in early spring; Increased supercell frequency	Supercells decrease from midsummer	Supercells decrease until early fall	Highest supercell risk in late winter Increased supercell frequency	Supercells will be more frequent and intense in future climates, robust spatiotemporal shifts; Supercells more frequent in eastern CONUS, less frequent in parts of the Great Plains;

[8] Decibel relative to Z, unit used for weather radar
[9] Intense, long-lived thunderstroms, responsible for most damaging hail and deadly tornadoes

Geogra-phical area	Geogra-phical restriction	Authors/ Reference	Considered phenomena	Spring	Summer/Warm Season	Fall	Winter	Without Seasonal Distinction
				and footprint			and footprint	Intense storm rotation more prevalent in future
	CONUS	Prein et al. [68]	Mesoscale convective systems (MCSs)					All regions (except Central US) increase in MCS frequency In Central US: decrease by 30%, but extreme MCSs increase by 380% Similar high increases for extreme MCSs for other regions Highest relative increase in MCS frequency: Canada and Northeast US Maximum hourly precipitation: • Increase by 25-40% northern regions • Increase by 15-20% otherwise Significant increase in CAPE allows MCSs to grow larger Rapid increase in MCSs with high hourly rainfall relative to their size yields higher flooding potential
	Colorado	Mahoney et al. [32]	Hail and flood risk		Near-elimination of surface hail			
	US Largest increases for regions close to the Gulf of Mexico and the Atlantic	Trapp et al. [18]	Severe thunderstorms		Largest increase in NDSEV			Increase in number of days with severe thunderstorm environmental conditions (NDSEV)
	Northeastern United States, the Great Lakes, and Southeastern Canada	Gensini et al. [41]	Convective environments					Increase in NDSEV

Geogra-phical area	Geogra-phical restriction	Authors/ Reference	Considered phenomena	Spring	Summer/Warm Season	Fall	Winter	Without Seasonal Distinction
	CONUS	Hoogewind et al. [17]	Hazardous convective weather (HCW): tornadoes, large hail, damaging wind gusts		Conditional probability of HCW given NDSEV declines over much of central US			Longer HCW season (perhaps by more than a month)
	US (Kansas + Oklahoma)	Trapp and Hoogewind [75]	Tornadoes					Combined effect of increased CIN and decreased parcel lifting led to failure of convection initiation in many ensemble members Ensemble members with sufficient matching between CIN and lifting: stronger convective updrafts + enhanced vertical rotation

Table A.4. 2 Future-trend studies using dynamical downscaling: time frame, RCM, horizontal grid spacing, GCM for initial and boundary conditions, emission scenarios considered in the different studies. Results for the end of the century are highlighted in gray, results for the middle of the century are highlighted in yellow.

Geographical area	Geographical restriction	Authors/ Reference	Time frame	RCM	Horizontal grid spacing	GCM for initial and boundary conditions	Scenario, other information
Europe		Kahraman et al. [72]	1998-2007 and 10 years corresponding to ~2100	UK Met Office UM v10.1	2.2 km	HadGEM3 (with 25km grid spacing)	RCP8.5

Geographical area	Geographical restriction	Authors/ Reference	Time frame	RCM	Horizontal grid spacing	GCM for initial and boundary conditions	Scenario, other information
North America		Trapp et al. [38]	1971-2000 vs. 2071-2100	WRF V3.6	4km	GFDL CM3	RCP8.5
	CONUS	Gensini et al. [52]	1990-2005 vs. 2085-2100	Weather Research and Forecasting (WRF-ARW) as RCM	3.75 km	Community Earth System Model (CESM) by National Center for Atmospheric Research (NCAR)	RCP8.5
	US, east of continental divide	Gensini and Mote [53[	1980-1990 vs. 2080-2090	WRF-ARW as RCM	4km	CCSM3	A2 emission scenario
	CONUS	Rasmussen et al. [54]	2000-2013 vs. that time frame plus perturbation for RCP8.5 scenario (pseudo global warming approach)	WRF V3.4.1	4km	ERA-Interim reanalysis; for the second period plus climate perturbation from a 19-model CMIP5 ensemble monthly mean	RCP8.5
	CONUS	Goodin [59]	1990-2005 vs. 2085-2100	WRF V4.1.2	3.75 km	GCM from the CESM, re-gridded and bias-corrected using ERA-Interim reanalysis data	RCP4.5 and RCP8.5
	CONUS	Haberlie et al. [61]	1990-2005 vs. 2085-2100	WRF-ARF V4.1.2	3.75 km	GCM from the CESM, re-gridded and bias-corrected using ERA-Interim reanalysis data	RCP 4.5 and RCP8.5

Geographical area	Geographical restriction	Authors/ Reference	Time frame	RCM	Horizontal grid spacing	GCM for initial and boundary conditions	Scenario, other information
	CONUS	Ashley et al. [63]	1990-2005 vs. 2085-2100	WRF-ARF V4.1.2	3.75 km	GCM from the CESM, re-gridded and bias-corrected	RCP 4.5 and RCP8.5
		Prein et al. [68]	2000-2013 vs. that time frame plus perturbation for RCP8.5 scenario (pseudo global warming approach	WRF V3.4.1	4km	ERA-Interim reanalysis; for the second period plus climate perturbation from a 19-model CMIP5 ensemble monthly mean for the periods 1976-2005 and 2071-2100	RCP8.5
		Mahoney et al. [32]	1971-2000 vs. 2041-2070		1.3 km	Geophysical Fluid Dynamics Labaratory CM2.1	Three-tiered downscaling, explicit simulation of intense thunderstorm events
	US Largest increases for regions close to the Gulf of Mexico and the Atlantic	Trapp et al. [18]	1962-1989 vs. 2072-2099	RegCM3	25 km (published in 2007)	NASA's Finite Volume GCM	A2 emission scenario
	Northeastern United States, the Great Lakes, and Southe	Gensini et al. [41]	1981-1995 vs. 2041-2065	WRF-G	50 km (published in 2014)	CCSM3	A2 emission scenario

Geo gra-phical area	Geographical restriction	Authors/ Reference	Time frame	RCM	Horizontal grid spacing	GCM for initial and boundary conditions	Scenario, other information
	astern Canada						
	CONUS	Hoogewind et al. [17]	1971-2000 vs. 2071-2100	WRF-ARW v.3.6	4km	GFDL CM3	RCP8.5
	US (Kansas + Oklahoma)	Trapp and Hoogewind [75]	Storms in 2007, 2010, 2013 vs. those with a delta from PGW for (1990-1999 vs. 2090-2099)	WRF-ARW v3.6.1	Nested: 3km and 1km	Three GCMs: MICRO5, GFDL CM3, NCAR CCSM4	RCP8.5 PGW Three extreme tormadic storm events from 2007, 2010, 2013

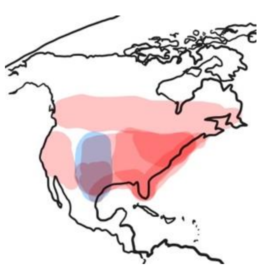

(a) Projections for convective storms using dynamical downscaling

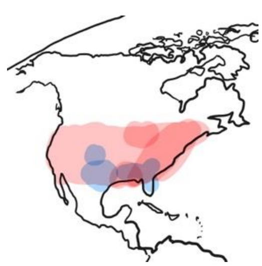

(b) Projections for hail using dynamical downscaling

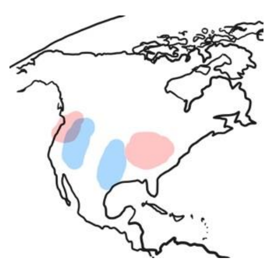

(c) Projections for precipitation using dynamical downscaling

(d) Projections for lightning using dynamical downscaling

Figure A.7 Dynamical downscaling future studies: blue and red represent a negative and a positive trend, respectively. Both trends on frequency and intensity are included.

A.4.3 Current Limitations for Using Dynamical Downscaling

Several obstacles remain for a widespread application of dynamical downscaling, for example:

1) First of all, the extremely high computational cost [11, 56, 57], which in particular means that the domain size must be considered carefully. During an interview in 2023, Gensini [57] stated during an interview in 2023 that a simulation for a manuscript in progress took 3.5 years to complete, accumulating 30 million core hours on a supercomputer.
2) Approximations that apply for larger grids are not valid at the scales used. Battaglioli and Groenemeijer [77] stated that very different proxies are needed when the resolution is so fine-grained that the updrafts can be explicitly resolved. Even if the model would be so fine-grained that it could model every single hailstone, a parameterization would still be needed for placing the storm correctly, and a good predictor for hail appearing in the storm remains necessary. Groenemeijer stated that he deems reliable simulations for hail or wind gust at this fine-grained resolution to still be quite a remote prospect. Also Gensini [57] stated that the microphysics at kilometer scale need to be developed.
3) Because convection is not parametrized, microphysical processes and processes contributing to the explicit triggering of clouds are more important than for other models.
4) Potential biases/systematic errors in the GCMs, which are passed on by downscaling [56,58], need to be understood.
5) Battaglioli and Groenemeijer [77] emphasized that the regional models also have biases, hence, just simulating in detail (with bias) is not in itself beneficial. They exemplified that some models are very eager to trigger storms even in conditions that are not that favorable (and where in radar data no convective storm was detected), other models do not produce a storm even when in radar data a convective storm was detected.
6) The very large amounts of output data [51,57] (Gensini [57] stated that it is close to a petabyte for a recent study)
7) The need for many ensemble simulations, in particular, to gauge the reliability and uncertainty of the results [56]

Giorgi and Gutowski [58] emphasize that dynamical downscaling and GCMs should be seen as complements to increase reliability and usefulness for local climate projections. Gensini [57] highlighted that GCMs are unable to simulate perils impacting humans, while dynamical downscaling is able to do so. Hence, he estimates that it will continue to play an important role. To address obstacle 6 from the list detailed in this section, the Coordinated Regional Downscaling Experiment (CORDEX)[10] project within the World Climate Research Programs was implemented to achieve worldwide coordination of downscaling research with a common experimental framework. Moreover, despite all these obstacles, Battaglioli and Groenemeijer [77] estimate that dynamical downscaling could help to see what type of storm will occur (i.e., isolated storms, long lines of storms, with high tops)—which could be very interesting for aviation.

[10] https://cordex.org

A.5 Lightning Trends

In this section, we present a preliminary review of results for lightning: various researchers used lightning as an indicator for the occurrence of severe convective storms, hence, while their main goal was not to project changes in the hazard lightning, these are projections for that hazard. Because of the importance of lightning as a hazard for aviation, we detail the results described in Sections A.3 and A.4 in this section to get an overview of this selection of results. In the future, we aim to expand this literature study to a conclusive review and emphasize that this is a very limited selection of results.

A.5.1 Past Trends

In the 2023 study described in Subsection A.2.1, Battaglioli et al. [76] presented also trends for lightning in both Europe and North America for the period 1950-2021, defining a lightning case as one hour with at least two lightning strikes. They concluded:

- The occurrence of lightning has significantly increased across most of Europe during the past 72 years.
- The largest absolute increase occurred in the Alpine and Caucasus Mountains with up to 5h of lightning more per decade.
- The largest relative increase occurred in Scandinavia with 2 more hours lightning per decade—with an annual mean of 20-25h.
- Increases in lightning appear throughout the year, but particularly during summer.
- In a belt Finland-Turkey only insignificant lightning changes occurred.
- Across parts of Russia, a significant decrease in lightning occurred.
- The strongest positive trends in the US occurred in the southern States, specifically Florida and the Texas-Louisiana coasts.
- Upward trends occurred also in the Midwest and southern Canada, mostly during summer.
- Significant negative trends occurred across the Colorado Plateau and the Great Basin.

A.5.2 Projections

All future-trend studies we considered account for Europe. As in previous sections, results for the midcentury are highlighted in italics.

- Rädler et al. [23] showed that the frequency of convective weather events (lightning, hail, severe wind gusts) will likely increase over Europe by the end of the century. They used 14

RCMs. The increase is attributed to increasing humidity near the earth's surface. They projected a slight decrease in thunderstorms for southwestern and southeastern Europe.

- In her PhD thesis, Rädler [66] used 14 ensemble members from EURO-CORDEX (with ca. 50km grid spacing) for 1971-2000 with 13 ensemble members for *2021-2050* and 2071-2100 for RCP2.6, 4.5 and 8.5. She modeled hazards separately: large hail, severe wind gusts, tornadoes, and heavy precipitation—and used cloud-to-ground lightning as an indicator for the occurrence of a convective storm (two cloud-to-ground lightning strikes within a grid cell in a period of a few hours). Already for the past, she analyzed that **thunderstorms have become more likely to produce severe weather over the last decades**. *For all future simulations, an increase in lightning cases is projected for central and eastern Europe, decreases are projected for southern Spain, northern Afrika, Greece, Turkey, northwest Ireland*. The largest increases are projected for RCP8.5 for the end of the century—with up to 60% more lightning cases. *Robust increases are projected only for the north-eastern part of the considered European domain and a small region in northern Italy and Austria*
- Kahraman et al. [72] studied lightning in Europe with dynamical downscaling, comparing the period 1998-2007 with a future period of 10 years corresponding to ~2100 under RCP8.5. For the RCM they used a horizontal grid spacing of 2.2km and a graupel and ice-flux-based scheme applied to a pan-European simulation of the UK Met Office Unified Model (UM), initial and boundary conditions stem from the HadGEM3 GCM (with ca. 25km grid spacing). They focus on cloud-to-ground lightning. They projected:
  - A net increase in lightning counts over southern parts of the Nordic countries, the British Isles and parts of the Atlantic Ocean further west; in Scandinavia they are projected to increase by a factor of 2.6 (future August in Scandinavia has a higher lightning density than current June in central Europe).
  - A decrease in lightning counts over most of the rest of Europe (except for higher terrain), which occurs mainly during summer and spring
  - Increases over north and south land areas and decreases over the sea, which are less pronounced towards the north; they project local increases over both the North and Baltic Sea
  - A summer increase in lightning in the north and a decrease in central Europe—an indication of a circulation regime shift
  - Decreases in lightning across most of Europe (in particular, in summer) accompanied by a pronounced reduction in mean cloud ice, which yields fewer lightning strikes/thunderstorm; this decrease is projected while a sharp increase in the fraction of unstable cases is projected (changes in microphysics and increase in CIN). This appears because of uncertainty in convective initiation, that is, a projected increase in unstable cases does not mean an increase in thunderstorm frequency.

- In the autumn, an increase in MLH of up to 1.5km (which is considered to be a large increase). This increase strongly reduces cloud ice, in particular, over northern and central Europe. Thus, increases in precipitating unstable cases must not yield an increase in lightning.
- For the North Sea during winter, increases in lightning days and lightning density (number of flashes per km per year)
- In Southern European mountains in spring, increases in lightning days

Their projected lightning changes for Europe are strongly correlated with elevation: grid points over 3km show an increase of more than 25flashes/km^2, while only a quarter of sea grid points show an increase; in the Alps, they projected a large increase in lightning counts and thunderstorm activity in summer. They find no single key driver for lightning changes over Europe, moisture, convective instability, CIN play a role. Kahraman et al. provided a very descriptive Figure on the changes in lightning and their drivers in Europe, see Figure 5 in their paper https://iopscience.iop.org/article/10.1088/1748-9326/ac9b78#erlac9b78s4.

A.6 Bibliography

[1] R. B. Smith, *Yale Meteorology,* https://youtube.com/playlist?list=PLkUjvobcQS8YGbXinRsEY_2WabKqrPJ4s, 2013.

[2] M. Strong, "Weather + Climate Lectures," [Online]. Available: melstrong.org/weather-lectures/. [Accessed October 2022].

[3] E. J. Tarbuck, F. K. Lutgens and D. G. Tasa, Earth Science, Pearson, 2015.

[4] G. Richard, "Ch.5 - Bergeron Process & Collision/Coalescence Process," [Online]. Available: https://youtu.be/WByQ3yKxj1s. [Accessed 2022].

[5] T. H. Raupach, O. Martius, J. T. Allen, M. Kunz, S. Lasher-Trapp, S. Mohr, K. L. Rasmussen, R. J. Trapp and Q. Zhang, "The effects of climate change on hailstorms," *Nature Reviews, Earth & Environment,* vol. 2, pp. 213-226, 09 February 2021.

[6] H. R. Pruppacher and J. D. Klett, Microphysics of clouds and precipitation, Boston: Kluwer Academic Publishers, 1997.

[7] J. C. Brimelow, G. W. Reuter and E. R. Poolman, "Modeling Maximum Hail Size in Alberta Thunderstorms," *Weather and Forecasting,* vol. 17, no. 5, pp. 1048-1062, 1 October 2002.

[8] E. J. Dennis and M. R. Kumjian, "The Impact of Vertical Wind Shear on Hail Growth in Simulated Supercells," *Journal of the Atmospheric Sciences,* vol. 74, no. 3, pp. 641-663, 2017.

[9] R. Fraile, A. Castro, L. Lopez, J. L. Sanchez and C. Palencia, "The influence of melting on hailstone size distribution," *Atmospheric Research,* Vols. 67-68, pp. 203-213, 2003.

[10] M. Kunz, S. Mohr and T. Raupach, Interviewees, *Hail formation and its impact on climate change.* [Interview]. 10 June 2022.

[11] J. T. Allen, Interviewee, *Impact of climate change on convective activity.* [Interview]. 3 October 2022.

[12] A. F. Prein and A. J. Heymsfield, "Increased melting level height impacts surface precipitation phase and intensity," *Nature Climate Change,* vol. 10, pp. 771-776, 2020.

[13] B. Xie, W. Zhang and Y. Wang, "Trends in hail in China during 1960–2005," *Geophysical Research Letters,* vol. 35, no. 13, 2008.

[14] NATIONAL WEATHER SERVICE, "What is CAPE?," [Online]. Available: https://www.weather.gov/ilx/swop-severetopics-CAPE#:~:text=What%20is%20CAPE%3F,updraft%20strength%20within%20a%20thunderstorm.. [Accessed 28 11 2022].

[15] Intergovernmental Panel on Climate Change, "CLIMATE CHANGE 2013 The Physical Science Basis; Working gorup I contribution to the fifth assessment report of the intergovernmental panel on climate change," Cambridge University Press, 2013.

[16] N. S. Diffenbaugh, M. Scherer and R. J. Trapp, "Robust increases in severe thunderstorm environments in response to greenhouse forcing," *PNAS,* vol. 110, no. 41, pp. 16361-16366, 2013.

[17] K. A. Hoogewind, M. E. Baldwin and R. J. Trapp, "The Impact of Climate Change on Hazardous Convective Weather in the United States: Insight from High-Resolution Dynamical Downscaling," *Journal of Climate,* pp. 10081-10100, 2017.

[18] R. . J. Trapp, N. S. Diffenbaugh, H. E. Brooks, M. E. Baldwin, E. D. Robinson and J. S. Pal, "Changes in severe thunderstorm environment frequency during the 21st century caused by anthropogenically enhanced global radiative forcing," *PNAS,* vol. 104, no. 50, pp. 19719-19723, 2007.

[19] "HAILCAST Homepage," [Online]. Available: http://hailcast.aer.com/. [Accessed 2022].

[20] E. R. Poolman, "Die voorspelling van haelkorrelgroei in Suid-Afrika (The forecasting of hail growth in South Africa)," 1992.

[21] R. Jewell and J. Brimelow, "Evaluation of Alberta Hail Growth Model Using Severe Hail Proximity Soundings from the United States," *Weather and Forecasting,* vol. 24, no. 6, pp. 1592-1609, 2009.

[22] S. Mohr and M. Kunz, "Recent trends and variabilities of convective parameters relevant for hail events in Germany and Europe," *Atmospheric Research,* vol. 123, pp. 211-228, 2013.

[23] A. T. Rädler, P. H. Groenemeijer, E. Faust, R. Sausen and P. Tomáš, "Frequency of severe thunderstorms across Europe expected to increase in the 21st century due to rising instability," *npj Climate and Atmospheric Science,* vol. 2, no. 30, 2019.

[24] M.-L. Kapsch, M. Kunz, R. Vitolo and T. Economou, "Long-term trends of hail-related weather types in an ensemble of regional climate models using a Bayesian approach," *Journal of Geophysical Research,* vol. 117, 2012.

[25] S. Mohr, M. Kunz and K. Keuler, "Development and application of a logistic model to estimate the past and future hail potential inGermany," *Journal of Geophysical Research: Atmospheres,* vol. 120, no. 9, pp. 3939-3956, 2015.

[26] F. Piani, A. Crisci, G. De Chiara, G. Maracchi and F. Meneguzzo, "Recent trends and climatic perspectives of hailstorms frequency and intensity in Tuscany and Central Italy," *Natural Hazards and Earth System Sciences,* vol. 5, pp. 217-224, 2005.

[27] M. G. Sanderson, W. Hand, P. Groenemeijer, P. Boorman, J. Webb and L. McColl, "Projected changes in hailstorms during the 21st century over the UK," *International Journal of Climatology,* vol. 35, no. 1, pp. 15-24, 2015.

[28] W. Botzen, L. Bouwer and J. van den Bergh, "Climate change and hailstorm damage: Empirical evidence and implications for agriculture and insurance," *Resource and Energy Economics,* vol. 32, no. 3, pp. 341-362, 2010.

[29] R. J. Trapp, N. S. Diffenbaugh and A. Gluhovsky, "Transient response of severe thunderstorm forcing to elevated greenhouse gas concentrations," *Geophysical Research Letters,* vol. 36, 2009.

[30] J. C. Brimelow, W. R. Burrows and J. M. Hanesiak, "The changing hail threat over North America in response to anthropogenic climate change," *Nature Climate Change,* vol. 7, 2017.

[31] S. J. Childs, R. S. Schumacher and S. M. Strader, "Projecting End-of-Century Human Exposure from Tornadoes and Severe Hailstorms in Eastern Colorado: Meteorological and Population Perspectives," *Weather, Climate, and Society,* vol. 12, pp. 575-595, 2020.

[32] K. Mahoney, M. A. Alexander , G. Thompson, J. J. Barsugli and J. D. Scott, "Changes in hail and flood risk in high-resolution simulations over Colorado's mountains," *Nature Climate Change,* vol. 2, pp. 125-131, 2012.

[33] H. McMaster, "The Potential Impact of Global Warming on Hail Losses to Winter Cereal Crops in New South Wales," *Climate Change,* vol. 43, pp. 455-476, 1999.

[34] S. Niall and K. Walsh, "The impact of climate change on hailstorms in southeastern Australia," *International Journal of Climatology,* vol. 25, no. 14, pp. 1933-1952, 2005.

[35] J. T. Allen and E. R. Allen , "A review of severe thunderstorms in Australia," *Atmospheric Research,* Vols. 178-179, pp. 347-366, 2016.

[36] L. M. Leslie, M. Leplastrier and B. W. Buckley, "Estimating future trends in severe hailstorms over the Sydney Basin: A climate modelling study," *Atmospheric Research,* vol. 87, pp. 37-51, 2008.

[37] Intergovernmental Panel on Climate Change (IPCC), "Towards New Scenarios for Analysis of Emissions, Climate Change, Impacts, and Response Strategies," Noordwijkerhout, The Netherlands, 2007.

[38] R. J. Trapp, K. A. Hoogewind and S. Lasher-Trapp, "Future Changes in Hail Occurrence in the United States Determined through Convection-Permitting Dynamical Downscaling," *Journal of Climate,* vol. 32, pp. 5493-5509, 2019.

[39] Intergovernmental Panel on Climate Change, "IPCC Special Report Emissions Scenarios; Summary for Policymakers," 2000.

[40] J. T. Allen, D. J. Karoly and K. J. Walsh, "Future Australian Severe Thunderstorm Environments. Part II: The Influence of a Strongly Warming Climate on Convective Environments," *Journal of Climate,* vol. 27, pp. 3848-3868, 2014.

[41] V. A. Gensini, C. Ramseyer and T. L. Mote, "Future convective environments using NARCCAP," *International Journal of Climatology,* vol. 34, no. 5, pp. 1699-1705, 2014.

[42] J. T. Allen, "Climate Change and Severe Thunderstorms," *Oxford Research Encyclopedias, Climate Science,* 2018.

[43] F. Tymvios, *Personal Communication,* 2022.

[44] C. A. Doswell III, "Severe Convective Storms -- an Overview," The American Meteorological Society, 2000.

[45] T. Púčik, P. Groenemeijer, A. T. Rädler, L. Tijssen, G. Nikulin, A. F. Prein, E. van Meijgaard, R. Fealy, D. Jacob and C. Teichmann, "Future Changes in European Severe Convection Environments in a Regional Climate Model Ensemble," *Journal of Climate,* vol. 30, pp. 6771-6794, 2017.

[46] Monthly Weather Review, vol. 134, 2006.

[47] P. T. Marsh, H. E. Brooks and D. J. Karoly, "Preliminary investigation into the severe thunderstorm environment of Europe simulated by the Community Climate System Model 3," *Atmospheric Research,* vol. 93, pp. 607-618, 2009.

[48] C. Viceto, M. Marta-Almeida and A. Rocha, "Future climate change of stability indices for the Iberian Peninsula," *International Journal of Climatology,* 2017.

[49] T. Muramatsu, T. Kato, M. Nakazato, H. Endo and A. Kitoh, "Future Change of Tornadogenesis-Favorable Environmental Conditions in Japan Estimated by a 20-km-Mesh Atmospheric General Circulation Model," *JJaonuuranrayl o2f0 t1h6e Meteorological Society of Japan,* vol. 94A, pp. 105-120, 2016.

[50] J. T. Allen and E. R. Allen.

[51] Prein, A. F., et al. (2015), A review on regional convection-permitting climate modeling: Demonstrations, prospects, and challenges, Rev. Geophys., 53, 323–361, doi:10.1002/2014RG000475.

[52] Gensini, V.A., Haberlie, A.M., Ashley, W.S. (2022), Convection-permitting simulations of historical and possible future climate over the contiguous United States, Climate Dynamics, 60, 109-125, https://doi.org/10.1007/s00382-022-06306-0

[53] Gensini, V.A., Mote, T.L. Downscaled estimates of late 21st century severe weather from CCSM3, Climate Change, 129, 307-321, DOI 10.1007/s10584-014-1320-z

[54] Rasmussen, K.L., et al. (2020), Changes in the convective population and thermodynamic environments in convection-permitting regional climate simulations over the United States, Climate Dynamics, 55, 383-408, https://doi.org/10.1007/s00382-017-4000-7

[55] Lucas-Picher, P., et al. (2021), Convection-permitting modeling with regional climated models: Latest developments and next steps, WIREs Climate Change, https://doi.org/10.1002/wcc.731

[56] Gensini, V.A. (2021), Severe convective storms in a changing climate, Climate Change and Extreme Events, https://doi.org/10.1016/B978-0-12-822700-8.00007-X

[57] Victor A. Gensini, Interviewee, Dynamical Downscaling, interview: September 6, 2023

[58] Giorgi, F., Gutowski Jr., W.J. (2015), Regional Dynamical Downscaling and the CORDEX Initiative, Annual Review of Environment and Resources, 40:467-90, 10.1146/annurev-environ-102014-021217

[59] Goodin, J.R. (2023), Convection Allowing Simulations of Hail in Historical and Future Climate Epochs, Graduate Research Theses & Dissertations 7146, Northern Illinois University.

[60] Gensini, V.A., and Mote, T.L. (2014), Estimations of Hazardous Convective Weather in the United States Using Dynamical Downscaling, Journal of Climate, 6581-6589, DOI: 10.1175/JCLI-D-13-00777.1

[61] Haberlie, A. M., Ashley, W. S.,Battisto, C. M., & Gensini, V. A. (2022). Thunderstorm activity underintermediate and extreme climate change scenarios. Geophysical Research Letters, 49, https://doi.org/10.1029/2022GL098779

[62] Kendon, E.J., Prein, A.F., Senior, C.A., Stirling, A. (2021), Challenges and outlook for convection-permitting climate modelling. Phil. Trans. R. Soc. A 379: 20190547. https://doi.org/10.1098/rsta.2019.0547

[63] Ashley, W.S., Haberlie, A.M., Gensini, V.A. (2023), The Future of Supercells in the United States, Bulleting of the American Meteorological Society, 104(1), https://doi.org/10.1175/BAMS-D-22-0027.1

[64] Takayabu, I., Rasmussen, R., Nakakita, E., Prein, A., Kawase, H., Watanabe, S.-I., Adachi, S.A., Takemi, T., Yamaguchi, K., Osakada, Y., Wu, Y.-H. (2022), Convection-Permitting Models for Climate Research, Bulletin of the American Meteorological Society, 103(1), https://doi.org/10.1175/BAMS-D-21-0043.1

[65] Lepore, C., Abernathey, R., Henderson, N., Allen, J. T., & Tippett, M. K. (2021). Future global convective environments in CMIP6 models. Earth's Future, 9, e2021EF002277. https://doi.org/10.1029/2021EF002277

[66] Rädler, A.T.(2018), Modeling of convective storm hazard occurrence, taking convective initiation explicitly into account, PhD thesis, LMU München, DLR, ESSL, Munich Re

[67] Liu, C., Ikeda, K., Rasmussen, R. *et al.* Continental-scale convection-permitting modeling of the Current and future climate of North America. *Clim Dyn* **49**, 71–95 (2017). https://doi.org/10.1007/s00382-016-3327-9

[68] Prein, A.F., Liu, C., Ikeda, K., Trier, S.B., Rasmussen, R.M., Holland, G.J., Clark M.P. (2017), Increased rainfall volume from future convective storms in the US, Nature Climate Change, 7: 880-884

[69] Muller, c. , Yang, D. Craig, G., Cronin, T., Fildier, B., Haerter, J.O., Hohenegger, C. Mapes, B., Randall, D., Shamek, S., Sherwood, S.C. (2021), Spontaneous Aggregation of Convective Storms, Annual Review of Fluid Mechanics, 54: 133-157

[70] Kumar Srivastava, A., Ullrich, P.A., Rastogi, D., Vahmani, P., Jones, A., Grotjahn, R. (2023), Assessment of WRF (v 4.2.1) dynamically downscaled precipitation on subdaily and daily timescales

over CONUS, Geoscientific Model Development, 16: 3699-3722, https://doi.org/10.5194/gmd-16-3699-2023

[71] Cheung, K.K.W., Ji, F., Nishant, N., Herold, N., Cook, K. (2023), Evaluation of Convective Environments in the NARCliM Regional Climate Modeling System for Australia, Atmosphere, 14, 690

[72] Kahraman, A., Kendon, E.J., Fowler, H.J., Wilkinson, J.M. (2022), Contrasting future lightning stories across Europe, Environmental Research Letters, 17

[73] Cui, R., Ban, N., Demory, M.-E., Schär, C. (2023), Exploring hail and lightning diagnostics over the Alpine-Adriatic region in a km-scale climate model, Preprint

[74] Powers, J. G., and Coauthors, 2017: The Weather Research and Forecasting Model: Overview, System Efforts, and Future Directions. Bull. Amer. Meteor. Soc., 98, 1717–1737, https://doi.org/10.1175/BAMS-D-15-00308.1

[75] Trapp, R.J., Hoogewind, K.A., 2016: The Realization of Extreme Tornadic Storm Evens under Future Anthropogenic Climate Change, Journal of Climate, 29(14), 5251-5265. https://doi.org/10.1175/JCLI-D-15-0623.1

[76] Battaglioli, F., P. Groenemeijer, T. Púčik, M. Taszarek, U. Ulbrich, and H. Rust, 2023: Modeled Multidecadal Trends of Lightning and (Very) Large Hail in Europe and North America (1950–2021). J. Appl. Meteor. Climatol., 62, 1627–1653, https://doi.org/10.1175/JAMC-D-22-0195.1

[77] Pieter Groenemeijer, Francesco Battaglioli, Interviewee, The European Severe Storms Labaratory (ESSL), interview: March 31, 2023

[78] National Oceanic and Atmospheric Administration: Radar Images: Reflectivity, https://www.noaa.gov/jetstream/reflectivity

[79] Markowski, P. and Richardson, Y. (2010). Mesoscale Meteorology in Midlatitudes. John Wiley & Sons, Ltd, Chichester, UK, DOI: 10.1002/9780470682104.

[80] Winterrath, T., Brendel, C., Junghänel, T., Klameth, A., Lengfeld, K., Walawender, E., Weigl, E., Hafer, M., Becker, A. (2018). An overview of the new radar-based precipitation climatology of the Deutscher Wetterdienst—Data, methods, products. In Proceedings of the UrbanRain18, 11th International Workshop on Precipitation in Urban Areas, Urban Areas, Zürich, Switzerland, 5–7 December 2018.

B Appendix – Task Force #2: Clear Air Turbulence

Note: *This appendix is a consolidated version of Appendix B from the report 2022 with additional results from 2023. The main author of this appendix is Nicole Viola.*

This appendix focuses on trends regarding Clear Air Turbulence, CAT, due to jet streams, with the aim to answer the question of impact of climate change on CAT. CAT due to mountain waves and convection are here disregarded.

The investigation has been performed through the interaction with experts (e.g. Paul Williams, Professor of Atmospheric Science, University of Reading, UK and CERFACS, Laurent Terray, Director of the Climate modeling and Global change (GLOBC) Team at CERFACS and Mohamed Foudad, PhD Student of the GLOBC Team at CERFACS). Literature review has also been extended to include the results of scientific research of other teams, like Ju Heon Lee, Jung-Hoon Kim, and Seok-Woo Son from Seoul National University (South Korea), Robert D. Sherman from the National Center for Atmospheric Research (NCAR, USA), and Joowan Kim from Gonju National University (South Korea).

B.1 Development of clear air turbulence near jet streams

An important source of CAT is strong vertical wind shear, which is prevalent within the atmospheric jet streams (see Fig. B.1). Jet streams are narrow currents of strong wind that generally blow from west to east all across the Earth (zonal flow) and less frequently from northern to southern directions and vice versa (meridional flow). They impact weather, air travel and many other weather phenomena that take place in our atmosphere. They are located close to the tropopause and are generated by strong temperature gradients between air masses with different characteristics. The most common jet streams are found in the cold air-mass adjacent to the polar and the mid-latitude zones (Polar Jet) and the mid-latitude and tropical zones (Sub-tropical Jet). Although not all jet streams have CAT associated with them, there can be significant vertical and horizontal wind shear on the edges of the jet stream, giving rise to sometimes severe clear air turbulence.

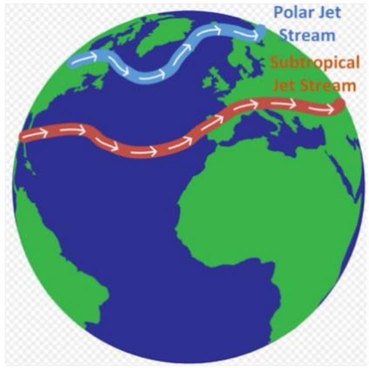

Figure B.1. Jet streams

Stronger jet-stream winds are likely to occur because increased carbon dioxide (CO_2) is increasing the column-averaged pole-to-equator temperature gradient in the mid-latitudes, through the combined effect of tropospheric warming and stratospheric cooling ([1], [2], [3], see Figure B.2). Climate change is therefore strengthening the wind shear and, consequently CAT is expected to increase in the next decades (see Figure B.3 and Figure B.4).

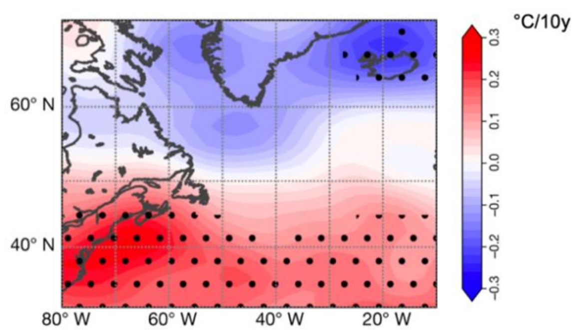

Figure B.2. Observed temperature trends in 1979–2017 at 250 hPa (10000 m, FL 350) in reanalysis data. Results reveal stronger north–south temperature gradient at flight cruising altitudes

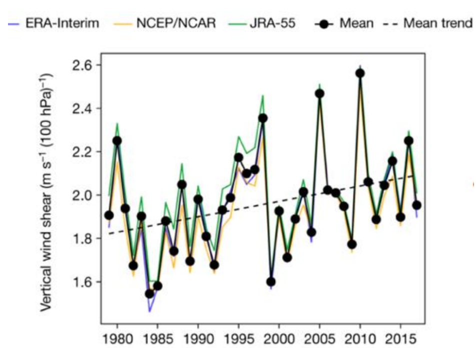

Figure B.3. Observed windshear trends at FL350: annual mean vertical wind shear in North Atlantic at 250 hPa (10000 m, FL 350) calculated with different climate models [4]

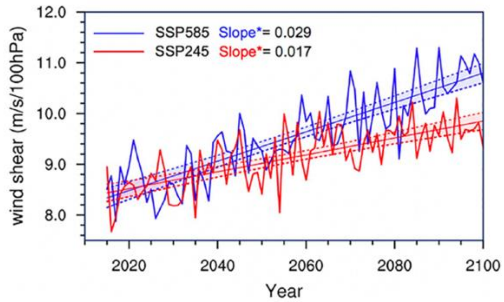

Figure B.4. Projected future windshear trends at FL350 (10000 m): winter mean, CMIP6 (Coupled Model Inter comparison Project) mean vertical wind shear in Northern Eurasia at 250 hPa (blue curve corresponding to IPCC SSP5-8.5: 29% increase over 85 years; red curve, corresponding to IPCC SSP2-4.5: 17% increase over 85 years).

B.2 Methodology to predict CAT

B.2.1 The turbulence diagnostic indices

The difficulty in turbulence long-term trend predictions regarding occurrence of CAT lies largely in the fact that, from the meteorological perspective, turbulence is a “multi-scale” phenomenon. In the atmosphere turbulent “eddies” are contained in a spectrum of sizes, from 100s of kilometres down to centimetres. The effect of the turbulence eddies on aircraft acceleration and trajectory are more pronounced when the size of the eddies is about the size of the aircraft.

While large scale eddies can be predicted, small scale eddies cannot. Fortunately, it appears that most of the energy associated with turbulent eddies at the aircraft scale cascade down from the larger scales of atmospheric motion (e.g., [5] and more recently [6] and [7]), and these larger scales eddies may be resolved by current weather observation networks and numerical weather prediction (NWP) models. Assuming the large-scale predictions are sufficiently accurate, the turbulence prediction problem is then to identify large-scale features that are conducive to the formation of aircraft-scale eddies.

The turbulent eddies that cause aviation turbulence typically occur on a reduced set of scales from around 100 m to 1 km. Computer processing speeds are currently not sufficient to explicitly simulate air motions on these scales [8], except for a few detailed case studies [9]. Therefore, diagnostic indices from numerical weather prediction models are used to identify and forecast regions likely to contain CAT. The diagnostics indices are mathematical models that generally assume that the smaller-scale turbulence is formed because of conditions set by the large-scale flow.

Commonly used indices include:

- variant 1 of the Ellrod and Knapp turbulence index (TI1). The Ellrod–Knapp turbulence index (TI) was developed in the early 1990s and it is in use at many aviation forecasting facilities worldwide.

It has been recognized, however, that TI often does not sufficiently account for situations where anticyclonic shear or curvature is present. Variations of the TI that address the weaknesses of the index have been proposed [10]: this is TI1. The TI1 variant has been shown to forecast up to 75% of CAT [11].

- the negative Richardson number (−Ri). The Richardson number is the ratio of the stability of the atmosphere (stability suppresses the generation of turbulence) by the turbulence generated by mechanical shear forces at a rate proportional to the square of the acceleration of the air. In essence, the Ri index measures the competition between the destabilizing influence of the wind shear and the stabilizing influence of the stratification of the atmosphere due to density. Strongly negative Richardson numbers indicate that convection predominates, winds are weak, and there is a strong vertical motion characteristic of an unstable atmosphere.
- the Colson – Panofsky index [12]. This index expresses the intensity of turbulence in a sloping baroclinic layer. This index is proportional to the turbulent energy and it allows to better discriminate between regions of varying intensity than vertical wind shear or Richardson number.
- the Brown index (Brown, 1973). The Brown index is a simplification of the Ri tendency equation, originally derived by Roach (1970) [13], relating synoptic scale[11] and mesoscale energetic coupling and gives more information on the relative intensity of these source regions. The simplifications involve use of the thermal wind relation, the gradient wind, as an approximation to the horizontal wind, and some empiricism.
- the potential vorticity (PV), which was found to give unrealistic results. The potential vorticity is the absolute circulation of an air parcel that is enclosed between two isentropic surfaces. PV consists of two factors, a dynamical element and a thermo-dynamical element. It is simply the product of absolute vorticity on an isentropic surface and static stability.
- Divergence (DIV). DIV is expressed by the following mathematical formulation:

$$DIV = \frac{\partial u}{\partial x} + \frac{\partial v}{\partial y}$$

  where u and v are the zonal and meridional wind components specified in Cartesian (x,y,z) coordinates.
- Deformation (DEF). DEF is the deformation of the wind composed of the stretching (DST) and shearing (DSH) components, as highlighted in the following mathematical relationship:

$$DST = \frac{\partial u}{\partial x} - \frac{\partial v}{\partial y}$$
$$DSH = \frac{\partial v}{\partial x} + \frac{\partial u}{\partial y}$$
$$DEF = (DST^2 + DST^2)^{1/2}$$

[11] In meteorology, the synoptic scale (also called the large scale or cyclonic scale) is a horizontal length scale of the order of 1,000 km (620 mi) or more. This corresponds to a horizontal scale typical of mid-latitude depressions (e.g. extratropical cyclones).

where u and v are the zonal and meridional wind components specified in Cartesian (x,y,z) coordinates.

Some indices, like the Richardson number, explicitly diagnose a physical mechanism in the atmosphere that is known to cause CAT and are rigorously derivable from the equations of fluid dynamics via a stability analysis. Others, like the Ellrod and Knapp indices, are more empirical.

B.2.2 Quantifying the turbulence strength

Then the clear-air turbulence diagnostics are converted into eddy dissipation rates (EDR). The eddy dissipation rate is a natural measure for quantifying the strength of turbulence. For a given aircraft type, aircraft weight, airspeed, and altitude, the root-mean-square vertical acceleration of the aircraft in turbulence is proportional to the cube-root of the eddy dissipation rate. For large commercial aircraft, the correspondence between cube-rooted eddy dissipation rates and turbulence strength categories is shown in Table B.1. In addition, values of cube-rooted eddy dissipation rates of 0.6–0.7 $m^{2/3}\,s^{-1}$ generate severe-to-extreme turbulence, and values greater than 0.7 $m^{2/3}\,s^{-1}$ generate extreme turbulence [9]. For large aircraft, severe air turbulence thus corresponds to $EDR^{1/3}$ higher than 0,5 $m^{2/3}s^{-1}$ and vertical acceleration higher than 1 g, whereas for light aircraft severe air turbulence corresponds to $EDR^{1/3}$ higher than 0,35 $m^{2/3}s^{-1}$ (https://www.aviationweather.gov/turbulence/gt). The threshold EDR value for severe turbulence is aircraft and mission dependent [14]. In contrast the condition of the root-mean-square aircraft vertical acceleration exceeding 1 g is a commonly used definition of severe turbulence for all aircraft.

Turbulence strength category	Null	Light	Light-to-moderate	Moderate	Moderate-to-severe	Severe
$EDR^{1/3}$ range ($m^{2/3}\,s^{-1}$)	0–0.1	0.1–0.2	0.2–0.3	0.3–0.4	0.4–0.5	>0.5
Vertical acceleration range (g)	0–0.2	0.2–0.4	0.4–0.6	0.6–0.8	0.8–1.0	>1.0
Percentile range (%)	0–97.0	97.0–99.1	99.1–99.6	99.6–99.8	99.8–99.9	99.9–100
Probability (%)	97.0	2.1	0.5	0.2	0.1	0.1

Table B.1: The defining characteristics of six turbulence strength categories for a large commercial aircraft. The eddy dissipation rate and g the acceleration due to gravity. The vertical acceleration assumes proportionality to EDR1/3, subject the onset of severe turbulence occurring at 1 g. The percentile ranges and probabilities are calculated using an assumed log-normal probability distribution [15].

Diagnostic	Units	Light	Light-to-moderate	Moderate	Moderate-to-severe	Severe
Negative Richardson number	—	−15.4	−9.8	−7.9	−6.7	−5.9
Magnitude of vertical shear of horizontal wind	10^{-3} s^{-1}	5.3	6.6	7.4	7.9	8.4
Colson–Panofsky index	10^{3} kt^{2}	−29.3	−27.0	−25.2	−23.7	−22.2
Frontogenesis function	10^{-9} m^{2} s^{-3} K^{-2}	770	1280	1660	1980	2340
Brown index	10^{-6} s^{-1}	99	106	110	113	118
Brown energy dissipation rate	10^{-6} J kg^{-1} s^{-1}	870	1370	1730	2030	2330
Variant 1 of Ellrod's turbulence index	10^{-9} s^{-2}	195	292	360	419	472
Variant 2 of Ellrod's turbulence index	10^{-9} s^{-2}	184	282	356	419	477
Flow deformation	10^{-6} s^{-1}	50.9	60.9	66.9	71.8	76.3
Magnitude of potential vorticity	PVU	8.33	8.73	8.98	9.19	9.41
Relative vorticity squared	10^{-9} s^{-2}	2.46	3.74	4.70	5.50	6.24
Magnitude of horizontal temperature gradient	10^{-6} K m^{-1}	14.7	17.6	19.4	20.8	22.0
Wind speed	m s^{-1}	40.9	48.4	52.4	55.3	58.5
Wind speed × directional shear	10^{-3} rad s^{-1}	3.21	3.94	4.39	4.72	5.08
Flow deformation × wind speed	10^{-3} m s^{-2}	1.65	2.29	2.76	3.17	3.54
Flow deformation × vertical temperature gradient	10^{-9} K m^{-1} s^{-1}	53	84	106	127	151
Magnitude of residual of nonlinear balance equation	10^{-12} s^{-2}	1230	1840	2270	2610	2960
Magnitude of horizontal divergence	10^{-6} s^{-1}	11.9	15.7	18.2	20.4	22.5
Version 1 of North Carolina State University index	10^{-18} s^{-3}	1200	3600	6300	9300	13 000
Negative absolute vorticity advection	10^{-9} s^{-2}	1.33	1.86	2.23	2.56	2.93
Magnitude of relative vorticity advection	10^{-9} s^{-2}	1.44	1.99	2.34	2.66	3.00

Table B.2: Onset thresholds for each turbulence strength category and each clear-air turbulence diagnostic. The thresholds are for turbulence diagnosed from the GFDL-CM2.1 climate model and apply to large commercial aircraft. In the units column, kt is knots and 1 PVU is 10−6 m2 s−1 K kg−1.

The log-normal distribution for the cube-rooted eddy dissipation rate yields percentile ranges for each turbulence strength category. These percentile ranges and their corresponding probabilities are listed in Table B.1. The thresholds of the diagnostic indices calculated according to the percentile and probabilities ranges of Table B.1 are listed in Table B.2 [15]. Note that the thresholds are dependent on the grid resolution of the atmospheric model. Therefore, the values listed in Table B.2 may differ from those computed in other studies [8]. The probabilities for each turbulence strength category agree reasonably well with the relative frequencies at which the categories appear in automated in-flight measurements [16] and in PIREPs (Pilot Reports of Turbulence) in the United States [17] and South Korea [18]. Exact quantitative agreement cannot be expected, because of inconsistent PIREP reporting practices and because automated measurements and PIREPs contain a substantial avoidance bias, which is caused by pilots attempting to avoid areas with the strongest turbulence [19]. It is then possible to apply the percentile ranges listed in Table B.1 to the probability distributions of the diagnostics indices. By doing so, we may infer the onset threshold for each strength category and each turbulence diagnostic, as shown in Table B.2.

B.3 CAT: future trends

Figure B.5 shows the results of the analysis of [15], which considers the North Atlantic flight corridor as geographic area (50°–75° N, 10°–60°W) at 200 hPa pressure (12 000 meters altitude of Flight Level 390).

This geographic area was chosen because the North Atlantic flight corridor is the busiest oceanic airspace in the world. It contains the majority of transatlantic traffic, as indicated by gridded global inventories of fuel burn and emissions obtained from the Federal Aviation Administration's Aviation Environment Design Tool [20], [21], [22], [23].

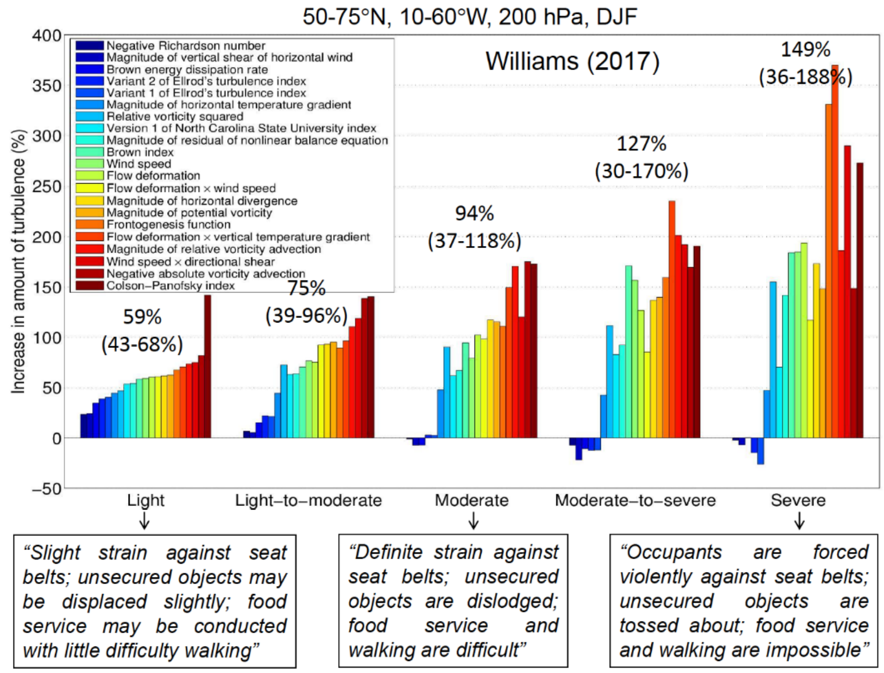

Figure B.5. Bar charts showing the percentage increase in the amount of light, light-to-moderate, moderate, moderate-to-severe, and severe CAT within the North Atlantic flight corridor at 200 hPa (12000 m) in winter. The increase refers to the change in simulation with doubled-CO2 concentration compared to a pre-industrial simulation [60] in a time horizon of 20 years, 2050-2070 (corresponding to IPCC SSP5-8.5).

The analysis refers to winter timeframe (i.e. December, January and February, DJF) because it is the season in which the prevalence of clear-air turbulence is higher in the North Atlantic sector [24]. GFDL-CM2.1 (NOAA Geophysical Fluid Dynamics Laboratory Climate Modelling 2.1, https://www.gfdl.noaa.gov/high-resolution-climate-modeling/) was selected as climate model because the simulated upper-level winds in the northern extra-tropics agree well with reanalysis data, and because the spatial pattern of clear-air turbulence over the North Atlantic diagnosed from reanalysis data is successfully captured by the model [15]. The numerical resolution of the atmosphere is 2.5° in longitude, 2.0° in latitude, and 50 hPa in pressure altitude around the 200 hPa level (12000 m of altitude, i.e. flight level 390). The probability distributions for 21 clear-air turbulence diagnostics are calculated from daily mean temperature and wind fields over 20 winters in each simulation.

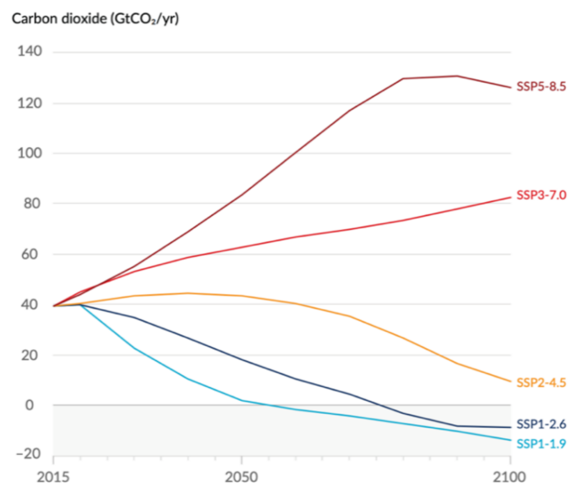

Figure B.6. Future annual emissions of CO_2 across five illustrative scenarios [25]

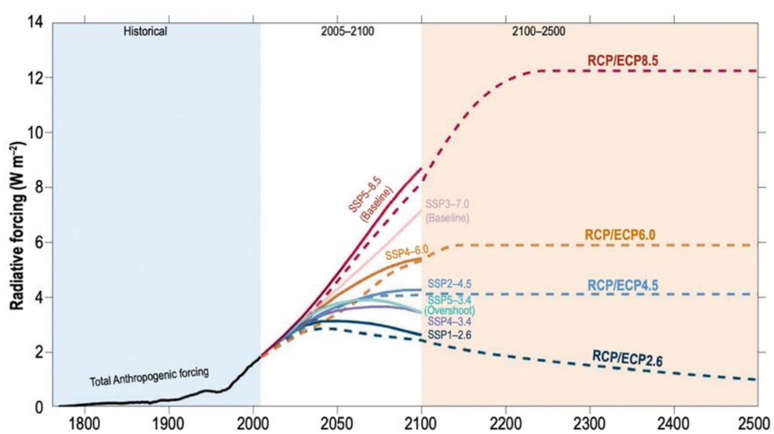

Figure B.7. Radiative forcing (Wm–2) time series for historical data (1765–2004), and for future scenarios from the Representative Concentration Pathways (RCP; 2005–2100) and their continuation as the extended RCPs (2100–2500), and the Shared Socioeconomic Pathways (SSP; 2005–2100). The RCP scenarios are shown as dashed curves, and SSPs are shown as solid curves [26]

The doubled-CO_2 simulation was chosen because the SSP5-8.5 (SSP, Shared Socioeconomic Pathways) scenario of the IPCC Sixth Assessment Report [25] foresees that CO_2 emissions will roughly double from current level by 2050. This is the scenario corresponding to very high green-house gases and CO_2 emissions. Other scenarios with high (SSP3-7.0), intermediate (SSP2-4.5), low (SSP1-2.6) and very low (SSP1-1.9) emissions of green-house gases are reported in Figure B.6 and in Figure B.7. The IPCC Sixth Assessment Report did not estimate the likelihoods of the scenarios. The SSP5–8.5 represents the high end of the range of future pathways, corresponding to RCP 8.5 (Representative Concentration Pathways).

The probability gains, expressed as percentage increases in the doubled-CO_2 concentration scenario relative to the pre-industrial CO_2 concentration, are shown in Figure B.5 per turbulence diagnostic and strength category. Specifically, all 21 diagnostics show increases in the amount of light and light-to-moderate turbulence, and at least 16 of the 21 diagnostics show increases in the amount of moderate, moderate-to-severe, and severe turbulence. To summarise, the 21 different estimates of the percentage increase within each strength category, the median (50^{th} percentile) and 25^{th}–75^{th} percentiles have been calculated, which respectively indicate an ensemble-average value and an intra-ensemble range. By these measures, the prevalence of:

- light turbulence increases by 59% (43%–68%)
- light-to-moderate turbulence increases by 75% (39%–96%)
- moderate turbulence increases by 94% (37%–118%)
- moderate-to-severe turbulence increases by 127% (30%–170%)
- severe turbulence increases by 149% (36%–188%).

The averages and ranges both increase substantially from light to severe turbulence, suggesting greater percentage increases for stronger turbulence than for weaker turbulence, but also implying a higher degree of uncertainty.

In [27] the probability distribution is calculated for 20 CAT diagnostics from 6-hourly global fields over 30 years (2050-2080) run of the HadGEM2-ES climate model (Hadley Centre Global Environment Model version 2 climate model, https://www.metoffice.gov.uk/research/approach/modelling-systems/unified-model/climate-models/hadgem2) in all seasons at both 200 hPa and 250 hPa, which correspond to typical cruising altitudes of approximately 12 km (39 000 ft or FL390) and 10 km (34,000 ft or FL340), respectively. The HadGEM2-ES climate model forms part of the fifth Coupled Model Intercomparison Project (CMIP5) ensemble [28]. The atmosphere model has a horizontal grid spacing of 1.25° in latitude and 1.875° in longitude, which is finer than the 2.0° by 2.5° GFDL-CM2.1 model used by [15] and [29]. Two HadGEM2-ES simulations are analysed to calculate how climate change could impact CAT in the upper troposphere and lower stratosphere in future: 1) a preindustrial control simulation (picontrol); 2) a climate change simulation using the Intergovernmental Panel on Climate Change (IPCC) Representative Concentration Pathway 8.5 (RCP8.5, which corresponds to the worst-case climate change scenario or SSP5-8.5, see Figure B.6 and Figure B.7) [25], [26], [30]. The picontrol run is a base state that uses constant preindustrial greenhouse gas concentrations to simulate the global climate before the industrial revolution. The RCP8.5 run assumes a net radiative forcing increase of 8.5 Wm^{-2} by 2100 [26], [31] which implies greenhouse gas concentrations equivalent to around 1370 ppmv of CO_2.

Figure B.8 shows the comparison of the results of the HadGEM2-ES simulations from [27] with the GFDL-CM2.1 simulations from [15]. The CAT increases in HadGEM2-ES are on average 30% smaller than in GFDL-CM2.1, possibly because of the different anthropogenic forcing used in the climate change simulations. Specifically, the GFDL-CM2.1 climate change simulation was allowed to converge after the CO_2 loading had been instantaneously doubled. In contrast, the HadGEM2-ES climate change simulation was a transient RCP8.5 run in which the radiative forcing was gradually increased, and so the atmospheric circulation is not expected to be in equilibrium with the contemporary radiative forcing. Therefore, the comparison is not strictly like for like. The comparison shows for the first time that the projected increase in transatlantic turbulence is robust: it occurs across multiple climate models; it does not depend on the parameterized physics or model resolution.

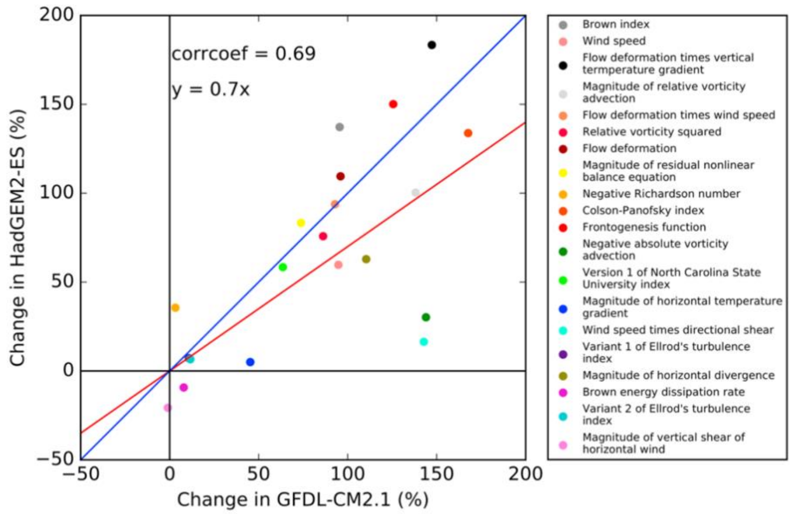

Figure B.8. Scatterplot comparing the HadGEM2-ES simulations from [27] with the GFDL-CM2.1 simulations from [15]. The plot shows the percentage change in the prevalence of moderate-or-greater (MOG) turbulence for 20 CAT diagnostics calculated at 200hPa (12000 m of altitude) over the North Atlantic (50-75° N and 10-60° W) in winter (December, January and February, DJF). The blue line (y=x) indicates parity and the red line (y=0,7x) is a least-squares fit constrained to pass through the origin.

Regarding the magnitude of moderate turbulence with respect to coverage, results [27] reveal that in the tropical regions (30°S–30°N), the percentage changes are generally smaller if compared with middle and high latitudes regions, probably because CAT is not a major hazard in the tropics, where turbulence caused by convective weather dominates. This is indeed because the main jet streams are extra-tropical. Moreover, it is worth underlying that in the tropical regions there is less agreement between the diagnostics, while in the middle and high-latitude regions there is more agreement between the diagnostics because CAT diagnostics were developed to diagnose and predict mid-latitude CAT near jet streams, so they are optimized to be skilful for these regions rather than the tropics. The percentage change in the amount of moderate CAT from preindustrial times (picontrol) to the period 2050–2080 (assuming RCP8.5) at 200 hPa are calculated for all 20 CAT diagnostics in December, January, and February using the HadGEM2-ES climate model. The seven GTG upper-level CAT diagnostics that are used operationally to forecast CAT in the short-term are included in the overall 20 CAT diagnostics. The GTG2,

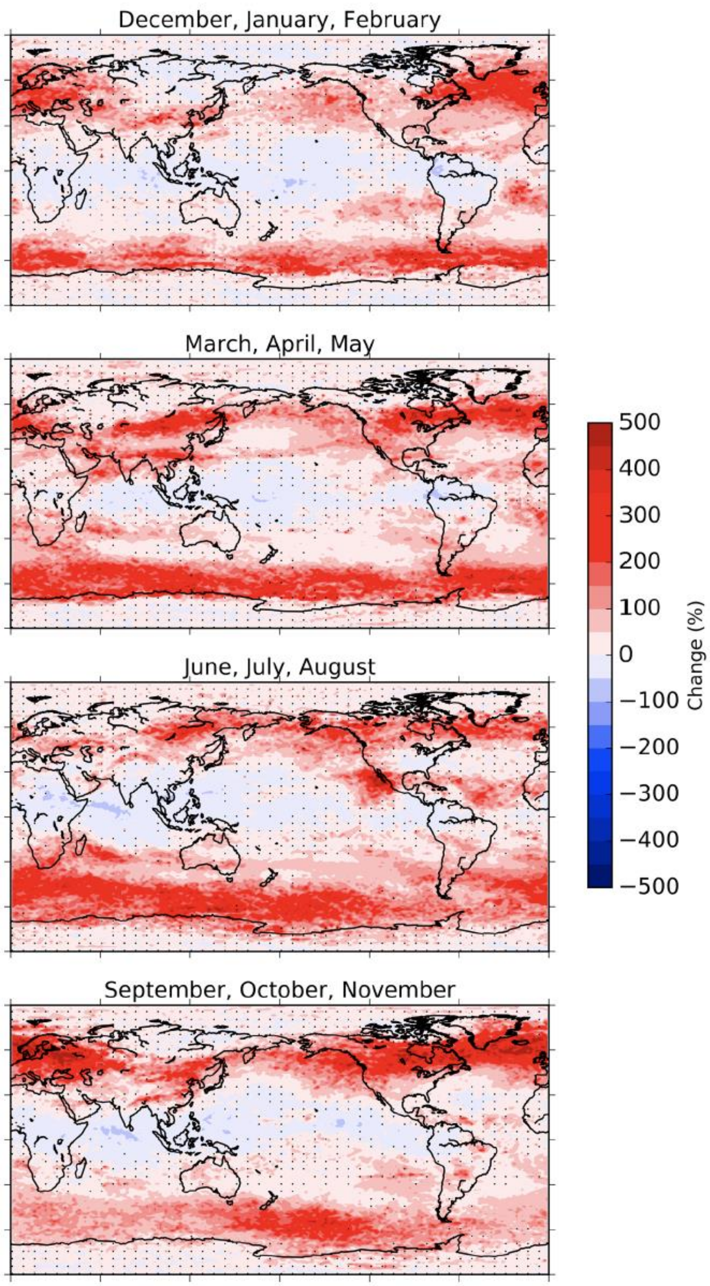

Figure B.9. Maps of the average percentage change in the amount of moderate CAT from preindustrial times (picontrol) to the period 2050–2080 (RCP8.5) at 200 hPa in each season. The average of the over all 20 CAT diagnostics, which are equally weighted [27].

Graphical Turbulence Guidance, the original Integrated Turbulence Forecasting Algorithm (ITFA) then renamed GTG, is a completely automated turbulence forecasting system, developed and tested by the Research Applications Laboratory at the National Center for Atmospheric Research (NCAR/RAL) and the National Oceanic and Atmospheric Administration's (NOAA) Earth System Research Laboratory/Global

Systems Division (NOAA- Research-ESRL/GSD), under sponsorship from the FAA's Aviation Weather Research Program).

Figure B.9 [27] shows the magnitude of the moderate turbulence with respect to seasonality, in addition to coverage. The averages being taken here are equally weighted, under the assumption that each of the 20 estimates of the diagnostics is equally plausible. This assumption was considered fair, depending on the level of details of the analysis and consequently the accuracy of expected results. To reach higher accuracy of results, the uncertainties in diagnostic indices cannot be neglected. The skill of the diagnostics is in fact not the same for all indices. Considering set of diagnostics or weighted average of set of diagnostics (instead of simple average), that have better skills, seems to be the most correct approach according to [8]. The skill of a diagnostic is considered higher if there is higher agreement with observation data. Weighted linear combinations of the clear-air turbulence diagnostics calculated from numerical weather prediction models have been found to have significant skill when verified against pilot reports (PIREPs), and these combinations are currently being used for operational turbulence predictions [8], [9].

Annual-Mean Percentage Changes in the Amount of CAT From Pre-Industrial Times (picontrol) to the Period 2050–2080 (RCP8.5)

Strength	North Atlantic		North America		North Pacific		Europe	
Category	200 hPa	250 hPa	200 hPa	250 hPa	200 hPa	250 hPa	200 hPa	250 hPa
Light	+75.4	+47.3	+110.1	+71.0	+120.7	+82.0	+90.5	+59.9
Light-to-moderate	+124.1	+80.7	+113.6	+57.5	+106.6	+53.8	+130.7	+75.8
Moderate	+143.3	+74.4	+100.3	+50.2	+90.2	+41.6	+126.8	+60.8
Moderate-to-severe	+148.9	+71.0	+94.3	+47.0	+73.1	+35.3	+142.1	+66.1
Severe	+181.4	+88.0	+112.7	+58.9	+91.6	+40.1	+160.7	+90.6

Strength	South America		Africa		Asia		Australia	
Category	200 hPa	250 hPa	200 hPa	250 hPa	200 hPa	250 hPa	200 hPa	250 hPa
Light	+18.3	+13.4	+24.2	+18.9	+102.5	+65.1	+18.0	+9.5
Light-to-moderate	+27.1	+18.0	+27.9	+23.3	+92.4	+48.7	+23.1	+12.9
Moderate	+34.3	+22.8	+34.3	+26.0	+78.1	+48.7	+29.6	+19.1
Moderate-to-severe	+43.3	+23.8	+36.6	+26.9	+59.2	+47.9	+36.9	+24.8
Severe	+62.0	+31.6	+51.1	+40.2	+64.1	+55.4	+52.5	+35.4

Note. The changes are calculated for five turbulence strength categories, at two pressure altitudes, and within eight geographic regions. The changes are averaged over 20 CAT diagnostics. The geographic regions are: North Atlantic (50–75°N, 10–60°W), North America (25–75°N, 63–123°W), North Pacific (50–75°N, 145°E–123°W), Europe (35–75°N, 10°W–30°E), South America (55°S–10°N, 35–80°W), Africa (35°S–35°N, 15°W–50°E), Asia (10–75°N, 45–140°E), and Australia (12–46°S, 113–177°E).

Table B.3. Annual-Mean Percentage Changes in the Amount of CAT From Pre-Industrial Times (picontrol) for the Period 2050–2080 (RCP8.5) [73]

The percentage changes generally display relatively little seasonality, with the same bulk spatial patterns occurring in all four seasons, although there does appear to be a moderate seasonal amplitude modulation locally in some regions. These bulk changes include large increases of several hundred per cent in the mid-latitudes in both hemispheres. In the Southern Hemisphere, these increases peak at around 45–75° S independently of longitude. In the Northern Hemisphere, the increases peak at around 45–75° N but they display more zonal variability, which appears to be associated with the presence of land masses. The bulk features also include small and statistically insignificant decreases of several tens of per cent in parts of the tropics (where convection is a more important source of turbulence and CAT is less relevant). The global-mean percentage changes in moderate CAT at 200 hPa are +30.8% (DJF), +46.5% (MAM), +42.7% (JJA), and +39.2% (SON), where large increases in the mid-latitudes are being partly offset by small decreases in the tropics.

Table B.3 tabulates the annual-mean percentage changes averaged within eight geographic regions, for all five turbulence strength categories and both pressure levels. The results indicate that the busiest international airspace around the middle and high latitudes (North Atlantic, North America, North Pacific, Europe, and Asia) experiences larger increases in CAT than the global average, with the volume of severe CAT approximately doubling at 200 hPa over North America (+112.7%), the North Pacific (+91.6%), and Europe (+160.7%). The less congested skies around the tropics (Africa, South America, and Australia) generally experience smaller, but still non-negligible increases in CAT (between 50% and 60%). Whereas globally, it is light turbulence that experiences the largest relative increase, locally, it can be severe turbulence (e.g., Europe). For each strength category and geographic region, the percentage change is larger at 200 hPa (12 000 m) than 250 hPa (10 000 m). To provide some context to aid with the interpretation of the magnitudes of these changes, in the North Atlantic (50–75° N, 10–60° W) at 200 hPa, we find that (i) in winter, severe CAT by 2050–2080 will be as common as moderate CAT in the control period, and (ii) for a range of turbulence strengths from light to moderate-to-severe, summertime CAT by 2050–2080 will be as common as wintertime CAT in the control period.

The same future trends for CAT is confirmed by multi-model climate projections [35], which indicate that the positive trend will continue to increase in the future with the global warming level. Results reveal that North Africa, East Asia and Middle East are MOG CAT hotspots with high agreement amongst the climate models and the CAT diagnostics. In general, models project a MOG-CAT increase within the 20-40°N latitudinal band and a weak decrease northwards. The projected increases in MOG-CAT frequency over these regions becomes greater when the global mean air surface temperature is higher. Unlike previous studies [15] [27], the research results of Foudad et al. [35] show a slight decrease in MOG-CAT frequency over the North Atlantic and increase in MOG CAT frequency in North Africa and Middle East. According to [35] the disagreement over the North Atlantic region could be explained by the fact that there are large uncertainties associated with the CAT indices used. This uncertainty may be linked to the competition between vertical wind shear and convective instability, both sources of turbulence. However, in [35] the authors recall that shear instability is the main source of clear-air turbulence, and that vertical wind shear is projected to decrease over the North Atlantic.

B.4 Sources of uncertainties in CAT projections

B.4.1 Sources of uncertainties in CAT projections: climate models versus diagnostic indexes

Even though the comparison of results shown in Figure B.8 validate the soundness of climate models to predict CAT, the question whether uncertainties are mainly related to climate models or to diagnostic indices to predict CAT remains substantially unresolved.

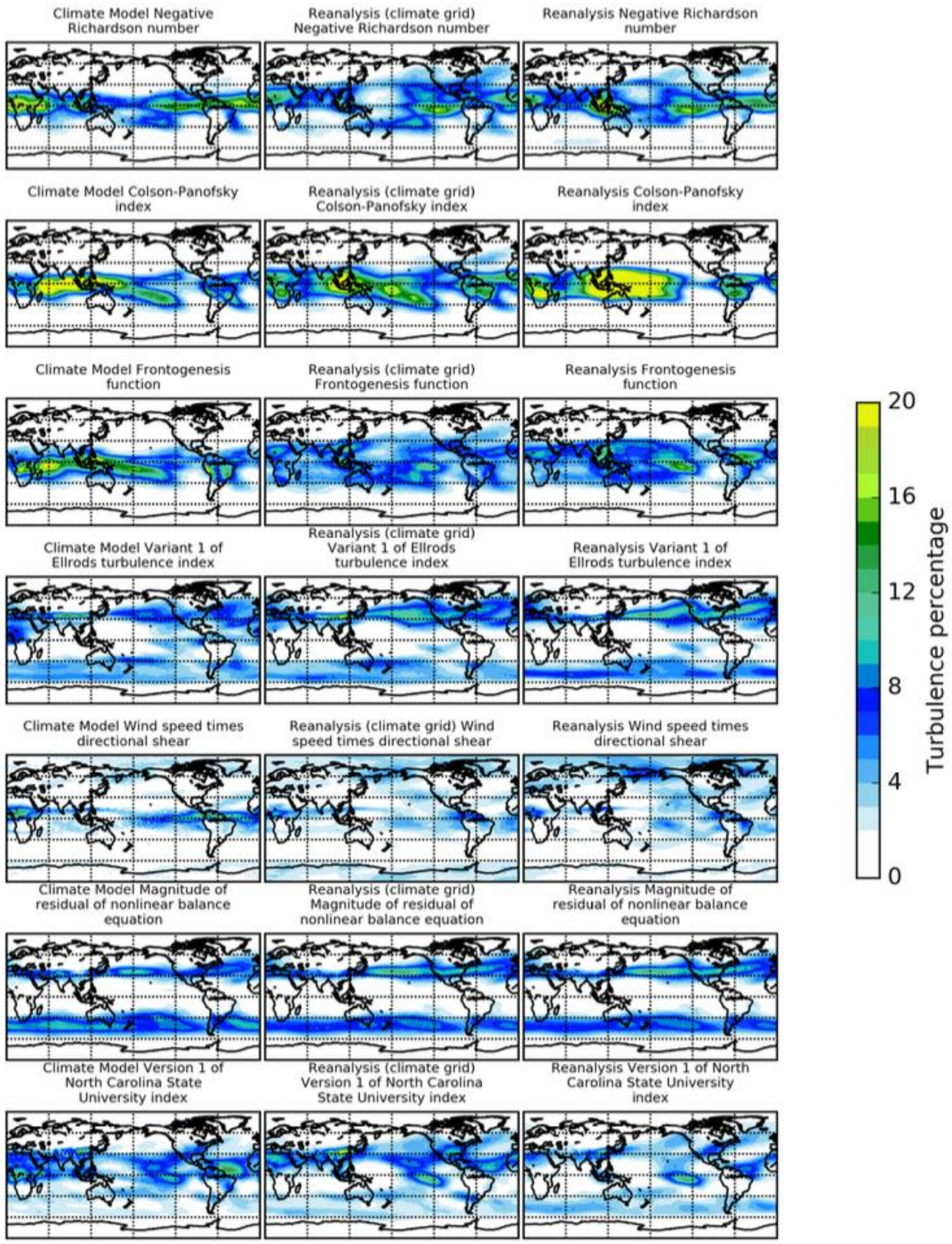

Figure B.10. Global maps of the probability (%) of encountering light CAT at 200 hPa in DJF. Seven turbulence diagnostics are shown (one per row). The turbulence probabilities are calculated from 38 years of the HadGEM2-ES historical climate simulation (left column), 38 years of ERA-Interim reanalysis data after re-gridding to have the same resolution as HadGEM2-ES (middle column), and 38 years of ERA-Interim reanalysis data at its original resolution (right column).

For this reason, in [32] Williams tackles this question. Results reveal that when computing the probabilities of encountering turbulence, most of the uncertainty stems from the turbulence diagnostics rather than the climate models.

Figure B.10 shows the result of the analysis to diagnose historic CAT (38 years: 1968–2005/1979-2016) from a climate model (Met Office Hadley Centre HadGEM2-ES model), reanalysis data (ERA-Interim from the European Centre for Medium-Range Weather Forecasts), re-gridded reanalysis data to have the same vertical and horizontal levels as the climate model. The global spatial distribution of historic CAT in December, January, and February (DJF) at 200 hPa is shown. Each map depicts the probability of encountering light CAT at each point on the globe, as diagnosed from the full 38 years of each dataset. Because there are seven different CAT diagnostics each applied to three different datasets, we have an ensemble of 21 different estimates of the global spatial distribution of the probability of encountering light CAT at 200 hPa in DJF.

To answer the question of whether the main differences between the 21 maps in Figure B.10 lie along the rows or down the columns, for each season each of the seven CAT diagnostics are taken in turn, and at each latitude and longitude the standard deviation of the probabilities across the three datasets is computed, before averaging them globally to produce a global-mean standard deviation. This procedure yields a quantification of the global-mean inter-dataset uncertainty for each diagnostic. Each of the three datasets are also taken in turn, and at each latitude and longitude the standard deviation of the probabilities across the seven CAT diagnostics is computed, before again averaging them globally. This procedure yields a quantification of the global-mean inter-diagnostic uncertainty for each dataset.

Turbulence diagnostic	DJF	MAM	JJA	SON
Negative Richardson number	0.68%	0.61%	0.69%	0.50%
Colson–Panofsky index	1.00%	0.96%	1.06%	0.87%
Frontogenesis function	0.75%	0.62%	0.78%	0.63%
Variant 1 of Ellrod's turbulence index	0.41%	0.36%	0.48%	0.33%
Wind speed × directional shear	0.38%	0.30%	0.40%	0.32%
Magnitude of residual of nonlinear balance equation	0.22%	0.20%	0.27%	0.24%
Version 1 of North Carolina State University index	0.53%	0.48%	0.50%	0.44%
Climate model	1.46%	1.23%	1.44%	1.22%
Reanalysis (climate grid)	1.46%	1.37%	1.63%	1.36%
Reanalysis	1.75%	1.62%	1.84%	1.56%

Table B.4: Breakdown of uncertainty sources for the change over time in the probability of encountering light CAT at 200 hPa. For each season (columns), the global-mean inter-dataset standard deviations (i.e., the variability across the three datasets for each diagnostic) are shown in the top seven rows, and the global-mean inter-diagnostic standard deviations (i.e., the variability across the seven diagnostics for each dataset) are shown in the bottom three rows.

For each season (columns in Table B.4), the global-mean inter-dataset standard deviations (i.e., the variability across the three datasets for each diagnostic) are shown in the top seven rows, and the global-mean inter-diagnostic standard deviations (i.e., the variability across the seven diagnostics for each dataset) are shown in the bottom three rows.

Results reveals that the variability across the datasets for each diagnostic is typically much smaller than the variability across the diagnostics for each dataset. The largest part of the uncertainty within the 21-member ensemble therefore stems from the use of multiple diagnostics rather than the use of multiple datasets. In other words, the spread between the climate model and reanalysis data is much smaller than the spread between the diagnostics.

It is therefore clear that further investigation is needed to understand how to use diagnostic indices for CAT future projections.

B.4.2 Sources of uncertainties in CAT projections: diagnostic indexes

To better understand the skilfulness of diagnostic indexes, the analysis of historical patterns and trends of CAT in the recent four decades (1979–2019/2020), using the highest resolution reanalysis data available, has been considered by two different research teams: the research team at University of Reading, UK (Paul Williams) [33] and the research team of Seoul National University, South Korea (Ju Heon Lee, Jung-Hoon Kim, and Seok-Woo Son), the National Center for Atmospheric Research, USA (Robert D. Sherman), and at Gonju National University, South Korea) Joowan Kim [34].

The results of both research teams are here considered and compared.

University of Reading [33] input data	Seoul National University et al. [34] input data
Global ERA5 reanalysis data	ECMWF Re-Analysis version 5 (ERA5) data
Cruise level: 197 hPA pressure level	Cruise level: 250 hPA pressure level
Timeframe: from 1 January 1979 to 31 December 2020	Timeframe: from January 1979 to December 2019
Horizontal resolution: 0.25° × 0.25° horizontal grid spacing at 3 hourly intervals	Horizontal resolution: 0.25° × 0.25° horizontal grid spacing at 6 hourly intervals
Vertical resolution: layers between 188 and 206 hPa levels (finer resolution, therefore possibly more accurate result if compared to Lee)	Vertical resolution: 12 vertical layers between 100 and 500 hPa levels.

Table B.5: Input data used by the studies conducted by University of Reading [33] (left column) and Seoul National University et al. [34] (right column).

University of Reading [33] methodology	Seoul National University et al. [34] methodology

The 21 turbulence diagnostics were calculated from the extracted reanalysis fields every three hours.	Two groups, which are defined as empirical indices and theoretical instability indicators, of CAT diagnostics are considered: • the empirical diagnostics are the Turbulence Index versions 1, 2, and 3 (TI1, TI2, and TI3) and their components (vertical wind shear (VWS), deformation (DEF), -divergence (DIV), and divergence tendency (DVT)); • three "theoretical" instability diagnostics are also considered: the Brunt-Väisälä frequency (N2), the Richardson number (Ri), and the potential vorticity (PV), which are directly related to convective, Kelvin-Helmholtz, and inertial instabilities, respectively.
The diagnostic values corresponding to the 97th, 99.1st, 99.6th, 99.8th, and 99.9th percentiles are derived globally for the reference year 2000, corresponding, respectively, to the thresholds for light-or-greater (LOG), light-to-moderate-or-greater (LMOG), moderate-or-greater (MOG), moderate-to-severe-or-greater (MSOG), and severe-or-greater (SOG) turbulence. **For each diagnostic and threshold, the number of exceedances at a given coordinate for each month, season, and year in the study period are computed. For each year, an average exceedance field is calculated by taking the mean of the 21 exceedance fields for each diagnostic.**	Given that this study focuses on the frequency of CAT in the upper troposphere/lower stratosphere near jet streams, the 95th percentile value as the threshold of each CAT index for MOG-level CAT is considered. To assess the veracity of the selected MOG thresholds, four case studies of observed CAT over the North Pacific and North Atlantic regions are performed. The frequency is calculated as the ratio (%) of the number of values that exceed the thresholds at each grid box in the 6-hourly data during the 41 years.
Exceedances were converted into percentage probabilities of exceedance, by normalizing by the number of three-hour periods in each year. Absolute changes in the probability of encountering turbulence over the 42 years were computed by subtracting the fitted 1979 values from the fitted 2020 values. For example, a 1% increase over one year would be equivalent to around 29 three-hour periods with exceedances, given the 2,920 three-hour periods in a single year. To calculate the relative changes, the absolute changes were divided by the fitted 1979 values and multiplied by 100, to yield a percentage relative change.	

Table B.6: Methodologies implemented by the studies conducted by University of Reading [33] (left column) and Seoul National University et al. [34] (right column).

These studies [33] [34] consider different inputs and implement different methodologies, as summarized respectively in Table B.5 and Table B.6.

Results of University of Reading (Williams et al. [33]) reveal that the largest increases both absolute and relative of frequency of MOG CAT are found over the North Atlantic and continental United States, over the total reanalysis period.

The above two hotspots for increased MOG CAT contrast with the East Asian and East Pacific hotspots identified by Seoul National University (Lee et al. [34]).

There are important differences both in terms of input data and in terms of methodology, as highlighted in Table B.5 and Table B.6, that may account for these different results. In particular, differences may arise because many CAT diagnostics require the computation of vertical derivatives (derivatives with respect to altitude). To compute these derivatives, Williams [33] used input field data at 206 hPa and 188 hPa to calculate the diagnostic values at 197 hPa. In contrast, Lee et al. [34] appear to have used input field data at 200 hPa and 300 hPa to calculate the diagnostic values at 250 hPa. Interestingly, of all the CAT diagnostics that the studies have in common, the two that do not require the computation of a vertical derivative (namely the deformation, DEF, and divergence, DIV) are very similar between the two studies, lending support to this explanation for the differences [33].

Figure B.11 and Figure B. 12 show the comparison between the results of the two research teams [33] [34] for the flow deformation and divergence diagnostic indexes.

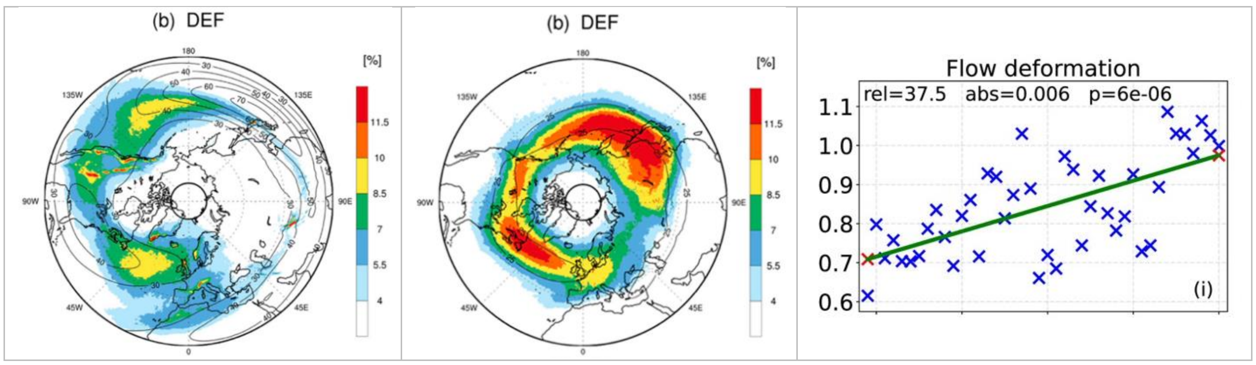

Figure B.11: Frequency (%) distributions MOG CAT (shading) for the Deformation, DEF at 250 hPa in the 20–80°N for 41 years (1979–2019) for the winter period (DJF) (left column) and summer period (JJA) (middle column). Averaged zonal wind speeds are also shown as black contours from 30 to 80 m s−1 at 10 m s−1 intervals (source: [33]). Linear regression analysis conducted on the ERA5 197 hPa annual-mean MOG CAT probability for the North Atlantic box (third row), for DEF (right column) (source: [34]).

In Figure B.11 the results of Lee et al. [34] (see left column for winter period and middle column for summer period) are expressed in terms of frequency (%) distributions of MOG CAT (shading) for the deformation index, DEF, at 250 hPa in the 20–80°N for 41 years (1979–2019). The frequency was calculated as the ratio (%) of the number of values that exceed the threshold (i.e. the values of the diagnostic index corresponding to the 95th percentile) at each grid box in the 6-hourly data during the 41 years, as was done in previous studies (e.g Williams [15]). The results of Williams [33] (see right column) are expressed in terms of annual-mean MOG CAT probability as diagnosed by the flow deformation index. The number of exceedances with respect to the threshold (i.e. the values of the diagnostic index corresponding to the 99,8th percentile) at a given coordinate for each month, season, and year in the study period were computed. Exceedances were converted into percentage probabilities of exceedance, by normalizing by the number of three-hour periods in each year. The 42 blue crosses indicate data from the 42 years, whereas the two red crosses show the fitted 1979 and 2020 values, in line with the linear regression conducted on the ERA5 197 hPa for the North Atlantic box. Solid green lines indicate trends that are statistically significant at the p = 0.05 level, according to a two-sided Wald test.

When comparing the results of the left and middle columns of Figure B.11 with those of the right column, it is therefore important to remember that while Lee et al. [34] show the frequency of exceedance of MOG CAT threshold (95th percentile) for two seasons over 40 years worldwide, Williams [33] show the annual-mean probabilities of exceedance of MOG CAT threshold (99,8th percentile) over 40 years for the North Atlantic corridor.In Figure B.12 the results of Lee et al. [34] (see left column for winter period and middle column for summer period) are expressed in terms of frequency (%) distributions of MOG CAT (shading) for the divergence index, DEF, at 250 hPa in the 20–80°N for 41 years (1979–2019). The results of Williams [33] (see right column) are expressed in terms of annual-mean MOG CAT probability. Dashed green lines indicate trends that are not statistically significant at the p = 0.05 level, according to a two-sided Wald test.

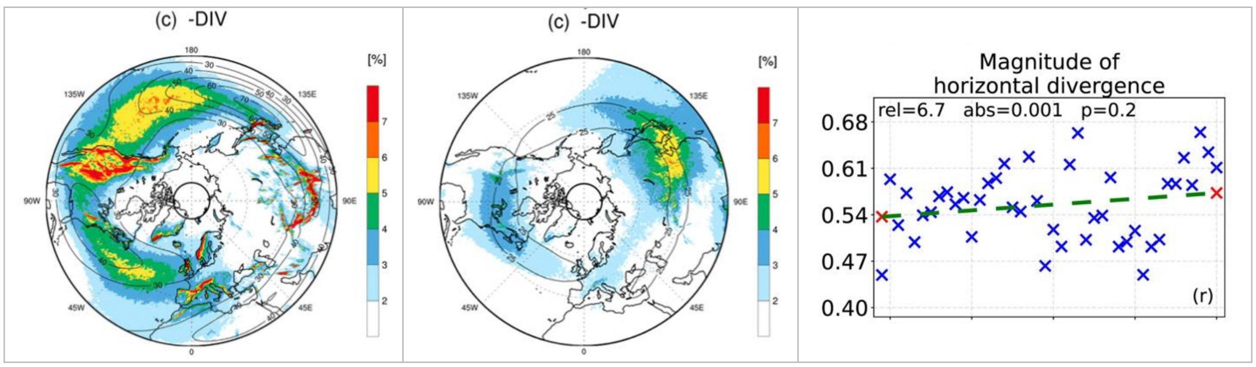

Figure B.12: Frequency (%) distributions MOG CAT (shading) for the Divergence, -DIV at 250 hPa in the 20–80°N for 41 years (1979–2019) for the winter period (DJF) (left column) and summer period (JJA) (middle column). Averaged zonal wind speeds are also shown as black contours from 30 to 80 m s−1 at 10 m s−1 intervals (source: [33]). Linear regression analysis conducted on the ERA5 197 hPa annual-mean MOG CAT probability for the North Atlantic box (third row), for -DIV (right column)(source: [34]).

Figure B.13 shows the annual-mean probabilities of encountering MOG CAT, according to Williams et al. [33], in (a) the year 1979, (b) the year 2020, (c) the year 1979 inferred from the linear regression model, and (d) the year 2020 inferred from the linear regression model. The probabilities are calculated from ERA5 at 197 hPa and are averaged over 21 CAT diagnostics.

Figure B.14 shows the frequency trends in winter season, calculated by regionally averaging over 41 years, of each CAT index within designated areas, according to Lee et al [34]. Again, East Asia showed the largest positive trend. Red boxes indicate East Asia (80–150°E, 30–45°N), Eastern Pacific (170°E−130°W, 35–55°N), and North-western Atlantic (80–20°W, 35–60°N) regions from the left.

Globally, results of two independent research teams [33] [34] on historical patterns and trends of CAT in the recent four decades (1979–2019/2020) show that high frequencies of the indices occurred on the northern side of the jet in the winter period (DJF) and three maxima patterns were found over the East

Asia, Eastern Pacific, and North-western Atlantic regions (and continental United States for [33]). There is substantial agreement between Williams et al. [33] and Lee et al. [34] on the number of hotspots for MOG CAT and on their geographical locations. However, there is no agreement on their prioritization, being the hottest spot East Asia for [34] and North Atlantic for [33].

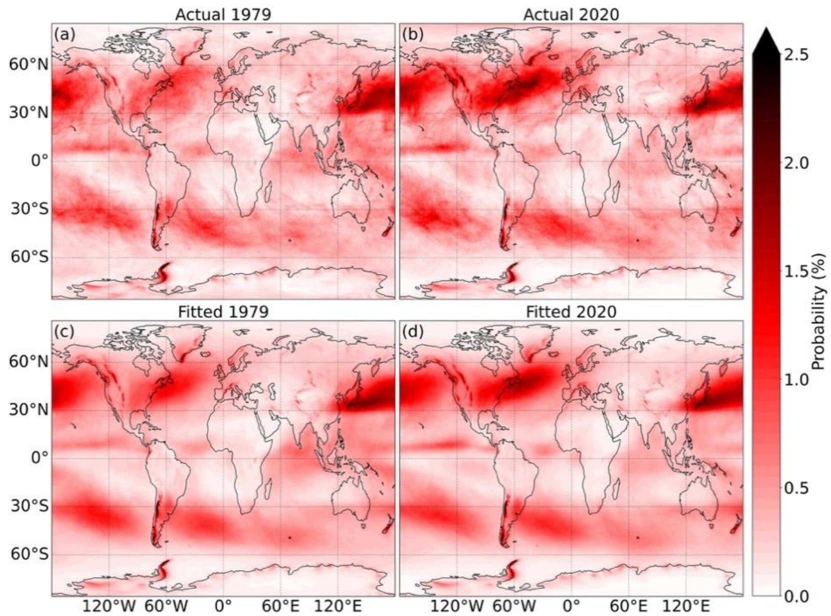

Figure B.13: Annual-mean probabilities of encountering moderate-or-greater clear-air turbulence (CAT) in (a) the year 1979, (b) the year 2020, (c) the year 1979 inferred from the linear regression model, and (d) the year 2020 inferred from the linear regression model (source: [33]). The probabilities are calculated from ERA5 at 197 hPa and are averaged over 21 CAT diagnostics. See Supporting Information S1 for light-or-greater and severe-or-greater CAT versions of this figure.

The East Asia maxima coincides with the entrance region of the strongest East Asian jet and has the highest frequencies frequency trends for TI1, TI2, and TI3 mainly due to large vertical wind shear (VWS). The Eastern Pacific and North-western Atlantic regions also have high frequencies trends for TI1, TI2, and TI3 largely attributed to large DEF, -DIV, and DVT at the exit of the jet stream as well as large VWS. In summer [34], the overall occurrence frequencies of MOG-level CAT were decreased and shifted poleward due to the northward shifted and weakened jet stream in the Northern Hemisphere. During this season, the three maxima patterns of TI1, TI2, and TI3 were found over East Asia, North-western Atlantic, and Mediterranean Europe mainly due to increased DEF. Particularly East Asia had the highest CAT potential again in summer, which is primarily related to the summer monsoon system.

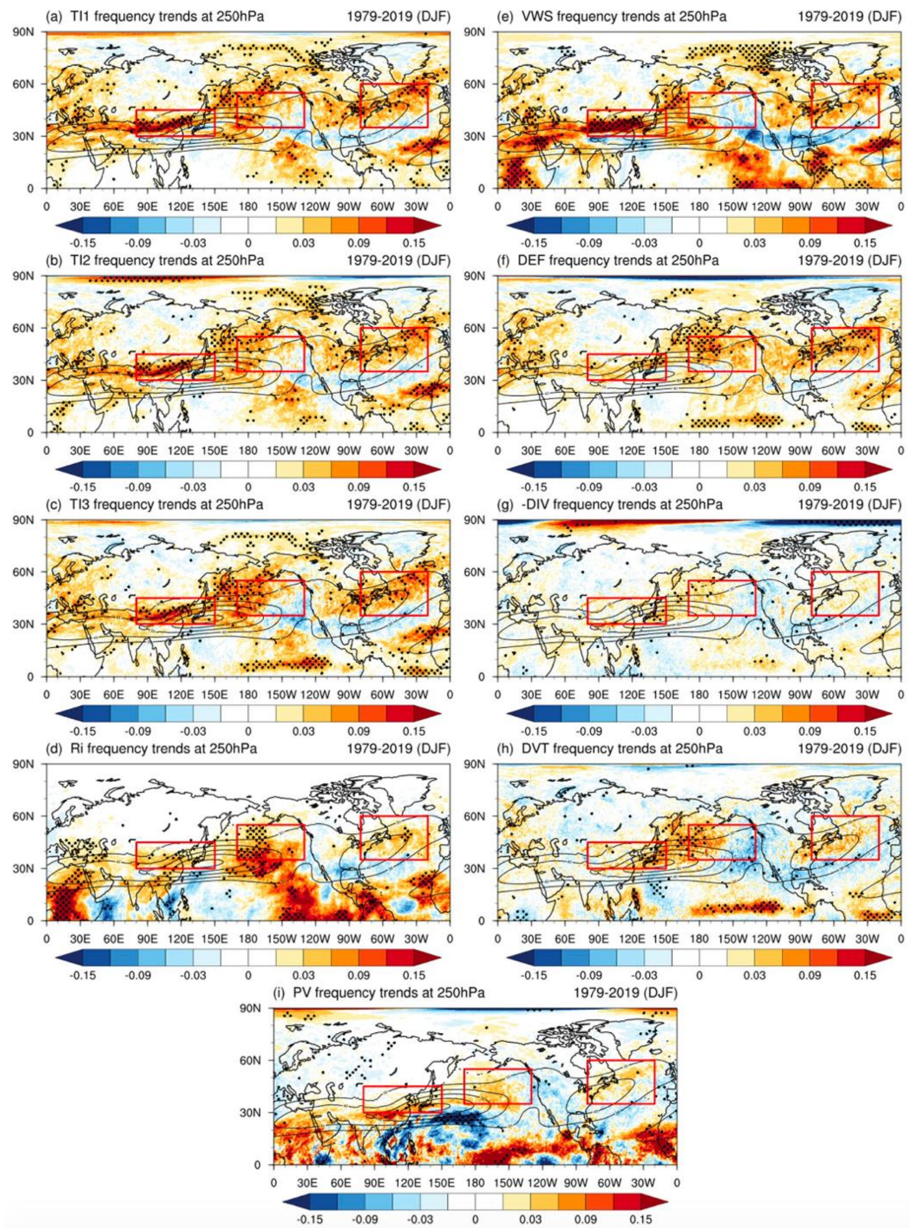

Figure B.14: DJF frequency trends at 250 hPa for (a) TI1, (b) TI2, (c) TI3, (d) Richardson number (Ri), (e) vertical wind shear (VWS), (f) deformation (DEF), (g) – divergence (-DIV), (h) divergence tendency (DVT), and (i) potential vorticity (PV) (shading) over 41 years (1979–2019). Black contours and stippling depict zonal wind speed at 250 hPa (30–80 m s−1 at 10 m s−1 interval) and significant trends (P-value <0.05, n = 41) respectively (source: [34])

Consistently with previous studies [33] [34], Foudad et el. [35] find that the highest frequencies of MOG CAT occurrence in the current climate are located on the northern side of the jets over different regions: the North Atlantic, North Pacific, East-Asia. However, unlike previous studies [33] [34], Foudad et al. [35] identified a new geographical region of higher frequencies of MOG CAT: North Africa. According to [35] the maxima of MOG CAT frequency were found over East-Asia (approximately 7.5%), which are due to strong vertical wind shear (VWS), where subtropical jet reaches its speed maximum, and which are also due to the presence of the Himalayas that could enhance VWS.

B.5 Conclusions

The following conclusions can be drawn by the current investigations on CAT:

- *the accuracy of predictability in time and space*. The accuracy of results depends on uncertainties and most of all on uncertainties possibly related to climate models and turbulence diagnostic indexes. According to [32] most of the uncertainties stems from the turbulence diagnostics rather than the climate models. The limiting factor that is preventing the reduction of uncertainty in projections of future CAT does not lie in climate models, but in CAT diagnostics. Therefore, to reduce these uncertainties, further research is needed to improve and refine the diagnostics. The development of new CAT diagnostics is ongoing and welcome, but may increase inter-diagnostic uncertainty if the new diagnostic lies outside the spread of the existing ensemble. Considering specific set of diagnostics, particularly weighted average of set of diagnostics, instead of simple average, can be an interesting approach to increase accuracy of results according to [8]. Weighted average allows in fact to make more skilful diagnostics count more. The skill of a diagnostic is considered higher if there is higher agreement with observation data. Weighted linear combinations of the clear-air turbulence diagnostics calculated from numerical weather prediction models have been found to have significant skill when verified against pilot reports (PIREPs), and these combinations are currently being used for operational turbulence forecasting [8]. Gaining further insights into the circumstances in which each diagnostic does (and does not) add useful information to the diagnosis of CAT could be crucial, so that a diagnostic may be down-weighted or eliminated from the ensemble on those occasions when it is merely adding noise. Reaching these insights will likely require further improvements to our fundamental understanding of the sources and dynamics of CAT. These could lead to consider different set of skilful diagnostic indexes to best represent CAT due to diverse physical phenomena in different geographical areas. This specific issue appears to be extremely challenging. Aircraft measurements may be very useful to push the limits of current research. However, aircraft measurements may not be directly available. For instance, results [27] reveal that in the tropical regions (30°S–30°N), there is less agreement between the diagnostics, while in the middle and high-latitude regions, there is more agreement between the diagnostics, because CAT diagnostics were developed to diagnose and predict mid-latitude CAT near jet streams, so they are optimized to be skilful for these regions rather than the tropics. The accuracy of results therefore appears to be higher in the middle and high-latitude regions than in the tropical regions.
- *The seasonality*. As far as CAT future trends are concerned, according to [27], the percentage changes generally display relatively little seasonality, with the bulk spatial patterns occurring in all four

seasons, although there does appear to be a moderate seasonal amplitude modulation locally in some regions. These bulk changes include large increases of several hundred per cent of amount of CAT in the mid-latitudes in both hemispheres. In the southern hemisphere, these increases are highest at around 45–75° S, while in the northern hemisphere, the increases are highest at around 45–75° N but they display more zonal variability, which appears to be associated with the presence of more land masses.

- *The hazard magnitude (intensity and duration)*. As far as CAT future trends are concerned, according to [27], the busiest international airspace around the middle and high latitudes (North Atlantic, North America, North Pacific, Europe, and Asia) are predicted to experience larger increases in CAT than the global average, with the volume of severe CAT approximately doubling at 200 hPa (12000 m) over North America (+112.7%), the North Pacific (+91.6%), and Europe (+160.7%). The less congested skies around the tropics (Africa, South America, and Australia) are predicted to experience somewhat smaller increases. Results of [27] reveal therefore that in the tropical regions (30°S–30°N), the percentage changes are generally smaller, while in the middle and high-latitude regions, the percentage changes are generally larger. Whereas globally, it is light turbulence that is expected to experience the largest relative increase, locally, it can be severe turbulence (e.g., Europe). For each strength category and geographic region, the percentage change is larger at 200 hPa (12000 m) than 250 hPa (10000 m). The same future trends for CAT are confirmed by multi-model climate projections [35], which indicate that the positive trend will continue to increase in the future with the global warming level. According to [35], North Africa, East Asia and Middle East are reported as MOG CAT hotspots in future trends. In general agreement with [27], the models of [35] project an increase in MOG CAT frequency within the 20-40°N latitudinal band and a weak decrease northwards. The projected increase in MOG-CAT frequency over these regions is greater when the global mean air surface temperature is higher. Unlike previous studies [15] [27], the research results of Foudad et al. [35] show a slight decrease in MOG-CAT frequency over the North Atlantic.
- *The hazard frequency*. As far as CAT future trends are concerned, according to [27], in the north Atlantic (50–75° N, 10–60° W) at 200 hPa, results of [15] [27] reveal that (i) in winter, severe CAT by 2050–2080 could be as common as moderate CAT in the control period, and (ii) for a range of turbulence strengths from light to moderate-to-severe, summertime CAT by 2050–2080 will be as common as wintertime CAT in the control period.
- *The geographical coverage*. The geographical coverage is complete.
- *The time coverage (within or beyond typical lifecycles of airplanes and runway pavements)*. Time coverage spans 30 years (2050-2080), when looking at future CAT trends, and 40 years (1980-2020), when looking at past CAT trends.
- *The reliability of climate models*. When using a climate model to calculate the probabilities of encountering turbulence of any strength, at any flight cruising level, and in any season, most of the uncertainty stems from the turbulence diagnostics rather than the climate model. It is well established [32] that climate models project increases in CAT in response to climate change, and the study

reported in [32] confirms the suitability of climate models for this task. According to [27], the comparison between the results of the HadGEM2-ES simulations from [27] with the GFDL-CM2.1 simulations from [29] supports the projected increase in transatlantic turbulence, as predicted in [15] and [27]. This also proves the robustness of climate models to predict future CAT trends due to climate change.

- *Uncertainties*. Uncertainties of current investigations are listed hereafter:
  - uncertainties in diagnostic indices do exist as diagnostics do not have all the same skills and their skilfulness may also depend on distinct geographical areas and diverse related physical phenomena, as different diagnostic indexes may be required to better represent CAT due to different physical phenomena in various geographical areas. The skill of a diagnostic is considered higher if there is higher agreement with observation data.
  - Future emissions of greenhouse gases depend on socioeconomic and political factors. The corresponding uncertainty in CAT should be quantified by using other radiative forcing scenarios in addition to the RCP8.5 scenario [30].
  - The jet streams in the upper troposphere and lower stratosphere in different climate models may respond differently to a given radiative forcing anomaly dependent of the parameterization scheme selected in the models.
- *Limitations*. Limitations of current investigations are listed hereafter:
  - only 200 hPa and 250 hPa, corresponding to 10000-12000 m of altitude have been investigated. Lower and higher altitudes to cover a wider range of civil passenger aircraft may be of interest in future analyses. Moreover, the current typical cruise altitudes of medium-large subsonic civil passenger aircraft of 10000-12000 m may also change in the future, depending on the rise of the tropopause and consequently the rise of the jet streams due to an increasingly warming environment, notwithstanding the optimal aircraft performance and the propulsive technology requirements.
  - Present results do not generally include all possible sources of CAT.

B.6 Bibliography

[1] Shine, K. P., and Coauthors, 2003: A comparison of model- simulated trends in stratospheric temperatures. Quart. J. Roy. Meteor. Soc., 129, 1565–1588

[2] Delcambre, S. C., D. J. Lorenz, D. J. Vimont, and J. E. Martin, 2013: Diagnosing northern hemisphere jet portrayal in 17 CMIP3 global climate models: Twenty-first-century roject- tions. J. Climate, 26, 4930–4946

[3] Goessling, H. F., and S. Bathiany, 2016: Why CO2 cools the mid- dle atmosphere—A consolidating model perspective. Earth System Dynamics, 7, 697–715

[4] Lee S.H., Williams P.D., Frame T.H., Increased shear in the North Atlantic upper-level jet stream over the past four decades (2019) Nature, 572 (7771), pp. 639 – 642. DOI: 10.1038/s41586-019-1465-z

[5] Dutton, J., and H. A. Panofsky, 1970: Clear air turbulence: A mystery may be unfolding. Science, 167, 937–944

[6] Tung, K. K., and W. W. Orlando, 2003: The *k*-3 and *k*-5/3 energy spectrum of atmospheric turbulence: Quasigeostrophic two- level model simulation. *J. Atmos. Sci.,* 60, 824–835

[7] Koshyk, J. N., and K. Hamilton, 2001: The horizontal energy spectrum and spectral budget simulated by a high-resolution tro- posphere–stratosphere–mesosphere GCM. *J. Atmos. Sci.,* 58, 329–348

[8] Sharman, R., C. Tebaldi, G. Wiener, and J. Wolff, 2006: An integrated approach to mid- and upper-level turbulence forecasting. Wea. Forecasting, 21, 268–287

[9] Lane, T. P., R. D. Sharman, S. B. Trier, R. G. Fovell, and J. K. Williams, 2012: Recent advances in the understanding of near-cloud turbulence. Bull. Amer. Meteor. Soc., 93, 499–515

[10] Ellrod, Gary P., Knox, John A., Improvements to an operational clear-air turbulence diagnostic index by addition of a divergence trend term, (2010) Weather and Forecasting, 25 (2), pp. 789 – 798, DOI: 10.1175/2009WAF2222290.1

[11] Ellrod, G. P., and D. L. Knapp, 1992: An objective clear-air turbulence forecasting technique: Verification and operational use. Wea. Forecasting, 7, 150–165

[12] Colson, D., and H. A. Panofsky, 1965: An index of clear-air turbulence. *Quart. J. Roy. Meteor. Soc.,* 91, 507–513

[13] Roach, W.T.. On the Influence of synoptic development on the production of High Level Turbulence. Quart. J. Roy. Meteor. Soc./ 96, 413-429 (1970)

[14] MacCready, P. B (1964). Standardization of gustiness values from aircraft. *Journal of Applied Meteorology*, *3*(4), 439–449

[15] Williams, P. D. (2017). Increased light, moderate, and severe clear-air turbulence in response to climate change. *Advances in Atmospheric Sciences*, *34*(5), 576–586

[16] Williams, J. K., 2014: Using random forests to diagnose aviation turbulence. *Machine Learning*, 95, 51–70

[17] Schwartz, B., 1996: The quantitative use of PIREPs in developing aviation weather guidance products. Wea. Forecasting, 11, 372–384

[18] Kim, J.-H., and H.-Y. Chun, 2011: Statistics and possible sources of aviation turbulence over South Korea. *J. Appl. Meteor. Climatol.*, 50, 311–324

[19] Sharman, R. D., L. B. Cornman, G. Meymaris, J. Pearson, and T. Farrar, 2014: Description and derived climatologies of automated in situ eddy-dissipation-rate reports of atmospheric turbulence. *J. Appl. Meteor. Climatol.*, 53, 1416–1432

[20] Kim, B., and Coauthors, (2005) System for assessing Aviation's Global Emissions (SAGE), Version 1.5, Technical Manual FAA-EE-2005-01, Federal Aviation Administration, Washington, DC

[21] Malwitz, A., and Coauthors, (2005) System for assessing Aviation's Global Emissions (SAGE), Version 1.5, Validation Assessment, Model Assumptions and Uncertainties. Tech. Rep. FAA-AA-EE-2005-03, Federal Aviation Administration, Washington, DC

[22] Wilkerson, J. T., M. Z. Jacobson, A. Malwitz, S. Balasubramanian, R. Wayson, G. Fleming, A. D. Naiman, and S. K. Lele, 2010: Analysis of emission data from global commercial aviation: 2004 and 2006. *Atmos. Chem. Phys.*, 10, 6391–6408

[23] Wilcox, L. J., K. P. Shine, and B. J. Hoskins, 2012: Radiative forcing due to aviation water vapour emissions. *Atmos. Environ.*, 63, 1–13

[24] Jaeger, E. B., and M. Sprenger, (2007) A Northern Hemispheric climatology of indices for clear air turbulence in the tropopause region derived from ERA40 reanalysis data. *J. Geophys. Res.*, 112(D20), D20106

[25] IPCC, 2021: Summary for Policymakers. In: Climate Change 2021: The Physical Science Basis. Contribution of Working Group I to the Sixth Assessment Report of the Intergovernmental Panel on Climate Change [Masson-Delmotte, V., P. Zhai, A. Pirani, S.L. Connors, C. Péan, S. Berger, N. Caud, Y. Chen, L. Goldfarb, M.I. Gomis, M. Huang, K. Leitzell, E. Lonnoy, J.B.R. Matthews, T.K. Maycock, T. Waterfield, O. Yelekçi, R. Yu, and B. Zhou (eds.)]. Cambridge University Press, Cambridge, United Kingdom and New York, NY, USA, pp. 3−32, doi:10.1017/9781009157896.001

[26] Abram, N., J.-P. Gattuso, A. Prakash, L. Cheng, M.P. Chidichimo, S. Crate, H. Enomoto, M. Garschagen, N. Gruber, S. Harper, E. Holland, R.M. Kudela, J. Rice, K. Steffen, and K. von Schuckmann, 2019: Framing and Context of the Report Supplementary Material. In: *IPCC Special Report on the Ocean and Cryosphere in a Changing Climate* [H.-O. Pörtner, D.C. Roberts, V. Masson-Delmotte, P. Zhai, M. Tignor, E. Poloczanska, K. Mintenbeck, A. Alegría, M. Nicolai, A. Okem, J. Petzold, B. Rama, N.M. Weyer (eds.)]

[27] Storer, L. N., Williams, P. D., & Joshi, M. M. (2017). Global response of clear-air turbulence to climate change. Geophysical Research Letters, 44, 9976–9984. https://doi.org/10.1002/2017GL074618

[28] Taylor, K. E., Stouffer, R. J., & Meehl, G. A (2012). An overview of CMIP5 and the experiment design. *Bulletin of the American Meteorological Society*, *93*(4), 485–498

[29] Williams, P. D., and M. M. Joshi, (2013) Intensification of winter transatlantic aviation turbulence in response to climate change. *Nature Clim. Change*, 3, 644–648

[30] Flato, G., Marotzke, J., Abiodun, B., Braconnot, P., Chou, S. C., Collins, W. J., ... Rummukainen, M. (2013). Evaluation of climate models. In T. F. Stocker et al. (Eds.), *Climate Change 2013: The Physical Science Basis. Contribution of Working Group I to the Fifth Assessment Report of the Intergovernmental Panel on Climate Change* (pp. 741–866). Cambridge, UK: Cambridge University Press

[31] Van Vuuren, D. P., Edmonds, J., Kainuma, M., Riahi, K., Thomson, A., Hibbard, K., … Rose, S. K. (2011). The representative concentration pathways: An overview. *Climatic Change*, *109*, 5–31.

[32] Williams, P.D. & Storer, L.N. (2022) Can a climate model successfully diagnose clear-air turbulence and its response to climate change?. Quarterly Journal of the Royal Meteorological Society, 148(744), 1424–1438. Available from: https://doi.org/10.1002/qj.4270

[33] Prosser, M. C., Williams, P. D., Marlton, G. J., & Harrison, R. G. (2023). Evidence for large increases in clear-air turbulence over the past four decades. Geophysical Research Letters, 50, e2023GL103814. https://doi.org/10.1029/2023GL103814

[34] Lee, J. H., Kim, J.-H., Sharman, R., D., Kim, J., & Son, S.-W. (2023). Climatology of Clear-Air Turbulence in upper troposphere and lower stratosphere in the Northern Hemisphere using ERA5 reanalysis data. Journal of Geophysical Research: Atmospheres, 128, e2022JD037679. https://doi.org/10.1029/2022JD037679

[35] Mohamed Foudad, Emilia Sanchez-Gomez, Thomas Jaravel, Melanie C. Rochoux, and Laurent Terray, Past and Future Trends in Clear-Air Turbulence over the Northern Hemisphere, JGR: Atmospheres 2023

C Appendix – Task Force #2: Increase of surface temperature due to climate change and its impact on aircraft take-off performance

Note: *The main author of this appendix is Suzanne Salles.*

C.1 Understanding future socio-economic scenarios

Between August 2021 and April 2022, the Intergovernmental Panel on Climate Change (IPCC) of the United Nations published its Sixth Assessment Report (Hereafter referred to as AR6) [1] which appraises the state of knowledge on Climate Change throughout the world through three working groups focusing on three issues: The Physical Science Basis (WGI); Impacts, Adaptation and Vulnerability (WGII) and Mitigation of Climate Change (WGIII).

In order to predict climatic changes and their effects, one has to make assumptions on how the future will unfold. Specifically, human actions to reduce greenhouse gas (GHG) emissions are subjected to various socio-economic factors, climate change mitigation measures and policies. For that, WGI issued five Shared Socio-economic Pathways (SSP) scenarios to '*cover the range of possible future development of anthropogenic drivers of climate change*'. SSP scenarios start in 2015 and cover high to low greenhouse gas emission scenarios. They are numbered from 1 (Sustainability) to 5 (Fossil-fueled Development) followed by the possible range of radiative forcing expected in 2100 (1.9 to 8.5 W/m^2). The radiative forcing is a measure of the net energetic imbalance in the Earth system that causes warming if positive. The SSP scenarios are comparable to Representative Concentration Pathway (RCP) scenarios that were used in the previous IPCC assessment report (AR5) in 2014 [2] that describe climate change scenarios depending on the amount of GHG emissions which are also labelled according to radiative forcing of 2100.

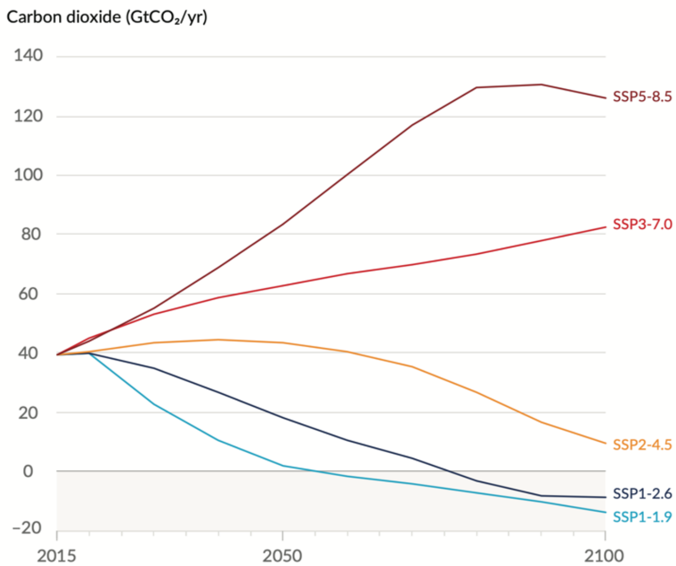

SSP scenarios

- SSP5: Fossil-fueled Development
- SSP4: Inequality
- SSP3: Regional Rivalry
- SSP2: Middle of the Road
- SSP1: Sustainability

Fig C.1: Global atmospheric CO2 concentration according to SSP scenarios [1]

Surface temperature, among other atmospheric variable is computed according to scenario projections with climate models. Figure C.1 and C.2 show respectively CO_2 emissions and the global mean air surface temperature (hereafter called 'global surface temperature') until the end of the century according to SSP scenarios.

C.2 Climate models' projection

Climate models are used to quantitatively simulate the behaviour of the Earth system and its components according to different scenarios in order to predict its behaviour. They solve physical equations governing the atmosphere and the ocean and their interactions with other sub-systems (land, clouds, ice sheets etc). The Earth is divided into grids cells inside of which atmospheric variables such as temperature, pressure, air density, etc., are solved by physical equations. Other factors are harder to model such as clouds, rain, snow, etc., which can be smaller than the grid cell size. These factors are often parameterized to be taken into account. Variables are set to represent initial conditions, forcings and sensitivity.

The size of grids cells depends on the geographical resolution of the model with global climate models (GCMs) grid size ranging between 100 and 300 km and regional models grid size ranging from 10 to 50 km [3]. GCMs are useful for describing overall tendencies across the whole Earth and regional climate models (RCMs) give a more detailed description of how local scales can be affected that can more easily be compared to real data. The accuracy of results also depends on temporal resolution with time steps ranging from minutes to years depending on what is being studied. The higher the geographical or temporal resolution is, the more expensive the computing will be, so choosing a resolution according to the level of accuracy needed is important.

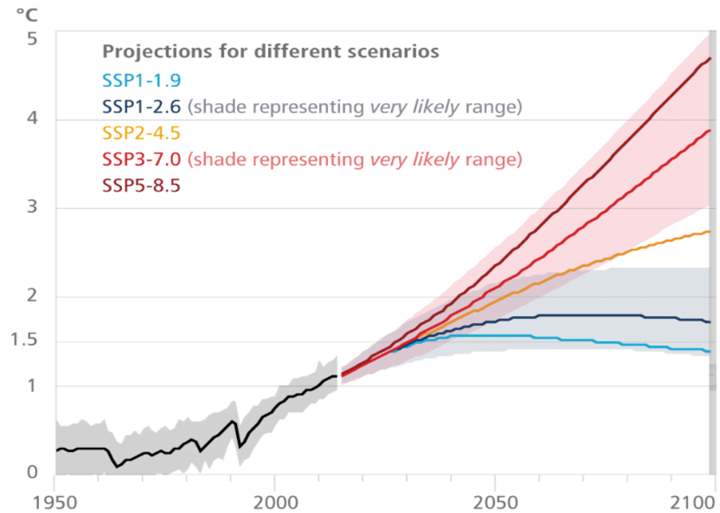

Fig C.2: Global surface temperature projections according to SSP scenarios [1]

A climate model is complex and relies on many factors and assumptions. Therefore, its outputs are subject to many uncertainties. In this light, the World Climate Research Program (WCRP)'s Working Group of Coupled Modelling (WGCM) created the Coupled Model Inter-comparison Project (CMIP). Its aim is to understand past and future climate by coordinating multiple climate model experiments done by international modelling teams [4]. Each model gives several simulation results called "members" corresponding to different parametrizations. The IPCC AR6 is based on the sixth phase of the project CMIP6. It allows to provide a multi-model approach database accessible to the large climate community for statistical analysis of outputs which is way more robust than just one model output.

According to this approach, it is possible to predict a level of global warming for long-, mid- and short-term periods. Compared to the pre-industrial period 1850–1900, the average global surface temperature over the period 2080–2100 is expected to rise by 1° C to 5.7° C according to socio-economic scenarios SSP 1-1.9 or 5-8.5 of respectively low-CO_2 or high-CO_2 emission. For mid-term projections (2041-2061), this average rise is expected between 1.2 to 3.0° C according to the same scenarios respectively. Short-term, mid-term and long-term projections are summarized in table C.1. Mid-term predictions give ideas on overall temperature rise within the lifespan of current aeroplanes lifespans.

	Short-Term 2021-2040		Mid-Term 2041-2060		Long-Term 2081-2100	
Scenario	Best estimate	Very likely range (°C)	Best estimate	Very likely range (°C)	Best estimate	Very likely range (°C)
SSP 1-1.9	1.5	1.2 to 1.7	1.6	1.2 to 2.0	1.4	1.0 to 1.8
SSP 1-2.6	1.5	1.2 to 1.8	1.7	1.3 to 2.2	1.8	1.3 to 2.4
SSP 2-4.5	1.5	1.2 to 1.8	2.0	1.6 to 2.5	2.7	2.1 to 3.5
SSP 3-7.0	1.5	1.2 to 1.8	2.1	1.7 to 2.6	3.6	2.8 to 4.6
SSP 5-8.5	1.6	1.3 to 1.9	2.4	1.9 to 3.0	4.4	3.3 to 5.7

Table C.1: Changes in global surface temperature, which are assessed based on multiple lines of evidence, for selected 20-year time periods and the five illustrative emissions scenarios considered. Temperature differences relative to the average global surface temperature of the period 1850–1900 are reported in ° C [1].

C.3 Impact of temperature on aircraft take-off performance

Among impacts and risks climate change has on aviation, the rise of air surface temperature can impact the sector by affecting aircraft take-off performance, increasing noise production, heat damage to aircrafts and airport infrastructure and higher heating/cooling requirements [5].

Aircraft take-off performance is impacted by high temperature in two ways. First, hotter air means a lower density. The lift force being a linear function of density, it is itself reduced with higher outside air temperature (OAT). Second, engine performance and resulting thrust is also reduced by a hot OAT, with the thrust sensitivity to OAT depending on the type of engine, flight level and regime.

The ability of an aircraft to take-off is limited by its capacity to reach sufficient velocities and climb gradient at specific phases of the take-off which are defined by certification according to safety margins [6]. In order to reach these velocities in the constraints of the distance available and margins of safety, a certain level of performance must be achieved. Otherwise, the take-odd distance (TOD) required might become longer, and in cases where the runway length is limiting restrictions would have to be imposed on Take-off weight (TOW) of the aircraft. A reduction in payload can have a significant economic impact on operators.

How much performance has been impacted by temperature rise in the last decades and how it will be affected in the future has started to be a subject of research in an effort to quantify how much climate change affects aircraft operations. Identifying trends of reduced performance could inform on future safety margins being decreased and calling for an adaptation of them. To root the problem into real world issues, it needs to be put in a context of climate change. Local short-term atmospheric conditions have to be linked to global long-term climatic trends. For that, two main approaches: looking at the past and the future. The following section summarizes published papers that have tackled this issue for mostly large aeroplanes. This is not an exhaustive list and other publications might be of interest.

C.4 Literature review of studies about the impact of rising temperatures on take-off performance of large aeroplanes

C.4.1 Past trends

Analysing historic observations can inform on trends of temperature rise or headwind decrease like in [7] that are harmful to take-off performance and help assess their impact by quantifying the reduction in resulting performance. This allows to quantify or qualify the effect climate change already has on take-off performance. In their article [7], Gratton et al. use observed meteorological data for temperature and wind in several Greek airports over a period of 62 years (1955-2017). For each airport, they look at time series of daily minimum temperatures and mean headwind component (component parallel to the runway) and compute annual means so as to visualize the trends with time. These two atmospheric variables should be indicative of climate change. They find that in all ten airports considered, the minimum air temperature has increased at a rate from 0.3 to 0.9°C/decade and that the mean headwind component decreased by a rate of 0.02 to 2.3 knots per decade in six of the ten cases. Now, looking at the impact it could have on air operations, they use performance models to simulate the take-off of two types of large aeroplanes: a short rate turboprop airliner (Havilland DHC-8-400) and a medium range turbofan airliner (Airbus A320). According to the performance models outputs and atmospheric variable evolution in the period considered, they show an overall decrease in performance with the most limiting cases being the airports with short runways where weight restrictions need to be imposed. Figure C.3 shows the evolution of atmospheric variables and resulting performance indicator maximum take-off weight (MTOW) for an A320 at Chios airport where the runway measured 1511m and has an orientation of 006°. The average MTOW reduction rate is of 132 kg/year which corresponds to the weight of 2 passengers.

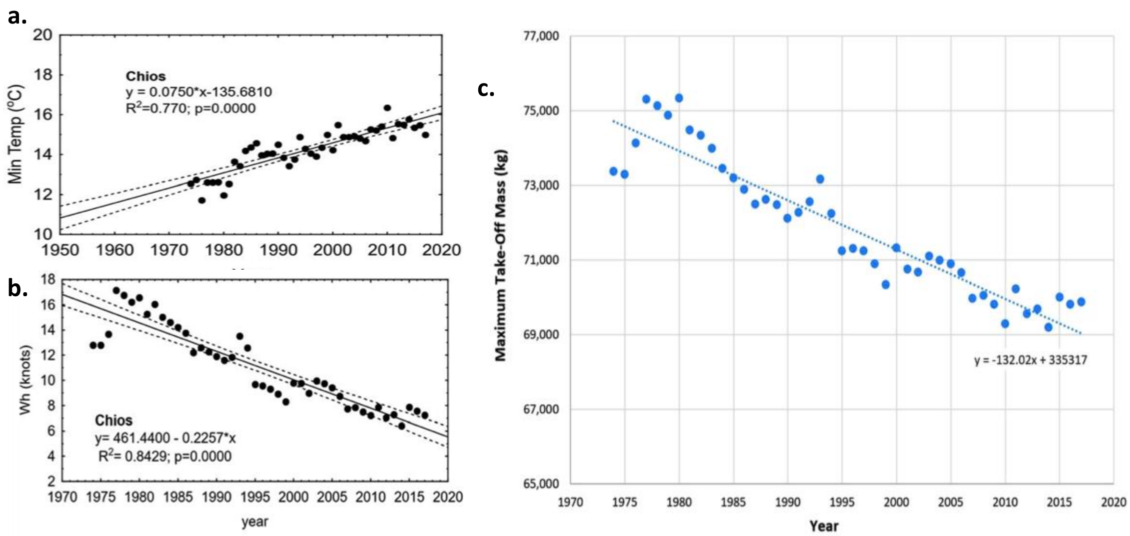

Fig. C.3: (a) Minimum daily temperature, (b) Average daily headwind component and (c) Resulting MTOW for the case of an A320 aircraft at Chios Airport. Figure from [7].

C.4.2 Future trends

For analysing future trends, one needs to rely on predictions from climate models. In [8] Coffel et al. explore the link between rising air surface temperatures caused by global warming and take-off performance. They use Boeing performance charts [10] illustrated in figure C.6.b to define a threshold temperature corresponding to levels of weight restrictions of a Boeing 737 aircraft for 4 different airports in the US: Phoenix Sky Harbor International Airport (PHX), Denver International Airport (DEN), New York's LaGuardia Airport (LGA), and Washington, D.C's Reagan National Airport (DCA). They then confront these thresholds to temperature projections according to 17 circulation models from the CMIP5 multi-model ensemble [13] under the RCP 8.5 high emissions scenario. This allows to categorize future days according to the level of restriction on weight that might be imposed.

They insist on the fact that the current aircrafts are planned to be used for several decades before being replaced by new generations and will most probably face weight restrictions due to climate change. They also state that take-off performance is not a priority in the development of new propulsion technology as the focus is on cruise performance so outlying the importance of take-off performance reduction is very important for future aircraft designs. As seen in figure C.4, depending on the airport, the thresholds related to a specific weight restriction are not the same because they are computed based on the airport (especially taking into account altitude and runway length available). For that reason, in Phoenix, where temperatures are overall higher than in New York, the threshold for a 10 000 lbs weight restriction compared to the reference MTOW is around 47°C whereas it is around 31°C in New York. Even though temperatures are higher in Phoenix, New-York LaGuardia (LGA) airport will be faced with more days of restrictions equal or higher than 10 000 lbs. This is partly due to LGA short runway (7003 ft or 2134.5 m).

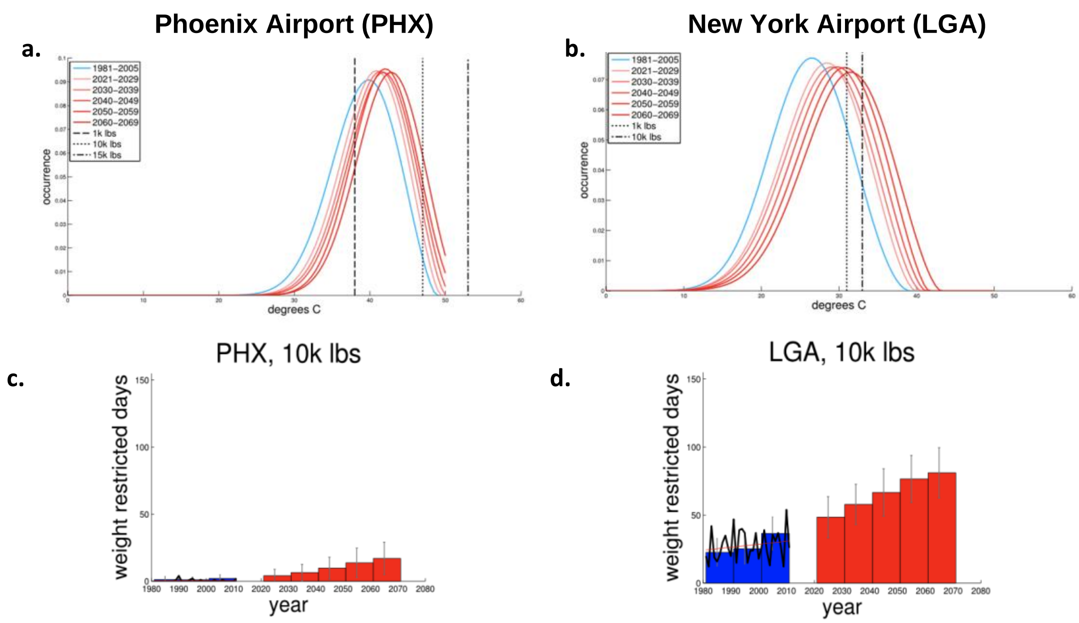

Fig. C.4: Top: Temperature distribution for several decades: reference historical period in blue and future periods according to SSP 5-8.5 scenario CMIP5 ensemble in red at (a) Phoenix Sky Harbor International Airport (PHX) and (b) New York's LaGuardia Airport (LGA) with three weight restriction temperature thresholds. Bottom: Number of days for which temperatures reach a higher value than the 10k lbs temperature threshold per decade for (c) PHX and (d) LGA. Blue color shows historical data and red shows future data. Figure from [8].

In [9], Coffel et al. extended the scope of their previous study to 19 airports around the world, mostly in America and Asia but they also include LHR (London), CDG (Paris) and MAD (Madrid) in Europe, and several common commercial large aeroplanes, the Boeing 737-800, Airbus A320, Boeing 787-8, Boeing 777-300, and Airbus A380. In the study they highlight temperature rise at different airports by plotting the number of days per year that exceeds the historical annual maximum temperature. They state that in most cities the frequency may rise to between 10 and 50 days per year by 2060-2080. They then proceed to compute weight restrictions based on public performance data like [10]. Since Take-off weight (TOW) is usually lower than MTOW depending on operations, they compute weight restrictions depending on an array of TOW for each aircraft at each airport. The aircrafts that seem the most impacted by high temperatures are the large Boeing 777-300 and Boeing 787-8 for take-offs at TOW close to MTOW. According to them, by mid- to late century, total fuel and payload capacity may be reduced by 3–5% with 30–40% of flights experiencing some restriction. Medium-haul aircrafts like Airbus A320 and Boeing 737-800 face less impact with approximately 5–10% of flights experiencing some restriction. They explain that mainly by the fact that most international commercial airport have runways dimensioned for larger aircrafts, so these medium-haul aircrafts have enough runway length available, even with degraded performance. Their results on the A380 show little impact, partly due to its exclusive operation at large airports. Finally, when comparing airports, the airports most affected by high temperatures would be those in high altitude and with short runways like Denver (DEN) (16000 ft runway and 5433 ft elevation) and LaGuardia New York (LGA) (7003 ft runway and 21 ft elevation) for instance.

In [11], Zhou et al. explore the effect of climate change on take-off performances of large aeroplanes, especially on the take-off distance and climb rate. For thirty major airports around the world (shown in figure C.5), based on observed climate data at each airport from 1976 to 2005 and 25 CMIP5 historical and future realisations according to scenario RCP 8.5, they study the evolution of atmospheric variables for summer days from mid 20th century to the end of the 21st century.
Depending on the temperature and pressure altitude, they compute the take-off distance according to the Koch chart [12] illustrated in figure C.6.a that provides a coefficient for increase of take-off distance (TOD) and decrease in climb gradient according to pressure altitude and temperature compared to sea level ISA conditions. This coefficient is not specific to one kind of aircraft. They show that the witnessed increase in air surface temperature and decrease in pressure in the past and future periods entails longer and longer TOD. They show that the rate of increase of the TOD is higher from the mid- to late- 21stcentury than from the historical period to now and that it is mostly attributable to temperature rise than pressure altitude changes. According to their simulation, the average take-off distance in summer will increase by 0.95–6.5% from the historical period (1976–2005) to the mid-century (2021–2050) and by 1.6–11% from the mid- (2021–2050) to late-century (2071–2100). With airports most impacted being MAD (Madrid, Spain), URC (Xinjiang/China) and LAX (Los Angeles/USA). More generally, results can be summarized in figure C.5 where the take-off factor is plotted depending on the airport for the reference historical period in the first plot and the two following plots show the change in take-off factor relative to the reference period. Taking the Boeing 737-800 aircraft as an example, they estimate an additional 3.5 to 168.7 m in TOD in future summers depending on airports.

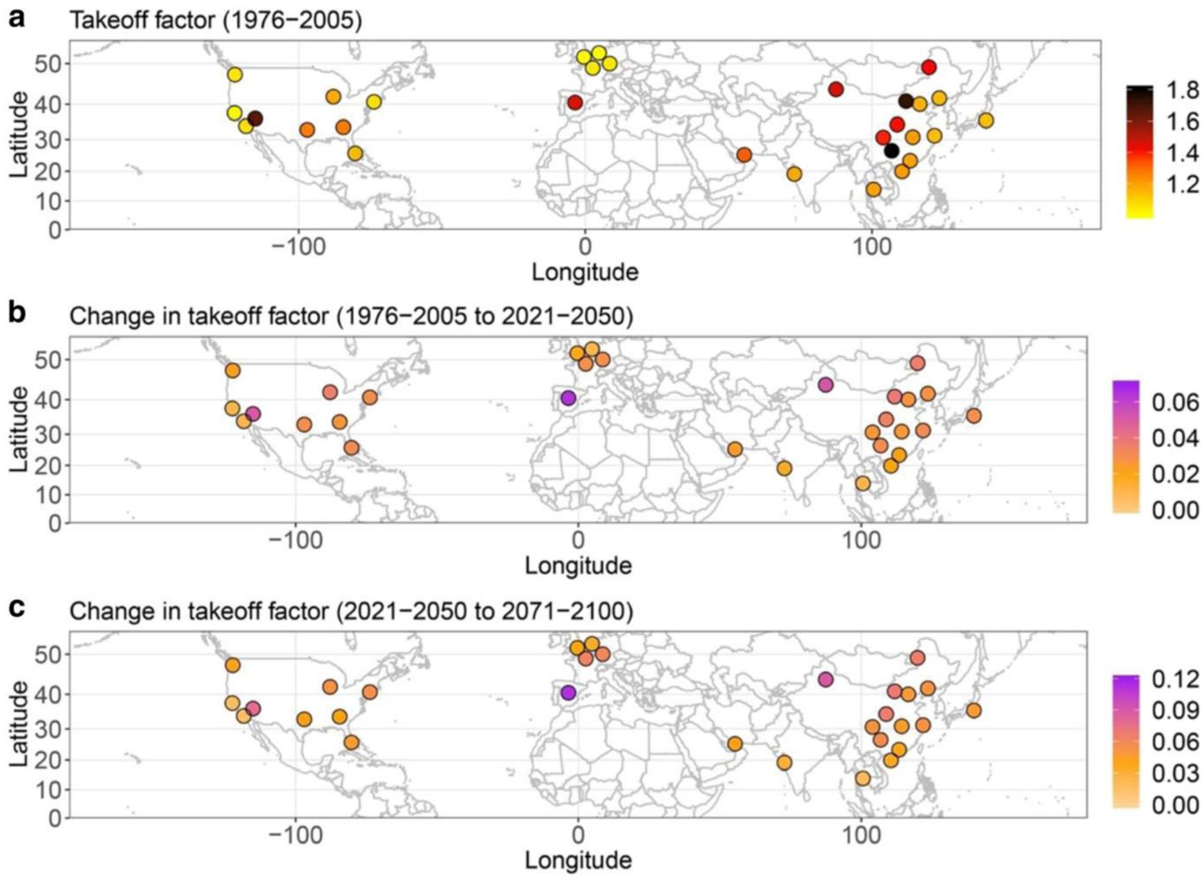

Fig. C.5: (a) shows historical (1976-2005) daily mean take-off factor. (b) and (c) show change in the daily mean take-off factor in mid-century (2021-2050) and late century (2071-2100), relative to historical period. [11]

Most of the studies published focus on North America and Asia it seems that few work has been focused on European regions, with the exception of Greece by [7]. In [3], an analysis is made of rising temperatures over the Euro-Mediterranean region with a focus on major European airports. They analyse the magnitude and trends of the daily maximum near-surface temperature extremes in summer. They compare historical period 1961–2014 to observation and reanalysis and future changes by 2021–2050 and 2071–2100, with respect to 1961–2005. By comparing regional and Global Climate models, they conclude that mean projected changes under the RCP8.5 scenario range between +1.7 and +3.2°C by the near term (2021–2050), and between +4.9 and +8.5°C by the long term (2071–2100), across the airports and the RCM and GCM ensembles. These results highlight that the Euro-Mediterranean region is largely impacted by temperature rise and implies that European airports might be highly impacted.

*'To find the effect of altitude and temperature, **connect** the temperature and airport altitude by a straight line. **Read** the increase in takeoff distance and the decrease in rate of climb from standard sea level values.' [12]*

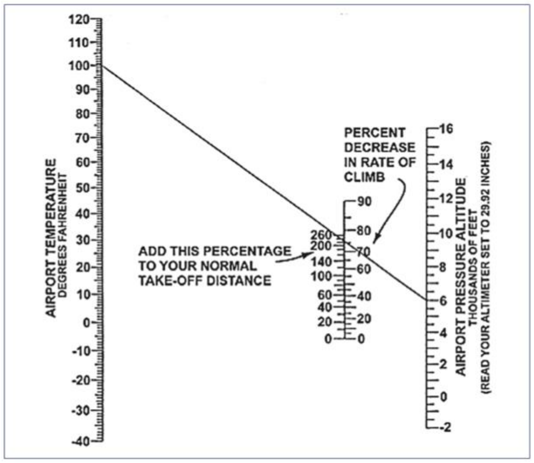

(a) Koch Chart from [12]: typical representative values for "personal" airplanes, it may be conservative for airplanes with supercharged engines and not take into account long grass, sand, mud, or deep snow that can elongate takeoff distance.

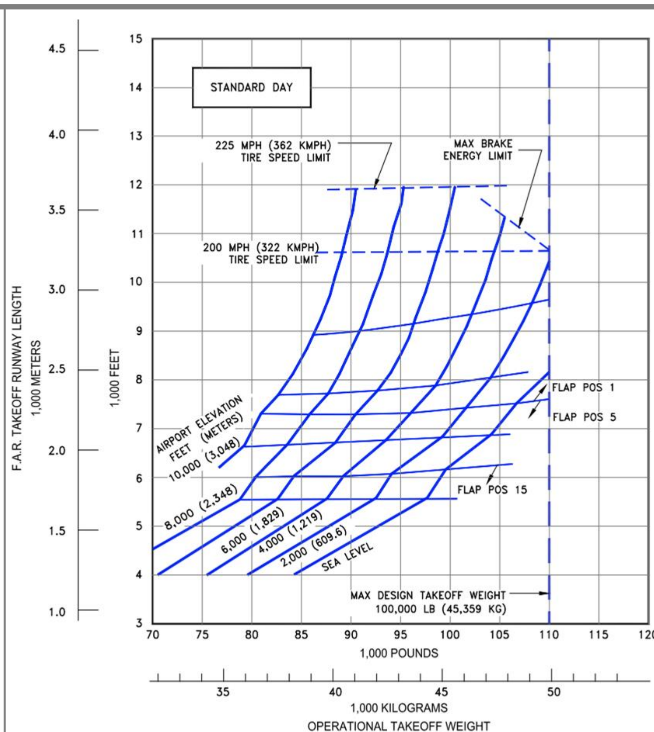

(b) Performance chart for a standard day for Boeing 737-100 (JT8D-7 Engines) [10]. They don't take into account engine airbleed for air conditioning, wind or runway gradient.

Fig. C.6: Examples of tools for performance computation at take-off, these are for information use only and real performance charts are provided in specific aircraft manuals.

C.5 Discussion and conclusion

C.5.1 Methods used

This last section presented a state of the art of studies on the impact of climate change on take-off performance of large aeroplanes. All these studies use different methodologies.

For prediction of atmospheric variables, ensemble multi-model approaches give the most robust results, as seen in [8, 9, 11, 3]. Many of these models have biases and it is preferable to conduct a bias correction based on a comparison with past observations and/or reanalysis when looking at future variables at specific coordinates. All these studies focus on changes in atmospheric temperature as their input for aircraft take-off performance computation and they all seem to agree that outside air temperature is one of the atmospheric variables with the most impact on take-off performance in a context of climate change.

In previously cited studies, the influence of pressure altitude [11] and wind pattern and intensity [7] is also analysed as having an impact on performance.

For computing take-off performance, different methods exist. Computing TOD according to atmospheric variable and limitations imposed by airport or environment requires information on how the aircraft responds in term of performance. Most of the studies cited here use publicly available performance charts like in figure C.6.b provided by the aircraft manufacturer to assess TOD depending on TOW and atmospheric conditions [8, 9,11]. These are given for information purpose and do not take into account many factors; specific performance charts are usually found in aircraft manuals which are not public. Access to protected performance data belonging to manufacturers or operators is difficult so many academic studies rely on publicly available data. Similarly, the Koch chart shown in figure C.6.a gives a correction on TOD and the climb gradient compared to conditions of standard atmosphere at sea level. These methods, apart from not taking into account many factors, don't allow for flexibility in the choice of input variables to consider. Variables linked to the aircraft itself could then be added as inputs and their influence could be evaluated. In [7], Gratton et al. use an in-house performance model for their studied aircrafts. This allows them not only to choose the hypotheses on which the model rely but also to include other variables like headwind intensity as an input variable.

Most of these studies focus on large commercial aircrafts, mostly A320 and B737, the main reason for this choice was to make the study's scope as wide as possible so choosing aircrafts that are largely used around the world, in many airports under a large range of atmospheric conditions. In most of the studies cited, most airports are in North America and Asia. This highlights the need for studies focusing on larger aircrafts that seem more impacted by loos of performance due to high temperatures and more data around the European and African regions.

Lastly, one should consider that in many of these studies, the MTOW and TOD are computed according to regulations for cases of take-off at maximum engine thrust. During actual operations, large aeroplanes do not usually take off at the MTOW, among other to keep additional safety margins. The operational take-off weight is usually lighter than MTOW and will depend on the mission which allows room for taking off at derated thrusts to preserve the engine and save on fuel. These practices are internal to airlines. The studies mentioned focus on the MTOW allowed by performance and on the TOD at a given take-off weight and analysing if they tend to change with time in a context of climate change.

C.5.2 Main takeaways of results

Even though the diversity in methodology and cases studied makes it hard to compare results, here are the main takeaways:

- The review has shown that according to the cited studies, the intensity and duration of heatwaves linked to climate change have a degrading impact on take-off performance of large aeroplanes.

The overall trends of rising temperatures in past and future periods are translatable in trends of lower performance for aircrafts.

- For past trends, [7] shows that in Greece, in the last decades, the average MTOW reduction rate across ten airports studied is of 132 kg/year for an A320 which corresponds to the weight of 2 passengers.
- For future trends, projections show an increase in restrictions between reference historical periods and an even sharper increase between mid-century and end of century periods which depend on aircrafts, airports and projected socio-economic scenario for the future. Of course, for aircraft technologies currently in use, mid-century projections are more relevant because given the usual economical life cycle of large aeroplanes (25 to 30 years), those manufactured today or in the coming years will still be in operation until the middle of the century. In addition, airport runways are typically designed to be operated for 50 years or longer. Projections for the end of century are given for information purposes as it is not known what kind of aircraft will be in use in the second half of the 21st century. Constant improvements in efficiency and objectives of energetic transition of the aviation sector makes it that future propulsion technologies might be very different.
- Studies show that airports most impacted are airports where daily temperatures are high with restrictive conditions like high altitude and short runways being additionally limiting factors. The severity of impact depends on the temperature increase of course but also on the type and weight of aircraft, the dimension of the runway considered and the altitude of the airport. It is also interesting to remark that these studies focus on trends with results based on a maximum daily temperature for example. This means that the computed impact is applicable for the hottest timestep of the day. This does not give indication on the duration of the period of critical temperature for performance, which would be helpful to assess how much daily operation organisation could be impacted.
- It is important to differentiate cases where the margin for degraded performance is high or not. For instance, in [7] at Corfu airport where the runway considered measures 2373 m, the TOD computed for an A320 aircraft rises from the reference historical TOD of 1789 m to 1956 m at the end of the period considered (+167 m or 2.8%). Even though we see a decrease in performance, the runway remains long enough for an A320 to take-off with considerably degraded performance. In that case, no restriction has to be imposed.
- It is important to note in these cases however that even though no restriction must be imposed, the TOD “safety margin” (ie. the remaining distance to the end of the runway when the aircraft reaches a height of 35 ft according to TOD computation) is reduced with degraded performance. The safety impact of this reduction might need to be investigated. All these studies compute theoretical values of TOD for certified cases assuming that during operations, everything is done according to the manufacturer’ recommendations. In reality, many operational factors can increase the actual TOD. For instance, if the pitch angle during rotation is too low, the actual TOD might significantly increase. The pitch angle effect added to high temperature effect might increase TOD to the point where safety margins are significantly reduced.

C.6 References

[1]	IPCC, 2021: Climate Change 2021: The Physical Science Basis. Contribution of Working Group I to the Sixth Assessment Report of the Intergovernmental Panel on Climate Change[Masson-Delmotte, V., P. Zhai, A. Pirani, S.L. Connors, C. Péan, S. Berger, N. Caud, Y. Chen, L. Goldfarb, M.I. Gomis, M. Huang, K. Leitzell, E. Lonnoy, J.B.R. Matthews, T.K. Maycock, T. Waterfield, O. Yelekçi, R. Yu, and B. Zhou (eds.)]. Cambridge University Press, Cambridge, United Kingdom and New York, NY, USA, In press, doi:10.1017/9781009157896.
[2]	IPCC, 2014: Climate Change 2014: Synthesis Report. Contribution of Working Groups I, II and III to the Fifth Assessment Report of the Intergovernmental Panel on Climate Change [Core Writing Team, R.K. Pachauri and L.A. Meyer (eds.)]. IPCC, Geneva, Switzerland, 151 pp.
[3]	Gallardo, V., Sánchez-Gómez, E., Riber, E. et al. Evolution of high-temperature extremes over the main Euro-Mediterranean airports. Clim Dyn 61, 1717–1740 (2023). https://doi.org/10.1007/s00382-022-06652-z.
[4]	Eyring, V., Bony, S., Meehl, G. A., Senior, C. A., Stevens, B., Stouffer, R. J., and Taylor, K. E.: Overview of the Coupled Model Intercomparison Project Phase 6 (CMIP6) experimental design and organization, Geosci. Model Dev., 9, 1937–1958 (2016), https://doi.org/10.5194/gmd-9-1937-2016.
[5]	Burbidge, R. (2018). Adapting aviation to a changing climate: Key priorities for action. Journal of Air Transport Management, 71, 167-174.
[6]	Easy Access Rules for Large Aeroplanes (CS- 25), EASA eRules, (2023), [Available online at https://www.easa.europa.eu/en/document-library/easy-access-rules/easy-access-rules-large-aeroplanes-cs-25]
[7]	Gratton, G., Padhra, A., Rapsomanikis, S. et al. The impacts of climate change on Greek airports. Climatic Change 160, 219–231 (2020). https://doi.org/10.1007/s10584-019-02634-z.
[8]	E. Coffel and R. Horton. Climate Change and the Impact of Extreme Temperatures on Aviation, Weather, Climate, and Society, 7(1):94-102 (2015). doi:10.1175/WCAS-D-14-00026.1.
[9]	Coffel, E.D., Thompson, T.R. & Horton, R.M. The impacts of rising temperatures on aircraft takeoff performance. Climatic Change 144, 381–388 (2017). https://doi.org/10.1007/s10584-017-2018-9.
[10]	Boeing, 2013: 737 airplane characteristics for airport planning. 737/BBJ Doc. D6-58325-6, 682 pp. [Available online at www.boeing.com/ boeing/commercial/airports/737.page.]
[11]	Zhou, Y., Zhang, N., Li, C. et al. Decreased takeoff performance of aircraft due to climate change. Climatic Change 151, 463–472 (2018). https://doi.org/10.1007/s10584-018-2335-7
[12]	Team FAAS. Density altitude. Federal Aviation Administration Pilot Education Pamphlet Federal Aviation Administration (2008).
[13]	The WCRP Coupled Model Intercomparison Project – Phase 5 (CMIP5) – CLIVAR Exchanges Special Issue, No. 56, Vol 16, 32pp, 2011.

D Appendix – Task Force #2: Sand and Dust

Note: *The main author of this appendix is Filippos Tymvios.*

D.1 Origin of atmospheric dust

D.1.1 Creation and transportation of dust (dust cycle)

The existence of dust in the atmosphere is caused by a combination of natural and human factors, including wind erosion of dry soils, desertification, land use changes and climate variability. The dust cycle in the atmosphere involves the movement of dust particles through various processes such as emission, transport, deposition, and re-suspension (Marticorena, B. and Bergametti, G., 1995).

1. Emission: Dust particles are emitted into the atmosphere through a process known as dust emission or dust entrainment. Natural sources of dust emission include wind erosion of dry soils, sand dunes, and exposed sediments in deserts and arid regions. Anthropogenic sources include activities like mining, construction, and agriculture. These processes release fine dust particles into the air. Once strong winds emit dust particles, fine dust particles are carried by turbulent diffusion and convection to higher tropospheric levels (up to a few kilometres in height) and then large-scale winds can transport them over long distances (Prospero, 1996; Goudie and Middleton, 2006). Dust particles in the atmosphere scatter and absorb solar radiation and, acting as cloud condensation nuclei/ice nuclei, modify clouds and their radiative and precipitation processes.

2. Transport: Once in the atmosphere, dust particles can be transported over long distances by wind currents. The transport of dust is influenced by meteorological factors such as wind speed, direction, and atmospheric stability. Large-scale weather systems like high-pressure systems, trade winds, and monsoons play a significant role in transporting dust across continents and even oceans. The duration and distance of transport depend on the size, density, and shape of the dust particles.

3. Deposition: Dust particles eventually settle out of the atmosphere through a process called deposition. Deposition can occur through dry deposition or wet deposition. Dry deposition happens when dust particles settle directly onto surfaces, such as land, vegetation, buildings, and bodies of water. Wet deposition occurs when dust particles are scavenged by precipitation (rain or snow) and settle out with the falling water droplets or snowflakes. The deposition of dust is influenced by factors such as particle size, density, Dust deposition is affected by factors such as particle size, density, and the presence of other elements that change the physical and chemical properties of the dust and that may affect its ability to settle.

Another factor to be considered is the re-suspension of the particles: After deposition, dust particles can be re-suspended back into the atmosphere. This can happen through processes such as wind erosion, vehicular traffic, and human activities. Resuspension is more common for fine particles and can contribute to the re-circulation of dust within a region or its long-range transport.

The dust cycle processes, their components, controlling factors and impacts on radiation and clouds is illustrated in Figure D.1 (Shao, 2008).

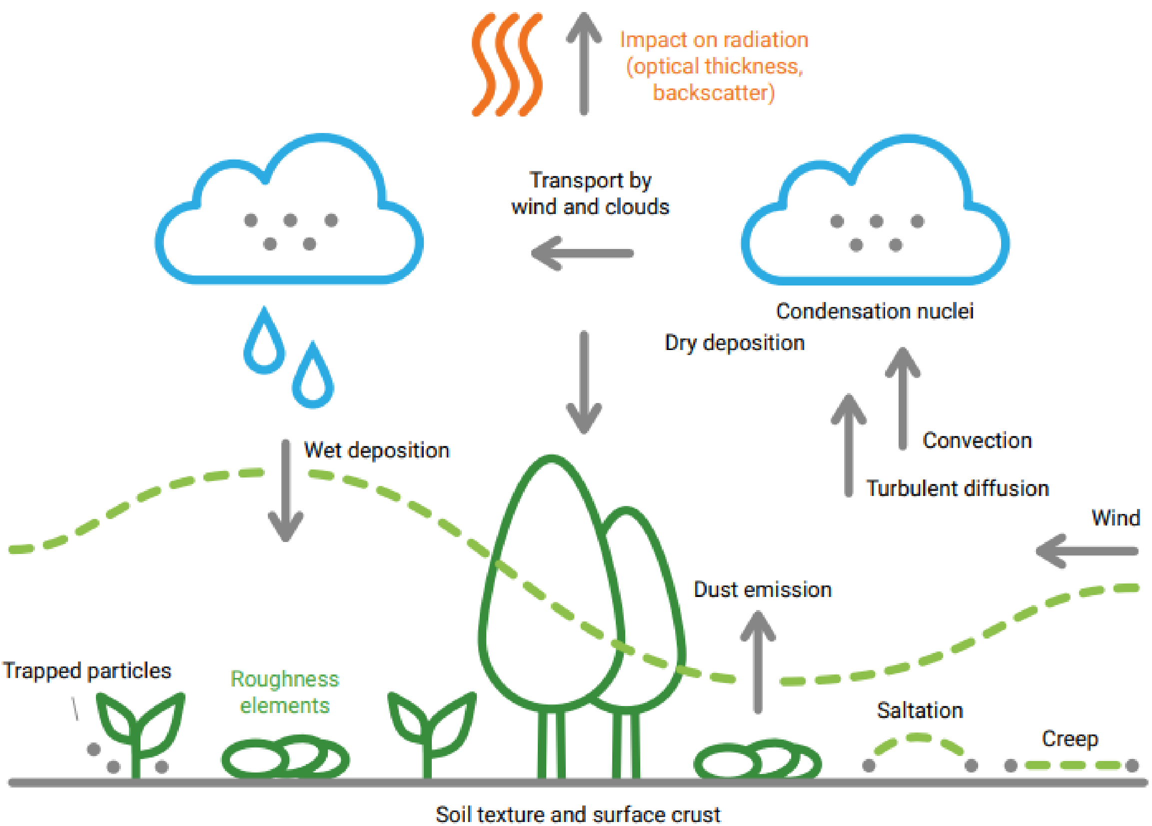

Figure D.1. The dust cycle processes, their components, controlling factors and impacts on radiation and clouds (Shao, 2008)

D.1.2 Composition of particles within a dust/sand storm event

The composition of dust in dust storms can be complex and diverse, and it can vary significantly from one storm to another and from one region to another (Wang, 2015). The specific composition will depend on factors such as the local geography, weather conditions, and human activities in the area (WMO; Copernicus 2022).

Common components found in dust/sand storms are:

- Mineral Dust

  Mineral Dust: Most of the dust in dust/sand storms is composed of mineral particles derived from the Earth's surface. These particles can include sand, silt, clay, and other small rock fragments. The specific composition depends on the region and the geological formations present.

- Silica

  Silica is a common component of dust/sand storms, especially in arid and desert regions. It is a mineral compound composed of silicon and oxygen, often found in the form of quartz. Silica dust can pose health risks if inhaled in large quantities.

- Organic Matter

  Dust/sand storms may contain organic matter, including pollen, plant debris, and other biological particles. These can come from nearby vegetation, agricultural activities, or other sources.

- Anthropogenic Particles

  In some cases, dust storms can carry anthropogenic (human-made) particles such as pollutants, industrial emissions, and combustion by-products. These particles can contribute to air pollution and have potential health impacts.

- Microorganisms

Dust storms can also transport microorganisms such as bacteria, fungi, viruses, and their spores. These microorganisms can be found in soil and can become airborne during dust storm events.

D.1.3 Source areas of atmospheric dust

1. The Sahara and Sahel regions in Africa, where frequent dust storms and desertification have significant impacts on public health, agriculture, and ecosystems.

2. The Arabian Peninsula, including Saudi Arabia, Kuwait, and Iraq, where sandstorms and dust storms are common during the spring and summer months.

3. Central Asia, including China, Mongolia, and Kazakhstan, where dust storms are becoming more frequent due to desertification, land-use changes, and climate change.

4. The southwestern United States and northern Mexico, where dust storms, including the historic 1930s Dust Bowl, have caused significant environmental and social impacts.

5. Australia, where severe dust storms occur in the arid and semi-arid regions of the country, including the eastern states, Western Australia, and the Northern Territory.

6. South Asia, including India and Pakistan, where dust storms and sandstorms are becoming more frequent due to deforestation, land-use changes, and climate change.

7. The Middle East and North Africa (MENA) region, where dust storms and sandstorms have significant impacts on public health, transportation, and infrastructure.

8. The South African desert known as the Kalahari Desert. It occupies almost all of Botswana, the eastern third of Namibia, and the northernmost part of Northern Cape province in South Africa.

9. The Atacama Desert, which is located in the northern part of Chile and extends into southern Peru. The Atacama Desert is considered to be one of the driest deserts in the world, with some areas receiving less than 1 millimetre of rainfall per year.

All the areas above are illustrated at Figure D.2. The main transportation mechanisms of dust are illustrated in Figure D.3 (Garrison et al., 2003).

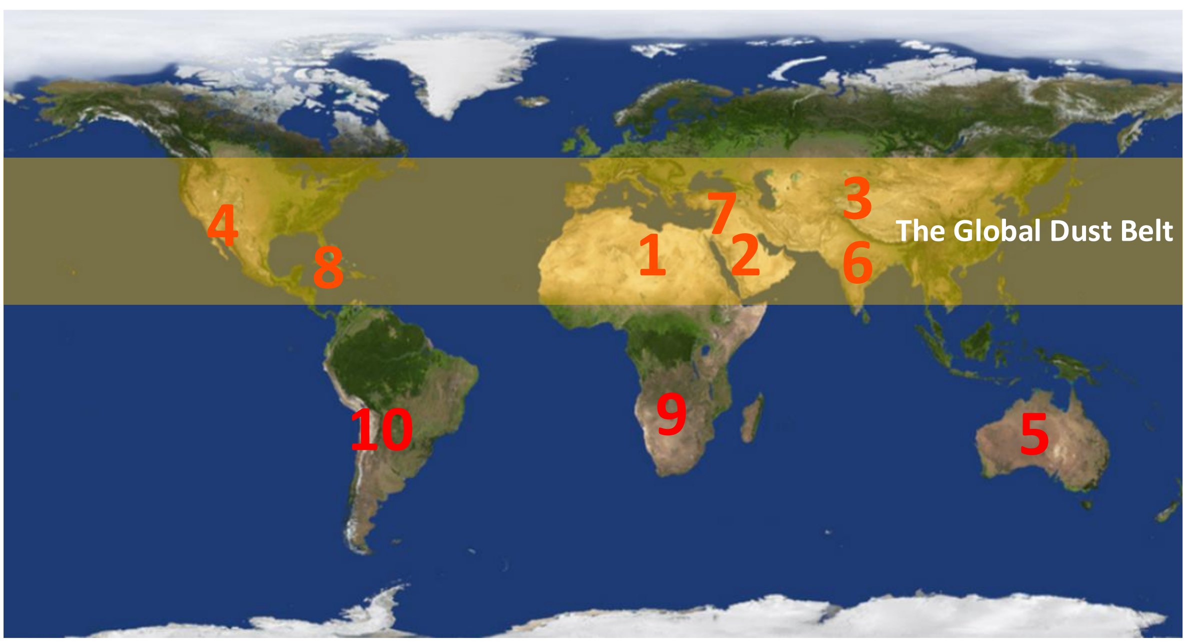

Figure D.2. Sources areas of atmospheric dust / sand and the Global Dust Belt.

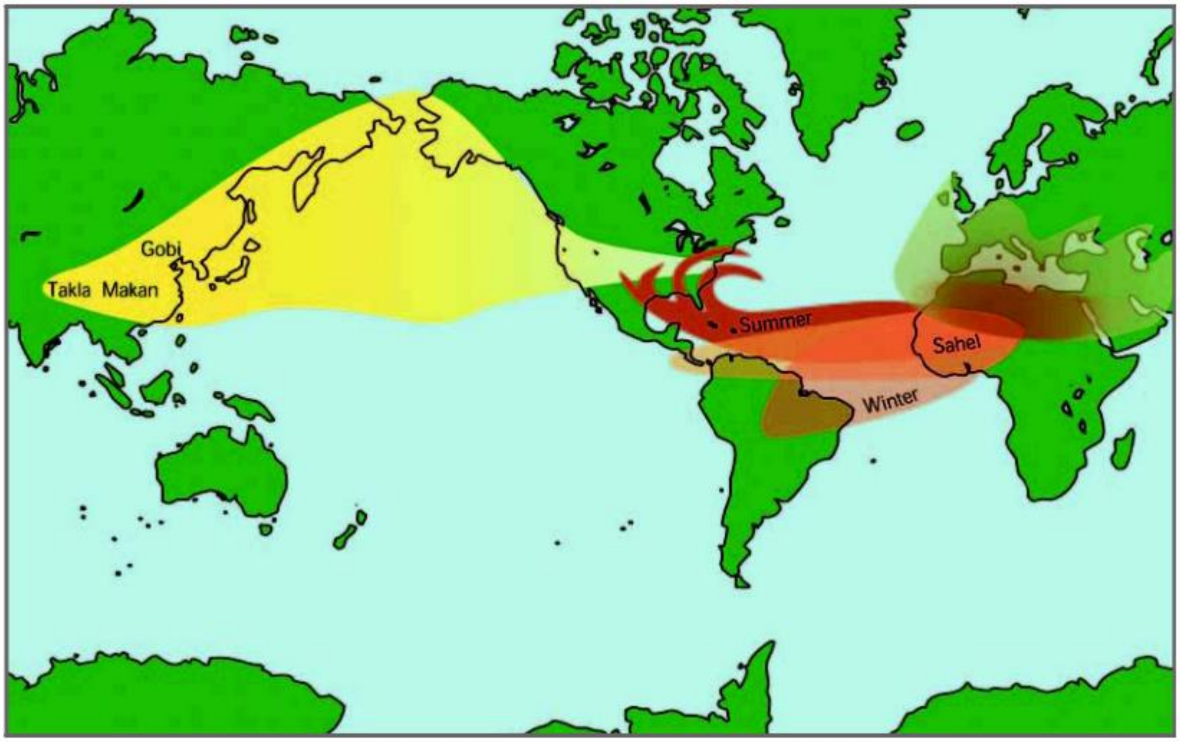

Figure D.3. Dust is transported in two major global dust transport systems: (1) from the Sahara and Sahel of Africa to the Americas, Europe, and Near East; and (2) from the Takla Makan and Gobi deserts of China, across China, Korea, Japan, and the northern Pacific to North America, sometimes exiting over the Atlantic Ocean. From V. Garrison et al., 2003, Illustration: Betsy Boynton.

D.2 Sand and dust storm events and dust in the upper troposphere

D.2.1 What are dust storms and sand storms?

Severe dust and sand storm events are extreme weather events that are characterized by strong winds on surface and usually aloft that transport large amounts of dust and sand along large distance from the source. These severe weather events often result in reduced visibility, air quality degradation, and health hazards. Sand storms and dust storms represent different types of weather systems, and they are reported accordingly to the synoptic weather observations by meteorologists. Dust storms are formally defined by the World Meteorological Organization (WMO) as the result of surface winds raising large quantities of dust into the air and reducing visibility at eye level (1.8 m) to less than 1 000 m (Mc Tainsh and Pitblado, 1987). There is no formal definition for sand storms. The difference between sandstorms and dust storms is down to the size of the particles carried and the distance the storms travel. Sand particles are larger than dust particles, are not transported far from the source and fall out of the air faster whilst particles in a dust storm are smaller in size and can be transported higher and further. In essence, sandstorms are more local phenomena than dust storms which affect far more areas, and this is the reason why the term "dust storm events" has prevailed in the everyday language.

A severe dust storm event that affected the eastern Mediterranean on 2/5/2022 associated with an easterly surface flow is illustrated in Figure D.4.

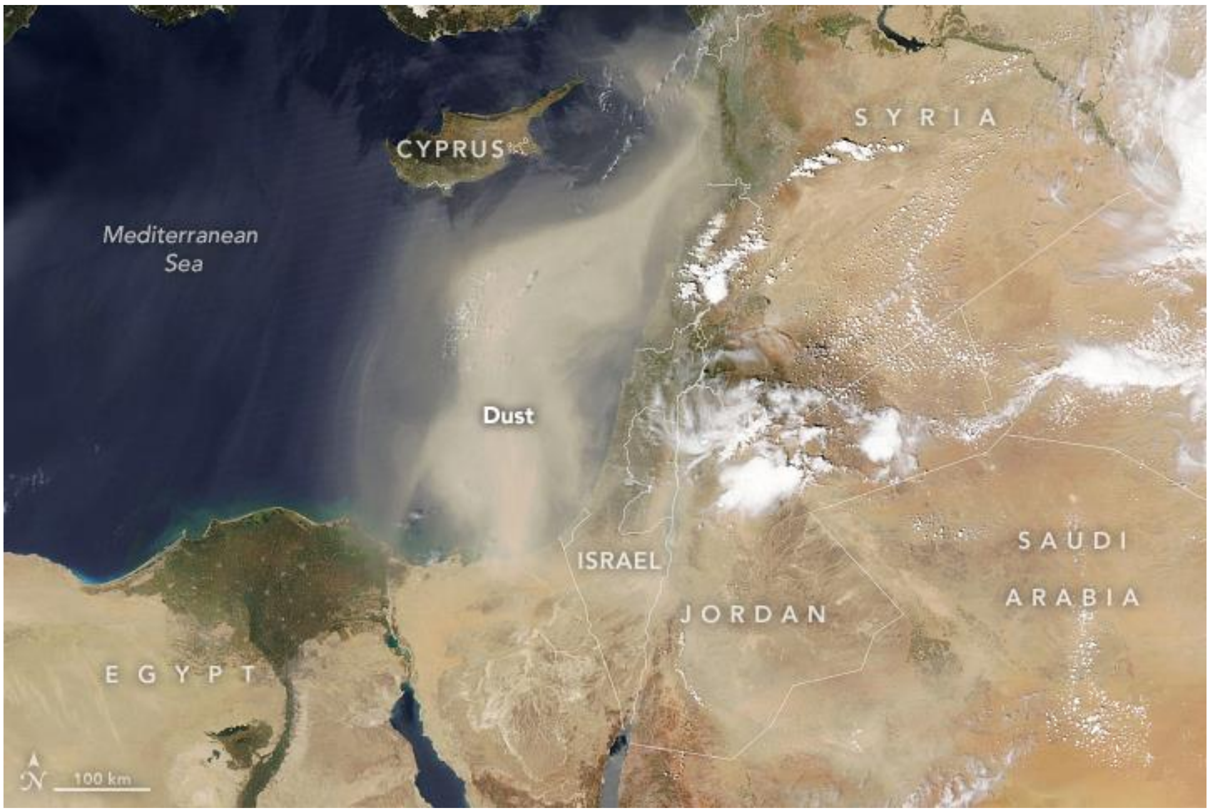

Figure D.4. A dust storm over the Eastern Mediterranean was accompanied by thunderstorms that also brought hail and flash floods. Image of the day for May 2, 2022, from Earth Observatory (NASA), Satellite Aqua; MODIS instrument.

D.2.2 Areas affected by severe dust storm events

Severe dust events can occur in many regions of the world. It is not a local phenomenon: due to the large-scale atmospheric circulation patterns involved, severe dust events may affect areas hundreds of kilometres away from the dust source. Some areas are more prone to such events than others due to their geographical and special climate characteristics (Tegenm I. and Fung, I., 1995; Prospero et al., 2002; Washington et al., 2004). The latitude zone within most events occur is often referred as the Global Dust Belt (GDB). The GDB is located primarily in the subtropical and tropical regions of the Earth, including parts of North Africa, the Middle East, South Asia and the Southwest part of USA (Prospero et al., 2002). Severe dust episodes occur in the opposite geographical zone of the southern hemisphere but these are characterized by phenomena of lesser intensity due to the smaller desert coverage, as Australia, South Africa and Chile. Large-scale weather patterns, such as the African Easterly Jet[12], the Hadley Cell[13], and the El Niño Southern Oscillation[14], can also influence the distribution and intensity of atmospheric dust. A strong relationship between interannual variations in North Atlantic tropical cyclone activity and atmospheric dust load has been evidenced although a direct causal relationship has yet to be proposed (Evan et al., 2006).

D.2.3 Dust in the upper troposphere

Dispersal of dust to areas other than source, occurs by its transport in the upper atmosphere which depends on atmospheric circulation patterns. In analogy with the surface global dust belt, the Upper-Troposphere Dust Belt is defined (UTDB) (Young et al., 2022). From satellite lidar and radar observations, dust layers detached from dust sources were identified, revealing a noticeable high dust concentration region (Luo et al., 2015; Young et al., 2022). The UTDB over the northern hemisphere has seasonally varying base height of 3.65 ± 2.84 km and top height of 8.35 ± 1.50 km above mean sea level[15] and its column loading is strongest during spring (March-April-May). The out-of-phase annual cycles of mid-level dust concentration and westerly wind over source regions control the seasonal upper-tropospheric dust loading variations. African deserts contribute the most (46.3%) to the UTDB in spring and the synoptic trough[16] is the leading (49%) dust lifting mechanism.

[12] The African Easterly Jet (AEJ) is a prominent atmospheric feature that occurs during the boreal summer (June to September) over the African continent. It is a narrow band of strong winds located in the lower troposphere, typically between 5 and 7 kilometres (3 to 4 miles) above the surface.

[13] The Hadley cell is a large-scale atmospheric circulation pattern that forms due to uneven solar heating. It involves rising air near the equator, descending air near 30 degrees latitude, and the creation of trade winds and climate zones.

[14] El Niño Southern Oscillation (ENSO) is a climate phenomenon characterized by periodic warming (El Niño) and cooling (La Niña) of the tropical Pacific Ocean, influencing global weather patterns and impacting oceanic and atmospheric circulations.

[15] In aviation terms, the zone base varies between FL025 and FL200 and the zone top varies between FL220 and FL320

[16] Atmospheric trough is a region within the upper troposphere where the air pressure is lower than the surrounding areas. It is like a valley in the air, where the air sinks and becomes denser. The air ahead of a trough is usually unstable, meaning it can rise and cool quickly, forming clouds and precipitation therefore a trough is considered a lifting mechanism for the atmosphere.

D.3 Dust and sand hazards for aviation

D.3.1 Aviation meteorology information on dust and sand

According to WMO, dust or sand events are observed and reported into the SYNOP code according to the Table D.1:

Table D.1. WMO weather codes for sand / dust

Code	Symbol	Weather
6		Wide spread dust in suspension in the air, not raised by the wind by the time of observation
7		Dust or sand raised by wind, at time of observation
8		Well-developed dust devil(s) within the past hour
9		Duststorm or sandstorm within sight of station or at station during past hour
30		Slight or moderate dust storm or sandstorm, has decreased during past hour
31		Slight or moderate dust storm or sandstorm, no appreciable change during past hour
32		Slight or moderate dust storm or sandstorm, has increased during past hour
33		Severe dust storm or sandstorm, has decreased during past hour
34		Severe dust storm or sandstorm, no appreciable change during past hour
35		Severe dust storm or sandstorm, has increased during past hour

To ensure flight safety, all aviation meteorological observation offices monitor sand and dust weather events. Sand and dust weather can be classified into four levels, namely ‘dust or sand’, ‘blowing dust or sand’, 'dust storm or sandstorm', ‘heavy dust storm or sandstorm’. In METAR, when the visibility is reduced to 5000m and below due to sand or dust event, the weather DU or SA (Dust or Sand) is reported.

In case of heavy dust storms or sandstorms, meteorological watch offices will issue Significant Weather Information (SIGMETs) and associated meteorological offices will issue aerodrome warnings to ensure flight safety.

D.3.2 Safety risks associated with dust and sand

Severe dust events caused by sand lifted from the surface of the deserts or any other mechanism such as dust devils (Lorenz R & Myers M., 2005) or downdrafts (Chen W. & Fryrear D., 2002) that are transported with the atmospheric circulation patterns within the troposphere (Monteiro et al., 2022), can pose a significant risk to airport operations (Strong sand and dust storms can cause disturbances in airport operations (Al-Hemoud et al., 2017; Al-Kheder and Al-Kandari, 2020; Cuevas et al.,2021), as well as mechanical problems including erosion, corrosion, dust melting in turbines, pitot-static tube blockage or engine flame out in flight (Clarkson and Simpson, 2017) and damages to the external surface of the aircraft (Lekas et al., 2011; Nickovic et al., 2021).

A comparison of the visibility at Nikos Kazantzakis airport (Crete, Greece) from meteorological visibility reports (METAR[17]) with simultaneous AOD[18] measurements from the Finocalia air quality station is presented in Figure 5.

[17] METAR: METeorological Aerodrome Reports

[18] AOD: Atmospheric Optical Depth is a measure of how much light is absorbed or scattered by the atmosphere. It is a dimensionless quantity that is calculated by dividing the intensity of light reaching the Earth's surface by the intensity of light at the top of the atmosphere. AOD is affected by a number of factors, including the amount of aerosols, water vapor, and ozone in the atmosphere.

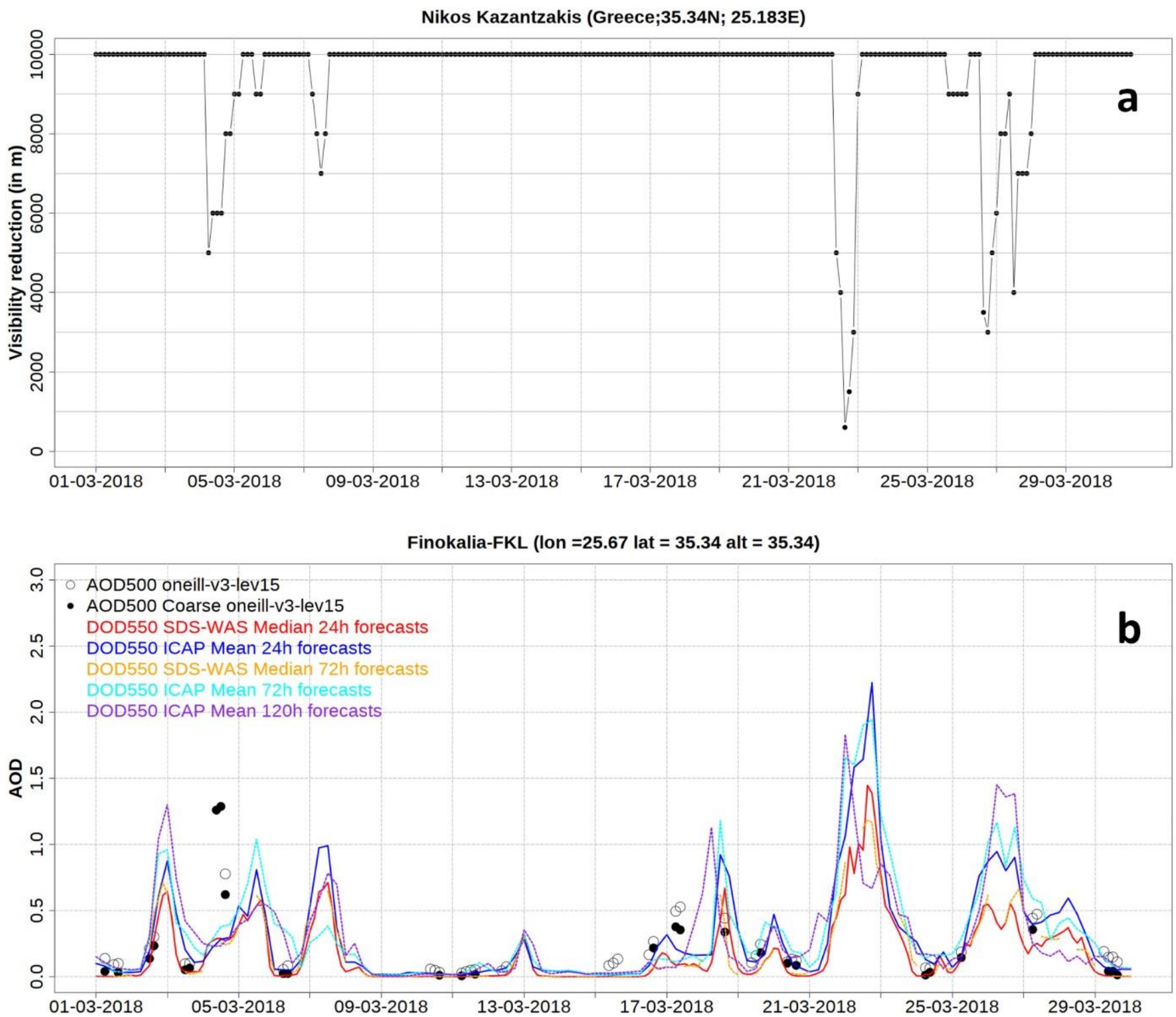

Figure D.5. Visibility (a) and aerosol column load and dust column load (namely Aerosol Optical depth and dust optical depth) b) time series over selected locations in Crete for March 2018. (a) Hourly visibility over the Heraklion airport's (also known as Nikos Kazantzakis airport. (b) 3-hourly dust-AOD over Finokalia air quality station. AOD observations from NASA-AERONET site are circles in black and solid lines show dust-AOD forecast from the SDS-WAS and ICAP ensemble forecasts for 24 (red and blue, respectively), 72 (orange and cyan, respectively) and 120-h forecasts (purple). From Monteiro et al., 2022.

D.3.2.1 Examples of problems attributed to dust storm events

- Dust can have a significant impact on the operation of aircraft engines by reducing their performance and increasing the risk of engine failure (Bravo et al., 2017; Bojdo et al., 2020). When dust enters the engine, it can cause abrasion and erosion of engine components, including the compressor blades and turbine vanes, which can lead to reduced engine efficiency and power output. In addition to the mechanical effects of dust, the presence of dust in the engine can also cause combustion instability, leading to increased emissions of pollutants and reduced engine performance. The ingestion of dust can also cause damage to the engine's air filters and other components, which can result in reduced airflow and increased engine wear.

- Dust can affect airplane windshields in several ways (Jensen R. & Roberts, J. 2010). First, airborne dust and other particulate matter can accumulate on the surface of the windshield, reducing visibility for pilots and potentially obscuring critical information such as runway markings, navigation aids, and other aircraft. This can create hazards for pilots during take-off, landing, and other phases of flight. Dust particles can also cause damage to the windshield by causing scratches and other abrasions on the surface. Over time, this can lead to reduced optical clarity and may require the replacement of the windshield.
- Reduced visibility can make it difficult for general aviation pilots operating in VFR to see the runway, other aircraft, and navigation aids, which can lead to conditions of distress, such as air collisions or accidents during take-off and landing (Baddock M. et al., 2014 & FAA, 2008). In exceptional weather conditions, a mixture of precipitation and dust particles may block the pilot's view completely during flight; the windscreen could be completely obstructed with dust, and the wipers would not be able to clean the deposit.
- Dust particles can interfere with the operation of sensitive electronic equipment, including navigational and communication systems compromising the safety of the flight (Zhang, 2007; FAA, 2020). This is because dust particles can accumulate on the surfaces of electronic equipment, causing electrical insulation breakdown, short circuits, and other problems. The presence of dust can also cause overheating in electronic equipment, as the dust particles can clog cooling fans and vents, or completely cover heat sinks reducing the efficiency of heat dissipation and consequently their ability to cool down critical parts of the aircraft. In addition to these complications, the existence of certain material in the dust composition can also affect electronic equipment by acting as a source of static electricity. This can result in electrostatic discharge (ESD), which can damage sensitive electronic components and circuits.
- Dust may also cause physical abrading and contamination of the surface of sensitive remote sensing equipment used for Meteorological Observations (laser and other optical instruments), resulting to scratches, wear, or damage to the protective coatings and optical elements, affecting the instrument's performance and data quality. This is enhanced in coastal airports where the dust mixed with water vapour will create larger aerosols with chemical properties able to interact with the sensitive surface of these instruments. Furthermore, the presence of sand particles on the instrument's surface can cause light scattering and attenuation. This can lead to reduced signal-to-noise ratio, decreased image contrast, and compromised data accuracy, particularly in remote sensing instruments that rely on optical measurements. Sand and particles deposited on the surfaces of sensors or optical elements can also interfere with calibration procedures. They can alter the instrument's response to incident radiation, leading to inaccurate measurements and calibration biases if not properly accounted for. The meteorological instruments affected are the HCB reader (height of the cloud base with a laser transmitter), RVR (runway visual range with an optical transmitter/receiver), forward scatter and parcivel distrometers (optical instruments for detection of the present weather in AUTO stations and led/laser transmitter respectively) and wind lidars (laser instruments necessary for the detection of wind shear).

D.3.2.2 Problems attributed to high background dust concentration

In addition to the problems being created by high concentrations of dust in the atmosphere due to severe dust events, there is another factor that causes problems in aviation but is not directly related to desert storms. In particular, airplanes that take off and land frequently at airports located in or near the Global Dust Belt, under normal background dust atmospheric conditions for the area, experience problems similar to those presented above for aggravated conditions; essentially, the long exposure to high background dust concentration levels creates cumulative problems. According to Zhou et al., Gomez et al., (2023) and WMO (2023), the average dust concentration is increasing steadily and will continue to increase in the future although great variations exist amongst different regions. Achakulwisut et al. (2019) and EPA (2022) argue and, for the United States the future air quality is projected to degrade by more abundant natural aerosols in a warmer environment.

D.3.2.3 Examples of severe dust storm events that affected aviation

The following are examples of recent severe dust storm events that have posed a risk to aviation and disrupted normal operations:

- The May 2022 event in the Middle East because of a Red Sea depression that usually brings hot air mass from the Arabian Peninsula, increasing atmospheric instability and triggers thunderstorms and dust storms. The storm drifted to the west and affected easter Mediterranean areas.
- The March 2021 dust event of northern China, characterized as the worst of the decade, caused by the combined effect of a dry cyclone in Mongolia and Siberian cold air mass was driven by the prevailing westerlies and reached all the way to South Korea. More than 50 flights to and from Beijing were cancelled.
- The April 2020 event of a massive Sahara dust plume that affected the Caribbean and Gulf Coast states in the US. The intensity of the storm earned for it the name ‘Godzilla’. It was the result of the transportation of dust from the African easterly jet towards the Mexican gulf, , the large scale atmospheric circulation of air of the Azores high pressure system of the north Atlantic that pushed the dust to Caribbean and the Caribbean low level jet that pushed the dust further, to reach the USA. The elevated concentration of dust particles in the atmosphere led to the closure or disruption of some airports, as reduced visibility and potential engine hazards posed risks to air travel.
- The June 2019 Saharan dust plume that swept across Europe and the Mediterranean, leading to flight cancellations and delays.
- The July 2018 dust storm in Phoenix, Arizona, which caused flight diversions and delays at Phoenix Sky Harbor International Airport.
- The July 2017 dust storm in Dubai, United Arab Emirates, which disrupted air traffic and caused several flight cancellations.

- The April 2016 dust storm in Riyadh, Saudi Arabia, which led to flight cancellations and diversions at King Khalid International Airport.
- In September 2015 one of the severest and unusual dust events on record occurred in the Eastern Mediterranean. Surprisingly, state-of-the-art dust transport models were unable to forecast the event that significantly reduced the visibility to all airports in the area.
- The June 2014 dust storm in Jeddah, Saudi Arabia, which caused flight cancellations and diversions at King Abdulaziz International Airport. It caused injuries, deaths, failures in power supply, and traffic disruption.
- The April 2013 dust storm in China's Xinjiang region, which affected flights at Urumqi Diwopu International Airport.
- The March 2012 dust storm in northern India, which disrupted air travel at several airports, including Indira Gandhi International Airport in Delhi.
- The July 2011 dust storm in Arizona, which caused flight cancellations and delays at Phoenix Sky Harbor International Airport.

D.4 Climate projections regarding dust storms and sand storms

D.4.1 General information

The IPCC's assessment report 6 (AR6) synthesis report on climate change, released in 2023 (IPCC 2023) advocates with high confidence that climate change is likely to increase the frequency and severity of extreme weather events and that with every increment of global warming, regional changes in mean climate and extremes become more widespread and pronounced. Future climate change is projected to increase the severity of impacts across natural and human systems and will increase regional differences.

It is important to note that climate projections are subject to uncertainty and depend on a variety of factors, including future greenhouse gas emissions, land use patterns, and regional climate variability (Harrighton et al., 2021). However, several publications indicate that the risks associated with dust storms are likely to increase in the coming decades, highlighting the importance of developing strategies to adapt to and mitigate the impacts of these events.

The complex interactions between climate factors and land surface conditions, and changes in precipitation patterns, temperature, and vegetation cover can affect wind erosion processes whilst deforestation and overgrazing can provide the conditions for uplifting of dust and can also increase the dust storm risks (Borreli et al., 2020). The emission of dust by human activities like intense conventional agriculture practices, deforestation, changes in land use (Stehfest et al., 2019) will be exacerbated by alterations in weather patterns bringing less rainfall and high temperatures that will dry out soil faster

(Cook et al., 2009). Extreme weather events, such as droughts, floods, and heatwaves can as well contribute to dust storms and severe dust episodes by drying out soils, reducing vegetation cover, and increasing wind erosion (Huang et al., 2016).

D.4.1.1 What do the climate projections regarding dust storms trends mean for aviation?

Predicting specific future climate conditions, including dust storms, in a particular region is challenging due to the complex and interconnected nature of the Earth's climate system. However, climate models and projections provide some insights into potential changes that could affect dust storms. It's important to note that these projections come with uncertainties, and regional variations on the uncertainties exist.

Climate projections suggest that dust episodes and aviation risks may increase in the future because of climate change. As global temperatures continue to rise, many regions are experiencing more frequent and intense droughts, making the soil more susceptible to wind erosion providing extended areas of dust and sand sources to be uplifted in the atmosphere. In Lu et al., 2019, the authors in their research about projections of agriculture drought, illustrate that under the four projection scenarios RCP2.6, RCP4.5, RCP6.0 and RCP8.5, the surface soil moisture is reduced compared to the reference period except for central Africa, central Asia and Alaska (Figure 6). The difference is amplified by the scenarios resulting in a larger increase of the Earth mean air surface temperature.

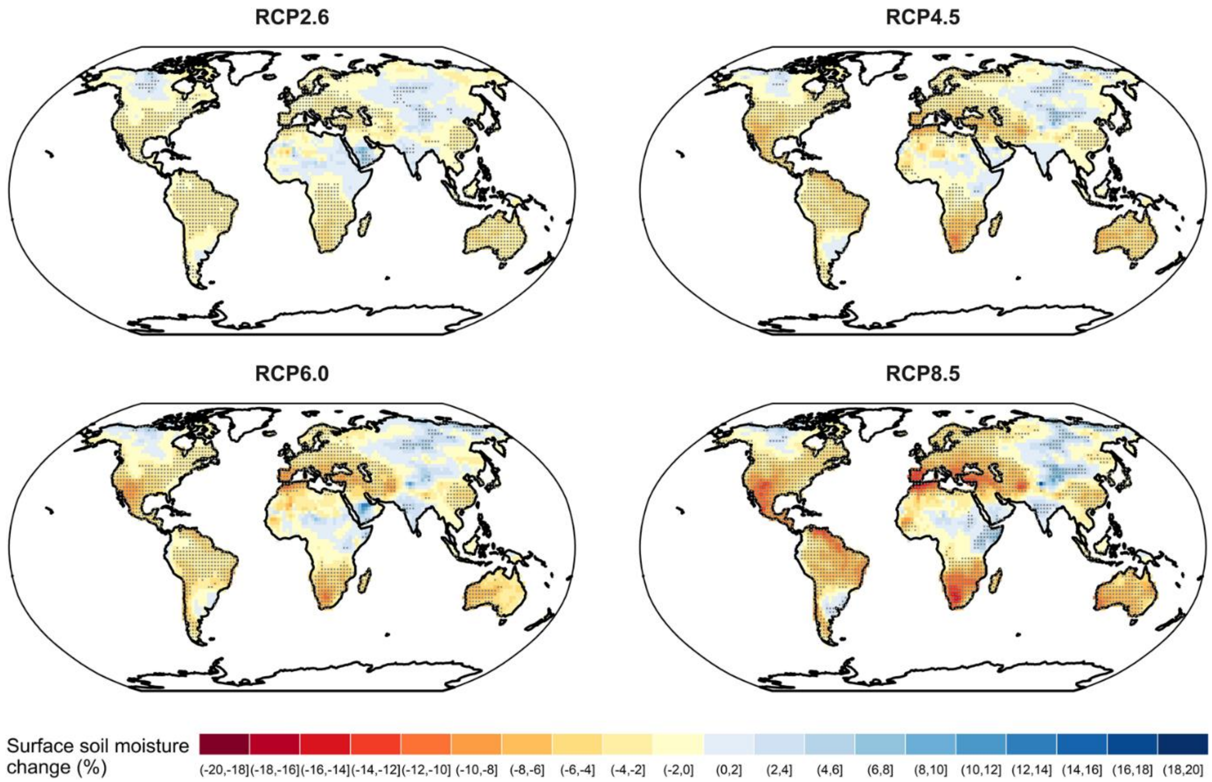

Figure D.6. Global multi-model mean percentage change in annual mean surface soil moisture for the period of 2071–2100 (RCP forcing) relative to 1976–2005 (historical forcing) based on CMIP5 multi-model ensembles (MMEs) under four scenarios: RCP2.6, RCP4.5, RCP6.0, and RCP8.5. The grids with stippling indicate statistical significance using the non-parametric Wilcoxon signed-rank test by controlling the false discovery rate (FDR) at a significance level of 0.05, i.e., there is a strong evidence that the distribution of annual mean surface soil moisture from different GCMs for period of 2071–2100 and the period of 1976–2005 is not the same for those grid cells. The results are based on all available models for each RCP scenario and the corresponding models in the historical forcing. The impacts of dust episodes on aviation are likely to be significant; reduced visibility and instrument malfunction can make it difficult for pilots to navigate safely during take-off, landing, and even during flight, potentially leading to accidents and disruptions in air travel. From Lu et al., 2019

The authors have also identified seasonality in their results; the changing signal is more pronounced in winter and summer than annually because of compensating effects during the whole year. Figure 7 illustrates the signal-to-noise ratio of the surface soil moisture anomalies to measure how large the expected change of drought is compared to the uncertainty in the projections of drought, according to Annual, Winter (NDJ) and Summer (JJA) conditions for the next 30, 60 and 90 years.

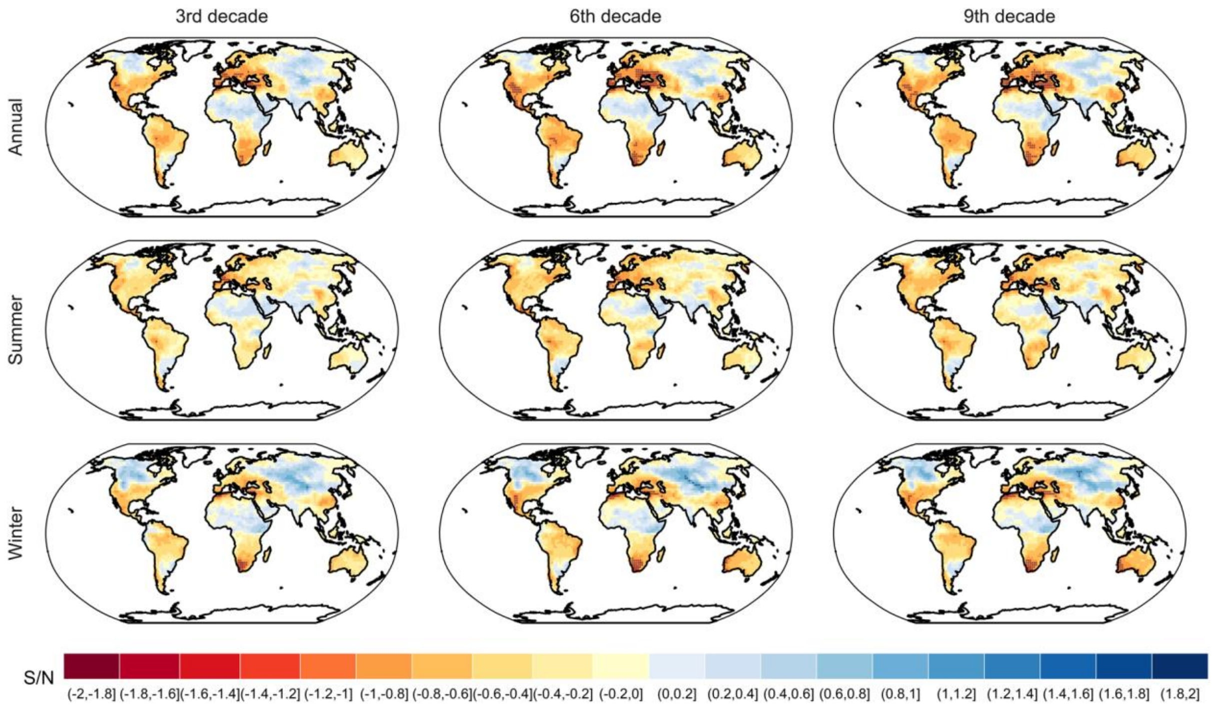

Figure D.7. The annual and seasonal signal to noise ratio of surface soil moisture anomalies for the 3rd decade, 6th decade, and 9th decade relative to mean of 1976–2005 based on CMIP5 MMEs (summer: JJA in North hemisphere and DJF in South hemisphere; winter: DJF in North hemisphere and JJA in South hemisphere). The negative values indicate drying and the positive values indicate wetting. From Lu et al., 2019

According to the following studies, climate change could increase the frequency and intensity of dust storms in regions such as the Middle East, North Africa, Southwest United States, East and South Asia and West Africa where dust episodes are already common. Changes are also likely to occur in Europe up to the Arctic circle. This could lead to more frequent disruptions in air travel, as airlines are forced to cancel or delay flights due to hazardous flying conditions.

- The Middle East and North Africa (MENA) region is known for its susceptibility to dust storms, and climate change projections indicate that the frequency and intensity of dust storms are likely to increase in this region. Studies have suggested that rising temperatures, changing precipitation patterns, and land degradation contribute to the exacerbation of dust storms in countries such as Saudi Arabia, Iran, Iraq, and Kuwait who act as a source for desert dust to the Middle East and Asia: (e.g., Middleton N., 2019; Zittis et al., 2019; Lelieveld et al. 2020; Zittis et al. 2021).
- Climate change models indicate that the southwestern, western and the great plains in the United States could experience more frequent and intense dust storms in the future. Drier conditions, increased temperatures, and potential changes in wind patterns are expected to contribute to dust storm events in this region (e.g., Mahowald et al., 2017; Tong et al., 2017).
- Studies suggest that Central and East Asian regions, may also face changes in the frequency and intensity of dust storms due to climate change. Factors such as land degradation, desertification,

and alterations in regional weather patterns can impact dust storm occurrence and severity in East Asian regions (e.g. Zong et al.,2021; Mao et al., 2021). However, research on the actual data evidenced that for central China, the frequency of occurrences of dust storms exhibits a decreasing trend since the mid of 18th century (Zhang et al., 2020). It is concluded by the authors that the observed anthropogenic global warming could have led to a decrease in atmospheric temperature gradients over the area and consequently a decline in wind speed and a decreasing dust storm frequency and intensity. Less and weaker dust storms are expected under a continuously anthropogenic warming scenario in this area.

- North Africa and the Sahel region is vulnerable to climate change-induced dust storms. Projections indicate that increased aridity, land degradation, and changes in rainfall patterns may contribute to more frequent dust storms in this region (e.g.; Evan et al., 2016; Biasutti et al., 2020). Other research identifies a zonal contrast in precipitation being developed at the end of the century with an increase in precipitation over the central Sahel and a decrease in precipitation over the western Sahel. Such a zonal contrast results from the antagonist effects of the fast (due to enhanced radiative warming over land, and over the North Hemisphere, relative to the South Hemisphere) and slow (associated with long-term changes in oceanic circulation) responses of precipitation to increasing greenhouse gases (Monerie et al., 2021).
- Although the occurrence of dust episodes in the Northern Europe and the Arctic circle is rare, the existence of intense dust episodes is evidenced by the existence of dust on glaciers. Varga et al., (2021) have studied 15 severe dust episodes between the years 2008 and 2020 and associated their existence with enhanced meridional[19] atmospheric flow patterns driven by unusual meandering jet streams. The future trends for dust episodes in the Northern Europe and the Artic circle have not been explicitly researched. However, the future increase of dust episodes is manifested by the likely increase in the conditions for uplift of dust in the Sahara Desert and the more frequent transportation mechanism for the dust, the amplified meridional jet. The importance of a more meandering polar jet and associated meridional flow patterns during the formation of the North African cyclone and poleward dust transport was discussed by Francis et al. (2018). According to the authors' findings, the intense warming of Arctic regions reduces the temperature difference between the high- and mid-/low-latitude areas, thus leading to increasing planetary wave[20] amplitudes and more meridional flow patterns at high altitudes (Francis et al., 2019). Moreover, the southward propagation of the upper-level atmospheric trough and the orographic blocking of the Atlas Mountains play vital roles in the formation of severe surface wind storms and dust entrainment in the northwest regions of the Sahara (Karam et al., 2010).

[19] Meridional flow is a type of atmospheric circulation pattern in which the north-south component of motion is unusually pronounced. The accompanying zonal component is usually weaker than normal.

[20] Planetary waves, also known as Rossby waves, are a type of wave that occurs naturally in rotating fluids, such as the atmospheres and oceans of planets. They are caused by the variation of the Coriolis force with latitude, which makes the fluid turn to the right in the northern hemisphere and to the left in the southern hemisphere. Planetary waves have very long wavelengths, ranging from hundreds to thousands of kilometers, and they move slowly in a westward direction.

D.5 Bibliography

Achakulwisut P., Anenberg S., Neumann J., Penn S., Weiss N., Crimmins A., Fann N., Martinich J., Roman H., Mickley L. (2019). Effects of Increasing Aridity on Ambient Dust and Public Health in the U.S. Southwest Under Climate Change. GeoHealth, V (5), p. 127-144.
https://doi.org/10.1029/2019GH000187

Al-Kheder, S., Al-Kandari, A., (2020). The impact of dust on Kuwait international airport operations: a case study. Int. J. Environ. Sci. Technol. 17, 3467–3474.
https://doi.org/10.1007/s13762-020-02710-3

Al-Hemoud, A., Al-Sudairawi, M., Neelamanai, S. et al. Socioeconomic effect of dust storms in Kuwait. Arab J Geosci 10, 18 (2017).
https://doi.org/10.1007/s12517-016-2816-9

Baddock M., Strong C., Leys K., Heidenreich S., Tews, E. end McTainsh, G. (2014). A visibility and total suspended dust relationship, Atmospheric Environment, Volume 89, Pages 329-336, ISSN 1352-2310.
https://doi.org/10.1016/j.atmosenv.2014.02.038

Biasutti, M., et al. (2020). Sahel rainfall variability and response to greenhouse warming in CMIP5 models. Journal of Climate, 33(18), 8011-8029.
https://doi.org/10.1029/2005GL023232

Bojdo N., Filippone A., Parkes B., Clarkson R., (2020). Aircraft engine dust ingestion following sand storms, Aerospace Science and Technology, Volume 106, 106072, ISSN 1270-9638,
https://doi.org/10.1016/j.ast.2020.106072

Borrelli P, Robinson DA, Panagos P, Lugato E, Yang JE, Alewell C, Wuepper D, Montanarella L, Ballabio C. Land use and climate change impacts on global soil erosion by water (2015-2070). Proc Natl Acad Sci U S A. 2020 Sep 8;117(36):21994-22001. doi: 10.1073/pnas.2001403117
https://pubmed.ncbi.nlm.nih.gov/32839306/

Bravo L., Xue Q., Murugan M., Ghoshai A., Walock M., Flatau A. (2017). Particle transport analysis of sand ingestion in gas turbine jet engines. AIAA 2017-4818. Session: Turbine.
https://arc.aiaa.org/doi/10.2514/6.2017-4818

Chen W. & Fryrear D. (2002), Sedimentary characteristics of a haboob dust storm, Atmospheric Research, Vol. 61, 1, Pages 75-85, ISSN 0169-8095,
https://doi.org/10.1016/S0169-8095(01)00092-8

Cook B., Miller R. and Seager R. (2009). Amplification of the North American ''Dust Bowl'' drought through human-induced land degradation. Proceedings of the National Academy of Sciences, 106 (13) 4997-5001 https://doi.org/10.1073/pnas.0810200106

Copernicus 2022: 'What is desert dust..': https://atmosphere.copernicus.eu/what-saharan-dust-and-how-does-it-change-atmosphere-and-air-we-breathe

Clarkson, R., Simpson, H. (2017). Maximising airspace use during volcanic eruptions: matching engine durability against ash cloud occurrence. Conference: NATO STO AVT-272 Specialists Meeting on "Impact of Volcanic Ash Clouds on Military Operations", https://www.researchgate.net/publication/317617735_Maximising_Airspace_Use_During_Volcanic_Eruptions_Matching_Engine_Durability_against_Ash_Cloud_Occurrence

Cuevas, E., Milford, C., Barreto, A., Bustos, J.J., García, R.D., Marrero, C.L., Prats, N., Bayo, C., Ramos, R., Terradellas, E., Suárez, D., Rodríguez, S., de la Rosa, J., Vilches, J., Basart, S., Werner, E., López-Villarrubia, E., Rodríguez-Mireles, S., Pita Toledo, M.L., González, O., Belmonte, J., Puigdemunt, R., Lorenzo, J.A., Oromí, P., del Campo-Hernández, R., 2021. In: Cuevas, E., Milford, C., Basart, S. (Eds.), Desert Dust Outbreak in the Canary Islands (February 2020): Assessment and Impacts. State Meteorological Agency (AEMET), Madrid, Spain and World Meteorological Organization, Geneva, Switzerland. https://repositorio.aemet.es/bitstream/20.500.11765/13221/2/GAW_Report_No_259.pdf

EPA: Our Nations's air (2022). Online, retrieved on 14/11/2023 https://gispub.epa.gov/air/trendsreport/2023/#introduction

Evan, A. T., J. Dunion, J. A. Foley, and A. K. Heidinger (2006), New evidence for a relationship between Atlantic tropical cyclone activity and African dust outbreaks, Geophys. Res. Lett., 33, L19813, doi:10.1029/2006GL026408. https://agupubs.onlinelibrary.wiley.com/doi/10.1029/2006GL026408

Evan, A., Flamant, C., Gaetani, M. et al (2016). The past, present and future of African dust. Nature 531, 493–495 (2016). https://doi.org/10.1038/nature17149

Federal Aviation Administration (FAA). Pilot's Handbook of Aeronautical Knowledge, 2008, FAA-H-8083-25B

Federal Aviation Administration (FAA). Aircraft Electrical Wiring Interconnect System (EWIS), 2020, AC 20-115D

Federal Aviation Administration (FAA). Jensen, R. R., & Roberts, J. (2010). Assessment of Windshield Contamination Effects on Visual Performance and Flight Safety. DOT/FAA/AR-10/12.

Francis, D., Eayrs, C., Chaboureau, J., Mote, T. & Holland, D. M. (2018). Polar jet associated circulation triggered a Saharan cyclone and derived the Poleward transport of the African dust generated by the cyclone. J. Geophys. Res. Atmos. 123, 11899–11917 (2018)
https://agupubs.onlinelibrary.wiley.com/doi/pdf/10.1029/2018JD029095

Francis, D., Eayrs, C., Chaboureau, J.-P., Mote, T. & Holland, D. M. (2019). A meandering polar jet caused the development of a Saharan cyclone and the transport of dust toward Greenland. Adv. Sci. Res. 16, 49–56 (2019)
https://asr.copernicus.org/articles/16/49/2019/asr-16-49-2019.pdf

Garrison V., Shin E., Foreman, T., Griffin D., Holmes C., Kellog C., Majewski M., Richardson L., Ritchie K., Smith G. (2003). African and Asian Dust: From Desert soils to Coral Reefs*BioScience*, Volume 53, Issue 5, May 2003, Pages 469–480,
https://doi.org/10.1641/0006-3568(2003)053[0469:AAADFD]2.0.CO;2

Gomez, J., Allen, R.J., Turnock, S.T. et al. The projected future degradation in air quality is caused by more abundant natural aerosols in a warmer world. Commun Earth Environ 4, 22 (2023). https://doi.org/10.1038/s43247-023-00688-7

Goudie, Andrew S., and Nicholas J. Middleton (2006). Desert Dust in the Global System. Berlin: Springer.
https://doi.org/10.1007/3-540-32355-4

Harrington, L.J., Schleussner, CF. & Otto, F.E.L. Quantifying uncertainty in aggregated climate change risk assessments. Nat Commun 12, 7140 (2021).
https://doi.org/10.1038/s41467-021-27491-2

Huang, J., Yu, H., Guan, X. et al. Accelerated dryland expansion under climate change (2016). Nature Clim Change 6, 166–171 (2016).
https://doi.org/10.1038/nclimate2837

IPCC (2023). Climate Change Synthesis Report 2023.
https://www.ipcc.ch/report/ar6/syr/downloads/report/IPCC_AR6_SYR_SPM.pdf

Karam, B., D., Flamant, C., Cuesta, J., Pelon, J. & Williams, E. (2010). Dust emission and transport associated with a Saharan depression: February 2007 case. J. Geophys. Res. 115, D00H27 (2010)
https://agupubs.onlinelibrary.wiley.com/doi/full/10.1029/2009JD012390

Lekas, T., Kallos, G., Kushta, J., Solomos, S., Mavromatidis, E., (2011). Dust impact on aviation. 6th International Workshop on Sand/Dust Storms and Associated Dust Fall, September 7-9, Athens, Greece

Lelieveld J., Y. Proestos, P. Hadjinicolaou, et al. (2016). Strongly increasing heat extremes in the Middle East and North Africa (MENA) in the 21st century. Climatic Change, 137 (2016), pp. 245-260, https://doi.org/10.1016/j.accre.2018.01.004

Monerie, PA., Pohl, B. & Gaetani, M. (2021). The fast response of Sahel precipitation to climate change allows effective mitigation action. npj Clim Atmos Sci 4, 24 https://doi.org/10.1038/s41612-021-00179-6

Lu, J., Carbone, G.J. & Grego, J.M. (2019). Uncertainty and hotspots in 21st century projections of agricultural drought from CMIP5 models. Sci Rep 9, 4922. https://doi.org/10.1038/s41598-019-41196-z

Luo, T. et al. (2015). Global dust distribution from improved thin dust layer detection using a–train satellite lidar observations. Geophys. Res. Lett. 42, 620-628 (2015). https://doi.org/10.1002/2014GL062111

Lorenz R. & Myers M., (2005), Dust Devil hazard to aviation: a review of United States Air accident reports, Journal of Meteorology Vol. 30, N. 298. https://www.lpl.arizona.edu/~rlorenz/dustdevilaviation.pdf

Mahowald, N., Lindsay, K., Rothenberg, D., Doney, S. C., Moore, J. K., Thornton, P., Randerson, J. T., and Jones, C. D. (2011): Desert dust and anthropogenic aerosol interactions in the Community Climate System Model coupled-carbon-climate model, Biogeosciences, 8, 387–414, https://doi.org/10.5194/bg-8-387-2011

Mao R., Gong D., Kim S., Zong Q., Feng X., Zhang X. (2021). Increasing spring dust storms in the future over the Taklimakan Desert, Northwest China: implications from changes in circulation pattern frequency in CMIP6. Environ. Res. Commun. 3 111002. https://dx.doi.org/10.1088/2515-7620/ac37ee

Marticorena, B., & Bergametti, G. (1995). Modelling the atmospheric dust cycle: Design of a soil-derived dust emission scheme. Journal of Geophysical Research: Atmospheres, 100(D8), 16415-16430 https://doi.org/10.1029/95JD00690

Middleton N. (2019). Variability and Trends in Dust Storm Frequency on Decadal Timescales: Climatic Drivers and Human Impacts, Geosciences 2019, 9(6), 261. https://www.mdpi.com/2076-3263/9/6/261

Monteiro A., S. Basart, S. Kazadzis, A. Votsis, A. Gkikas, S. Vandenbussche, A. Tobias, C. Gama, C. Pérez García-Pando, E. Terradellas, G. Notas, N. Middleton, J. Kushta, V. Amiridis, K. Lagouvardos, P. Kosmopoulos, V. Kotroni, M. Kanakidou, N. Mihalopoulos, N. Kalivitis, P. Dagsson-Waldhauserová, H. El-Askary, K. Sievers, T. Giannaros, L. Mona, M. Hirtl, P. Skomorowski, T. H. Virtanen, T. Christoudias, B. Di

Mauro, S. Trippetta, S. Kutuzov, O. Meinander, S. Nickovic, (2022). Multi-sectoral impact assessment of an extreme African dust episode in the Eastern Mediterranean in March 2018, Science of The Total Environment, Volume 843, 2022, 156861, ISSN 0048-9697, https://doi.org/10.1016/j.scitotenv.2022.156861

McTainsh, Grant H., and Pitblado, J. R. (1987). Dust storms and related phenomena measured from meteorological records in Australia. Earth Surface Processes and Landforms, 12(4), pp. 415–424. https://doi.org/10.1002/esp.3290120407

Nickovic, S., Cvetkovic, B., Petković, S., et al., 2021. Cloud icing by mineral dust and impacts to aviation safety. Sci. Rep. 11, 6411 https://doi.org/10.1038/s41598-021-85566-y

Prospero, J.M. (1996). Saharan Dust Transport Over the North Atlantic Ocean and Mediterranean: An Overview. In: Guerzoni, S., Chester, R. (eds) The Impact of Desert Dust Across the Mediterranean. Environmental Science and Technology Library, vol 11. Springer, Dordrecht. https://doi.org/10.1007/978-94-017-3354-0_13

Prospero, J. M., Ginoux, P., Torres, O., Nicholson, S. E., & Gill, T. E. (2002). Environmental characterization of global sources of atmospheric soil dust identified with the Nimbus 7 Total Ozone Mapping Spectrometer (TOMS) absorbing aerosol product. Reviews of Geophysics, 40(1), 2002. https://agupubs.onlinelibrary.wiley.com/doi/pdf/10.1029/2000RG000095

Rotstayn, L. D., M. A. Collier, R. M. Mitchell, Y. Qin, and S. K. Campbell (2011), Simulated enhancement of ENSO-related rainfall variability due to Australian dust, Atmos. Chem. Phys., 11, 1595– 1639 https://acp.copernicus.org/preprints/11/1595/2011/acpd-11-1595-2011.pdf

Shao, Yaping (2008). Physics and Modelling of Wind Erosion. Netherlands: Springer https://link.springer.com/book/10.1007/978-1-4020-8895-7

Stehfest, E., van Zeist, WJ., Valin, H. et al. (2019). Key determinants of global land-use projections. Nat Commun 10, 2166 https://doi.org/10.1038/s41467-019-09945-w

Tegen, I., & Fung, I. (1995). Contribution to the atmospheric mineral aerosol load from land surface modification. Journal of Geophysical Research: Atmospheres, 100(D4), 18707-18726. https://doi.org/10.1029/95JD02051

Tong, D. Q., Wang, J. X. L., Gill, T. E., Lei, H., and Wang, B. (2017), Intensified dust storm activity and Valley fever infection in the southwestern United States, Geophys. Res. Lett., 44, 4304– 4312, doi:10.1002/2017GL073524 https://agupubs.onlinelibrary.wiley.com/doi/full/10.1002/2017GL073524

United Nations Convention to Combat Desertification (UNCCD) (2022). Sand and Dust Storms Compendium: Information and Guidance on Assessing and Addressing the Risks. Bonn, Germany https://www.unccd.int/sites/default/files/2022-08/Full%20report%20ENG.pdf

Varga, G., Dagsson-Waldhauserová, P., Gresina, F. et al., (2021). Saharan dust and giant quartz particle transport towards Iceland. Sci Rep 11, 11891 (2021).
https://doi.org/10.1038/s41598-021-91481-z

Wang, J.X.L. (2015). Mapping the Global Dust Storm Records: Review of Dust Data Sources in Supporting Modeling/Climate Study. Curr Pollution Rep 1, 82–94 (2015).
https://doi.org/10.1007/s40726-015-0008-y

Washington, R., Todd, M.C., Middleton, N.J., & Goudie, A.S. (2003). Dust-Storm Source Areas Determined by the Total Ozone Monitoring Spectrometer and Surface Observations. Annals of the Association of American Geographers, 93, 297 – 313. DOI:10.1111/1467-8306.9302003
https://doi.org/10.1111/1467-8306.9302003

WMO (2021): Sand and Dust storms.
https://public.wmo.int/en/our-mandate/focus-areas/environment/sand-and-dust-storms

WMO (2023): Airborne dust bulletin (19102023), downloaded on 14/11/2023
WMO Airborne Dust Bulletin highlights present, future hotspots | World Meteorological Organization

Yang, K., Wang, Z., Luo, T. et al. (2022). Upper troposphere dust belt formation processes vary seasonally and spatially in the Northern Hemisphere. Commun Earth Environ 3, 24 (2022).
https://doi.org/10.1038/s43247-022-00353-5

Zittis, G., Hadjinicolaou, P., Klangidou, M. et al. (2019). A multi-model, multi-scenario, and multi-domain analysis of regional climate projections for the Mediterranean. Reg Environ Change 19, 2621–2635
https://doi.org/10.1007/s10113-019-01565-w

Zittis, G., Almazroui, M., Alpert, P., Ciais, P., Cramer, W., Dahdal, Y., et al. (2022). Climate change and weather extremes in the Eastern Mediterranean and Middle East. Reviews of Geophysics, 60, e2021RG000762
https://doi.org/10.1029/2021RG000762

Zhang J. G. (2007). Effect of Dust Contamination on Electrical Contact Failure, Electrical Contacts - 2007 Proceedings of the 53rd IEEE Holm Conference on Electrical Contacts, Pittsburgh, PA, USA, 2007, pp. xxi-xxx, doi: 10.1109/HOLM.2007.4318186
https://ieeexplore.ieee.org/document/4318186

Zhou, Y., Wu, T., Zhou, Y. et al. Can global warming bring more dust?. Clim Dyn 61, 2693–2715 (2023).

https://doi.org/10.1007/s00382-023-06706-w

Zong, Q., Mao R., Gong D., Yao-Yi, Chenglai Pu, Bing F., Xingya S., (2021). Changes in Dust Activity in Spring over East Asia under a Global Warming Scenario. Asia-Pacific Journal of Atmospheric Sciences. 57. 10.1007/s13143-021-00224-7
https://link.springer.com/article/10.1007/s13143-021-00224-7

E Appendix – Task Force #2: Clear Air Turbulence

Note: The main author of this appendix is Nicole Viola

The present appendix presents preliminary results regarding the evolution of airborne icing conditions in the past and in the future, possibly due to climate change. The investigation has been performed through interactions with experts and particularly with Christian Pagé and his research team at CERFACS. Literature review has also been extended to include the results of scientific research of other teams, like the team of Bernstein B.C. at National Center for Atmospheric Research, Boulder, Colorado, USA.

E.1 Airborne icing physics

Aircraft icing has always been a hazardous issue since it was recognized because it causes degradation in the aerodynamic performance and malfunction of essential flight instruments.

The early stages of icing research were carried out mainly by experiments geared toward understanding icing physics and the development of icing mitigation techniques [1]. In the 1970s, the development of numerical simulations for aircraft icing began growing. The motivation for simulations was reducing the cost and lowering the risk of accidents during the certification process for icing mitigation devices. Since then, experimental and numerical investigation have been used side by side to establish more accurate icing simulation tools [2].

From a meteorological perspective, initial icing research focused on icing caused by small water droplets up to 40 µm in diameter. New regulations were then introduced, which describes meteorological conditions with potential for icing with water droplet diameter up to approximately 2 mm. Since the 1990s, icing caused by water droplets larger than 40 µm in diameter has been referred to as supercooled large droplet (SLD) icing. It has remained a challenging topic for aircraft icing researchers. In addition to SLD icing, the 1990s saw a significant increase in the interest in jet engine icing [3]. Engine icing is often referred to as ice crystal icing since it is considered to be caused by ice crystals rather than the supercooled droplets that cause icing on wings. For the ice crystal icing, knowledge of the underlying physics is currently limited.

E.2 Methodology to predict airborne icing

Because of a lack of regular, direct measurements, limited information is available about the frequency and the spatial and temporal distribution of icing conditions aloft, including supercooled large drops (SLD). Research aircraft provide in situ observations of these conditions, but the sample set is small and can be biased. Surface observations of freezing fog and freezing precipitation provide additional insight, but cannot be used alone to assess the presence of icing aloft. Climatology based solely on such observations can underestimate their presence in areas where subfreezing temperatures are uncommon. Other techniques can be used in an effort to reduce some of these biases and limitations. More information on frequency, spatial and temporal distribution of icing can be inferred from methods such as the icing index from Meteo France's System of Icing Geographic Identification in Meteorology for Aviation (SIGMA) algorithm [4] [5] or the Current Icing Product (CIP) method or CIP-sonde method [6]. Both methods are used to assess the potential for icing conditions aloft in combination with observations. The CIP-sonde method uses a version of CIP that was tailored to determine the potential for icing and SLD using coincident observations from balloon borne soundings and surface stations (CIP-sonde) [12]. The second method, SIGMA is an algorithm to assess the potential presence of icing from global-scale model reanalyses of temperature (T) and relative humidity (RH).

E.2.1 CIP and CIP-sonde method to predict airborne icing

The CIP method [13] was developed as a multiple data source, hybrid approach to the diagnosis of icing. CIP became an official Federal Aviation Administration and National Weather Service icing product in 2002. It combines satellite, radar, surface, and lightning observations with numerical model output and PIREPs to create an hourly, 3D diagnosis of icing and SLD. CIP uses these datasets to estimate the locations of clouds and precipitation, and then combines those using physically based decision trees and fuzzy logic.

CIP-sonde similarly examines the vertical structure of the atmosphere using coincident observations from soundings and surface stations. Based on this information, each profile is described by one of several icing scenarios (e.g., classical freezing rain). Within each scenario, fuzzy logic membership functions are applied to the data and then the potential for icing and SLD is determined at each level. The icing and SLD potentials are essentially the confidence or likelihood that those conditions were present, on a scale of 0 to 1. At high potentials, the presence of icing or SLD is considered to be very likely.

E.2.2 SIGMA method to predict airborne icing

To assess the location and severity of in-flight icing over western Europe, scientists at Meteo France developed SIGMA in the years 2000. The goal of SIGMA is to identify the areas for which the factors supporting icing conditions are present. SIGMA is based on observations and experience from international icing flight campaigns (e.g. [7]), which indicated that certain observations and model-based fields were strong indicators of the presence of icing.

The operational version of SIGMA combines model forecasts of temperature, T, relative humidity, RH, and vertical velocity with real-time observations of cloud and precipitation characteristics from satellite and radar.

R1	**weak risk, SIGMA ≥ 1**	R8	**severe risk, SIGMA ≥ 8**
R4	**moderate risk, SIGMA ≥ 4**	R8 SAFIRE	**SLD-probable conditions: SIGMA ≥ 8** **T ≥ 0°C below 3000m**

Figure E.1: SIGMA airborne icing risks

Real-time runs of SIGMA first examine model forecasts of T and RH to produce an icing index that ranges from 0 (no icing) to 10 (icing very likely), as shown in Figure E.1. The SIGMA index only exceeds 0 where -15°C<=T<=0°C and RH>=80%. While icing can certainly occur when the model indicates lower T and/or RH, most icing occurrences fall within the ranges described above. Output from the icing index is then overlaid with the observational data to produce a more complete analysis of icing in three dimensions and in clouds information on the physical icing scenario and the expected icing severity [2].

E.2.3 Evolution of the SIGMA method to predict airborne icing

The current research activity on airborne icing at CERFACS focuses on actions:

- to revisit the SIGMA method considering new temperature values as thresholds and new atmospheric reanalysis data:
  - Temperature ranges: -21°C<=T<=0°C (and RH>=80%);
  - Reanalysis data:
    - NCEP (National Center of Environmental Prediction) Reanalysis: time period 1950-2020; spatial resolution 2,5°; 7 altitudes (corresponding to the following pressure values 1000, 925, 850, 700, 600, 500, 400, 300 hPa);
    - ERA5 (European Center for Medium Range Weather Forecast, ECMWF) Reanalysis: time period 1979-2020; spatial resolution 0,5°, 20 vertical levels between 1000 and 300 hPa;
- to estimate uncertainty associated with atmospheric reanalysis;
- to determine atmospheric conditions related to high level of icing probability;
- to study trends in the past period;
- to study impact of climate change on icing risks from climate models.

E.3 Airborne icing: past trends

The analysis of past trends of airborne icing is crucial to accurately predict the future trends and to possibly understand the impact of climate change on the physical phenomenon. Past trends of in-flight icing have been assessed over the entire globe and throughout all seasons through CIP-sonde method and SIGMA algorithms.

In [5] the results of CIP-sonde method and SIGMA algorithm are compared to validate the approaches. As the complete information needed for the operational SIGMA was not readily available for climatological analysis and because the SIGMA index only required grids of T and RH to produce its initial analysis, Le Bot in [4] was able to estimate the frequency of icing over Europe and the globe, using 13 years (1989–2001) of 40-yr European Centre for Medium-Range Weather Forecasts (ECMWF) Re-Analysis (ERA-40) model reanalyses of the state of the atmosphere. ERA-40 analyses were created using observations from soundings, surface stations, and satellites (among others) and were placed onto a 1° x 1° grid covering the globe. Available fields included T and RH, and these fields were interpolated from constant pressure levels to constant height levels from 500 to 16000 m [10]. Values of the SIGMA index were calculated at each point in the ERA-40 grids valid at 0000, 0600, 1200, and 1800 UTC each day. Using this output, icing frequencies were estimated by calculating the percentage of time that SIGMA index values were greater than or equal to 4 (corresponding to moderate and severe icing risks, R4 and R8) anywhere in the column. This threshold was chosen based upon experience from forecasters and researchers who examined output from SIGMA on a day-to-day basis, as well as statistical verification. Because PIREPS are difficult to obtain over Europe, SIGMA was adapted to run over the United States and southern Canada on the datasets used by the operational CIP. A large database of SIGMA runs was compared with PIREPs and results compared favourably to those of CIP [11].

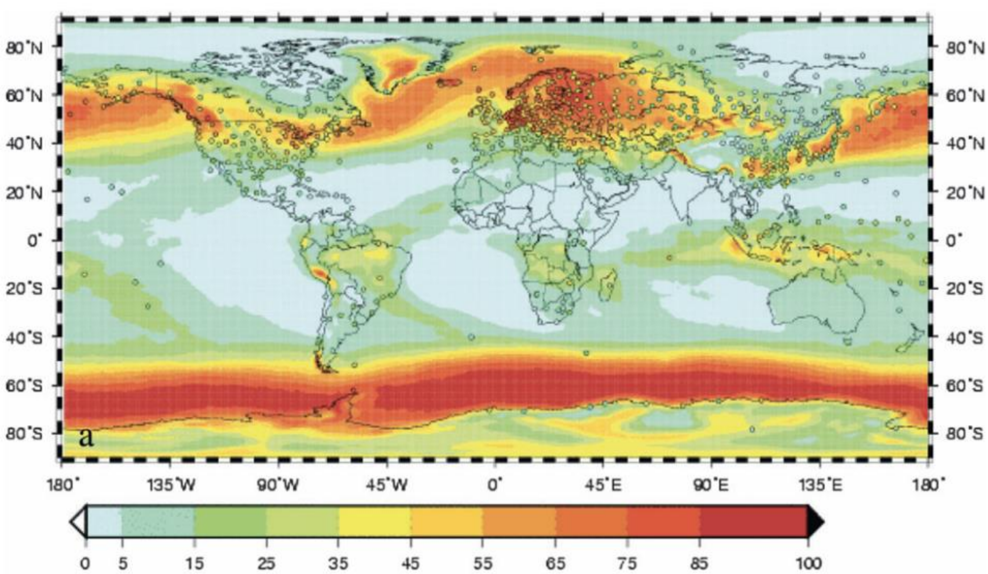

Figure E.2: Frequencies of weak to medium in-flight icing risks for one full-year past trend for the globe for January: SIGMA index (contours) and CIP-sonde (dots)

Figure E.2-Figure E.5 [5] shows the global icing frequencies for a past full-year for weak and medium risks, estimated by SIGMA index (contours) and CIP-sonde (dots) icing in different months. Frequencies are calculated using low-to-moderate thresholds [5]. In general, the Northern Hemisphere icing tend to be most common in a somewhat zonal band poleward of about 40°N latitude, with broad extensions to southern latitudes at different longitudes. These variations appear to be connected to the large-scale storm tracks and their interaction with major landmasses. They are quite evident in January (Figure E.2), when the northern jet stream is strong and there tends to be sharp boundaries between polar and mid-latitude air masses. There is also a fairly distinct southwest– northeast orientation to the icing maxima over both the Atlantic and Pacific Oceans, from the Great Lakes to northwestern Europe and from southeast China to southern Alaska. Large mountain ranges like the Rocky Mountains disrupt the pattern via the impact of their large-scale upslope and downslope forces on cloudiness. Other large terrain features like the Alps and Himalayas also tend to have large changes in icing frequency across them since they act as barriers to flow on a regional scale. The meridional nature of the Northern Hemisphere pattern weakens slightly in April (Figure E.3), as the storm track moved northward. It becomes almost nonexistent in July (Figure E.4), when most of the icing tends to be confined to the Arctic. As the Arctic quickly cools during the fall and the storm tracks move southward, meridional deviations are reestablished by October (Figure E.5). In the tropics, a high-altitude weak icing belt is generally found within 20° of the equator and moves across the latitudes throughout the year. In the Southern Hemisphere, icing risks is wide spread longitudinally and most common between 50° and 70°–80°S of latitude, with the southern limit along the coast of Antarctica. Elevated icing frequencies are semipermanent, but maximized in July, the peak of winter there.

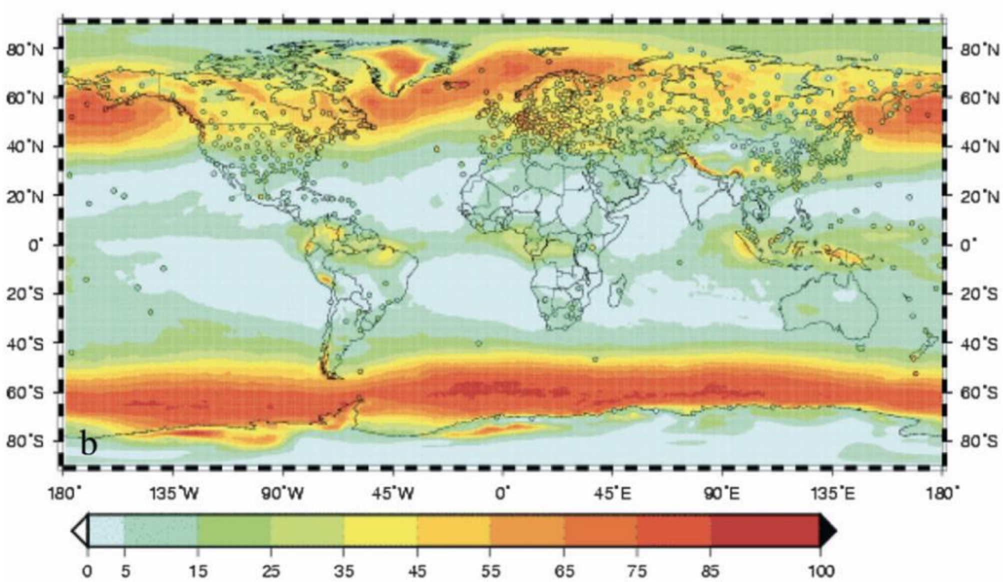

Figure E.3: Frequencies of weak to medium in-flight icing risks for one full-year past trend icing frequencies for the globe for April: SIGMA index (contours) and CIP-sonde (dots)

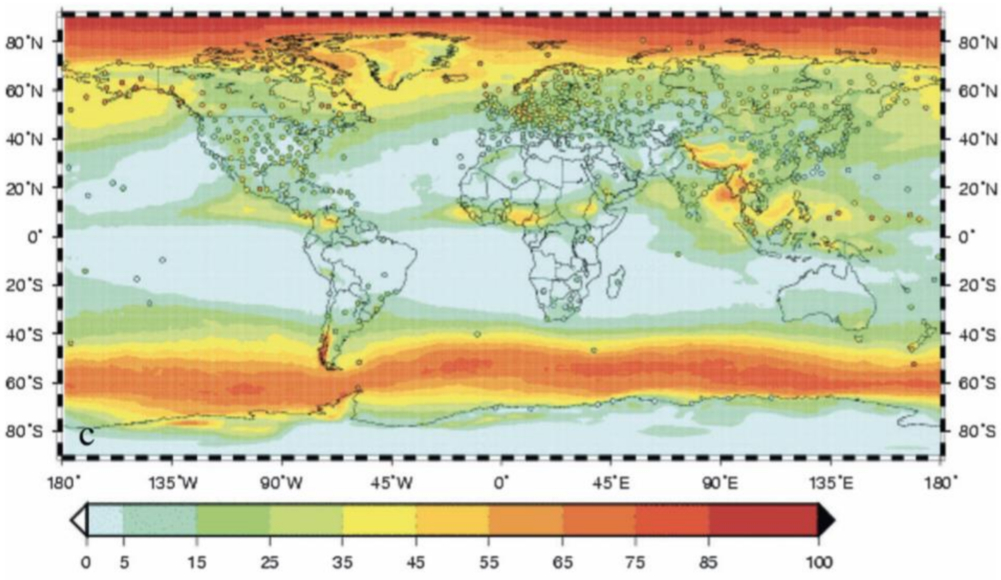

Figure E.4: Frequencies of weak to medium in-flight icing risks for one full-year past trend icing frequencies for the globe for July: SIGMA index (contours) and CIP-sonde (dots)

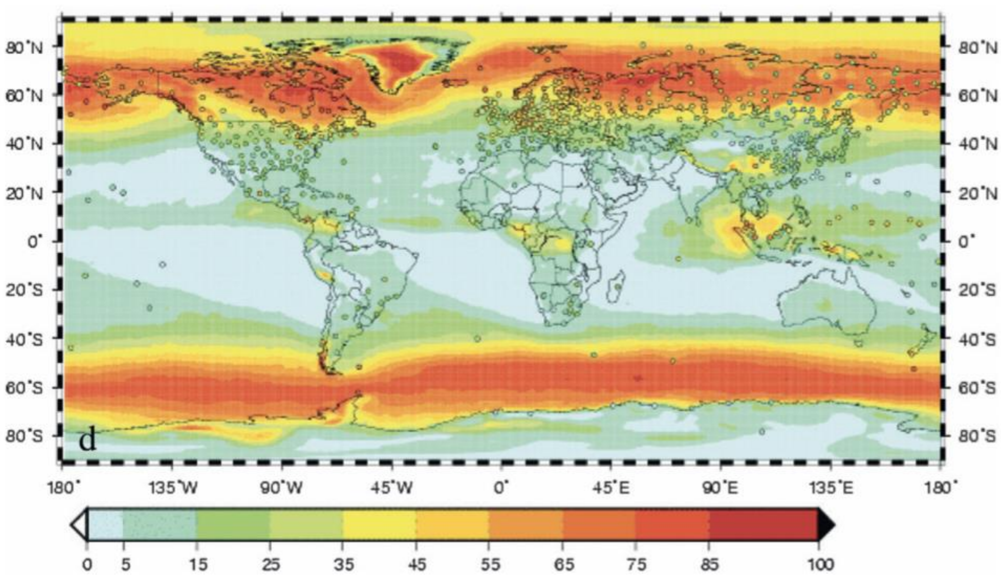

Figure E.5: Frequencies of weak to medium in-flight icing risks for one full-year past trend icing frequencies for the globe for October: SIGMA index (contours) and CIP-sonde (dots)

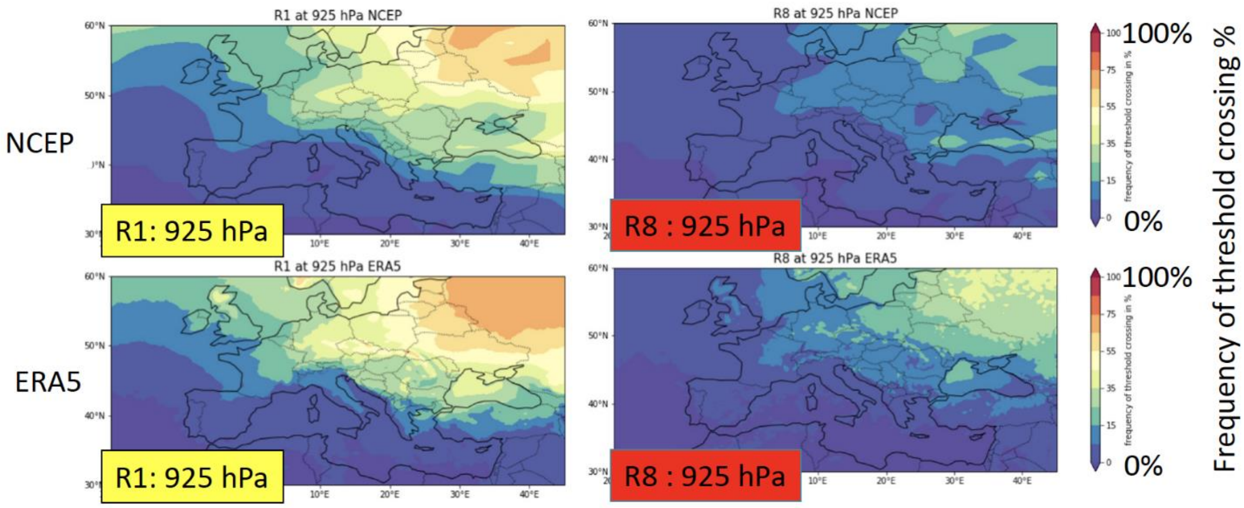

Figure E.6: Frequencies of threshold crossing expressed as percentages for R1(weak risk) at 925 hPa NCEP reanalysis data (top left); frequencies of threshold crossing expressed as percentages for R1(weak risk) at 925 hPa ERA5 reanalysis data (bottom left); frequencies of threshold crossing expressed as percentages for R8 (severe risk) at 925 hPa NCEP reanalysis data (top right); frequencies of threshold crossing expressed as percentages for R8 (severe risk) at 925 hPa ERA5 reanalysis data (bottom right). For all maps, the considered season is winter (DJF) [8]

On the basis of the two-data set of reanalysis data, NCEP and ERA5, new icing risk climatologies have been estimated by SIGMA algorithm for the past four decades up to 2020 [8].

Figure E.6 shows the results of airborne icing risks during the winter season (December, January, February, DJF) at 925 hPa of altitude (925 hPA = FL 25 = 762 m altitude). Results reveal the frequency of threshold crossing for weak risk (R1) and severe risk (R8). ERA5 shows finer spatial scales with higher values of frequencies of threshold crossing both for weak and severe risk than NCEP. Results based on NCEP and ERA5 data show some differences at local scale, but the global structure of icing risk climatology is very similar.

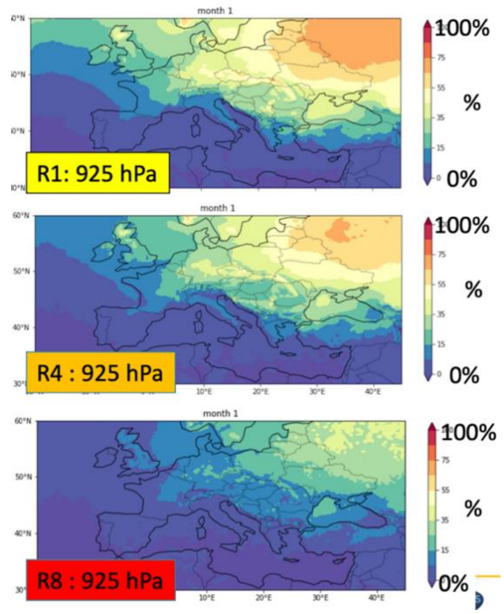

Figure E.7: Frequencies of threshold crossing expressed as percentages at 925 hPa based on ERA5 data for R1(weak risk) (top), R4 (medium risk) (middle) and R8 (severe risk) (bottom) [8]

As expected, Figure E.7 shows that the frequencies of airborne icing risks at the same altitude decreases when moving from weak to severe risk. The figure represents the average mean over about 40 years (1979-2020) in January. The same trend is observed in Figure E.4, which shows the seasonal trend in winter of the frequencies of airborne icing risks based on NCEP reanalysis data for weak and severe risks at two different altitudes (925 hPa and 700 hPa) and two different seasons, winter and summer. Results shown in Figure E.8 also reveal the seasonality of the airborne icing phenomenon: the altitude of 925 hPa has a higher risk of airborne icing in winter season, while the altitude of 700 hPa (FL 100, 3012 m altitude) has a higher of airborne icing in summer season. This highlights that in winter season the highest frequencies of airborne icing are at lower altitudes, while in summer season are at higher altitudes.

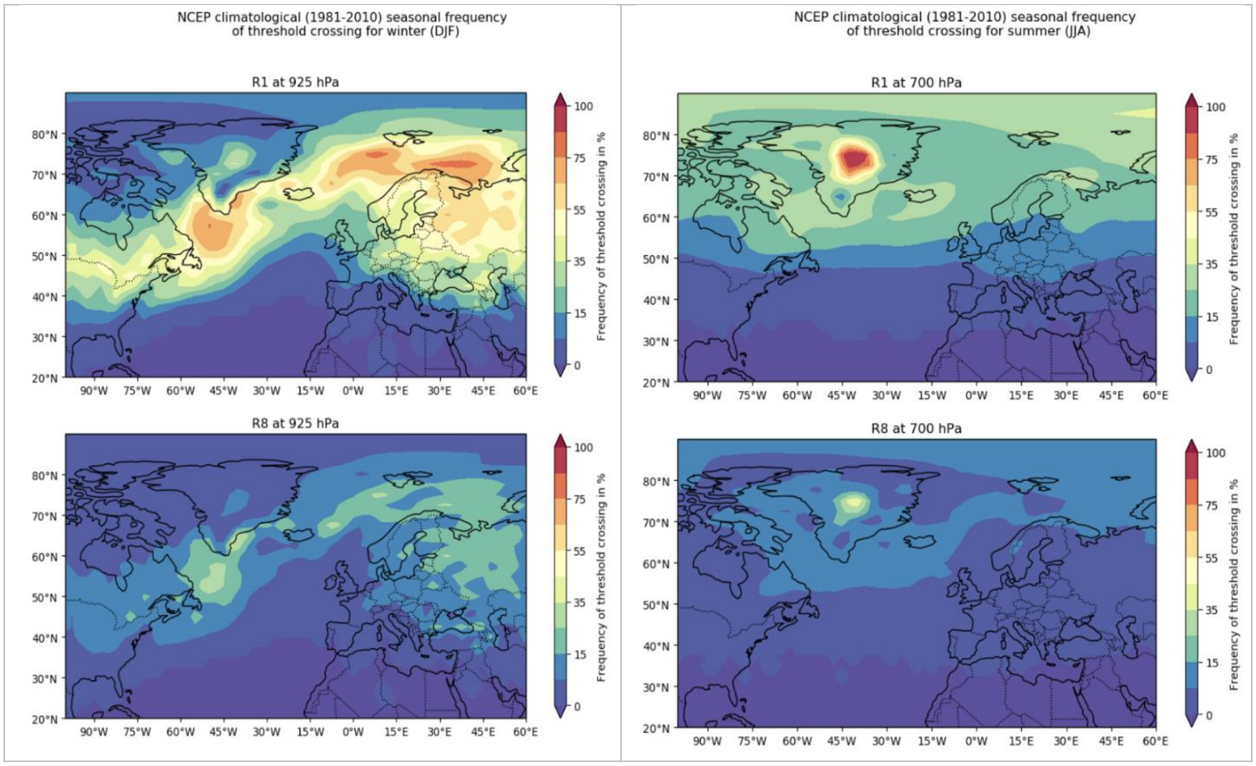

Figure E.8: Seasonal (DJF) frequencies in winter of threshold crossing expressed as percentages at 925 hPa based on NCEP reanalysis data over the time period 1981-2010 for R1(weak risk) (top left); seasonal (DJF) frequencies in winter of threshold crossing expressed as percentages at 925 hPa based on NCEP reanalysis data over the time period 1981-2010 for R8(severe risk) (bottom left); seasonal (JJA) frequencies in summer of threshold crossing expressed as percentages at 700 hPa based on NCEP reanalysis data over the time period 1981-2010 for R1(weak risk) (top right); seasonal (JJA) frequencies in summer of threshold crossing expressed as percentages at 700 hPa based on NCEP reanalysis data over the time period 1981-2010 for R8(severe risk) (bottom right)

E.4 Airborne icing: future trends

To better understand the impact on climate change on airborne icing, research studies have been carried out at CERFACS [5] to compare the past trends with the future trends of seasonal frequencies of icing risk. Past trends have been based on ERA5 reanalysis data over the time period 1979-2014, whereas future trends have been based on the CNRM-CM6-1 climate model considering Global Warming Level equal to +4°C (SSP 585). The CNRM-CM6-1 climate model has been developed by the CNRM/CERFACS modelling group for CMIP6. It is the successor of the CNRM-CM5.1 climate model that participates to CMIP5. Figure E.9 shows seasonal frequencies in autumn of threshold crossing expressed as percentages at 700 hPa and 500 hPa for weak icing risk (R1). For both altitudes (700 hPa = FL100 = 3048 m and 500 hPa = FL180 =5500 m) the frequencies of icing risk R1 increases from past to future trends, being more significant at higher than lower altitudes.

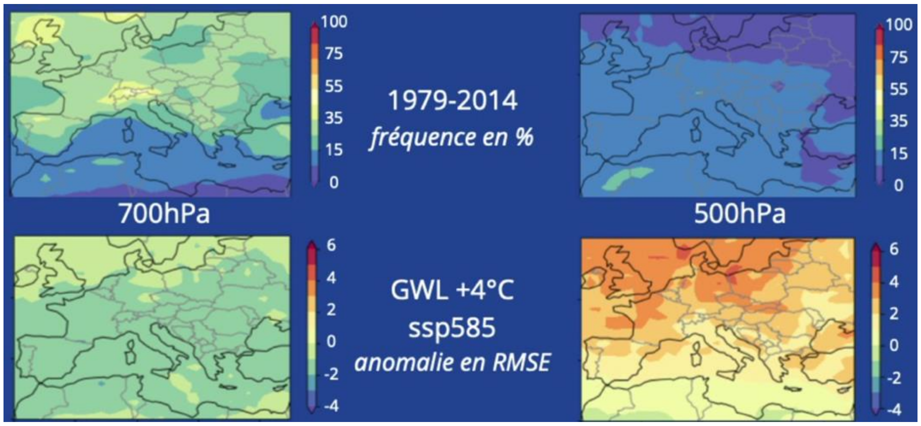

Figure E.9: Seasonal (September, October, November, SON) frequencies in autumn of threshold crossing expressed as percentages at 700 hPa based on ERA5 reanalysis data over the time period 1979-2014 for R1 (weak risk) (top left); seasonal (SON) frequencies in autumn of threshold crossing expressed as RMSE (Root Mean Square Error) anomaly with respect to the 1979-2014 scenario at 700 hPa based on CNRM-CM6-1 climate model and GWL +4°C over the time period 2063-2082 for R1 (weak risk) (bottom left); seasonal (SON) frequencies in autumn of threshold crossing expressed as percentages at 500 hPa based on ERA5 reanalysis data over the time period 1979-2014 for R1(weak risk) (top right); seasonal (SON) frequencies in autumn of threshold crossing expressed as RMSE (Root Mean Square Error) anomaly with respect to the 1979-2014 scenario at 500 hPa based on CNRM-CM6-1 climate model and GWL +4°C over the time period 2063-2082 for R1 (weak risk) (bottom right) [5]

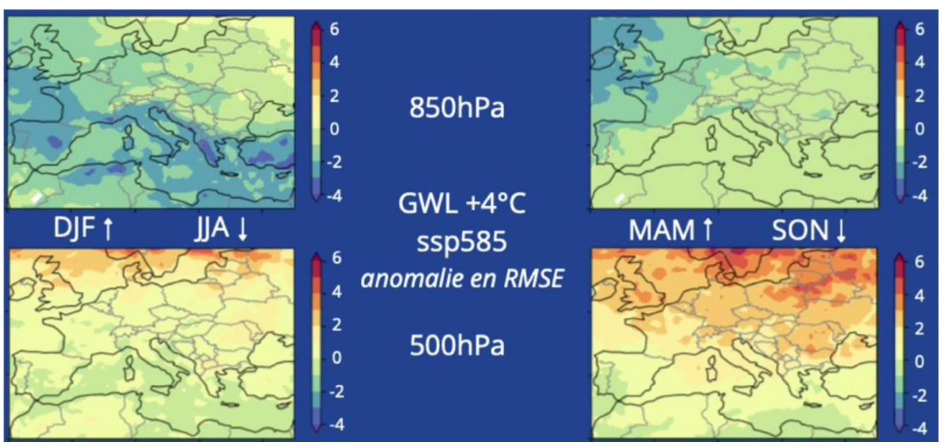

Figure E.10: Seasonal (December, January, February, DJF) frequencies in winter of threshold crossing expressed as RMSE (Root Mean Square Error) anomaly with respect to the 1979-2014 scenario at 850 hPa based on EC-Earth3 climate model and GWL +4°C over the time period 2063-2082 for R1 (weak risk) (top left); seasonal (JJA) frequencies in summer of threshold crossing expressed as RMSE anomaly with respect to the 1979-2014 scenario at 500 hPa based on EC-Earth3 climate model and GWL +4°C over the time period 2063-2082 for R1(weak risk) (bottom left); seasonal (March, April, May, MAM) frequencies in spring of threshold crossing expressed as RMSE anomaly with respect to the 1979-2014 scenario at 850 hPa based on EC-Earth3 climate model and GWL +4°C over the time period 2063-2082 for R1 (weak risk) (top right); seasonal (SON) frequencies in autumn of threshold crossing expressed as RMSE anomaly with respect to the 1979-2014 scenario at 500 hPa based on EC-Earth3 climate model and GWL +4°C over the time period 2063-2082 for R1(weak risk) (bottom right) [9]

The increase of frequencies of icing risk at higher altitudes seem to be confirmed by the results shown in Figure E.10, where the analysis of the impact of climate change on future trends of airborne icing is depicted. Results are based on EC-Earth3 climate model, considering a Global Warming Level equal to +4°C (SSP 585). Moving from 850 hPa (850 hPa = FL50 =1524 m) to 500 hPa altitudes the frequencies of weak icing risk (R1) increase significantly in summer and autumn seasons.

E.5 Uncertainties in airborne icing projections

Models to predict airborne icing and the climate models used to analyse future trends of in-flight icing due to climate change are important source of uncertainties.

As far as climate models are concerned, recent research studies at CERFACS [9] have selected a subsets of climate models based on their performance in predicting the past trends of climate compared to ERA5 reanalysis data. The comparison has focused on the capability of climate models to predict the frequency of icing risk indexes for weak, medium and severe risk. Figure E.7 highlights the climate models that perform better with respect to ERA5 reanalysis data for R1 (left), R4 (middle) and R8 (right), i.e. all climate models included in the light blue circle, expressed in terms of space correlation versus RMSE (Root Mean Square Error).

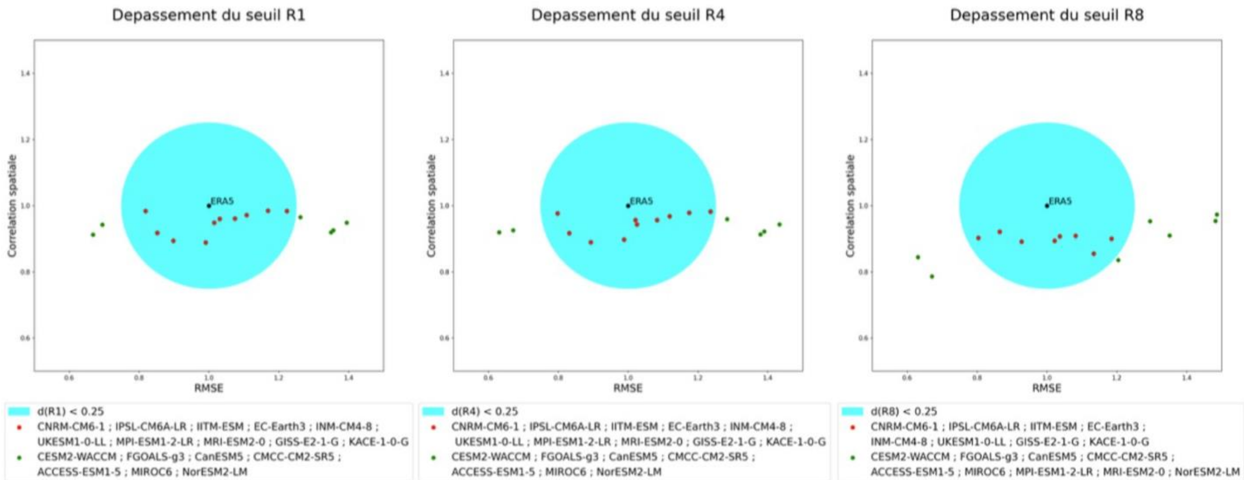

Figure E.7: Comparison between different climate models and ERA5 reanalysis data to predict the frequency of weak icing index R1 (left), medium icing index R4 (medium) and severe icing index R8 (right): the climate models within the light blue circle perform better from the point of view of space correlation versus RMSE [9]

E.6 Conclusions

The following conclusions can be drawn by the current investigations on airborne icing:

- *the accuracy of predictability in time and space*. The accuracy of results depends on uncertainties and mostly on uncertainties related to climate models and models/algorithms to predict in-flight icing risks. As far as models/algorithms are concerned, different sources of uncertainties do exist:
    - according to [5], both SIGMA and CIP-sonde methods use somewhat coarse spatial data, so they are likely to miss fine details associated with topographic features and land–sea interfaces.
    - Guan et al. [14] report that the application of an icing algorithm based solely on T and RH to model output result in significant over-forecasting and a lack of skill. Though the SIGMA index is based on T and RH, when it is applied to model reanalyses data that are based on observational data sources, it is expected that the overestimation of icing frequencies is reduced [5]. As far as past trends for airborne icing are concerned, while no statistical verification of the SIGMA index was done in [5], the seasonal frequencies and patterns that it generated over North America were quite similar to those from CIP-sonde [5], which in [12] was shown to capture 87.3% (PODy) of ‘’good-quality’’ positive icing PIREPs while warning for a small volume of air space.
    - In CIP-sonde, any SLD aloft that is not reflected as freezing or liquid precipitation at the surface is missed [5]. A 100-km-radius circle is used to find surface reports in the vicinity of balloon launches. Appropriate precipitation types are almost always observed by a subset of the stations within the circle. To a lesser extent, this is also true for cloud cover. Thus, only a portion of the 100-km radius cylinder is likely to have contained icing or SLD.
    - CIP-sonde and SIGMA index results in [5] are based on data from 0000 and 1200 UTC and from 0000, 0600, 1200, and 1800 UTC, respectively. Thus, SIGMA results coverthe diurnal cycle more thoroughly.
- *The seasonality*. As far as future trends of airborne icing due to climate change are concerned, the current publicly available research results do not allow to draw any conclusions. Further elaborations of results are necessary to compare icing risks at the same altitudes in all seasons. Present results show an increase of frequency of weak icing risk (R1) in summer and autumn at higher altitudes. Results need however to be confirmed by future analyses. As far as past trends of airborne icing are concerned, In general, the Northern Hemisphere icing tend to be most common in a zonal band poleward of about 40°N latitude, with broad extensions to southern latitudes that vary depending on seasons. In the tropics, a high-altitude weak icing belt is generally found within 20° of the equator and moves across the latitudes throughout the year. In the Southern Hemisphere, icing risks is wide spread longitudinally and most common between 50° and 70°–80°S of latitude, with the southern limit along the coast of Antarctica. Elevated icing frequencies are semipermanent, but maximized in July, the peak of winter there.
- *The hazard magnitude (intensity and duration)*. The hazard magnitude shall be investigated more deeply as currently publicly available research results do not cover the entire spectrum from weak

to severe icing risks. This holds true both for past and future trends of airborne icing. Therefore, nothing can be inferred on the evolution of intensity and duration of airborne icing as weather hazard.

- *The hazard frequency*. For different altitudes (700 hPa and 500 hPa) the frequencies of icing risk R1 increases from past to future trends, being more significant at higher than lower altitudes. Even though R1 is a weak risk and thus not necessarily considered as weather hazard, the increase of frequency of icing risk R1 from past to future trends is still relevant and requires further investigations. Taking a closer look at past trends of in-flight icing, Brown et al. [15] demonstrate a diurnal pattern in the frequency of icing PIREPs and make the hypothesis that much of this is driven by the daily cycle of air traffic. Diurnal patterns in the frequency of FZDZ (frizzing drizzle) and FZRA (frizzing rain) have been found at the surface [16], and may also be present aloft. The potential influence of the diurnal cycle on the results should be taken into account.
- *The geographical coverage*. As far as past trends of airborne icing are concerned, the complete geographical coverage of the physical phenomenon is reached. However, global coverage appears not to be met yet, both in terms of longitudes and latitudes for future trends of in-flight icing.
- *The time coverage (within or beyond typical lifecycles of airplanes and runway pavements)*. Current investigations focus both on past trend and future trends of in-flight icing, up to about 2080.
- *The reliability of climate models*. Current research works are assessing the accuracy and performance of climate models in predicting icing conditions compared to ERA5 reanalysis data. The comparison has focused on the capability of climate models to predict the frequency of icing risk indices for weak, medium and severe risk of SIGMA algorithm.
- *Uncertainties*. Uncertainties of current investigations are listed hereafter:
  - models and algorithms to predict icing conditions, like CIP/CIP-sonde method and SIGMA algorithm, do have uncertainties that affect their accuracy and that depend on the implemented approach and methodology. In addition, these methods were not designed for estimating the risk of ice crystal icing.
  - The climate models used to analyse future trends of in-flight icing due to climate change are important sources of uncertainties. Current research works are assessing the accuracy and performance of climate models in predicting icing conditions compared to ERA5 reanalysis data.
  - Future emissions of greenhouse gases depend on socioeconomic and political factors.
- *Limitations*. Limitations of current investigations are listed hereafter:
  - generally the models/algorithms, like SIGMA and CIP-sonde, do not take deep convection into account [5]. This is done because aircraft specifically avoid flying into thunderstorms because of the many hazards they present, such as hail and lightning. Thus, their inclusion would extend the areas of potential exposure to in-flight icing. This choice is likely to result in underestimating actual icing frequencies in areas prone to thunderstorms, especially at relatively high altitudes.
  - Current models/algorithms do not include the impact of aerosols on ice formation but research activities reveal that there is a relationship between aerosols and super-cooled water droplets. It seems that super-cooled water form more when there are less aerosols but this requires further investigations.

- Analyses of future trends of airborne icing should extend to higher altitudes of cruise phase and include ice crystal icing, which are rarely considered in present investigations.
- Analyses of future trends of airborne icing should cover the entire globe at all latitudes.

E.7 Bibliography

[1] Thomas, S.K.; Cassoni, R.P.; MacArthur, C.D. Aircraft Anti-Icing and De-Icing Techniques and Modeling. J. Aircr. 1996, 33, 841–854

[2] Yamazaki,M.;Jemcov,A.; Sakaue, H. A Review on the Current Status of Icing Physics and Mitigation in Aviation. Aerospace 2021, 8, 188. https://doi.org/10.3390/ aerospace8070188

[3] Oliver, M.J. Validation Ice Crystal Icing Engine Test in the Propulsion Systems Laboratory at NASA Glenn Research Center. In Proceedings of the 6th AIAA Atmospheric and Space Environments Conference, Atlanta, GA, USA, 16–20 June 2014

[4] Le Bot, C., 2004: SIGMA: System of Icing Geographic Identification in Meteorology for Aviation. Preprints, 11th Conf. on Aviation Range and Aerospace Meteorology, Hyannis, MA, Amer. Meteor. Soc., P6.5. [Available online at http://ams. Confex.com/ams/pdfpapers/81704.pdf]

[5] Ben C. Bernstein, Christine Le Bot, An Inferred Climatology of Icing Conditions Aloft, Including Supercooled Large Drops. Part II: Europe, Asia, and the Globe, Journal of Applied Meteorology and Climatology 2009, DOI: https://doi.org/10.1175/2009JAMC2073.1, Page(s): 1503–1526

[6] Bernstein, B. C., M. K. Politovich, B. G. Brown, T. P. Ratvasky, D. R. Miller, C. A. Wolff, and G. Cunning, 2005: Current Icing Potential (CIP): Algorithm description and comparison with aircraft observations. J. Appl. Meteor., 44, 969–986

[7] Stewart G. Cober, George A. Isaac, Alexei V. Korolev, and J. Walter Strapp, Assessing Cloud-Phase Conditions, Journal of Applied Meteorology and Climatology 2001, DOI: https://doi.org/10.1175/1520-0450(2001)040<1967:ACPC>2.0.CO;2, Page(s): 1967–1983

[8] Inès Vongpasseut, Florian Mequignon, Christine Le Bot, Christian Pagé , Emilia Sanchez-Gomez, Study of icing conditions over Europe from atmospheric reanalysis, CERFACS presentation 2022

[9] Christian Pagé, Emilia Sanchez-Gomez, Jules Boulard, Tom Cocogne, Perrine Abjean, Inès Vongpaseut, Florian Mequignon, Coralie Février, Climate Change and Aviation In-flight icing, CERFACS presentation 2023

[10] Kallberg, P., A. Simmons, S. Uppala, and M. Fuentes, 2004: The ERA-40 archive. ECMWF Tech. Rep., ERA-40 Project Rep. Series 17, 31 pp. [Available online at http://www.ecmwf.int.]

[11] Chapman, M. B., A. Holmes, and C. Wolff, 2006: Verification of aviation icing algorithms from the Second Alliance Icing Research Study. Preprints, 12th Conf. on Aviation Range and Aerospace Meteorology, Atlanta, GA, Amer. Meteor. Soc., 7B.3. [Available online at http://ams.confex.com/ams/ pdfpapers/104158.pdf.]

[12] Bernstein, B.C. , C. A. Wolff, and F. McDonough, 2007: An inferred clima- tology of icing conditions aloft, including supercooled large drops. Part I: Canada and the Continental United States. J. Appl.

Meteor. Climatol., 46, 1857–1878.

[13] Bernestein, B.C., M. K. Politovich, B. G. Brown, T. P. Ratvasky, D. R. Miller, C. A. Wolff, and G. Cunning, 2005: Current Icing Potential (CIP): Algorithm description and comparison with aircraft observations. J. Appl. Meteor., 44, 969–986.

[14] Guan, H., S. G. Cober, and G. A. Isaac, 2001: Verification of su- percooled cloud water forecasts with in situ aircraft mea- surements. Wea. Forecasting, 16, 145–155.

[15] Brown, B. G., G. Thompson, R. T. Bruintjes, R. Bullock, and T. Kane, 1997: Intercomparison of in-flight icing algorithms. Part II: Statistical verification results. Wea. Forecasting, 12, 890–914

[16] Cortinas, J. V., Jr., B. C. Bernstein, C. C. Robbins, and J. W. Strapp, 2004: An analysis of freezing rain, freezing drizzle, and ice pellets across the United States and Canada: 1976–90. Wea. Forecasting, 19, 377–390

F Appendix – Task Force #3: Artificial Intelligence

F.1 Results of the state-of-the-art review for the Unmanned Aircraft Systems (UAS)/Innovative Air Mobility (IAM) domains

Overview of available papers

The state-of-the-art review in the context of UAS/IAM was classified according to the following categories: UAS autonomy, UAS automation and advanced automation. The literature review considered publications in the Scopus database based on the following keywords:

- «Autonomous UAV» – 7.847 results
- «Autonomous MAV» – 863 results
- «Autonomous UAV» & «Autonomous MAV» – 699 results
- «Autonomous drone» – 2.580 results
- «Autonomous UAV» & «Autonomous drone» – 1.971 results

One difficulty is that this constitutes a vast and rapidly growing literature (7.847 documents available):

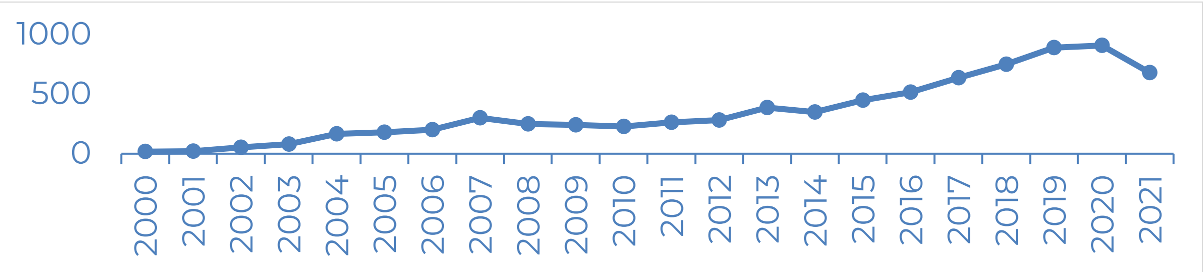

In terms of geographic distribution, US and China are significantly more active than the EU:

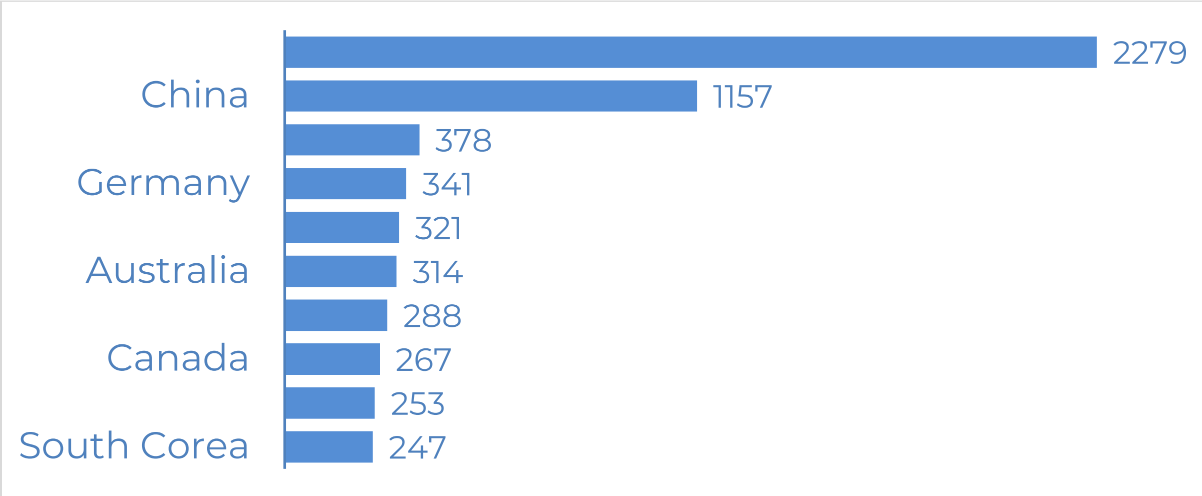

Revised search strategy consisted in refining the search to years 2015-2021 focusing on journal and conference papers, which refined the number of results to 359, with the following distribution by university:

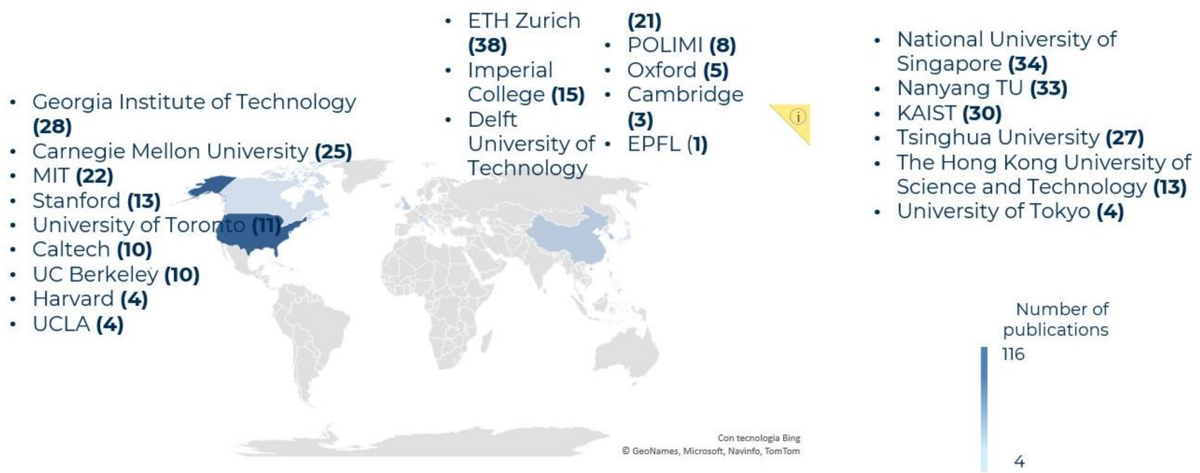

And a more balanced distribution at this level:

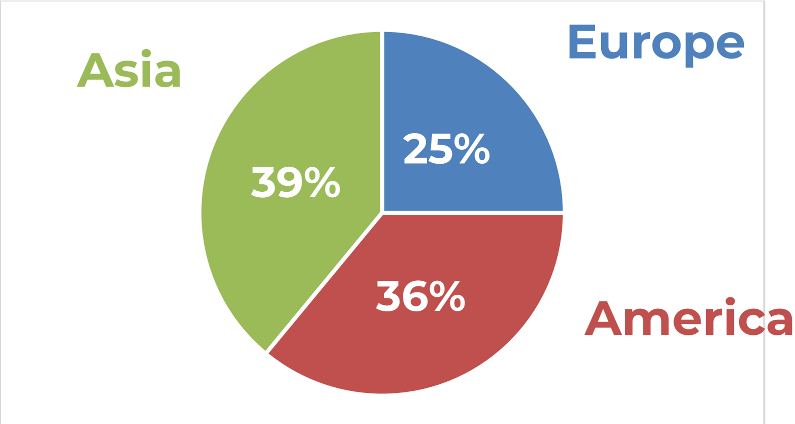

The papers can be classified under the following categories, 'Navigation' being the most active one, followed by 'Planning and Vision':

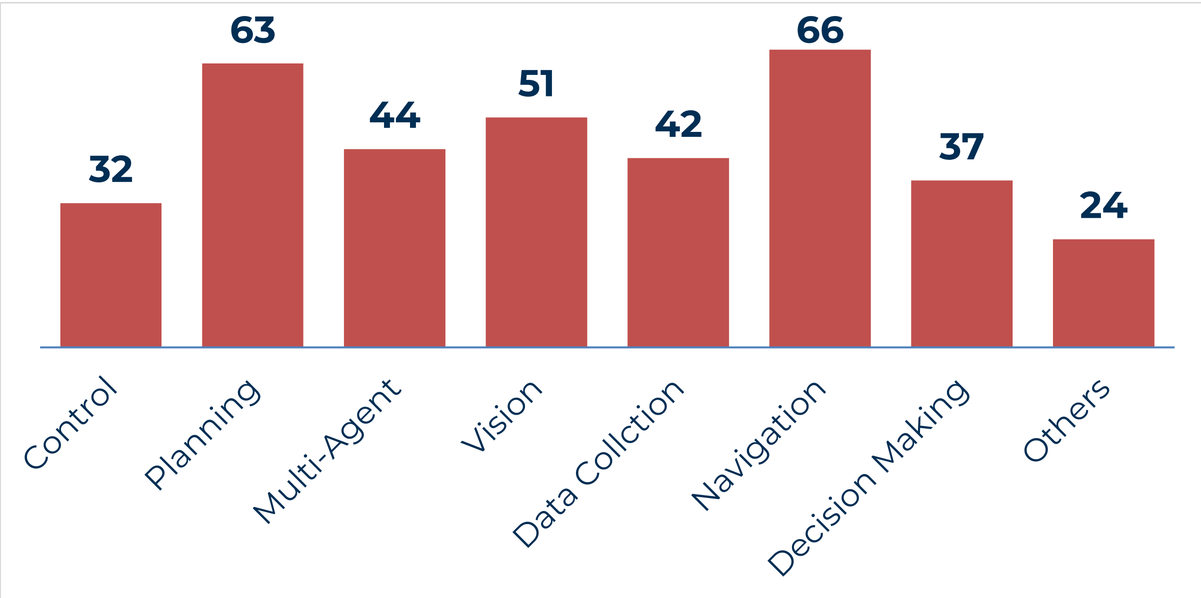

In the analysis of categories versus geography, no strong correlation emerges:

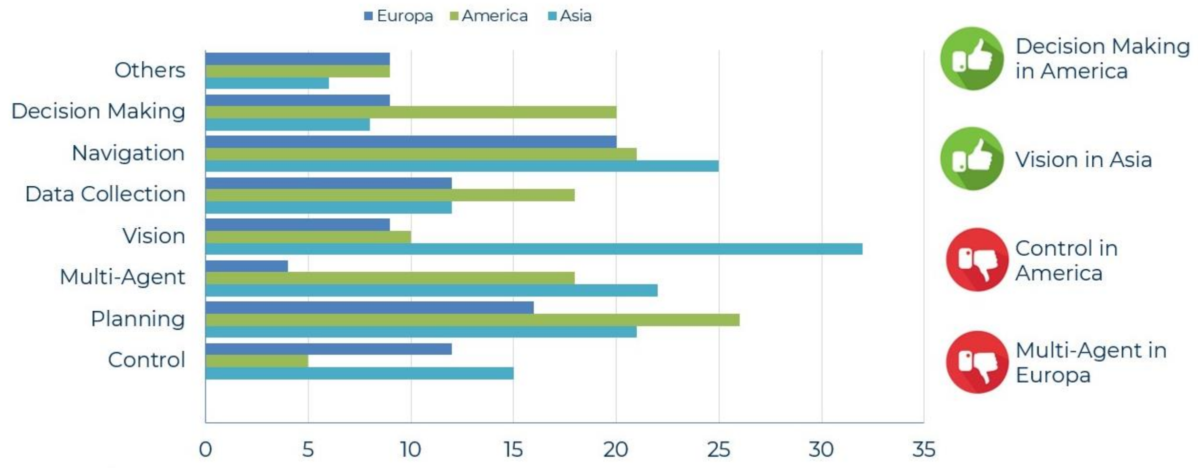

Conclusion:

- Scientific and technological research in the field is increasing rapidly
- Prevalence of categories such as Navigation, Planning and Vision
- Decision Making and Multi-Agent categories still growing

Available definitions for the domain

In order to analyse the definitions , the search from Polimi (Marco Lovera, Gabriele Roggi) has been completed on EASA side (Guillaume Soudain) by are view of the available regulations and standards. In terms of definitions, most publications refer to autonomy, without real distinction with the term automation. Advanced automation does not appear consistently.

Definition of automation		
No.	Author(s) and Year	Definition
1	(EASA, 2023)	The use of control systems and information technologies reducing the need for human input, typically for repetitive tasks.
2	(EASA, 2020)	An automatic drone flies pre-determined routes defined by the drone operator before starting the flight. For this type of drone, it is essential for the remote pilot to take control of the drone to intervene in unforeseen events for which the drone has not been programmed.
3	(SAE, 2021)	The performance by hardware/software systems of part or all of the [tasks] on a sustained basis.
4	(ECA, 2020)	Technique, method, system of operation or controlling a process by a highly automatic means, reducing human intervention to a minimum
Definition of advanced automation		
1	(EASA, 2023)	The use of a system that, under specified conditions, functions without human intervention.

2	(ECA, 2020)	ECA finds the use of the word “autonomous” often somewhat inflated, when the system referred to is not autonomous, but rather highly (perhaps fully) automated.
3	(National Research Council, 2014)	NASA does not define automation, but defines advanced automation/autonomy through a set of characteristics (table 1.1).
Definition of autonomy		
1	(EASA, 2023)	Characteristic of a system that is capable of modifying its intended domain of use or goal without external intervention, control or oversight.
2	(EASA, 2020)	An autonomous drone is able to conduct a safe flight without the intervention of a pilot. It does so with the help of artificial intelligence, enabling it to cope with all kinds of unforeseen and unpredictable emergency situations.
3	(NIST, 2008)	An Unmanned System’s (UMS) own ability of integrated sensing, perceiving, analyzing, communicating, planning, decision-making, and acting/executing, to achieve its goals as assigned by its human operator(s) through designed Human-Robot Interface (HRI) or by another system that the UMS communicates with. UMS’s Autonomy is characterized into levels from the perspective of Human Independence (HI), the inverse of HRI. Autonomy is further characterized in terms of Contextual Autonomous Capability (CAC)
4	(Kendoul, 2013)	The condition or quality of being self-governing.
5	(NATO RTO, 2002)	The capability to make decisions.
6	(SAE, 2021)	Systems that have the ability and authority to make decisions independently and self-sufficiently. Over time, this usage was casually broadened to not only encompass decision making, but to represent the entire system functionality, thereby becoming synonymous with automated.
7	(ICAO, 2022)	An unmanned aircraft that does not allow for pilot intervention in the management of the flight.
8	(ECA, 2020)	Autonomous aircraft: An unmanned aircraft that does not allow pilot intervention in the management of the flight

Table 1. Summary of the reviewed studies about issues automation / advanced automation / autonomy in UAS/IAM

Conclusion:

- The term « autonomy » is often used in lieu and place of « automation / advance automation » in most of the UAS/UAM related papers.
- The automation schemes identified in UAS/UAM rarely go as far as « full autonomy », mentioning the human in most of the « full automation » definitions.
- There are no mention of full autonomous UAS/UMS in the litterature (most probably due to limitation in current regulations).

Overview of the classification schemes applicable for the domain

No.	Author(s) and Year	**Schemes for UAS**	**The EASA AI Levels**
1	(SAE, 2021)	Level 0 to 5	See mapping in conclusion table
2	(JARUS, 2023)	Level 1 to 5 adapted from SAE J3016	See mapping in conclusion table

3	(ICAO, 2022)	Using the JARUS scheme	See mapping in conclusion table
4	(NIST, 2008)	Based on notion of Contextual Autonomous Capability (CAC)	See mapping in conclusion table
5	(NATO RTO, 2002)	Progression of Operator Authority and Computer Autonomy (PACT) 4 levels (Assisted -> Automatic)	See mapping in conclusion table
6	(ECA, 2020)	Refined the SAE scheme to a 6 level scheme	See mapping in conclusion table
7	(NASA, 2018)	Automation scheme based on 10 Sheridan levels and SAE J3016	n/a

Table 2. Summary of the reviewed studies about comparing schemes for UAS/IAM with the EASA AI Levels

Conclusion:

Level of AI (EASA AI Roadmap and Concept Paper)	UAS (JARUS AutoMethod 1.0)	UAM/UAS (NIST ALFUS V1.0)	PACT (NATO R&T)	UAS (ECA paper)	Automotive (SAE J3016) For reference	Applicable EASA Concept Paper Guidance			
						ET	AIA	HF	SRM
Level 1A - Human augmentation	Level 1 – Assisted operations	Low Contextual Autonomous Capability (CAC)	Assisted – At Call / Advisory	-	Level 0 – no driving automation				
Level 1B - Human cognitive assistance	-	-	Assisted – In Support	-	-				
Level 2A - Human-AI cooperation	Level 2/3: Task reduction / supervised automation	Mid CAC	Assisted – Direct Support / Automatic	Level 1/2/3 – Pilot Assistance / Partial / Conditional automation	Level 1/2 – Assistance / Partial automation				
Level 2B - Human-AI collaboration	-	-	-	-	-				
Level 3A – Supervised advanced automation	Level 4: Manage by Exception	High CAC	Automatic	Level 4/5 – High Automation / Full Automation	Level 3 - Conditional automation				
Level 3B – Non-supervised advanced automation	Level 5: Full automation	Highest CAC	-	-	Level 4 – High automation				Extended AI SRM
Level 3C – Autonomous AI	-	-	-	-	Level 5 – Full automation				

Estimation of the maturity of available papers and guidance in the domain

Note: considering the mixed nature of the reviewed papers (regulatory support, research papers), the maturity scale has not been used in this UAS/IAM review.

Examples of applications and implementations in the domain

No.	Author(s) and Year	Examples
1	(Kendoul, 2013)	Smart Skies CSIRO autonomous robotic helicopter
2	(NIST, 2008)	Defense domain (war fighting, surveillance, medical assistance and logistic support, border security, bomb disposal) Production support and Urban Search and Rescue robots
3	(Baomar & Bentley, 2017)	Intelligent Autopilot System (IAS) which is capable of autonomous landing, and go-around of large jets such as airliners under severe weather conditions
4	(Sa, 2017)	Visual-inertial drone
5	(Xu, 2021)	Autonomous UAV Exploration of Dynamic Environments
6	(Warren, 2018)	Visual Teach and Repeat for Emergency Return of Multirotor UAVs During GPS Failure

Table 3. Summary of the reviewed studies about examples of applications and implementations in UAS/IAM

Available regulations, guidance material, standards

No.	Author(s) and Year	Regulations
1	EASA	EU Regulations 2019/947 and 2019/945
2	(EASA, 2023)	Pre-rulemaking exploratory guidance from EASA in form of a Concept Paper for Level 1 & 2 Machine Learning Applications

Table 4. Summary of the reviewed studies about regulations in UAS/IAM

Conclusion:

The main regulations are the EU regulations 2019/947 and 2019/945 published for drones, considering that advanced automation/autonomy is not feasible in the open category and should be managed under the specific category.

The EASA AI Concept Paper upcoming Issue 03 will deal specially with Level 3 AI and advanced automation. Through Rulemaking activities, the subsequent versions of the AI Concept Paper will be turned into a set of rules and acceptable means of compliance (AMCs) unde the frame of RMT.0742.

Standards are under development, e.g. under the frame of the joint EUROCAE /SAE WG-114/G-34.

Summary of anticipated important directions for the EASA AI Roadmap (Level 3 AI)

After analyzing the literature, it can be concluded that:

- The term « autonomy » is often used in lieu and place of « automation / advance automation » in most of the UAS/UAM related papers. The automation schemes identified in UAS/UAM rarely go as far as « full autonomy », mentioning the human in most of the « full automation » definitions.
- The current classification scheme proposed by EASA AI Concept Paper fits rather well the capability to map to the various automation schemes. It presents the advantage of clear boundary definitions which is not always the case with the automation schemes, where some imprecise criteria blur some of the boundaries.
- Team work (collaboration at Level 2B) is rather absent (possibly because of the focus on the UAS/IAM domain), but it should be present.
- The notion of Mission Complexity / Environment Complexity (EC/MC) form ALFUS could be the basis for the SRM building-block extension.

Bibliography

Baomar, H., & Bentley, P. J. (2017). *Autonomous landing and go-around of airliners under severe weather conditions using Artificial Neural Networks.*

Bijjahalli, S. e. (2020). *Advances in intelligent and autonomous anivgation systems for small UAS.*

EASA. (2020). *What is the difference between autonomous and automatic drone - FAQ n.116449.*

EASA. (2023). *Concept Paper : Guidance for Level 1 & 2 machine learning applications - Proposed Issue 02.* Cologne: European Union Aviation Safety Agency (EASA).

EASA. (2023). *EASA Artificial Intelligence Roadmap 2.0.* Cologne: European Union Aviation Safety Agency (EASA).

ECA. (2020). *Briefing Paper: Unmanned Aircraft Systems and the concepts of Automation and Autonomy.*

ICAO. (2022). *AUTOMATION AND THE CHANGING ROLE OF THE PILOT.*

JARUS. (2023). *Methodology for Evaluation of Automation for UAS Operations.*

Kendoul, F. (2013). *Towards a Unified Framework for UAS Autonomy and Technology Readiness Assessment (ATRA).*

NASA. (2018). *Assurance Reasoning for Increasingly Autonomous Systems.*

National Research Council. (2014). *Autonomy Research for Civil Aviation: Toward a New Era of Flight.*

NATO RTO. (2002). *Capability, Cognition and Autonomy.*

NIST. (2008). *Autonomy Levels for Unmanned Systems (ALFUS) Framework.*

Sa, I. K. (2017). Build your own visual-inertial drone: A cost-effective and open-source autonomous drone. *IEEE Robotics & Automation Magazine, 25(1), 89-103*, 25(1), 89-103.

SAE. (2021). *J3016 Taxonomy and Definitions for Terms Related to Driving Automation Systems for On-Road Motor Vehicles.*

Warren, M. G. (2018). There's No Place Like Home: Visual Teach and Repeat for Emergency Return of Multirotor UAVs During GPS Failure. *IEEE Robotics and automation letters*, 4(1), 161-168.

Xu, Z. D. (2021). Autonomous UAV Exploration of Dynamic Environments Via Incremental Sampling and Probabilistic Roadmap. *IEEE Robotics and Automation Letters*, 6(2), 2729-2736.

F.2 Results of the state-of-the-art review for the Railway domain

Overview of available papers

The state-of-the-art **review in the context of the railway** was classified according to the following issues: **autonomy in the railway, automation in the railway and advanced automation in the railway**. The literature review contains 104 publications.

There are no advanced publications describing the use of artificial intelligence in fully autonomous trains.

Number of papers available:

number of papers initially selected for the literature review (SCOPUS, WoS, mdpi databases) exceeds 1,000 items.
advanced automation railway and automation railway – 94
autonomy railway – 10

The following keywords were used: *Railway Automation, Autonomous train, Driverless train, Railway Optimization, Particle swarm algorithm in railway, Genetic Algorithm in railway, Fuzzy logic in railway, Neural Network in railway, Reinforcement learning method in railway, Deep learning in railway, Ant Colony Optimization in railway, Unattended train*.

Available definitions for the domain

Four grades of automation are used, but automation in the railway is now based mainly on the second degree. The second degree determines semi-automated train operation, where most operations are automated, like speed control and braking. However, an onboard driver is still required to start and stop the train.

Automation in the railway: some operations, such as starting and stopping or changing the rail tracks are automated, but on-board operator is needed (**GoA2**)

Advanced automation in the railway: autonomous train operations are possible, but in case of emergency on-board operator takes control (**GoA3**)

Autonomy in the railway: train runs fully autonomous with no onboard operator (**GoA4**)

The definitions in the domain of automation / advanced automation / autonomy in railway transport are summarised in Table 1.

Definition of automation		
No.	*Author(s) and Year*	*Definition*
1	Singh et. al., 2021	According to the four grades of automation (GoAs): GoA2: Some of the train operations, such as starting train, stopping, changing the rail tracks, are automated but an onboard driver is still needed.
8	Lagay et. al., 2018	GoA2: traction and braking automatically by the ATO system which is added to the ATP system separately to ensure the overall safety level. The driver ensures the environment monitoring and is able to switch towards manual driving if necessary.

9	Habib et. al., 2021	GoA-2 is characterized by the manual driving of the train with ATP and ATO systems (most common today), the driver operates the doors and starts the train. The system is responsible for controlling the speed and stopping the train at the stations. The train driver must be ready to take over control at any time and handle emergency situations.
10	Gadmer et. al., 2022	GoA-2: The driver is still present within the train's cabin and makes sure nothing will disrupt the course of the train (obstacles, defects on the infrastructure, …). The autonomous system will, however, perform the driving activity by controlling the thrusting and braking of the train and respecting timetables and signalling.
		Definition of advanced automation
1	Singh et. al., 2021	According to the four grades of automation (GoAs): GoA3: This level provides autonomous train operations, but in case of an emergency an onboard attendant takes control of the train.
8	Lagay et. al., 2018	GoA3: autonomous driving with onboard staff. The ATO system provides all driving functions including environment monitoring (including signal recognition and obstacle detection) which is completely automatized. Onboard staff provide customized functions depending on the railway company (railway undertaking), e.g. open and closing doors.
10	Gadmer et. al., 2022	GoA-3:There is no more driver within the train's cabin. The autonomous system performs the driving activity and detects any external event that requires action on the train (braking, whistles, communication, …). However, there is still a train attendant able to perform security procedures and managed degraded modes.
		Definition of autonomy
4	Trentesaux et. al., 2018	The GOA4 is unattended train operation. It corresponds to a fully automated train or metro. Autonomous: it is the decision-making capability, enabling the train to adapt to different situations that makes a train autonomous and not automatic.
5	Gely et. al., 2020	An autonomous train: an autonomous train is a train able to fulfill at least an assigned complete transportation mission from one railway station to another in an open environment. It must thus be able to perceive, analyze, decide and act in an autonomous manner while interacting with its environment. In addition to this mission, an autonomous train can fulfill related integrated logistics functions enabling it to maintain its level of availability, maintainability and safety in conjunction with maintenance centers and organizations. It may be able to learn from training and from simulated or real experiences (supervised and unsupervised learning)".
11	Lagay et. al., 2018	GoA4: completely autonomous driving without onboard staff. All unexpected situations are handled by the ATO system along with the ATS system that operates as the traffic management system (TMS).
13	Gadmer et. al., 2022	GoA4 There is no more train attendant able to drive the train if necessary. The train is completely autonomous. A supervising center can communicate with the train and manage eventual degraded modes and drive the train remotely.

Table 1. Excerpt from the reviewed studies about automation / advanced automation / autonomy in railway

Overview of the classification schemes applicable for the domain

Levels 3A, 3B and 3C of Artificial intelligence might be compared with the railway's automation grades (Table 2).

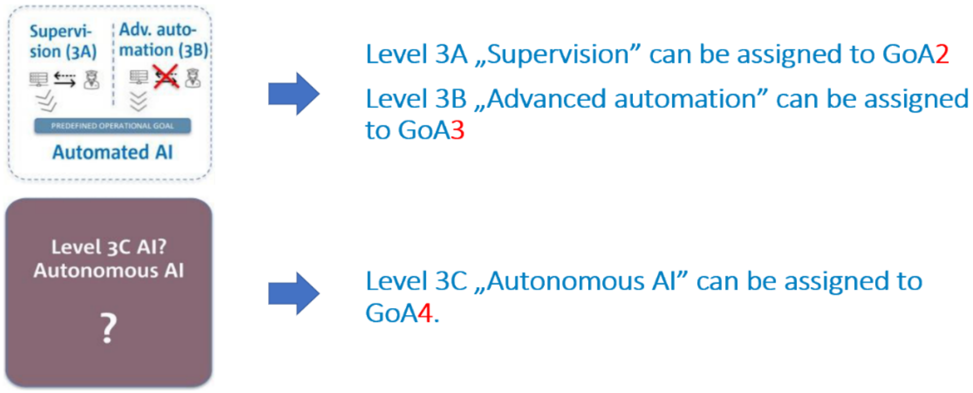

Level 3A, Supervision, can be assigned to the second degree of automation, while Level 3B, Advanced automation, to the third degree. Level 3C can be assigned to the fourth degree of automation when artificial intelligence algorithms should do all operations. Crew supervision is not necessary. Neural networks and machine learning are proposed at this level for complex decision-making.

No.	Author(s) and Year	**Schemes for railway**	**The EASA AI Levels**
1	Singh et. al., 2021	Four levels of automation have been defined: GoA1-GoA4.	Level 3A Supervision can be assigned to GoA2, Level 3B Adv. automation can be assigned to GoA3, Level 3C can be assigned to GoA4.
7	Mohammed et. al., 2014	The grades of automation (GoA2, GoA3, GoA4) are corresponding to Semi-automated Train Operation (STO), Driverless Train Operation (DTO), and Unmanned Train Operation (UTO).	Level 3A Supervision can be assigned to GoA2, Level 3B Adv. automation can be assigned to GoA3, Level 3C can be assigned to GoA4.
9	Gadmer et. al., 2022	Four levels of automation have been defined: GoA1-GoA4.	Level 3A Supervision can be assigned to GoA2, Level 3B Adv. automation can be assigned to GoA3, Level 3C can be assigned to GoA4.

Table 2. Excerpt from the reviewed studies about comparing schemes for railway with the EASA AI Levels

Estimation of the maturity of available papers and guidance in the domain

The maturity of the concepts presented in the reviewed works should be considered high. Due to objectively easier implementation conditions, the development of automatic and autonomous railway vehicle traffic systems began earlier and continues on an evolutionary basis.

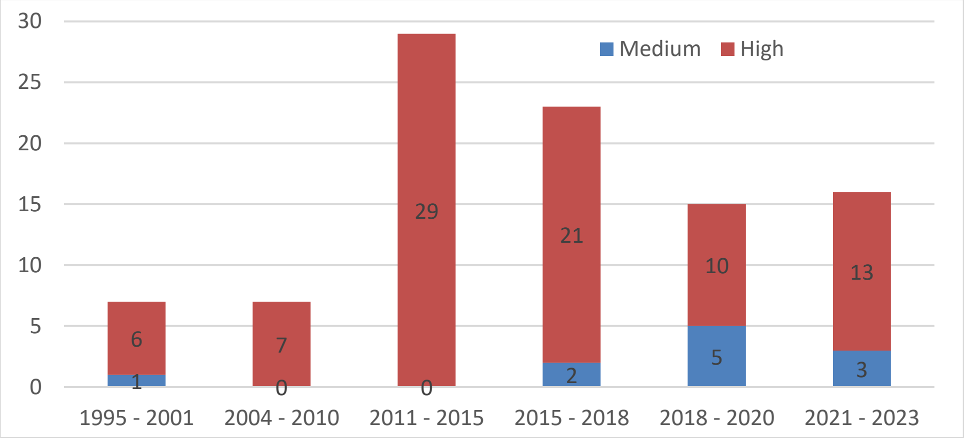

The subject of the publication focused on artificial intelligence algorithms. Various research topics were discussed, e.g. minimization of energy and travel time, characteristics of autonomous train, energy saving, train speed profile optimization. The representation of papers according to the maturity of technology grade is presented in Table 3.

No.	Medium	High
1995	-	Sekine et. al., 1995; Sekine et. al., 1995
1997	-	Chang et. al., 1997
1999	-	Han et. al., 1999; Huang et. al., 1999
2000	-	Fay, 2000
2001	Matsumoto et. al., 2001	-
2004	-	Wong and Ho 2004
2005	-	Zhu et. al., 2005
2008	-	Chuang et. al., 2008
2009	-	Fu et. al., 2009
2010	-	Lechelle et. al., 2010; Dong et. al., 2010; Kim, S. Chien 2010
2011	-	DING et. al., 2011; Lu & Feng 2011; Lin and Sheu 2011
2012	-	McClanachan, Cole 2012; Yang et. al., 2012; Sun and Xu 2012; Cucala et. al., 2012; Carvajal-Carreño et. al., 2012
2013	-	Lu et. al., 2013; Chen et. al., 2013; Xiao et. al., 2013; Dong et. al., 2013; Wang et. al., 2013
2014	-	Yin et. al., 2014; Su et. al., 2014; Sicre et. al., 2014; Domínguez et. al., 2014; Li et. al., 2014; Bai et. al., 2014; Carvajal-Carreño et. al., 2014; Rong, Yu 2014; Zhang et. al., 2014
2015	-	Barman et. al., 2015; Gao et. al., 2015; Zhao et. al., 2015; ShangGuan et. al., 2015; Tang et. al., 2015; Fernández-Rodríguez et. al., 2015; Keskin and A. Karamancioglu. 2015
2015	Cohen et. al., 2015	-
2016	-	Song et. al., 2016; Yang et. al., 2016; Huang et. al., 2016; Brenna et. al., 2016; Yin et. al., 2016; Hamid et. al., 2016
2016	Wang et. al., 2016	-
2017	-	Scheepmaker et. al., 2017; Yang et. al., 2017; Lesel et. al., 2017; Zhao et. al., 2017; Keskin, Karamancioglu 2017
2018	-	Liu et. al., 2018; Rocha et. al., 2018; Wang et. al., 2018; Huang et. al., 2018; Ning et. al., 2018; Jia et. al., 2018; Fernández-Rodríguez et. al., 2018; Fernández-Rodríguez et. al., 2018; Zhi-yu et. al., 2018; Gao et. al., 2018
2018	Trentesaux et. al., 2018	-

No.	Medium	High
2019	-	Zhang et. al., 2019; Liang et. al., 2019; Feng et. al., 2019; Fernández et. al., 2019; Lu et. al., 2019; Fernández-Rodríguez et. al., 2019
2019	Corlu et. al., 2019	-
2020	-	Li et. al., 2020; Kuppusamy et. al., 2020; Yin et. al., 2020; Pan et. al., 2020
2020	Gely et. al., 2020; Kulkarni et. al., 2020; Dimitrova et. al., 2020	-
2021	-	Singh et. al., 2021; Liao et. al., 2021; Liu et. al., 2021
2022	-	Zongyi et. al., 2022; Li et. al., 2022; Arikan et. al., 2022
2022	Peleska et. al., 2022; Besinovic et. al., 2022	-
2023	-	Zongyi et. al., 2023; Song et. al., 2023; Lu et. al., 2023; Lin et. al., 2023; Sandidzadeh, Havaei, 2023; Zhang et. al., 2023; Kaleybar et. al., 2023
2023	Jansson et. al., 2023	-

Table 3. Summary of the reviewed studies about an estimation of the maturity of available papers and guidance in railway

1) Review articles. These articles present a comprehensive approach to the problem of railway automation and autonomy. Additionally, mathematical models illustrating the movement of autonomous or automated vehicles were explained. An essential part of the literature review in these publications is the characterization of algorithms and methods managing the movement of vehicles with advanced automation or autonomous vehicles. The publications emphasize that artificial intelligence algorithms play a decisive role. Most publications present examples of lines on which autonomous or automatic trains were introduced.
2) Articles describing mathematical models and AI algorithms. Models and algorithms in these publications are presented in a very advanced way. These works explain the principle of operation of algorithms in specific research problems. Additionally, a method of verifying these algorithms was shown, confirming their high effectiveness in controlling autonomous or automatic trains.
Medium – Articles without describing mathematical models or AI algorithms. The articles generally describe the topic of autonomous and automatic trains.
Low - the rest of the articles not included in the high and medium categories.

Examples of applications and implementations in the domain

The literature provides examples of successful implementations of AI algorithms in operational conditions as well as computer simulations. The results in general confirmed high effectiveness of these algorithms (table 4):

- In the Pilbara region of Western Australia
- The genetic algorithm was applied on a real Spanish high-speed line.
- Driverless Train Operation in France, Korea, Singapore
- The Guangzhou Haizhu tramway
- Beijing subway Changping line
- The Shanghai Metro Line One

Year	Author(s) and Year	**Examples**
1995	Sekine et. al., 1995; Sekine et. al., 1995	computer simulation
1997	Chang et. al., 1997	computer simulation
1999	Huang et. al., 1999; Han et. al., 1999	computer simulation
2000	Fay, 2000	computer simulation
2001	Matsumoto et. al., 2001	the Yamanote and Keihin Tohoku Lines
2004	Wong and Ho 2004	computer simulation
2005	Zhu et. al., 2005	route Xianqian by Guangzhou Railway Group
2008	Chuang et. al., 2008	computer simulation
2009	Fu et. al., 2009	computer simulation
2010	Lechelle et. al., 2010	computer simulation
2010	Dong et. al., 2010	Development of high-speed rail traffic in China.
2010	Kim, S. Chien 2010	Implemented in the New Haven line of the Metro-North Commuter Railroad
2011	Lin and Sheu 2011; Lu & Feng 2011; DING et. al., 2011	computer simulation
2012	Carvajal-Carreño et. al., 2012	An interstation in Line 3 of Metro de Madrid
2012	Sun and Xu 2012; Yang et. al., 2012	computer simulation
2012	Cucala et. al., 2012	the Spanish high speed line Madrid–Barcelona
2013	Wang et. al., 2013; Dong et. al., 2013; Xiao et. al., 2013; Chen et. al., 2013; Lu et. al., 2013	computer simulation
2014	Carvajal-Carreño et. al., 2014	a case study of Metro de Madrid
2014	Domínguez et. al., 2014	Beijing subway Changping line is provided as an example – computer simulation
2014	Zhang et. al., 2014; Rong, Yu 2014; Su et. al., 2014; Yin et. al., 2014	computer simulation
2014	Li et. al., 2014	Data of Beijing Metro Yizhuang Line of China – computer simulation.
2014	Sicre et. al., 2014	The genetic algorithm was applied on a real Spanish high speed line.
2014	Bai et. al., 2014	The system is tested on the Ning'xi line in China.

Year	Author(s) and Year	**Examples**
2015	ShangGuan et. al., 2015	case studies are presented based on the data from Beijing-Shanghai High-speed Railway in China
2015	Keskin and A. Karamancioglu. 2015; Zhao et. al., 2015; Gao et. al., 2015	computer simulation
2015	Fernández-Rodríguez et. al., 2015	real data from a Spanish high speed line - computer simulation
2015	Tang et. al., 2015	simulation section is a part of the Xi'an metro line in China.
2015	Cohen et. al., 2015	UTO for Paris metro
2016	Hamid et. al., 2016; Brenna et. al., 2016; Huang et. al., 2016; Yang et. al., 2016; Song et. al., 2016	computer simulation
2016	Wang et. al., 2016	Driverless Train Operation in France, Korea, Singapore.
2016	Yin et. al., 2016	Yizhuang Line of Beijing Subway - computer simulation
2017	Keskin, Karamancioglu 2017	A particular segment of Eskisehir Urban Rail Network was taken into account for the case study.
2017	Zhao et. al., 2017	China's Guangzhou metro line 7
2017	Yang et. al., 2017; Scheepmaker et. al., 2017	computer simulation
2017	Lesel et. al., 2017	Simulation results based on experiments conducted on Torino metro line
2018	Jia et. al., 2018	a real-world instance of Beijing–Tianjin Intercity Railway
2018	Gao et. al., 2018; Zhi-yu et. al., 2018; Ning et. al., 2018; Wang et. al., 2018; Rocha et. al., 2018; Liu et. al., 2018	computer simulation
2018	Huang et. al., 2018	From Huagong Station to the Jiulongshan Station - computer simulation
2018	Fernández-Rodríguez et. al., 2018	real data from a Spanish high speed line
2019	Lu et. al., 2019	based on the real data of Yizhuang Line, Beijing Subway
2019	Zhang et. al., 2019	computer simulation
2019	Fernández-Rodríguez et. al., 2019	data from a Spanish high-speed line
2019	Feng et. al., 2019	Data were collected from the No. 2 metro line in Nanjing, China - computer simulation
2019	Liang et. al., 2019	Shanghai Metro Line 11 - computer simulation
2020	Li et. al., 2020	computer simulation – case study of the Chengdu Metro
2020	Kuppusamy et. al., 2020	Model is simulated using Chennai Metro Train Station.
2020	Kulkarni et. al., 2020	The driverless train on Tyne and Wear Metro
2020	Pan et. al., 2020	Xinjiang section of the Lanzhou–Xinjiang high-speed railway in China
2021	Liu et. al., 2021	computer simulation
2021	Liao et. al., 2021	the Shanghai Metro Line One - computer simulation
2021	Singh et. al., 2021	Use of autonomous trains: - In the Pilbara region of Western Australia, mining corporation ``Rio Tinto'' has moved to driverless fully autonomous operations for its entire rail system (heavy haul) in June 2019., - The Société Nationale des Chemins de Fer Français (SNCF), the French National Railway, successfully finished the first test using a locomotive-hauled AT that was remotely controlled in July 2019.
2022	Li et. al., 2022	computer simulation
2022	Zongyi et. al., 2022	The Guangzhou Haizhu tramway is taken as an example to illustrate the effectiveness of the developed method.

Year	Author(s) and Year	**Examples**
2022	Arikan et. al., 2022	the whole line of the Ankaray - computer simulation
2023	Zhang et. al., 2023	computer simulation
2023	Lu et. al., 2023	computer simulation based on the urban rail transits in Nanning, China
2023	Lin et. al., 2023	data of Beijing–Guangzhou Railway Line and HXD1B electric locomotive - computer simulation
2023	Zongyi et. al., 2023	Guangzhou Metro Line 7 is taken as an example to verify the effectiveness of the developed optimization model.
2023	Sandidzadeh, Havaei, 2023	Simulations are conducted using the route information of Tehran Metro Lines 3, 5, and Shiraz Metro Line 1.

Table 4. Summary of the reviewed studies about examples of applications and implementations in railway

Available regulations, guidance material, standards (if applicable)

The applicable standards in the area of Artificial Intelligence (Table 5):

- The International Electro-Technical Commission (IEC) standard IEC 62290-1 - in which the four grades of automation were defined.
- ANSI/UL 4600 provides a way to assess the safety case for an autonomous vehicle. This was the first comprehensive standard for public road autonomous vehicle safety to cover both urban and highway use cases.

No.	Author(s) and Year	**Regulations**
1	Wang et. al., 2016	IEC 62290-1 (2006) Railway applications: urban guided transport management and command/control systems. Part 1: system principles and fundamental concepts. International ElectroTechnical Commission, Geneva
2	Cohen et. al., 2015	IEC 62290-1 (2006) Railway applications: urban guided transport management and command/control systems. Part 1: system principles and fundamental concepts. International ElectroTechnical Commission, Geneva
3	Jansson et. al., 2023	IEC 62290-1 (2006)
4	Peleska et. al., 2022	ANSI/UL 4600 pre-standard
5	Habib et. al., 2021	IEC 62290-1 (2006)

Table 5. Summary of the reviewed studies about regulations in railway

Summary of anticipated important directions for the EASA AI Roadmap (Level 3 AI)

1. Available definitions of automation / advanced automation/autonomy used in the railway were the same as in EASA Roadmap 2.0. The railway uses four grades of automation (GoAs). GoA 2: Semi-automated train operation (according to the definition "automation" based on the EASA AI Roadmap), GoA3: This level provides autonomous train operations, but in case of an emergency an onboard attendant takes control of the train (according to the definition "advanced automation" based on the EASA AI Roadmap), GoA4: At this level, the train runs entirely

autonomous with no onboard driver/attendant (according to the definition "autonomy" based on the EASA AI Roadmap).

2. The classification schemes applicable for the railway are as follows: Level 3A Supervision can be assigned to GoA2, Level 3B Adv. automation can be assigned to GoA3, Level 3C can be assigned to GoA4.
3. Autonomous trains and trains with advanced automation use artificial intelligence algorithms such as neural networks, genetic algorithms, and machine learning algorithms. Further work in artificial intelligence should focus on improving optimization algorithms to generate optimal results. The optimization algorithms are heuristic algorithms that create a sub-optimal solution, not an optimal one. The optimization algorithms used should be improved. Optimization algorithms often determine train speed profiles' efficient energy use.
4. In most cases, algorithms AI are tested in a simulation environment.
5. Available regulations, guidance material, and standards used in railway:
    a. The International Electro-Technical Commission (IEC) standard IEC 62290-1 - in which the four grades of automation were defined.
    b. ANSI/UL 4600 provides a way to assess the safety case for an autonomous vehicle. The first edition was issued in April 2020, with a second edition published in March 2022. This was the first comprehensive public road autonomous vehicle safety standard to cover urban and highway use cases.
6. Experiences from rail transport can be used for rail transport but cannot be directly transferred.
7. Despite similarities in levels of autonomy, air transport is a more complex area of AI implementation.
8. AI algorithms support decision-making in problematic and controversial situations, e.g. accidents or random events.
9. Machine learning and deep neural networks are essential in this area.

Bibliography

P. Singh, M. A. Dulebenets, J. Pasha, E. D. R. S. Gonzalez, Y. -Y. Lau and R. Kampmann (2021). Deployment of Autonomous Trains in Rail Transportation: Current Trends and Existing Challenges. IEEE Access, vol. 9, pp. 91427-91461, doi: 10.1109/ACCESS.2021.3091550.

G. M. Scheepmaker, R. M. P. Goverde, and L. G. Kroon (2017). Review of energy-efficient train control and timetabling, Eur. J. Oper. Res., vol. 257, no. 2, pp. 355-376.

C. S. Chang, S. S. Sim (1997). Optimising train movements through coast control using genetic algorithms. Electric Power Applications, IEE Proceedings - 144 (1), 65–73.

S.A., Lechelle, Z. S. Mouneimne (2010). OptiDrive: A practical approach for the calculation of energy-optimised operating speed profiles. In: IET Conference on Railway Traction Systems. pp. 1–8.

S. Lu, Hillmansen, S., T. K. Ho, C. Roberts (2013). Single-train trajectory optimization. IEEE Transactions on Intelligent Transportation Systems 14 (2), 743–750.

J. Yin, D. Chen and L. Li (2014). Intelligent Train Operation Algorithms for Subway by Expert System and Reinforcement Learning. In IEEE Transactions on Intelligent Transportation Systems, vol. 15, no. 6, pp. 2561-2571, doi: 10.1109/TITS.2014.2320757.

D. Chen, R. Chen, Y. Li, and T. Tang (2013). Online learning algorithms for train automatic stop control using precise location data of balises. IEEE Trans. Intell. Transp. Syst., vol. 14, no. 3, pp. 1526–1535.

R. Su, Q. Gu, T. Wen (2014). Optimization of High-Speed Train Control Strategy for Traction Energy Saving Using an Improved Genetic Algorithm. Journal of Applied Mathematics. Volume 2014, Article ID 507308, 7 pages.

C. Sicre, A. P. Cucala, and A. Fernández-Cardador (2014). Real time regulation of efficient driving of high speed trains based on a genetic algorithm and a fuzzy model of manual driving. *Eng. Appl. Artif. Intell.*, vol. 29, pp. 79_92.

A. Fay (2000). *Fuzzy Knowledge-base system for railway traffic control*. Engineering Applications of Artificial Intelligence 13,719–729.

H. Dong, B. Ning, B. Cai and Z. Hou (2010). *Automatic Train Control System Development and Simulation for High-Speed Railways*. In IEEE Circuits and Systems Magazine, vol. 10, no. 2, pp. 6-18, doi: 10.1109/MCAS.2010.936782.

S.-H. Han, Y.-S. Byen, J.-H. Baek, T.-K. An, S.-G. Lee, and H.-J. Park (1999). *An optimal automatic train operation (ATO) control using genetic algorithms*. In Proc. IEEE Region 10 Conf. TENCON, vol. 1, pp. 360–362.

Y. Huang and S. Yasunobu (1999). *A practical design method of fuzzy controller based on control surface*. J. Jpn. Soc. Fuzzy Theory Syst., vol. 11, no. 5, pp. 841–847.

S. Sekine and M. Nishimurat (1995). *Application of fuzzy neural network control to automatic train operation*. In Proc. IEEE Int. Conf. Fuzzy Systems, 1995, vol. 5, pp. 39–40.

Y. Song and W. Song (2016). *A novel dual speed-curve optimization-based approach for energy-saving operation of high-speed trains*. IEEE Trans. Intell. Transp. Syst., vol. 17, no. 6, pp. 1564-1575.

H. Yang, K.-P. Zhang, and H.-E. Liu (2016). *Online regulation of high speed train trajectory control based on T-S fuzzy bilinear model*. IEEE Trans. Intell. Transp. Syst., vol. 17, no. 6, pp. 1496-1508.

H. Liu, C. Qian, Z. Ren, and G. Wang (2018). *Research on running curve optimization of automatic train operation system based on genetic algorithm*. In Proc. 3rd Int. Conf. Electr. Inf. Technol. Rail Transp. (EITRT), vol. 482, 2018, pp. 899-913.

Y. Wang, M. Zhang, J. Ma, and X. Zhou (2016). *Survey on driverless train operation for urban rail transit systems*. Urban Rail Transit, vol. 2, nos. 3-4, pp. 106-113.

Cohen JM, Barron AS, Anderson R, Graham DJ (2015) *Impacts of unattended train operations on productivity and efficiency in metropolitan railways*. Transportation Research Board of the National Academies, Washington, DC, pp 75–83.

X. Zongyi & Z. Junlin & Z. Zhenyu & Q. Yong & J. Limin (2022). *Energy consumption optimization of tramway operation based on improved PSO algorithm*. Energy, Elsevier, vol. 258(C).

Xing, Zongyi & Zhang, Zhenyu & Guo, Jian & Qin, Yong & Jia, Limin (2023). *Rail train operation energy-saving optimization based on improved brute-force search*. Applied Energy, Elsevier, vol. 330(PA).

H. Zhang, J. Limin, W. Li; X. Xinyue (2019). *Energy consumption optimization of train operation for railway systems*: Algorithm development and real-world case study. Journal of Cleaner Production, 214(), 1024–1037. doi:10.1016/j.jclepro.2019.01.023.

A. Rocha & A. Araújo & A. Carvalho & J. Sepulveda (2018). *A New Approach for Real Time Train Energy Efficiency Optimization*. Energies, MDPI, vol. 11(10), pages 1-21.

Y. Huang, C. Yang, S. Gong (2016). E*nergy Optimization for Train Operation Based on an Improved Ant Colony Optimization Methodology*. Energies, 9, 626.

M. Domínguez, A. Fernández-Cardador, A.P. Cucala, T. Gonsalves, A. Fernández (2014). *Multi objective particle swarm optimization algorithm for the design of efficient ATO speed profiles in metro lines*. Eng. Appl. Artif. Intell. 2014, 29, 43–53.

C. G. Corlu & R. de la Torre & A. Serrano-Hernandez & A. A. Juan & J. Faulin (2020). *Optimizing Energy Consumption in Transportation: Literature Review, Insights, and Research Opportunities*. Energies, MDPI, vol. 13(5), pages 1-33.

Chuang, H.J.; Chen, C.S.; Lin, C.H.; Hsieh, C.H.; Ho, C.Y. (2008). *Design of optimal coasting speed for saving social cost in mass rapid transit systems*. In Proceedings of the IEEE Third International Conference on Electric Utility Deregulation and Restructuring and Power Technologies, Nanjing, China, 6–9 April 2008; pp. 2833–2839.

Li Wenxin & Peng, Qiyuan & Wen, Chao & Wang, Pengling & Lessan, Javad & Xu, Xinyue (2020). *Joint optimization of delay-recovery and energy-saving in a metro system: A case study from China*. Energy, Elsevier, vol. 202(C).

X. Li & H.K. Lo (2014). *An energy-efficient scheduling and speed control approach for metro rail operations*. Transportation Research Part B: Methodological, Elsevier, vol. 64(C), pages 73-89.

H. Song, S. Gao, Y. Li, L. Liu, H. Dong (2023). *Train-Centric Communication Based Autonomous Train Control System*. IEEE Transactions on Intelligent Vehicles, vol.8, no.1, pp.721-731.

D. Trentesaux, R. Dahyot, A. Ouedraogo, D. Arenas, S. Lefebvre, W. Schon, B. Lussier, and H. Cheritel (2018). *The autonomous train*. In 2018 13th Annual Conference on System of Systems Engineering (SoSE). IEEE, 2018, pp. 514–520.

C. Gely, D. Trentesaux, and A. Le Mortellec (2020). *Maintenance of the autonomous train: A human-machine cooperation framework*. In Towards User-Centric Transport in Europe 2. pp. 135–148.

A. D. Kulkarni, B. B. Joshi, A. A. Panse, K. M. Shah (2022). *Autonomous Metro - A Step Towards Automation*. IEEE Pune Section International Conference (PuneCon), pp.1-6.

E. Dimitrova (2019). Analysis of Automatic Control Systems for Metro Trains. 2019 11th Electrical Engineering Faculty Conference (BulEF), pp. 1-4, doi: 10.1109/BulEF48056.2019.9030782

L. Li, H. Song, J. Ma, H. Dong (2022). Description and Analysis of Train-centric Communication based Autonomous Train Control System. IEEE 25th International Conference on Intelligent Transportation Systems (ITSC), pp.3315-3320.

E. Jansson, N. O.E. Olsson, O. Fröidh (2023). *Challenges of replacing train drivers in driverless and unattended railway mainline systems—A Swedish case study on delay logs descriptions*. Transportation Research Interdisciplinary Perspectives, vol.21, pp.100875.

J. Peleska, A.E. Haxthausen, T. Lecomte (2022). *Standardisation considerations for autonomous train control.* pp. 286–307. http://dx.doi.org/10.1007/978-3-031- 19762-8_22

M. Fisher, V. Mascard, K.Y. Rozier, B.H. Schlingloff, M. Winikoff, N. Yorke-Smith (2020). *Towards a framework for certification of reliable autonomous systems*. Auton. Agent. Multi-agent Syst. 35(1), 8 , https://doi.org/10.1007/s10458-020-09487-2.

N. Besinovic, L. De Donato, F. Flammini, R.M.P. Goverde, Z. Lin, R. Liu, S. Marrone, R. Nardone, T. Tang, V. Vittorini (2022). *Artificial intelligence in railway transport: Taxonomy, regulations, and applications*. IEEE Trans. Intell. Transp. Syst. 23 (9), 14011–14024.

R. Barman et al. (2015). *Automated train scheduling system using genetic algorithm*. Proc. Int. Symp. Adv. Comput. Commun. (ISACC), pp. 28-33.

L. Xiao, Z. Ya-Dong and G. Jin. (2013). *Application of genetic algorithm in automatic train protection*. Proc. 5th Int. Conf. Intell. Hum.-Mach. Syst. Cybern. (IHMSC), vol. 2, pp. 152-154.

G. Wang, S. Xiao, X. Chen,. et al. (2018). *Application of Genetic Algorithm in Automatic Train Operation*. Wireless Pers Commun 102, 1695–1704, https://doi.org/10.1007/s11277-017-5228-6.

S. Gao, H. Dong, B. Ning, Y. Chen, & X. Sun (2015). *Adaptive fault-tolerant automatic train operation using RBF neural networks*. Neural Computing and Applications, 26(1), 141–149.

H. Dong, S. Gao, H, B. Ning, L. Li (2013). *Extended fuzzy logic controllers for high speed train*. Neural Comput Appl 22(2): 321–328.

Y. Fu, Z. Gao, K. Li (2009). Optimization Method of Energy Saving Train Operation for Railway Network, Journal of Transportation Systems Engineering and Information Technology. Journal of Transportation Systems Engineering and Information Technology 9, 4, p90: https://doi.org/10.1016/S1570-6672(08)60074-4.

G. Lu , D. He and J. Zhang (2023). *Energy-Saving Optimization Method of Urban Rail Transit Based on Improved Differential Evolution Algorithm*. Sensors 2023, 23(1), 378; https://doi.org/10.3390/s23010378.

Y. DING, H. LIU, Y. BAI, F. ZHOU (2011). A Two-level Optimization Model and Algorithm for Energy-Efficient Urban Train Operation. Journal of Transportation Systems Engineering and Information Technology 11, 1, p96: https://doi.org/10.1016/S1570-6672(10)60106-7.

P. Kuppusamy, S. Venkatraman, C.A. Rishikeshan, Y.C.A. Padmanabha Reddy (2020) . *Deep learning based energy efficient optimal timetable rescheduling model for intelligent metro transportation systems*. Physical Communication .Volume 42, https://doi.org/10.1016/j.phycom.2020.101131.

J. Liao, F. Zhang, S. Zhang, G. Yang, Ch. Gong (2021). *Energy-saving optimization strategy of multi-train metro timetable based on dual decision variables: A case study of Shanghai Metro line one*. Journal of Rail Transport Planning & Management, Volume 17, 2021, Article 100234.

Q. Lu & X. Feng (2011). *Optimal control strategy for energy saving in trains under the four-aspect fixed autoblock system*, Journal of Modern Transportation. Journal of Modern Transportation 19, 2, p82: https://doi.org/10.1007/BF03325744.

K. Kim, S. Chien (2010). *Optimal Train Operation for Minimum Energy Consumption Considering Track Alignment*, Speed Limit, and Schedule Adherence, Journal of Transportation Engineering. Journal of Transportation Engineering 137, 9, p665: https://doi.org/10.1061/(ASCE)TE.1943-5436.0000246.

W. -S. Lin and J. -W. Sheu (2011). Optimization of Train Regulation and Energy Usage of Metro Lines Using an Adaptive-Optimal-Control Algorithm. IEEE Transactions on Automation Science and Engineering, vol. 8, no. 4, pp. 855-864, doi: 10.1109/TASE.2011.2160537.

M. McClanachan, C. Cole (2012). C*urrent train control optimization methods with a view for application in heavy haul railways*. Proceedings of the Institution of Mechanical Engineers, Part F: Journal of Rail and Rapid Transit .Proceedings of the Institution of Mechanical Engineers, Part F: Journal of Rail and Rapid Transit 226, 1, p36: https://doi.org/10.1177/0954409711406352.

K.K. Wong and T.K. Ho (2004). *Dynamic coast control of train movement with genetic algorithm*. Int. J. Syst. Sci., 2004, 35(13), 835–846.

J. Zhu, X. Feng, Q. He and J. Ziao (2005). *The simulation research for the ATO model based on fuzzy predictive control*. In proceeding of the Autonomous Decentralized Systems. ISADS 2005, pp. 235– 241.

S. Sekine, N. Imasaki, and T. Endo (1995). *Application of fuzzy neural network control to automatic train operation and tuning of its control rules*. International Joint Conference of the Fourth IEEE International Conference on Fuzzy Systems and The Second International Fuzzy Engineering Symposium. Proceedings of 1995 IEEE International Conference on, pp. 1741–1746, vol. 1744.

L. Yang, K. Li, Z. Gao, Xiang Li (2012). *Optimizing trains movement on a railway network*. Omega 40, 5, p619: https://doi.org/10.1016/j.omega.2011.12.001.

X. Lin, Z. Liang, L. Shen, F. Zhao, X. Liu, P. Sun, T. Cao (2023) *Reinforcement learning method for the multi-objective speed trajectory optimization of a freight train*. Control Engineering Practice. Volume 138.

M.A. Sandidzadeh, P. Havaei, (2023). A comprehensive study on reinforcement learning application for train speed profile optimization. Multimedia Tools and Applications. https://doi.org/10.1007/s11042-023-15051-3.

Y. Arikan, T. Şen, E. Çam (2022). *Actual-time modeling of a subway vehicle and optimal driving management with GA and ABC algorithms*. Journal of Engineering Research (Kuwait) Vol 10 No 4A.

S. Sun, Y. Li and H. Xu (2012). *Energy Consumption Optimization for High-Speed Railway Based on Particle Swarm Algorithm*. Fourth International Conference on Computational Intelligence and Communication Networks, pp. 879-882, doi: 10.1109/CICN.2012.214.

M. Yin, K. Li, X. Cheng (2020). A review on artificial intelligence in high-speed rail. Transportation Safety and Environment, Vol. 2, No. 4, 1–13.

L. S. Wang, H. Z. Xu, H. Y. Luo (2013). *An Intelligent Cruise Controller for High-Speed Train Operation Based on Fuzzy Neural Network Theory*, Applied Mechanics and Materials. Applied Mechanics and Materials, Vols. 300-301, p1405.

Y. Bai, T. K. Ho, B. Mao, Y. Ding and S. Chen (2014). *Energy-Efficient Locomotive Operation for Chinese Mainline Railways by Fuzzy Predictive Control*. IEEE Transactions on Intelligent Transportation Systems, vol. 15, no. 3, pp. 938-948, doi: 10.1109/TITS.2013.2292712.

J. Yang, L. Jia, Y. Fu and S. Lu (2017). *Speed Tracking Based Energy-Efficient Freight Train Control Through Multi-Algorithms Combination*. *IEEE Intelligent Transportation Systems Magazine*, vol. 9, no. 2, pp. 76-90, doi: 10.1109/MITS.2017.2666580.

W. Carvajal-Carreño, A. P. Cucala, A. Fernández-Cardador (2014). *Optimal design of energy-efficient ATO CBTC driving for metro lines based on NSGA-II with fuzzy parameters*. Engineering Applications of Artificial Intelligence, vol.36, pp.164, 2014.

H. Rong, C. Z. Yu (2014). Multiple Objective of Train Operation Process Based on Modified Particle Swarm Optimization, Applied Mechanics and Materials, Applied Mechanics and Materials, Vols. 513-517, p2927.

M. Zhang, Y. Chen, X. Sun, X. Hou and H. Cai (2014). *Particle-optimized control for automatic train operation based on sliding mode observer*. Proceedings 2014 International Conference on Informative and Cybernetics for Computational Social Systems (ICCSS), pp. 79-84, doi: 10.1109/ICCSS.2014.6961820.

N. Zhao, C. Roberts, S. Hillmansen and G. Nicholson (2015). *A Multiple Train Trajectory Optimization to Minimize Energy Consumption and Delay*. IEEE Transactions on Intelligent Transportation Systems, vol. 16, no. 5, pp. 2363-2372, doi: 10.1109/TITS.2014.2388356.

C. Zhang, G. Zeng, J. Wu, S. Wei, W. Zhang and B. Sun (2023). *A Bi-Level Optimization of Speed and Energy Management for Diesel-Electric Hybrid Train. IEEE Transactions on Vehicular Technology*, vol. 72, no. 8, pp. 10077-10089, doi: 10.1109/TVT.2023.3262579.

J. Liu, T. Shi, X. Ma, R. Xue, M. Liu (2021). *Optimal Train Speed Optimization under Several Safety Points by the PSO Algorithm*. IEEE Congress on Evolutionary Computation (CEC), pp.1333-1340.

W. ShangGuan, X. -H. Yan, B. -G. Cai and J. Wang (2015). *Multiobjective Optimization for Train Speed Trajectory in CTCS High-Speed Railway With Hybrid Evolutionary Algorithm*," in *IEEE Transactions on Intelligent Transportation Systems*, vol. 16, no. 4, pp. 2215-2225, doi: 10.1109/TITS.2015.2402160.

H. J. Kaleybar, M. Davoodi, M. Brenna, D. Zaninelli (2023). *Applications of Genetic Algorithm and Its Variants in Rail Vehicle Systems: A Bibliometric Analysis and Comprehensive Review*", *IEEE Access*, vol.11, pp.68972-68993.

Y. Huang, H. Yu, J. Yin, H. Hu, S. Bai, X. Meng, et al.,(2018). *An integrated approach for the energy-efficient driving strategy optimization of multiple trains by considering regenerative braking. Comput. Ind. Eng.*, vol. 126, pp. 399-409, Dec. 2018.

J. Ning, Y. Zhou, F. Long and X. Tao (2018). *A synergistic energy-efficient planning approach for urban rail transit operations*. *Energy*, vol. 151, pp. 854-863.

A. P. Cucala, A. Fernández, C. Sicre and M. Domínguez (2012). *Fuzzy optimal schedule of high speed train operation to minimize energy consumption with uncertain delays and driver's behavioral response*, *Eng. Appl. Artif. Intell.*, vol. 25, no. 8, pp. 1548-1557.

Tang, H., Dick, C. T., & Feng, X. (2015). *Improving Regenerative Energy Receptivity in Metro Transit Systems: Coordinated Train Control Algorithm*. Transportation Research Record, 2534(1), 48–56. https://doi.org/10.3141/2534-07.

W. Carvajal-Carreño, A. P. Cucala García, A. Fernández-Cardador and L. Söder (2015). *Efficient driving algorithms for non-disturbed and disturbed trains with the CBTC signalling system*. 2015

International Conference on Models and Technologies for Intelligent Transportation Systems (MT-ITS), Budapest, pp. 418-425, doi: 10.1109/MTITS.2015.7223289.

A. Fernández-Rodríguez, A. Fernández-Cardador and A. P. Cucala (2015). *Energy efficiency in high speed railway traffic operation: a real-time ecodriving algorithm*. IEEE 15th International Conference on Environment and Electrical Engineering (EEEIC), pp. 325-330, doi: 10.1109/EEEIC.2015.7165181.

K. Keskin and A. Karamancioglu. (2015). *A hybrid optimization algorithm for energy efficient train operation*. International Symposium on Innovations in Intelligent SysTems and Applications (INISTA), pp. 1-6, doi: 10.1109/INISTA.2015.7276732.

M. Brenna, F. Foiadelli, M. Longo (2016). *Application of Genetic Algorithms for Driverless Subway Train Energy Optimization*. International Journal of Vehicular Technology, Volume 2016, p1: https://doi.org/10.1155/2016/8073523.

J. Yin, D. Chen, L. Yang, T. Tang and B. Ran (2016). *Efficient Real-Time Train Operation Algorithms With Uncertain Passenger Demands*. IEEE Transactions on Intelligent Transportation Systems, vol. 17, no. 9, pp. 2600-2612, doi: 10.1109/TITS.2015.2478403.

J. Lesel, D. Bourdon, G. Claisse, P. Debay, B. Robyns (2017). *Real time electrical power estimation for the energy management of automatic metro lines*. Mathematics and Computers in Simulation. Volume 131, Pages 3-20, https://doi.org/10.1016/j.matcom.2016.06.003.

H. A. Hamid, G. L. Nicholson, H. Douglas, N. Zhao and C. Roberts (2016). *Investigation into train positioning systems for saving energy with optimised train trajectories*. IEEE International Conference on Intelligent Rail Transportation (ICIRT), pp. 460-468, doi: 10.1109/ICIRT.2016.7588769.

N. Zhao, C. Roberts, S. Hillmansen, Z. Tian, P. Weston, L. Chen (2017). *An integrated metro operation optimization to minimize energy consumption*, Transportation Research Part C: Emerging, Volume 75 , p168: https://doi.org/10.1016/j.trc.2016.12.013.

Jiannan Jia, Kai Yang, Lixing Yang, Yuan Gao & Shukai Li (2018). *Designing train-speed trajectory with energy efficiency and service quality*, Engineering Optimization, 50:5, 797-818, DOI: 10.1080/0305215X.2017.1358712

K. Keskin, A. Karamancioglu (2017). *Energy-Efficient Train Operation Using Nature-Inspired Algorithms*, Journal of Advanced Transportation. Volume 2017. https://doi.org/10.1155/2017/6173795.

Y. Jiateng, T. Tao, Y. Lixing; X. Jing, H. Yeran, G. Ziyou (2017). *Research and development of automatic train operation for railway transportation systems: A survey*. Transportation Research Part C: Emerging Technologies, 85, 548–572. doi:10.1016/j.trc.2017.09.009.

P. Caramia, G. Lauro, M. Pagano and P. Natale (2017). *Automatic train operation systems: A survey on algorithm and performance index*. AEIT International Annual Conference, pp. 1-6, doi: 10.23919/AEIT.2017.8240522.

Y. Liang, Hao Liu, C. Qian & G. Wang (2019). *A Modified Genetic Algorithm for Multi-Objective Optimization on Running Curve of Automatic Train Operation System Using Penalty Function Method.* nternational Journal of Intelligent Transportation Systems Research volume 17, pages74–87.

A. Fernández-Rodríguez, A. Fernández-Cardador, A. P. Cucala (2018). Balancing energy consumption and risk of delay in high speed trains: A three-objective real-time eco-driving algorithm with fuzzy parameters. Volume 95, Pages 652-678. https://doi.org/10.1016/j.trc.2018.08.009.

A. Fernández-Rodríguez, A. Fernández-Cardador, A. P. Cucala (2018). *Real time eco-driving of high speed trains by simulation-based dynamic multi-objective optimization*. Simulation Modelling Practice and Theory 84, p50: https://doi.org/10.1016/j.simpat.2018.01.006.

H. Zhi-yu, Y. Zhi-jie and L. Jing-yang (2018). *Trajectory Optimization for High-Speed Train Operation*. 2018 37th Chinese Control Conference (CCC), Wuhan, China, 2018, pp. 2065-2070,

F. Gao, F. Wang, Y. Wu, X. Cai, Xinqin Li, Z. Yu (2018). *Study on Speed Controller of Automatic Train Operation for High-speed Train Based on Grey Genetic Algorithm*. APCIM & ICTTE 2018: Proceedings of the Asia-Pacific Conference on Intelligent Medical 2018 & International Conference on Transportation and Traffic Engineering, Pages 27–31https://doi.org/10.1145/3321619.3321635.

J. Feng, Z. Ye, C. Wang, M. Xu and S. Labi (2019). *An Integrated Optimization Model for Energy Saving in Metro Operations*," in IEEE Transactions on Intelligent Transportation Systems, vol. 20, no. 8, pp. 3059-3069, doi: 10.1109/TITS.2018.2871347.

P. M. Fernández, I. V. Sanchís, V. Yepes, R. I. Franco (2019). *A review of modelling and optimisation methods applied to railways energy consumption*. Journal of Cleaner Production 222, p153: https://doi.org/10.1016/j.jclepro.2019.03.037.

J. Lu, S. Dai and X. Sun (2019). *The Application of Multi-objective PSO Algorithm in Energy-efficient optimization of Metro Systems*. IEEE 5th International Conference on Computer and Communications (ICCC), pp. 170-177, doi: 10.1109/ICCC47050.2019.9064487.

A. Fernández-Rodríguez, S. Su, A. Fernández-Cardador, A. P. Cucala & Y. Cao (2021). *A multi-objective algorithm for train driving energy reduction with multiple time targets*, Engineering Optimization, 53:4, 719-734, DOI: 10.1080/0305215X.2020.1746782.

Z. Pan, M. Chen, S. Lu, Z. Tian and Y. Liu (2020) *Integrated Timetable Optimization for Minimum Total Energy Consumption of an AC Railway System*. IEEE Transactions on Vehicular Technology, vol. 69, no. 4, pp. 3641-3653, doi: 10.1109/TVT.2020.2975603.

J. P. Powell, A. Fraszczyk, C. N. Cheong, and H. K. Yeung (2016). *Potential benefits and obstacles of implementing driverless train operation on the tyne and wear metro: A simulation exercise*,'' *Urban Rail Transit*, vol. 2, nos. 3_4, pp. 114_127.

M. Matsumoto, S. Kitamura, and M. Sato (2001). *High assurance technologies for autonomous decentralize train control system*, in *Proc. 6th IEEE Int. Symp. High Assurance Syst. Eng.*, pp. 220_227, doi: 10.1109/HASE.2001.966822.

T. S. Mohammed, W. F. Al-Azzo, M. A. Akaak, and M. L. Suroor, (2014). Full automation in driverless trains: A microcontroller-based prototype,'' *Int. J. Adv. Res. Electr., Electron. Instrum. Eng.*, vol. 3, no. 7, pp. 10417_10422, Jul. 2014.

R. Lagay and G. M. Adell (2018). *The autonomous train: A game changer for the railways industry*,'' in *Proc. 16th Int. Conf. Intell. Transp. Syst. Telecommun. (ITST)*, pp. 1_5, doi: 10.1109/ITST.2018.8566728.

L. Habib, O. Oukacha, S. Enjalbert (2021). Towards Tramway Safety by Managing Advanced Driver Assistance Systems depending on Grades of Automation. IFAC PapersOnLine 54-2, 227–232.

Q. Gadmer, P. Richard, J.Ch. Popieul, Ch. Sentouh (2022). *Railway Automation: A framework for authority transfers in a remote environment*. IFAC-PapersOnLine Volume 55, Issue 29, Pages 85-90.

F.3 Results of the state-of-the-art review for the Spacecraft domain

Spacecraft operations are always characterized by the presence of automation on-board, corresponding to the attitude and orbit control subsystems implemented on-board as well as the automatic management of other functions beyond the reach of human operators. Some functions corresponding to the definition of advanced automation are already part of normal spacecraft operations (e.g., reconfiguring the spacecraft to manage faulty hardware by means of redundancy) to deal with the long-time delays associated with ground control.

In view of this, the automation level is very mature and the study of advanced automation, mainly in connection with deep space missions and actually leading to effective implementations started very early with respect to other fields. In terms of the classical Guidance, Navigation and Control (GNC) paradigm,

Overview of available papers

The state-of-the-art review in the context of spacecraft autonomy was classified according to the following categories: spacecraft autonomy, spacecraft automation and spacecraft advanced automation. The literature review considered publications in the Scopus database based on the following keywords, over the 2000-2023 range:

- «Spacecraft autonomy» – 1217 results
- «Autonomous spacecraft guidance» & «Autonomous spacecraft navigation» – 709 + 1723 results

Focusing on the «Spacecraft autonomy» keyword, the results can be summarized as follows in terms of time evolution of the number of publications:

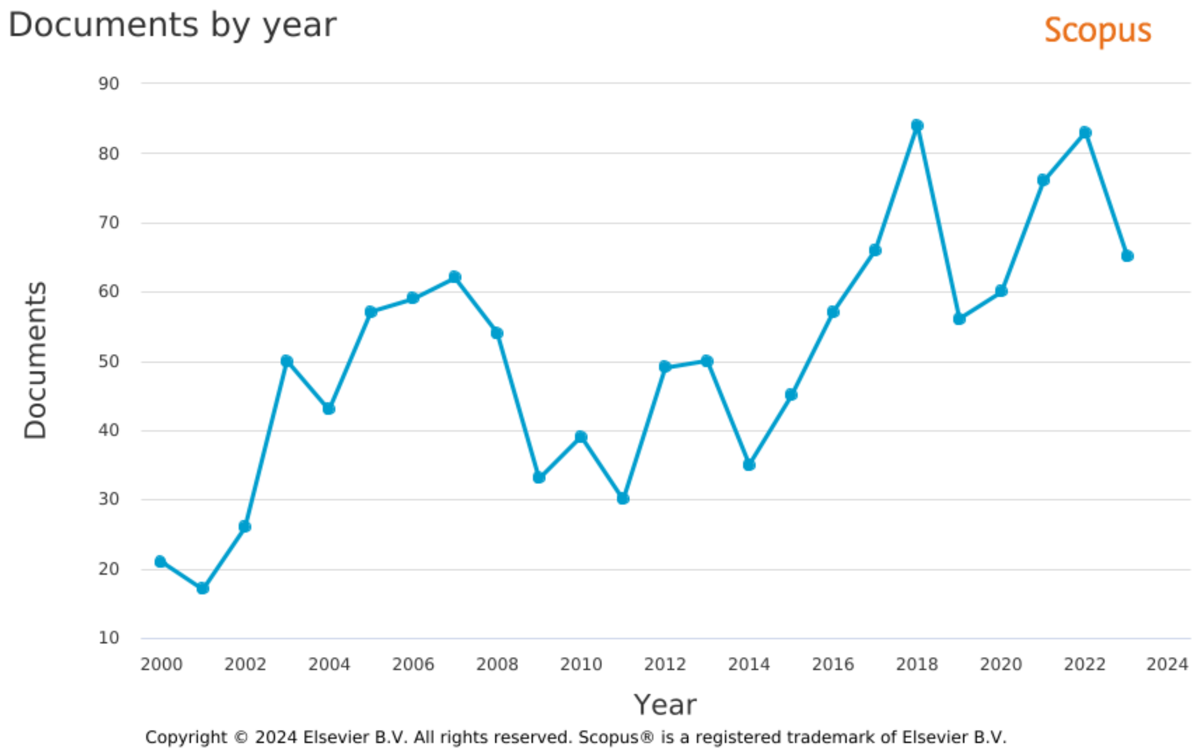

As can be seen the production is not as extensive as for other sectors. In terms of geographic distribution, the US clearly dominates, followed by the EU, which outperforms China collectively:

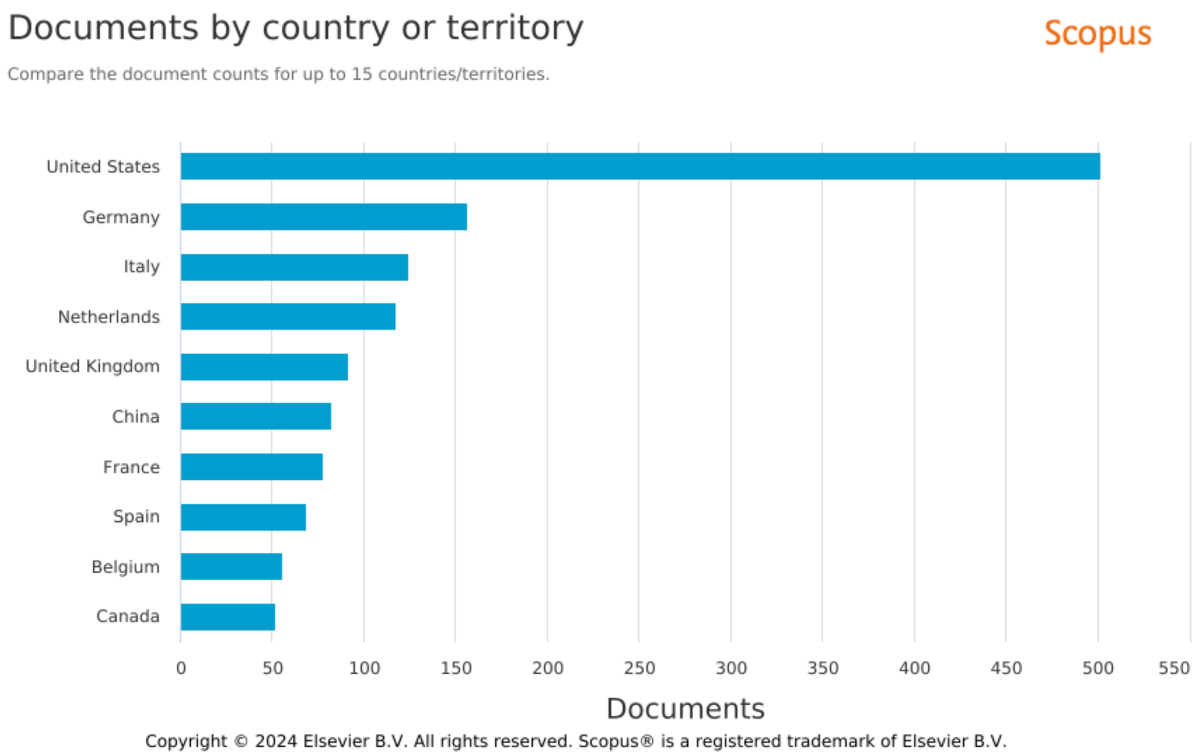

On the other hand, in terms of most productive institutions worldwide the results can be summarized as follows:

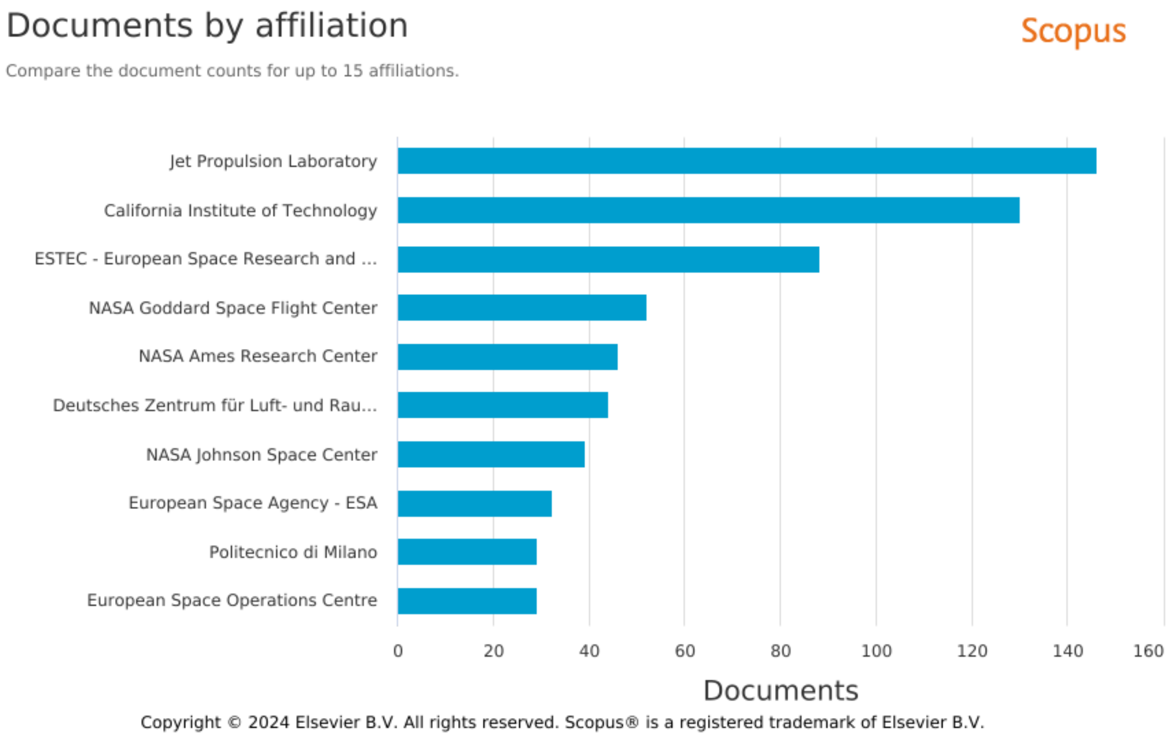

As for the «Autonomous spacecraft guidance» & «Autonomous spacecraft navigation» keywords, similar considerations can be made, the corresponding analysis has been omitted for the sake of conciseness.

Conclusions:

- Scientific and technological research in the field is increasing, though not as rapidly as in other domains (small dimension of the scientific community).
- There is a lack of a systematic set of definitions in the field, most of the literature refers generically to “autonomy” without considering a unified and consistent scale.
- Many publications provide contributions (in terms of hardware, algorithms, software) for the implementation of advanced automation in several functions, chiefly guidance and navigation.
- In terms of applications, the most challenging areas appear to be planetary exploration, satellite formations, proximity operations and docking and of course deep space missions.